

Deformation behavior of extruded magnesium alloys ME21, WE54, L4 and LA41

vorgelegt von

Dipl.-Ing.

Martin Christoph Lentz

aus Berlin

von der Fakultät III - Prozesswissenschaften

der Technischen Universität Berlin

zur Erlangung des akademischen Grades

Doktor der Ingenieurwissenschaften

- Dr.-Ing. -

genehmigte Dissertation

Promotionsausschuss:

Vorsitzender: Prof. Dr.-Ing. M.H. Wagner

Gutachter: Prof. Dr. rer. nat. W. Reimers

Gutachter: Prof. Dr.-Ing. K.U. Kainer

Tag der wissenschaftlichen Aussprache: 20 April 2015

Berlin 2015

D83

Acknowledgements

The present dissertation was elaborated during my employment at the Technische Universität Berlin – Metallic Materials. Before proceeding, I would like to express my sincere gratitude to many people, who enabled the completion of this study through their long-lasting support.

First, I would like to thank Prof. Walter Reimers (TU Berlin, Metallic Materials) for the scientific and financial support making this project possible, for helpful discussion and guidance. Moreover, I would like to thank Prof. Reimers for supporting my abroad research activities at the Los Alamos National Laboratory and for being my academic supervisor. Further, I would like to express my gratitude to Prof. Karl Ulrich Kainer (Helmholtz-Zentrum Geesthacht, MagIC) for his interest in my work and his willingness to be my second academic supervisor. I would like to thank Prof. Manfred Wagner (TU Berlin, Polymer Engineering and Physics) for being the chairman of the thesis committee.

I'm indebted to Bjørn Clausen for enabling my research visit at the Los Alamos National Laboratory (LANL, LANSCE-LC) being the starting point for many subsequent investigations and collaborations, the introduction to the EPSC code as well as manifold helpful discussions. In this regard I would like to thank Carlos Tomé (LANL, MST-8) and Marko Knezevic (University of New Hampshire, Mechanical Engineering) for providing access to their versions of the EPSC code as well as introduction to the model and discussion. Moreover, I would like to express my sincere gratitude to Irene J. Beyerlein (LANL, Theoretical Division) for helpful discussion and guidance as well as close collaboration regarding the investigation of twinning and EPSC modeling.

In the context of the conducted synchrotron and neutron diffraction studies, I would like to thank Christoph Genzel, Manuela Klaus (Helmholtz-Zentrum Berlin, Mikrostruktur- und Eigenspannungsanalyse) Sven Vogel (LANL, LANSCE-LC) and Levente Balogh (Queen's University Kingston) for their great support running the experiments at BESSY II or LANSCE-LC and their help during the data evaluation as well as helpful discussion. In addition, I would like to thank Katrin Brömmelhoff, Dirk Gräning, Felix Hohlstein, Florian Schmack, Christoph Seyfert, Alexander Treff and Michael Wagner for performing experiments at the EDDI beamline enabling two successful weeks of 24/7 synchrotron investigations. Moreover, I gratefully acknowledge the support of Rodrigo S. Coelho (SENAI, CIMATEC), Norbert Schäfer (Helmholtz-Zentrum Berlin, Nanoarchitectures for Energy Conversion), Dirk Berger, Christoph Fahrenson, Iryna Driehorst, Sören Selve, Jörg Nissen (TU Berlin, ZELMI), Bettina Camin and Thomas Link (TU Berlin, Metallic Materials) during electron microscopy studies including, SEM, (HR-)TEM, EBSD and FIB.

Furthermore, I would like to thank all my colleagues at the chair of Metallic Materials and at LANSCE-LC for their long-lasting support during the last couple of years including experimental support and encouragement. Last, I would like to thank my family, my girlfriend Claudia Brieger and my friends for the continuous encouragement and for enduring all my moods.

Abstract

The present study investigates the deformation behavior of the extruded magnesium alloys ME21, WE54, L4 and LA41. Altering the extrusion parameters billet temperature, extrusion ratio and cooling medium as well as post extrusion heat treatments enabled the generation of materials featuring different grain sizes, textures, precipitate and solute contents.

In order to assess their effect on the deformation behavior, the initial condition as well as deformed materials were characterized using optical microscopy, scanning electron microscopy including ex-situ and in-situ EBSD investigations, transmission electron microscopy, laboratory X-ray diffraction, in-situ energy-dispersive X-ray synchrotron diffraction during loading and in-situ TOF neutron diffraction during heat treatments as well as elastoplastic self-consistent modeling. The combination of these complementary techniques enabled the interpretation of the very different deformation behavior of the investigated alloys.

By applying different extrusion parameters and heat treatments within the temperature range from 475 °C to 550 °C a variety of textures can be produced within the ME21 extrusions. 550 °C heat treatments enable the generation of remarkably high elongations to failure in compression, which were explained by an enhanced rare earth texture and concurrent optimum grain size and precipitate distributions. Compression tests parallel to the extrusion direction result in the extensive activation of $\{10\bar{1}2\}\langle 10\bar{1}\bar{1}\rangle$ tension twinning in this alloy.

In contrast the WE54 extrusions feature very weak textures and a very low $\{10\bar{1}2\}\langle 10\bar{1}\bar{1}\rangle$ tension twinning activity particularly in as-extruded conditions. In this case the alloying elements are almost completely retained in solid solution. Post extrusion heat treatments resulting in the generation of precipitates within the grains or at grain boundaries substantially increase the tension twinning activity through the reduction of the solute concentrations. In addition, it was found that plate-shape precipitates on the $\{10\bar{1}0\}_\alpha$ planes harden $\langle a \rangle$ basal slip more than the other slip systems.

Deviating from conventional magnesium extrusions the L4 and LA41 alloys feature a remarkably low tension-compression yield asymmetry. In addition, the compression yield strength is higher than the tensile yield strength indicating a significant hardening of tension twin formation through solute Li. In addition, secondary $\{10\bar{1}1\}\langle 10\bar{1}\bar{2}\rangle$ compression twinning (CTW-ing) and tertiary $\{10\bar{1}\bar{1}\}\langle 10\bar{1}\bar{2}\rangle$ double twinning (DTW-ing) are remarkably active in the Li based alloys. A pronounced double twin variant selection was observed and analyzed using EBSD and (HR-)TEM. In-situ EBSD analysis tracking the transition from a secondary CTW into a DTW showed a very slow propagation of a secondary CTW, while the tertiary DTWs propagate substantially faster once nucleated. (HR-)TEM analysis displays an important basal slip activity and many basal stacking faults within the primary tension twin and the secondary compression twin. Additionally, the HR-TEM investigations revealed a high number of basal dislocations in the vicinity of the compression twin to double twin transition providing strong evidence of a relation between the observed predominance of type 1 double twins and the dissociation of extended basal dislocations. The analysis of extrusions featuring different grain sizes, but similar textures, revealed a strong grain size dependence of compression twinning and double twinning, where grain refinement appears to hinder compression twinning more than tension twinning. However, the compression twin to double twin transition was found to be insensitive to the grain size.

Kurzfassung

Die vorliegende Arbeit untersucht das Verformungsverhalten der stranggepressten und wärmebehandelten Magnesiumknetlegierungen ME21, WE54, L4 und LA41. Durch die Variation der Strangpressparameter Bolzeneinsatztemperatur, Pressverhältnis und Abkühlmedium sowie nachgeschaltete Wärmebehandlungen konnten die Korngröße, die Texturen sowie der Ausscheidungs- und Lösungszustand in weiten Grenzen eingestellt werden. Die Produkte wurden mittels Lichtmikroskopie, Rasterelektronenmikroskopie (inkl. ex-situ und in-situ EBSD Untersuchungen), Transmissionselektronenmikroskopie, Röntgendiffraktion, in-situ energie-dispersiver Synchrotron Röntgen- und in-situ TOF Neutronendiffraktion sowie elastoplastic self-consistent Simulationen untersucht, um den Einfluss der obengenannten mikrostrukturellen Parameter auf das Verformungsverhalten zu analysieren.

Wärmebehandlungen bei Temperaturen zwischen 475 °C und 550 °C ermöglichen es im Falle der ME21 Legierung eine Vielzahl unterschiedlicher Texturen einzustellen. Dabei führen insbesondere 550 °C Wärmebehandlungen zu außergewöhnlich hohen Bruchdehnungen im Druckversuch, die durch die verstärkte Seltene Erden Textur und optimale Korngrößen- und Ausscheidungsverteilungen zu erklären sind. Im Druckversuch parallel zur Strangpressrichtung weist diese Legierung eine hohe $\{10\bar{1}2\}\langle 10\bar{1}\bar{1}\rangle$ Zugzwillingsaktivität auf.

Im Gegensatz dazu zeichnen sich die WE54 Strangpressprodukte durch sehr schwache Texturen und eine sehr niedrige Zugzwillingsaktivität aus, wobei die Legierungselemente im stranggepressten Zustand vorwiegend im Mischkristall gelöst vorliegen. Durch nachgelagerte Wärmebehandlung kommt es zur Bildung von Ausscheidungen in den Körnern oder an den Korngrenzen, die mit einer deutlich erhöhten Zugzwillingsaktivität einhergeht. Die durchgeführten Untersuchungen haben gezeigt, dass die verstärkte Zugzwillingsaktivität auf die reduzierten Lösungselementkonzentrationen, die durch die Ausscheidungsbildung hervorgerufen werden, zurückzuführen ist. Des Weiteren konnte gezeigt werden, dass plattenförmige Ausscheidungen auf $\{10\bar{1}0\}_\alpha$ Ebenen insbesondere die basale $\langle a \rangle$ Gleitung behindern.

Die Legierungen L4 und LA41 weisen eine wesentlich geringere Zug-Druck-Asymmetrie als die meisten Magnesiumlegierungen auf. Dabei ist die Druckfließgrenze geringfügig höher als die Zugfließgrenze, was auf eine deutlich verfestigte Zugzwillingsbildung durch gelöstes Lithium hinweist. Zusätzlich wurden in dieser Legierung eine hohe Aktivität von sekundären $\{10\bar{1}1\}\langle 10\bar{1}2 \rangle$ Druckzwillingen (CTW) und tertiären $\{10\bar{1}1\}\text{-}\{10\bar{1}2\}$ Doppelzwillingen (DTW) sowie eine ausgeprägte Dominanz der DTW Variante "Typ 1" beobachtet. Mittels in-situ EBSD Messungen konnte der Übergang von einem CTW in einen DTW verfolgt und das deutlich schnellere Wachstum des internen Zugzwillings (TTW) gegenüber dem langsamen Wachstum des CTWs gezeigt werden. Durch den Einsatz von (HR-)TEM Untersuchungen konnte eine starke Aktivität der basalen Gleitung sowie eine Vielzahl von basalen Stapelfehlern im primären TTW und im sekundären CTW beobachtet werden. Des Weiteren zeigten HR-TEM Analysen im Umfeld des CTW-DTW-Übergangs eine hohe Anzahl von basalen Versetzungen, was auf einen Zusammenhang zwischen der Dissoziation basaler Versetzungen und der Vorherrschaft der Typ 1 DTW Variante hinweist. Die Untersuchung von Strangpressprodukten, die ähnliche Texturen aber signifikant unterschiedliche Korngrößen aufweisen, hat eine starke Korngrößenabhängigkeit der Druckzwillingsbildung und der Doppelzwillingsbildung nachgewiesen, wobei die Druckzwillingsbildung eine stärkere Korngrößenabhängigkeit als die Zugzwillingsbildung zeigt. Darüber hinaus scheint Kornfeinung den Übergang von sekundären Druckzwillingen zu tertiären Doppelzwillingen nur wenig zu beeinflussen.

Table of contents

Acknowledgements.....	I
Abstract	II
Kurzfassung.....	III
Table of contents	IV
Index of figures	VII
Index of tables	X
Abbreviations	XI
1. Introduction	1
2. Literature review	2
2.1 Magnesium and its deformation mechanisms.....	2
2.1.1 Stacking fault energy of Mg.....	2
2.1.2 Crystallographic slip.....	2
2.1.3 Slip systems	3
2.1.4 Deformation twinning	4
2.1.5 Microstructure effects on the deformation behavior.....	7
2.1.5.1 Grain size.....	8
2.1.5.2 Precipitates	8
2.1.5.3 Texture.....	9
2.2 Recrystallization in Mg alloys.....	10
2.3 Extrusion	11
2.3.1 Extrusion of Mg alloys.....	12
2.4 Influence of alloying elements	13
2.4.1 ME21	13
2.4.2 WE54.....	14
2.4.3 L4 and LA41	16
3. Aim	18
4. Materials and characterization techniques	19
4.1 Alloys and metallographic sample preparation.....	19
4.2 Extrusion and heat treatments.....	20
4.3 Mechanical testing.....	20
4.4 Electron microscopy	20
4.4.1 Scanning electron microscopy	20
4.4.2 Transmission electron microscopy.....	22
4.5 Diffraction.....	23
4.5.1 Laboratory X-ray texture measurements.....	23
4.5.2 Time-of-flight neutron diffraction for texture analysis.....	24
4.5.3 In-situ energy-dispersive X-ray synchrotron diffraction.....	24
4.6 Elastoplastic self-consistent modeling	26

4.6.1 Voce hardening law	26
4.6.2 Finite initial fraction and continuity twin model	27
4.6.3 Dislocation based hardening law	27
4.6.4 Composite grain based twinning model and related barrier effects	28
5. Results.....	29
5.1 ME21.....	29
5.1.1 Extrusion billets	29
5.1.2 Extrusion products	29
5.1.2.1 Microstructure and texture.....	29
5.1.3 Heat treatments	31
5.1.3.1 In-situ TOF neutron diffraction.....	31
5.1.3.2 Microstructure and texture.....	32
5.1.4 Mechanical properties.....	37
5.1.4.1 Flow curves.....	37
5.1.4.2 Deformed microstructure.....	39
5.1.4.3 EPSC simulations	43
5.2 WE54	46
5.2.1 Extrusion billets	46
5.2.2 Extrusion products	47
5.2.2.1 Microstructure and texture.....	47
5.2.3 Heat treatments	48
5.2.3.1 Microstructure and texture.....	48
5.2.4 Mechanical properties.....	51
5.2.4.1 Flow curves.....	51
5.2.4.2 Deformed microstructure.....	52
5.2.4.3 EPSC simulations	57
5.3 L4.....	63
5.3.1 Extrusion billets	63
5.3.2 Extrusion products	63
5.3.2.1 Microstructure and texture.....	64
5.3.3 Mechanical properties.....	65
5.3.3.1 Flow curves.....	65
5.3.3.2 Deformed microstructure.....	66
5.3.3.3 EPSC simulations	75
5.4 LA41	80
5.4.1 Extrusion billets	80
5.4.2 Extrusion products.....	80
5.4.2.1 Microstructure and texture.....	80
5.4.3 Mechanical properties.....	82

5.4.3.1 Flow curves	82
5.4.3.2 Deformed microstructure	83
5.4.3.3 EPSC simulations	84
6. Discussion	88
6.1 Cast billets.....	88
6.2 Effect of the extrusion parameters on RX, microstructure and texture	88
6.2.1 ME21	89
6.2.2 WE54.....	91
6.2.3 L4 and LA41	92
6.3 Effect of heat treatments on the microstructure and texture.....	93
6.3.1 ME21	93
6.3.2 WE54.....	95
6.4 Deformation behavior	97
6.4.1 ME21	97
6.4.1.1 Grain size effects	97
6.4.1.2 Twinning.....	98
6.4.1.3 Texture effects	99
6.4.1.4 Precipitate effects.....	101
6.4.1.5 Deformation mode activity and hardening parameters.....	103
6.4.2 WE54.....	104
6.4.2.1 Grain size effects	104
6.4.2.2 Twinning.....	105
6.4.2.3 Texture effects	105
6.4.2.4 Precipitate and solute effects	106
6.4.2.5 Deformation mode activity and hardening parameters.....	108
6.4.3 L4 and LA41	109
6.4.2.1 Grain size effects	109
6.4.2.2 Twinning.....	110
6.4.2.3 Texture effects	115
6.4.2.4 Precipitates	115
6.4.2.5 Deformation mode activity and hardening parameters.....	116
6.5 Mg-Li superlattice	117
7. Summary and conclusions	118
8. Directions for future research	121
9. References	122
Project related own publications.....	129

Index of figures

Fig 2.1: Hexagonal close packed lattice.....	2
Fig 2.2: Determination of the resolved shear stress	3
Fig 2.3: Slip systems.....	3
Fig 2.4: Schematic drawings of TTWs (a, c) and CTWs (b, d))	5
Fig 2.5: Schematic drawing of internal TTW-ing within a preexisting CTW	6
Fig 2.6: Sequence of primary TTW-ing, secondary CTW-ing and tertiary TTW-ing	6
Fig 2.7: Schematic illustrating changes of the MDFs during sequential twinning	6
Fig 2.8: Schematic illustrating different DTW variants	7
Fig 2.9: Orowan strengthening of different precipitates	9
Fig 2.10: Schematic drawing of the indirect extrusion process.....	12
Fig 2.11: Schematic drawing of typical extrusion textures	12
Fig 2.12: a) Tension – compression asymmetry of an ME21 extrusion, b) SF distribution	13
Fig 2.13: Binary phase diagrams: a) Mg-Mn, b) Mg-Ce.....	14
Fig 2.14: Binary phase diagrams: a) Mg-Nd, b) Mg-Y	15
Fig 2.15: Precipitation sequence of Mg-Y-Nd alloys.....	15
Fig 2.16: Precipitation in WE54 aged at 250 °C	16
Fig 2.17: a) Binary Mg-Li phase diagram, b) section through the Mg-Li-Al phase diagram ...	17
Fig 4.1: Specimen geometry	20
Fig 4.2: Schematic drawing of an EBSD setup.....	22
Fig 4.3: Schematic of a TEM in imaging mode and diffraction mode	22
Fig 4.4: Schematic of the HIPPO diffractometer.....	24
Fig 4.5: Setup of the EDDI beamline.....	25
Fig 4.6: Illustration of the effect of the hardening parameters on the hardening rate	26
Fig 5.1: a) Macrosection of a homogenized ME21 cast billet.....	29
Fig 5.2: Exemplary micrographs illustrating the effect of extrusion parameters on the d_g	30
Fig 5.3: Histograms showing the effect of the extrusion parameters on d_g	30
Fig 5.4: Measured extrusion texture (IPF ED)	30
Fig 5.5: Time resolved analysis of the texture development (IPF ED)	31
Fig 5.6: EBSD maps showing the microstructure after 5 min annealing	32
Fig 5.7: EBSD maps showing the microstructure after 10 h annealing	33
Fig 5.8: Histograms of the d_g : a) 475 °C, b) 500 °C, c) 525 °C, d) 550 °C.	33
Fig 5.9: Texture evolution determined from the recorded EBSD data.....	34
Fig 5.10: Quasi-in-situ EBSD analysis of a 45 min 475 °C heat treatment.....	35
Fig 5.11: Longitudinal section of the initial microstructure	36
Fig 5.12: SEM images of the coarse precipitate fraction (mainly $Mg_{12}Ce$)	36
Fig 5.13: TEM images of the fine precipitate fraction	37
Fig 5.14: Comparison of the extrusion and annealing textures.....	37
Fig 5.15: Flow curves of the extruded bars tested in uniaxial compression and tension.	38
Fig 5.16: Flow curves of heat treated extrusion B	39
Fig 5.17: EBSD maps, BC maps highlighting twin boundaries	40
Fig 5.18: MDFs: a) strain (ϵ) = -5 %, b) ϵ = -10 %, c) ϵ = -12 %, d) ϵ = -18 %.....	41
Fig 5.19: Cross sections of compression samples	42
Fig 5.20: IPFs as a function of the strain	42
Fig 5.21: EPSC simulation	44
Fig 5.22: EPSC simulation	44
Fig 5.23: Simulated IPFs as a function of the strain	45
Fig 5.24: Simulation of the effect of the texture on the flow curves.....	46

Fig 5.25: Micrograph of a homogenized WE54 cast billet.....	46
Fig 5.26: Optical micrographs showing the microstructure in the extruded bars	47
Fig 5.27: Histogram showing the effect of the extrusion parameters on the d_g	47
Fig 5.28: Y-rich precipitates in an extruded WE54 bar	48
Fig 5.29: Measured extrusion texture (IPFs ED).....	48
Fig 5.30: Micrographs showing the microstructure	49
Fig 5.31: SEM images showing precipitates.....	49
Fig 5.32: TEM images of precipitates	50
Fig 5.33: Effect of heat treatments on the texture.....	50
Fig 5.34: Flow curves of the extruded bars tested in uniaxial compression and tension	51
Fig 5.35: Effect of heat treatments on the flow curves.....	51
Fig 5.36: EBSD maps, BC maps highlighting twin boundaries	53
Fig 5.37: MDFs of compression samples (extrusion A)	54
Fig 5.38: EBSD maps of deformed samples (based on extrusion C).....	55
Fig 5.39: Histograms showing MDFs at -5 % strain.....	56
Fig 5.40: IPFs showing texture development during deformation	56
Fig 5.41: Comparison of the experimental and simulated flow curves	58
Fig 5.42: Comparison of the measured and predicted ϵ_{hkl} during compression.....	59
Fig 5.43: Comparison of the measured and predicted ϵ_{hkl} during tension	60
Fig 5.44: IPFs showing the simulated textures	61
Fig 5.45: Relative activities of the active deformation modes predicted by the EPSC model	62
Fig 5.46: Micrograph of a L4 cast billet.....	63
Fig 5.47: Microstructure of extrusions, which were processed using R 41 : 1	64
Fig 5.48: Histograms showing the effect of the extrusion parameters on d_g	64
Fig 5.49: SEM images showing (Al-)Si-rich phases (ED \uparrow).....	65
Fig 5.50: IPFs showing the effect of extrusion parameters	65
Fig 5.51: Flow curves of the extruded bars tested in uniaxial compression and tension	66
Fig 5.52: Sequential activation of TTW-ing, CTW-ing and DTW-ing	67
Fig 5.53: MDFs: a) strain (ϵ) = -5 %, b) ϵ = -10 %, c) ϵ = -12 %, d) ϵ = -18 %	68
Fig 5.54: a, b) experimental setup of the in-situ EBSD analysis	69
Fig 5.55: a) Bright field image at the [2110] ZA	70
Fig 5.56: HR-TEM analysis of the a) primary TTW (A) – secondary CTW (B) interface	72
Fig 5.57: HR-TEM and inverted FFT using the 0002 spots.....	73
Fig 5.58: HR-TEM and inverted FFT using the 0110 spots.....	73
Fig 5.59: a) and b) EBSD maps highlighting CTW (yellow) and type 1 DTW (green).....	75
Fig 5.60: Comparison of the experimental and simulated flow curves	76
Fig 5.61: Comparison of the measured and simulated texture evolution	77
Fig 5.62: Comparison of the experimental ϵ_{hkl} data (colored) and simulation (gray lines)	78
Fig 5.63: Evolution of the average CRSS during compression	78
Fig 5.64: Relative activities of the active deformation modes predicted by the EPSC model	79
Fig 5.65: Micrograph of a LA41 cast billet	80
Fig 5.66: Microstructure of extrusions, which were processed using R 41 : 1	81
Fig 5.67: Histograms showing the effect of the extrusion parameters on the d_g	81
Fig 5.68: SEM images showing (Al-)Si-rich phases (ED \uparrow).....	81
Fig 5.69: IPFs showing the effect of the extrusion parameters	82
Fig 5.70: Flow curves of the extruded bars tested in uniaxial compression and tension	82
Fig 5.71: a) and b) EBSD maps highlighting CTWs (yellow) and type 1 DTWs (green)	83
Fig 5.72: Comparison of the experimental and simulated flow curves	84
Fig 5.73: Comparison of the measured and simulated texture evolution	85

Fig 5.74: Comparison of the experimental ε_{hkl} data (colored) and simulation (gray lines)	86
Fig 5.75: Evolution of the average CRSS during compression	87
Fig 5.76: Relative activities of the active deformation model predicted by the model	87
Fig 6.1: Micrographs of the front-ends of ME21 extrusion	90
Fig 6.2: IPFs (\parallel ED) illustrating the shifting maximum density as a function of the applied R 90	90
Fig 6.3: Effect of SBN (left) and GBN (right) on texture randomization	92
Fig 6.4: Effect of a 1 h 350 °C annealing on the texture of extrusions: a) L4, b) LA41	93
Fig 6.5: Comparison of the IPFs of all grains and AGG grains (10 h 475 °C)	94
Fig 6.6: EPMA line scans illustrating the Y and Nd concentration	96
Fig 6.7: SEM images displaying the effect of two step ageing	96
Fig 6.8: Hall-Petch plots considering CYS and TYS of the extrusions	97
Fig 6.9: Compression flow curves of extruded and heat treated samples	98
Fig 6.10: EPSC simulations of texture effects	101
Fig 6.11: Effect of T_B and annealings on the mean equivalent diameter of precipitates	102
Fig 6.12: a) Orowan strengthening	102
Fig 6.13: Hall-Petch plots considering CYS and TYS of the extrusions	104
Fig 6.14: EPSC simulations of texture effects	106
Fig 6.15: Orowan strengthening for prismatic plate-shaped precipitates	107
Fig 6.16: Hall-Petch plots considering CYS and TYS of the extrusions: a) L4, b) LA41	109
Fig 6.17: a) Compression flow curves \perp ED	112
Fig 6.18: EBSD analysis of compression samples (\perp ED) of the extrusion L	113
Fig 6.19: EBSD analysis of compression samples (\perp ED) of the extrusion J	114
Fig 6.20: Optical micrograph of a compression sample of the MG material (extrusion L) ...	114
Fig 6.21: EPSC simulations of texture effects	115

Index of tables

Table 2.1: Calculated SFE (meV) for different types of stacking faults	2
Table 2.2: Independent deformation modes in magnesium	3
Table 2.3: Initial CRSS of various alloys, which were determined via constitutive modeling... 4	4
Table 4.1: Chemical compositions of the investigated alloys (wt%).....	19
Table 4.2: Applied etching solutions.....	19
Table 4.3: Applied experimental parameters	25
Table 5.1: Summary of the applied extrusion parameters	29
Table 5.2: Applied extrusion parameters and resulting average d_g (μm)	30
Table 5.3: Tension compression yield asymmetry	39
Table 5.4: Hardening parameter of the Voce hardening law (FIF = 0.001)	43
Table 5.5: Summary of the applied extrusion parameters	47
Table 5.6: Applied extrusion parameters and resulting average d_g (μm).	47
Table 5.7: Tension compression yield asymmetry	52
Table 5.8: Hardening parameters for slip	57
Table 5.9: Hardening parameters for TTW-ing	57
Table 5.10: Summary of the applied extrusion parameters	63
Table 5.11: Applied extrusion parameters and resulting average d_g (μm)	64
Table 5.12: Tension compression yield asymmetry	66
Table 5.13: Hardening parameters for slip systems	76
Table 5.14: Hardening parameters for TTW-ing	76
Table 5.15: Summary of the applied extrusion parameters	80
Table 5.16: Applied extrusion parameters and resulting average d_g (μm)	81
Table 5.17: Tension compression yield asymmetry	83
Table 5.18: Hardening parameters for slip systems	85
Table 5.19: Hardening parameters for TTW-ing	85
Table 6.1: Macroscopic Hall-Petch parameters.....	97
Table 6.2: Precipitate corrected Hall-Petch parameters	103
Table 6.3: Macroscopic Hall-Petch parameters.....	104
Table 6.4: Precipitate geometry	107
Table 6.5: Macroscopic Hall-Petch parameters.....	110

Abbreviations

AGG	Abnormal grain growth	ODF	Orientation distribution function
BC	Band contrast		
BSE	Backscattered electrons	PSN	Particle stimulated nucleation
CG	Coarse grained		
CGG	Continuous grain growth	PTS	Predominant twin system
CRSS	Critical resolved shear stress	φ	Azimuthal angle
		Ψ	Polar angle
CTW	Compression twin	R	Extrusion ratio
CTW-ing	Compression twinning	RE	Rare earth
CYS	Compression yield strength	RV	Recovery
d_{hkl}	Lattice plane spacing	RX	Recrystallization
DFT	Density functional theory	SAD	Selected area diffraction
d_g	Grain size	SB	Shear band
DRV	Dynamic recovery	SBN	Shear band nucleation
DRX	Dynamic recrystallization	SDE	Strength differential effect
DTW	Double twin	SE	Secondary electrons
DTW-ing	Double twinning	SEM	Scanning electron microscope
EBSD	Electron backscatter diffraction		
ED	Extrusion direction	SF	Schmid factor
EDXRSD	Energy-dispersive X-ray synchrotron diffraction	SFE	Stacking fault energy
		SRV	Static recovery
ε_e	Engineering strain	SRX	Static recrystallization
ε_{hkl}	Elastic lattice strain	SSSS	Supersaturated solid solution
EPMA	Electron probe microanalysis	θ_0^s	Initial hardening rate
		θ_1^s	Final hardening rate
EPSC	Elastoplastic self-consistent	T_B	Billet temperature
EVPC	Elastoviscoplastic self-consistent	T_P	Product temperature
		TEM	Transmission electron microscopy
FIF	Finite initial fraction		
FFT	Fast Fourier Transformation	TOF	Time-of-flight
FG	Fine grained	TTW	Tension twin
GBN	Grain boundary nucleation	TTW-ing	Tension twinning
GC	Grain coarsening	TYS	Tensile yield strength
Γ	Accumulated shear strain	τ^s	CRSS
HP	Hall-Petch	τ_0^s	Initial CRSS
l_1	Stacking fault (...ABABCBCB...)	$\tau_{0,f}^s$	Friction stress
		τ_{HP}^s	Barrier effect term
l_2	Stacking fault (...ABABCACA...)	τ_{for}^s	Forest dislocation interaction stress
IGMA	Intragranular misorientation analysis	τ_{sub}^s	Dislocation substructure interaction stress
IPF	Inverse pole figure	τ^t	Twin activation stress
λ	Wavelength	τ_0^t	Friction stress
MDF	Misorientation distribution function	VPSC	Viscoplastic self-consistent
		XRD	X-ray diffraction
		ZA	Zone axis

1. Introduction

Mg and its alloys, featuring the lowest density (1.74 gcm^{-3}) of the structural metals [Kam00], are attractive for lightweight applications and therefore, have received continuous interest during the past several decades. In addition, Mg is the 7th most abundant element in the earth's crust [Kam00, Pek13] and its recyclability [Fri06, Fec13] could facilitate a wide application of Mg alloys. While Mg castings nowadays are frequently applied, Mg wrought alloys still are seldom used for industrial applications [Boh07b]. However, to exploit the full weight-saving capacity of Mg parts, wrought alloys are required as they usually exhibit improved mechanical properties such as higher strength and ductility than cast alloys [Pek13]. The application of Mg wrought alloys is restricted by their limited room temperature formability, which is related to the complex deformation behavior of hexagonal close packed Mg alloys involving several slip and twin modes. The combination of these manifold deformation modes and the typical crystallographic textures, which are introduced during forming processes, commonly result in a pronounced anisotropy of the mechanical properties [Pek13].

Alloy development and process design allow reducing the anisotropy via tailoring the texture and promoting or hindering the activation of individual deformation modes. The latter can be achieved through texture modification (e.g. [Geh05, Boh07a, Sta08b, Sta08c, Gal13, Len13]), grain refinement (e.g. [Bar04, Bar08b, Pek13]), precipitates (e.g. [Nie03, Sta09, Rob10, Nas14, Rob14]) or solutes (e.g. [Kel68, Agn01, Agn02, Sta14, Sta15]), which in turn are related to the alloying elements and the processing. In addition, these parameters are often interconnected. For instance the generation of precipitates will at the same time reduce the solute concentration in the Mg matrix. Consequently, a profound understanding of the relations between each processing parameter and the resulting microstructure as well as between each microstructural parameter and the mechanical properties is required to take full advantage of the high specific strength (YS/ρ or US/ρ) and specific stiffness (E/ρ , E/ρ^2 , E/ρ^3), with YS , US , E and ρ being the yield strength, the ultimate strength, the Young's modulus and the density.

Therefore, the present study analyzes the effect of the extrusion parameters (billet temperature, extrusion ratio and cooling rate) and of post-extrusion heat treatments on the microstructural development and the resulting mechanical properties of Mg-Mn-Ce (ME21) Mg-Y-Nd (WE54), Mg-Li (L4) and Mg-Li-Al (LA41) alloys. The alloys are denominated following the ASTM norm (cf. [Kam00, Kai03]). This alloy selection enables the analysis of the effects of the texture through alloying rare earth elements (ME21, WE54), of precipitates (ME21, WE54), of solutes (WE54, L4, LA41) and of the grain size (ME21, WE54, L4, LA41). Through the careful examination of the initial and the deformed microstructure using optical microscopy, scanning electron microscopy, electron backscatter diffraction, transmission electron microscopy, X-ray diffraction and in-situ energy-dispersive X-ray synchrotron diffraction experiments during loading as well as elastoplastic self-consistent (EPSC) modelling, the above-mentioned effects on the activity of the individual deformation modes were evaluated.

2. Literature review

2.1 Magnesium and its deformation mechanisms

Mg and the majority of its alloys feature a hexagonal closed packed lattice (hcp; space group: $P6_3/mmc$; Fig 2.1) [JCP00], where atoms are located at the atomic coordinates $(0, 0, 0)$ and $(1/3, 2/3, 1/2)$. The c/a ratio of pure Mg is ≈ 1.623 ($a \approx 3.209$ nm, $c \approx 5.211$ nm) [Kam00, JCP00] and can be modified through alloying [Hau56, Als09].

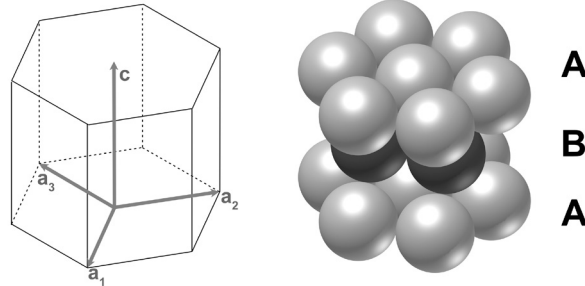


Fig 2.1: Hexagonal close packed lattice.

Typically, a 4-axes coordinate system is used with 3 a -axes lying in the hexagonal basal plane and 1 c -axis, which is aligned parallel to the basal plane normal. Accordingly, planes are usually denominated using Miller-Bravais-Indices ($hkil$) and directions using $\langle uvtw \rangle$.

2.1.1 Stacking fault energy of Mg

The c/a ratio of Mg results in a larger primitive cell volume compared to other hcp metals, which in turn leads to small stacking fault energies (SFE). Stacking faults are planar defects bounded by partial dislocations, which can be generated during growth processes or deformation. Extrinsic stacking faults result from an extra layer of atoms being introduced, while intrinsic stacking faults are due to vacancy condensation. In Mg the intrinsic stacking faults I_1 (...ABABCBCB...), I_2 (...ABABCACA...) and the extrinsic stacking faults E (...ABABCABABABA...) as well as a twin-like stacking fault T (...ABABCBABABA...) occur [Pek13].

Generally, SFE values control twinning, ease of climb, cross-slip of dislocation and consequently work hardening. The activation energies of these processes are inversely correlated to the SFE, where decreasing fault energies correspond to increasing activation energies. Furthermore, high SFE values lead to smaller dislocation-cores and facilitate dislocation motion. Table 2.1 summarizes the SFE for different types of stacking faults on basal planes [Pek13], while effects of alloying elements on SFE values can be found in [Han11, Muz12, Sha14, San14].

Table 2.1: Calculated SFE (meV) for different types of stacking faults on basal planes [Pek13].

I_1	I_2	E	T_2	Reference
11	23	36	27	[Cet97]
10	20	32	22	[Smi07]
16	34	59	38	[Wen09]

2.1.2 Crystallographic slip

Ductile metals deform predominantly via crystallographic slip, where blocks of a crystal are displaced parallel to crystallographic planes by integer multiples of the atomic spacing [Got07, Als08a]. This displacement occurs through dislocation movements on closed packed planes and is driven by the resolved shear stress parallel to the slip plane in slip direction [Got07, Als08a]. The resolved shear stress can be calculated using the equation:

$$\tau = \frac{F}{A} \cdot \cos\kappa \cdot \cos\lambda = \sigma \cdot SF \quad (2.1)$$

with τ being the shear stress resolved in the slip plane in slip direction, κ the angle between slip plane normal and stress axis, λ the angle between slip direction and stress axis and SF the Schmid factor [Got07, Abb09, Pek13] (cf. Fig 2.2). In polycrystalline material the different slip systems usually exhibit different SF ($0 \leq |SF| \leq 0.5$) and hence experience different resolved shear stresses. If the resolved shear stress exceeds the critical resolved shear stress (CRSS) of a slip system, dislocations will glide on the corresponding planes. In Mg several slip systems and twin modes exist and significant differences of their CRSS were observed. These deformation modes are introduced in the following sections.

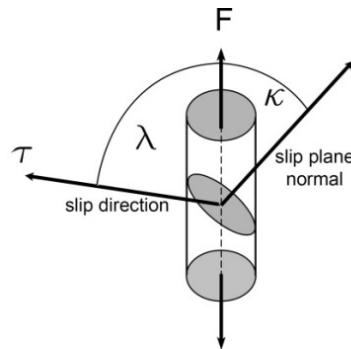


Fig 2.2: Determination of the resolved shear stress [Got07, Abb09].

2.1.3 Slip systems

A variety of perfect and partial dislocations were observed in hcp metals [Par67, Yoo81, Lou07]. Nevertheless, the room temperature formability of Mg and its alloys is generally low, which is attributed to the limited number of easily activated slip systems. This section focuses on the most important slip systems in Mg (Fig 2.3), while a detailed description of other dislocations can be found in e.g. [Par67, Chr70, Hir82].

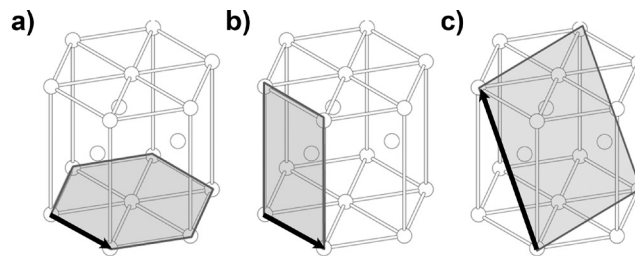


Fig 2.3: Slip systems: a) $\langle 11\bar{2}0 \rangle \{0002\}$ - $\langle a \rangle$ basal, b) $\langle 11\bar{2}0 \rangle \{1\bar{1}00\}$ - $\langle a \rangle$ prismatic, c) $\langle 11\bar{2}3 \rangle \{11\bar{2}\bar{2}\}$ - 2nd order $\langle c+a \rangle$ pyramidal slip.

Fig 2.3 a) illustrates the $\langle a \rangle$ basal slip system corresponding to slip on the closed packed direction $\langle 11\bar{2}0 \rangle$ on the closed packed $\{0002\}$ (basal) plane. Consequently, this deformation mode exhibits the by far lowest CRSS [Kel58, Lou07]. Single crystal experiments revealed a CRSS in the order of 0.5 MPa [Bur52, Kel58]. However, this slip mode provides only 2 independent slip systems and hence does not fulfill the von Mises criterion [Mis28, Tay38]. In addition, it does not allow c-axis deformation.

Table 2.2: Independent deformation modes in magnesium [Yoo81].

Direction	Plane	Crystallographic element	Independent slip modes
$\langle a \rangle$	basal	$\langle 11\bar{2}0 \rangle \{0002\}$	2
$\langle a \rangle$	prismatic	$\langle 11\bar{2}0 \rangle \{1\bar{1}00\}$	2
$\langle c+a \rangle$	pyramidal	$\langle 11\bar{2}3 \rangle \{11\bar{2}\bar{2}\}$	5

Consequently, additional non-basal deformation modes are required to enable polycrystal deformation. $\langle a \rangle$ prismatic slip on $\{1\bar{1}00\}$ planes (Fig 2.3 b)) and $\langle c+a \rangle$ pyramidal slip on $\{11\bar{2}2\}$ planes (Fig 2.3 c)) provide 2 and 5 additional slip systems (Table 2.2) [Lou07, Yoo81]. In contrast to the $\langle a \rangle$ slip modes, $\langle c+a \rangle$ pyramidal slip enables c-axis deformation. However, the CRSS of non-basal slip modes are up to 2 orders of magnitude higher than for $\langle a \rangle$ basal slip at room temperature [Kel58, Lou07]. Table 2.3 summarizes the initial CRSS of $\langle a \rangle$ basal, $\langle a \rangle$ prismatic and $\langle c+a \rangle$ pyramidal slip systems for a variety of Mg alloys.

Here, it should be noted that the CRSS of the non-basal slip modes are significantly influenced by the deformation temperature [Oba73, Ion82]. Therefore, non-basal slip modes contribute to the strain accommodation during hot deformation processes such as extrusion or hot rolling.

Table 2.3: Initial CRSS of various alloys, which were determined via constitutive modeling.

Material / method	$\langle a \rangle$ basal τ_0 , MPa	$\langle a \rangle$ prismatic τ_0 , MPa	$\langle c+a \rangle$ pyramidal τ_0 , MPa	CRSS ratio ba : pri: pyr	Reference
Pure Mg (VPSC)	11	30	50	1 : 2.7 : 4.5	[Opp12]
AZ31B (EPSC)	10	55	60	1 : 5.5 : 6.0	[Agn03]
AZ31 (EPSC)	20	90	95	1 : 4.5 : 4.8	[Agn06a]
AZ31 (EPSC)	10	55	60	1 : 5.5 : 5.0	[Agn06a]
AZ31 (EPSC)	12	60	100	1 : 5.0 : 10.0	[Cla08]
AZ31 (EPSC)	30	85	95	1 : 2.8 : 3.2	[Mur08]
AZ31 (FEM) CRSS ratio	1	5	6		[Kne10]
AZ31B (EVPSC)	9	79	100	1 : 8.7 : 11.1	[Wan10]
Mg-3Li (VPSC)	10		80	1 : - : 8.0	[Agn01]
Mg-1Y (VPSC)	10		170	1 : - : 17.0	[Agn01]
ME21 (EPSC)	15	72	85	1 : 4.8 : 5.7	[Len13]
WE43 (EPSC) Solutionized	12	78	130	1 : 6.5 : 10.8	[Agn13]
WE43 (EPSC) Peak-aged ¹	30	86	130	1 : 2.9 : 4.3	[Agn13]
WE43 (EPSC) Over-aged	37	92	130	1 : 2.5 : 3.5	[Agn13]
ZM20 (EPSC) Fine grained	12	38	60	1 : 3.2 : 5.0	[Mur10a]
ZM20 (EPSC) Coarse grained	2	18	25	1 : 9.0 : 12.5	[Mur10a]

Based on the high CRSS of $\langle c+a \rangle$ pyramidal slip strain accommodation along the c-axis via crystallographic slip is impeded in Mg alloys, giving rise to the importance of deformation twinning, which will be introduced in the following section.

2.1.4 Deformation twinning

Deformation twinning is a shear deformation in which a part of a crystal is shifted into an orientation featuring mirror symmetry with respect to the parent orientation. The deformation behavior of Mg and its alloys is significantly influenced by the activation of deformation twinning [Kel58, Bar07a, Bar07b, Pro09, Cap09a, Bey11a, Bey11b, Kha11, Kur14]. The most important twin mode in Mg is $\{10\bar{1}2\}\langle 10\bar{1}\bar{1} \rangle$ tension twinning (TTW-ing), which is associated

¹ Here, peak-aged denominates an optimization of the properties and the required time in the furnace to obtain them [Agn13].

with a low flow stress and little work hardening [Kel58, Bar07a, Lou09]. Additionally, $\{10\bar{1}1\}$ $\langle 10\bar{1}2 \rangle$ compression twinning (CTW-ing) is frequently observed. In contrast to crystallographic slip, deformation twinning is a uniaxial deformation mode. Hence, TTW-ing can be activated only, if a tensile load is applied parallel to the c-axis and CTW-ing can be activated if compression occurs parallel to the c-axis. Both twin modes are represented in Fig 2.4. Tension twins (TTWs; Fig 2.4 a) and c)) feature a $\approx 86^\circ$ rotation about a $\langle 1\bar{2}10 \rangle$ -axis, while CTW-ing (Fig 2.4 b) and d)) reorients the grains by $\approx 56^\circ$ about a $\langle 1\bar{2}10 \rangle$ -axis. In contrast to compression twins (CTWs), which feature a high CRSS and usually appear as relatively thin needles in metallographic sections, TTWs readily nucleate at low stresses, thicken and appear to overtake grains in some cases [Bar07a, Bar07b, Lou07, Len14a].

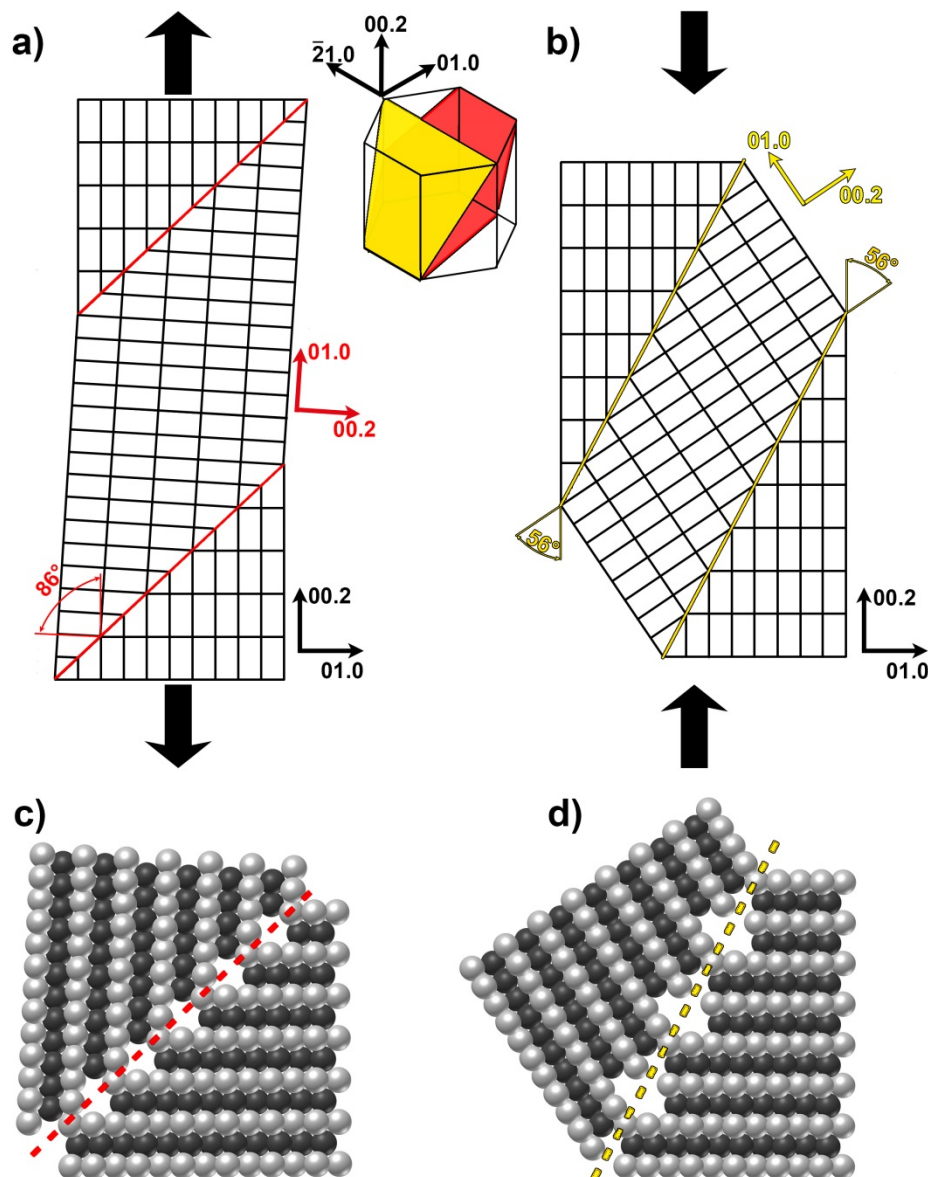


Fig 2.4: Schematic drawings of TTWs (a), c)) and CTWs (b), d)) using a $\langle 2\bar{1}10 \rangle$ zone axis (ZA).

In addition, internal twinning is frequently observed in Mg alloys, where a secondary twin is formed within a preexisting twin. The most common example of internal twinning is $\{10\bar{1}1\}$ - $\{10\bar{1}2\}$ double twinning (DTW-ing), where a secondary TTW nucleates and grows within a primary CTW [Won67, Nav04, Ciz08, Bar08a, Len14a, Len14b]. Fig 2.5 illustrates the transition of a preexisting CTW into a $\{10\bar{1}1\}$ - $\{10\bar{1}2\}$ double twin (DTW). DTW-ing is particularly important as it has been correlated to the onset of flow localization and failure

and therefore, is detrimental for the ductility of Mg alloys. Based on their limited thickness DTWs form a narrow band that provides a much higher SF for $\langle a \rangle$ basal slip than the surrounding parent grain creating a narrow band in which slip is concentrated [Won67, Bar07b, Ciz08]. Even tertiary twinning, where DTWs form within a preexisting TTW (primary TTW), has been reported [Mu12, Len14a, Len14b]. Fig 2.6 illustrates the sequential formation of tertiary DTWs [Len14a].

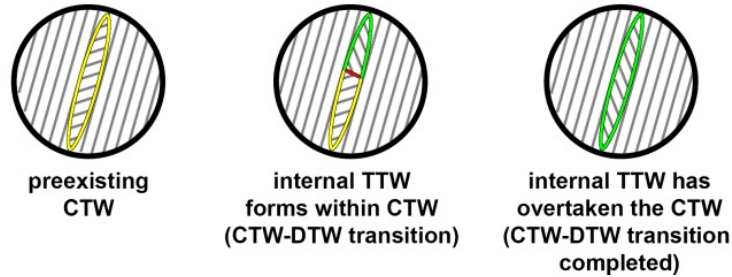


Fig 2.5: Schematic drawing of internal TTW-ing within a preexisting CTW forming a type 1 DTW.

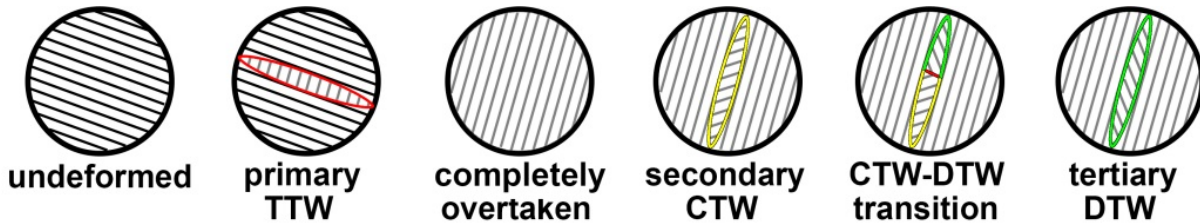


Fig 2.6: Sequence of primary TTW-ing, secondary CTW-ing and tertiary TTW-ing within the secondary CTW forming a tertiary DTW [Len14a].

In order to analyze this sequence, misorientations distribution functions (MDFs) can be employed. Fig 2.7 illustrates the changes of the MDFs, which are generated through the sequential activation of primary TTW-ing, secondary CTW-ing and tertiary DTW-ing (Fig 2.6, [Len14a]). The intense activation of TTW-ing generates a high number of TTW boundaries featuring a misorientations angle of $\approx 86^\circ$ about a $\langle 11\bar{2}0 \rangle$ ZA (Fig 2.7 a)). As TTW-ing proceeds the parent grains are continuously overtaken. Consequently, TTW boundaries coalesce causing a lower frequency of TTW boundaries (Fig 2.7 b)). If different TTW variants intersect a misorientation of 60° about a $\langle 10\bar{1}0 \rangle$ ZA is generated (Fig 2.7 b)) [Nav04, Mu12]. The latter maximum is superimposed by the activation CTW-ing, which feature a misorientation of $\approx 56^\circ$ about a $\langle 11\bar{2}0 \rangle$ ZA (Fig 2.7 c)). TTW-TTW boundaries and CTW boundaries can be distinguished through the standard triangle illustration of the rotation axis. Further deformation can introduce DTWs (Fig 2.7 d)). Here, several variants can occur which feature characteristic misorientation relations and will be introduced below.

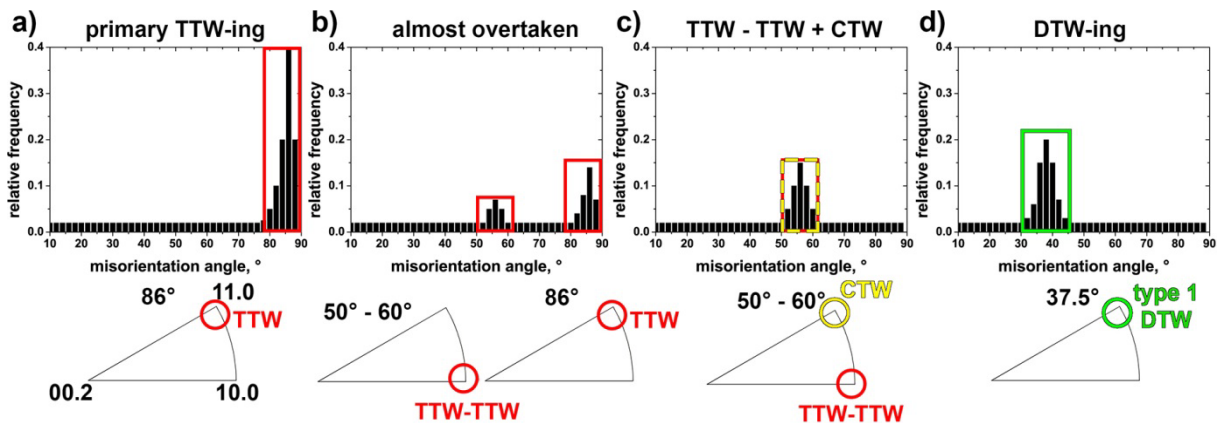


Fig 2.7: Schematic illustrating changes of the MDFs during sequential twinning: Primary TTW-ing, secondary CTW-ing and tertiary DTW-ing.

Both TTWs and CTWs contain six crystallographically equivalent twin variants and hence 36 DTW variants can occur. These can be regrouped into four geometrically equivalent types [Bar08a, Bey12, Len14a]. These feature misorientation angles of 37.5° (type 1), 30.1° (type 2), 66.5° (type 3) and 69.9° (type 4) of the basal planes of the matrix and the DTW. Type 1 and type 2 share the same ZA ($\langle 11\bar{2}0 \rangle$) with the basal plane of the preexisting CTW, while type 3 and type 4 have ZAs that do not lie in the basal plane of the preexisting CTW [Bey12]. Fig 2.8 illustrates the geometric relationship between the TTW planes and a primary CTW plane. In Fig 2.7 the effect of type 1 DTWs on the MDF is illustrated.

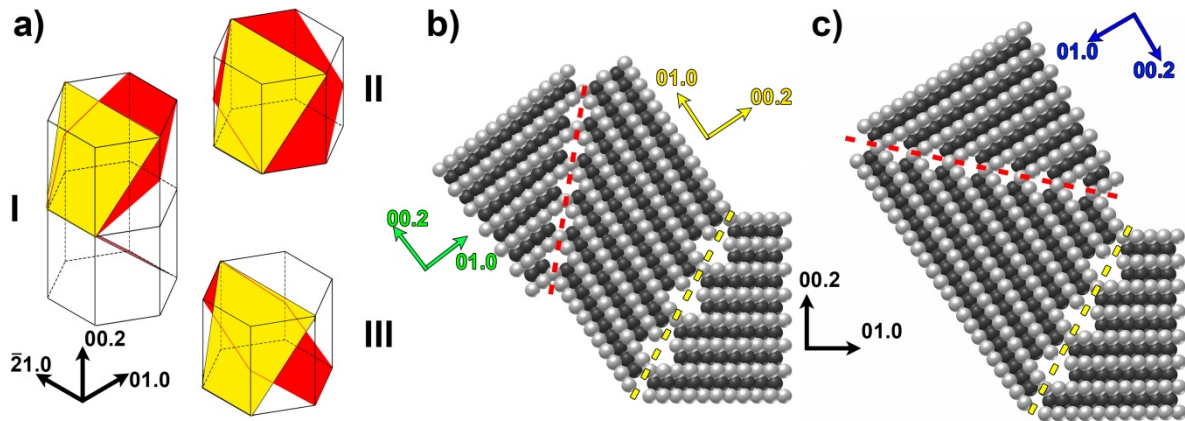


Fig 2.8: Schematic illustrating different DTW variants (Geometric relationship between the secondary TTW planes (red) and a given primary CTW plane (yellow)). a) I: type 1 and type 2 DTWs, II: type 3 DTW, III: type 4 DTW, b) type 1 DTW ($\langle 2\bar{1}10 \rangle$ ZA), c) type 2 DTW ($\langle 2\bar{1}10 \rangle$ ZA).

Currently the mechanisms of twin variant selection are not fully understood. Usually, the SF is used to determine, which twin variant is selected. However, recent studies have shown non-SF behavior in twin variant selection [Cap09a, Cap09b, Bey10, Bey11a, Len14a, Len14b]. This deviation might be caused by the complex local stress state and twin nucleation mechanisms, which are not taken into account by SF calculations based on the macroscopic load. With respect to DTW-ing, a predominance of type 1 DTWs was observed revealing non-Schmid behavior in the activation of secondary TTW-ing [Bar08a, Mar10, Len14a, Len14b]. Several explanations for twin variant selection in DTW-ing were proposed. Barnett et al. [Bar08a] explained the predominance of type 1 DTWs by its optimal shape for strain compatibility, and its best match between the preexisting primary CTW and secondary twinning planes of the type 1 DTW. Mu et al. [Mu12] studied primary, secondary and tertiary twins in AZ31 samples compressed in plane strain and suggested that nucleation of primary TTWs is controlled by the macroscopic SF, while twin growth is controlled by the accommodation strain between the twins and the adjacent grains. This approach was successfully transferred to secondary and tertiary twin variant selection in pure titanium [Qin14]. Beyerlein et al. [Bey12] explained the nucleation and growth of a TTW within a preexisting CTW by a sequence of dissociations of slip dislocations into $\{10\bar{1}2\}$ dislocations at the CTW boundary. According to this study type 1 and type 2 DTW-ing are triggered by the dissociation of basal dislocations, while type 3 and type 4 DTW-ing result from the dissociation of $\langle c+a \rangle$ pyramidal dislocations. As $\langle c+a \rangle$ pyramidal slip features a much higher CRSS than $\langle a \rangle$ basal slip (cf. Table 2.3), type 2 and particularly type 1 DTWs are expected to be predominant.

2.1.5 Microstructure effects on the deformation behavior

The mechanical properties and the deformation behavior can be influenced significantly through modifications of the microstructure and alloying. This section focuses on the effect of the grain size (d_g), precipitates and texture on the deformation behavior of Mg alloys, while the effect of alloying elements will be discussed in the following section.

2.1.5.1 Grain size

Almost all polycrystalline metals show a strong effect of d_g on the hardness and the strength, where the strength increases with decreasing d_g [Hal51, Pet53, Got07, Abb09]. The effect of the d_g (Hall-Petch (HP) effect) can be described using the following equation:

$$\sigma = \sigma_0 + \frac{k}{\sqrt{d_g}} \quad (2.2)$$

where σ is the flow stress, k the HP constant and σ_0 the CRSS of the single crystal [Got07, Abb09]. Although the HP relation was derived for crystallographic slip, it has been shown in many classes of metals that it is also valid in case of twinning [Hul61, Lin63, Eco83, Chr95, Mey01, Bar04, Cer07, Bar08b, Jai08].

In Mg it was found that TTW-ing is more sensitive to d_g changes than crystallographic slip [Bar04, Bar08b, Pek13]. Therefore, d_g reduction is a promising approach to hinder twinning and consequently reduce the mechanical anisotropy of Mg alloys. However, statistical EBSD analyses on hcp metals indicate that this trend may not always be the case [Bey10, Cap09]. In [Bey10] pure polycrystalline Mg was investigated. It was found that d_g had little influence on whether or not a grain had formed at least one TTW, while it had a significant impact on the number of twins per grain. The number of twins per grain increased as the grain area increased, while the twin thickness was not affected by the grain area [Bey10]. In addition, Liu et al. [Liu14] observed a twinning-like lattice rotation without a twin plane in submicron-sized pure Mg single crystals via in-situ mechanical testing in TEM and atomistic simulations. The study suggests that basal planes can be directly converted into prismatic planes and vice versa. Hence, this twin-like deformation mode might be viable in ultrafine grained materials.

The effect of d_g on CTW-ing and DTW-ing is studied seldom. Tsai et al. [Tsa13] reported a decreasing frequency of twinned grains (CTWs or DTWs) with decreasing d_g in an AZ31 alloy using optical microscopy.

2.1.5.2 Precipitates

In addition, to grain refinement, precipitation is an effective approach to increase the strength and to modify the relative activities of deformation modes [Nie03, Sta09, Rob10, Rob11a, Nie12, Rob13, Nas14, Rob14, Agn13]. Nie [Nie03] developed Orowan equations appropriate for Mg alloys and analyzed the effect of the precipitate shape on the strengthening of basal slip considering identical volume fractions and number densities. It was found that prismatic plates cause more pronounced strengthening than basal precipitate plates, $[0001]_\alpha$ precipitate rods and spherical precipitates. Stanford et al. [Sta09] have analyzed twinning in an age-hardened Z5 alloy forming c-axis rods. The study revealed that age-hardened samples contain a larger number of twins (at -5 % strain) than precipitate free samples. In a subsequent study [Rob10] it was shown that the c-axis rod precipitates in age-hardened Z5 alloy suppress TTW growth, but promote TTW nucleation. In [Sta12] the effect of plate-shaped particles on the deformation behavior of AZ91 was investigated. While the effect of the precipitates on slip systems could be modeled using Orowan equations, the predicted Orowan strengthening on TTW-ing was much lower than the experimental data. The authors proposed that the additional hardening increment is caused by a back-stress of the particles on the twin plane and hardening of the slip systems, which accommodate the twin shape change.

Robson et al. [Rob11a] applied Orowan equations and conducted experiments using a Z5 and an AZ91 alloy to analyze the effect of the precipitate morphology (spheres, basal plates and c-axis rods) on basal and prismatic slip and on TTW-ing. This study indicates that c-axis rods are more effective hardening basal and prismatic slip than basal plates or spheres, with basal plates being particularly ineffective in hardening basal slip. As basal plates become orientated perpendicular to the basal plane within the TTWs, these are very effective hindering basal slip in the TTW and hence TTW growth, while c-axis rods are poor obstacles to prevent slip in the TTW [Rob11a]. In addition, the study [Rob11a] indicates that basal plates reduce the tension compression asymmetry in extruded bars, while c-axis rods can increase the asymmetry.

In [Rob13] and [Rob14] VPSC simulations and Orowan calculations were performed to analyze precipitate morphology effects on basal and prismatic slip and TTW-ing. Fig 2.9 summarizes the Orowan strengthening of different precipitate morphologies and orientations on $\langle a \rangle$ basal and $\langle a \rangle$ prismatic slip as well as TTW-ing [Rob14].

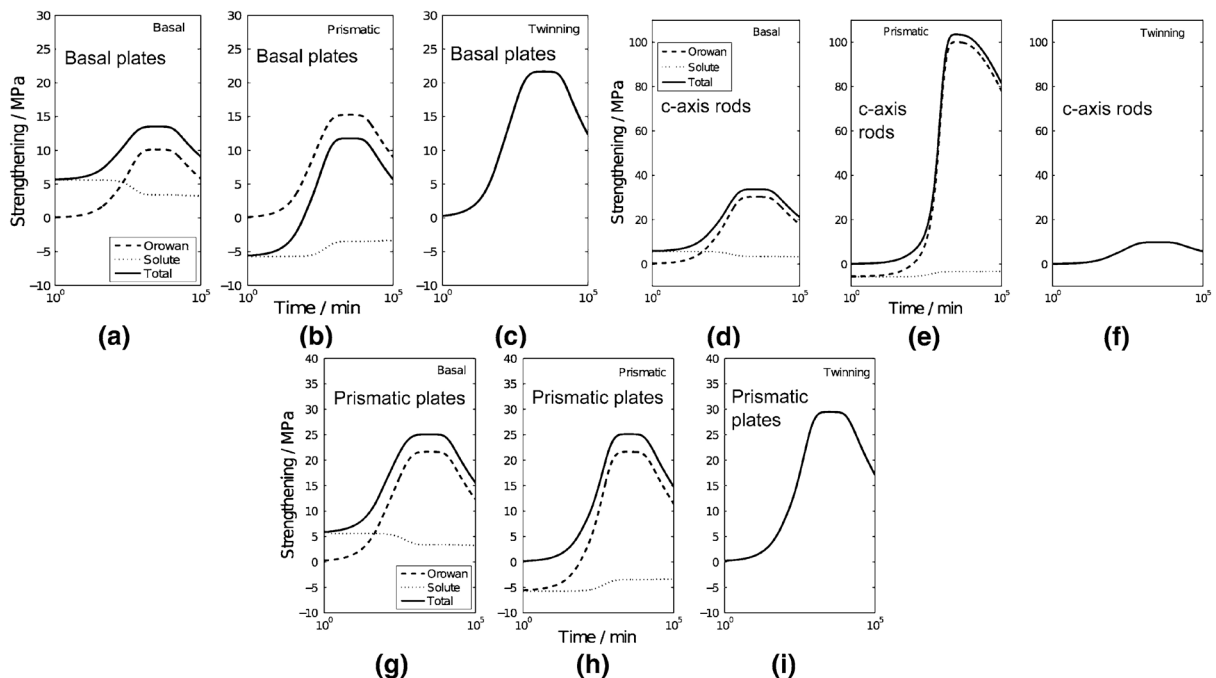


Fig 2.9: Orowan strengthening of different precipitates on $\langle a \rangle$ basal slip, $\langle a \rangle$ prismatic slip and TTW-ing: a) - c) basal plates, d) - f) c-axis rods, g) - i) prismatic plates [Rob14].

Agnew et al. [Agn13] analyzed the effect of prismatic plates, which formed during the age-hardening of a cast WE43 alloy, on the deformation modes using in-situ neutron diffraction and EPSC simulations and found predominant hardening of $\langle a \rangle$ basal slip, while TTW-ing appeared to soften during age-hardening.

2.1.5.3 Texture

Based on the anisotropy of Mg single crystals [Kel58] and the uniaxial character of deformation twinning the texture of polycrystalline material has a pronounced impact on the deformation behavior of Mg wrought products. If anisotropic grains are randomly orientated in a sample, the macroscopic sample loses its anisotropy, while textured samples exhibit anisotropic properties [Koc00]. The extent of the anisotropy of a polycrystalline sample is coupled to the sharpness of the texture. The texture of semi-finished products and parts is influenced by the alloying elements, the applied process and the process parameters, which will be discussed in the following sections.

2.2 Recrystallization in Mg alloys

During thermo-mechanical processing of metals softening mechanisms (recovery – RV and recrystallization – RX) occur. While RX denominates the formation of a new grain structure within deformed materials by the formation and migration of high angle grain boundaries ($> 10^\circ - 15^\circ$), RV can be defined as all annealing processes in a deformed material that occur without the migration of high angle grain boundaries. The driving force of both processes is the stored energy of deformation. Grain coarsening (GC) can be defined as processes involving the migration of grain boundaries, which are driven solely by the reduction of the grain boundary area. RV and RX are subdivided into dynamic (DRV, DRX) or static processes (SRV, SRX), where DRV and DRX refer to the occurrence of RV and RX during deformation, while SRV and SRX occur subsequent to deformation [Doh97, Got07]. Nucleation occurs within regions that provide high misorientations or strain gradients such as shear bands and high angle grain boundaries or the vicinity of large precipitates ($> 1 \mu\text{m}$) and twins [Doh97]. As RV, RX and GC cause microstructural changes they have an important impact on the mechanical properties of the product. DRX was observed in Mg alloys at temperatures $> 150^\circ\text{C}$ [Ion82, Gal01, Als08b] and is therefore expected during Mg hot forming processes such as extrusion. Several nucleation mechanisms were observed:

- Ion et al. [Ion82] observed grain boundary nucleation (GBN) during DRX of an Mg-Al alloy, which involved dynamic polygonisation of rotated lattice regions adjacent to grain boundaries. Subsequently, Galiyev et al. [Gal01] analyzed DRX in a ZK60 alloy within a wide range of temperatures and extended the model proposed by Ion et al. [Ion82]. According to [Gal01] $\langle a \rangle$ basal slip and deformation twinning operate to comply with strain compatibility at grain boundaries, where basal dislocations accumulate near the twin boundary. The internal stresses, which are the result of remaining large elastic distortions at the grain boundaries, exceed the CRSS of non-basal slip modes causing a rearrangement of dislocations and the formation of high-angle grain boundaries. At intermediate temperatures ($200^\circ\text{C} - 250^\circ\text{C}$) cross-slip of $\langle a \rangle$ dislocations occurs on non-basal planes. During cross-slip of an $\langle a \rangle$ dislocation a transition from screw to edge orientation occurs, which is associated with a high SFE enabling climb of this dislocation. The interaction of cross-slip and climb generates a low-angle grain boundary network in vicinity of the original grain boundary. Subsequently, continuous absorption of dislocations in the low-angle boundaries occurs and causes continuous DRX. At high temperatures ($300^\circ\text{C} - 450^\circ\text{C}$) volume self-diffusion causes a transition to dislocation climb controlled RX. Microscopic slip lines cause the formation of bulges of grain boundaries resulting in nucleation of DRX grains [Gal01]. The orientation of the recrystallized grains does not deviate significantly from the orientation of the existing grain in case of GBN and hence, texture changes are marginal [Han14].
- During DRX of Mg nucleation was observed at shear bands (SB) [Ion82], which feature an orientation that is favorable for the easily activated basal slip mode and arise at strongly deformed grain boundaries or twinned regions. The concentration of basal slip within the SBs results in a high dislocation density promoting DRX grain nucleation. SB nucleation (SBN) was observed particularly in rare earth (RE) containing Mg alloys and has been correlated to texture modifications generating weaker textures and additional RE texture components [Sta08a, Sen08, Han10, Hup10a, Gal12, Had12, Bas13, Bas14, Han14].
- While small precipitates can pin grain boundaries and thereby hinder RX at sufficient precipitate densities, larger precipitates $> 1 \mu\text{m}$ can promote DRX via particle stimulated nucleation (PSN) [Doh97]. Robson et al. [Rob11b] analyzed Mg-Mn alloys and showed that the presence of a fine particle dispersion allows retaining a largely unrecrystallized

microstructure after hot rolling. PSN is a frequently reported DRX mechanism in Mg alloys [Bal94, Rob09, Gal12, Hir13, Als13, Bas14]. Ball and Prangnell [Bal94] explained the very weak texture of a WE43 alloy by the observation of PSN. In [Rob09] it was found PSN contributes in a minor extent to RX grain nucleation, but produces random grain orientations. Although studies on dilute solid solution RE alloys indicate that PSN is not a prerequisite for weak RE textures [Sta08a, Had12], other recent studies indicate that PSN introduces a grain refinement and randomness of grain orientations and hence is a potential source of texture modification during hot processing [Als13, Hir13]. In [Hir13] it is suggested that precipitate density and precipitate size are important factors in magnifying the impact of particles on the texture development.

- With respect to the RE texture development solutes effects were reported during RX, where solute segregate to the grain boundaries and affect grain boundary motion [Boh10, Sta10a, Als11, Sta11, Had12, Hir13]. Stanford et al. [Sta10a] investigated binary Mg-Gd alloys observing a significant Gd enrichment of the grain boundary region hindering RX grain nucleation. In [Sta11] the level of solute segregation was found to be dependent on the extrusion temperature. A maximum was observed at 490 °C, which is caused by the two competing effects solute diffusivity and grain boundary mobility. At temperatures < 490 °C a RE texture was observed, while temperatures > 500 °C caused a conventional extrusion texture. Hadorn et al. [Had12] analyzed binary Mg-Y and Mg-Zn alloys and revealed an important Y enhancement at grain boundaries, while Zn was distributed homogeneously. The study indicates that slow grain growth respectively low grain boundary mobility can be achieved through slow diffusing grain boundary solutes. According to the authors this might affect the DRX mode and ultimately the texture development. In [Hir13] it is argued that solute segregation may have little influence on the nucleation process, but strongly retard the boundary mobility of RX nuclei. This can cause a retardation of RX and deformation heterogeneities with large crystallographic misorientations and thereby alter the RX mechanism (orientated nucleation) or affect the growth advantage of specific orientation relationships (oriented growth). Furthermore, both aspects, orientated nucleation and growth, might be superimposed [Hir13].

Here it should be noted that in most cases several DRX mechanisms occur simultaneously hindering an unambiguous correlation of texture effects and a single DRX mechanism.

2.3 Extrusion

Extrusion is a forming process to create products featuring a fixed cross-sectional profile, where the material is pushed through a die of the desired cross-section. Important advantages of the process are the realization of complex cross-sections and high true strains, based on the confining compressive stresses in the shear zone. Extrusion processes are usually subdivided based on the billet temperature T_B (hot / cold extrusion) and the relative movement of the extruded material and the ram [Bau01, Mül03, Mül07]. In the present study indirect extrusion was performed.

In indirect extrusion the billet and container move together while the die is stationary (Fig 2.10). After heating, the billet is loaded into the container. Subsequently, the container and the ram move simultaneously towards the die, which is supported by a hollow stem. Consequently, no relative motion of the container and the billet occurs avoiding friction between these and reducing the required extrusion force. Additionally, the flow of the material is much more homogeneous. However, in indirect extrusion the cross-sectional area of the product is limited by the diameter of the hollow stem [Bau01, Mül07, Gal12].

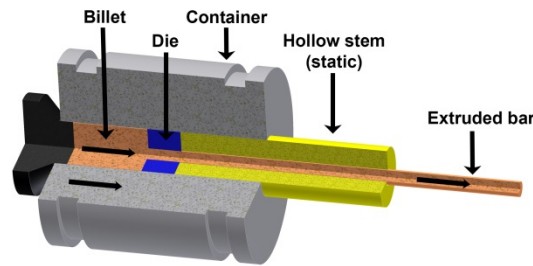


Fig 2.10: Schematic drawing of the indirect extrusion process.

2.3.1 Extrusion of Mg alloys

Mg alloys are usually extruded using T_B in the range of 250 °C – 450 °C [Swi06]. As pressure welding is possible a variety of cross-sections can be produced including hollow profiles [Bau01, Kai03, Las05]. However, increasing alloying element concentrations complicate extrusion resulting in extrusion speeds being ten times lower [Kai03, Las05].

The extrusion parameters such as the T_B , extrusion ratio R and the cooling conditions affect the DRX, the resulting microstructure and ultimately the mechanical properties. Usually, higher T_B result in high product temperatures (T_P), which in turn results in more pronounced GC and a higher average d_g [Mur03, Mü107, Hup10b, Hup11, Gal12]. Increased cooling rates, which can be obtained via changes of the cooling medium (e.g. water cooling), result in a refined microstructure [Mü107, Boh08, Hup10b, Hup11]. An increased R has multiple effects. On the one hand an increased R is equivalent to a higher true strain, which in turn is related to a higher dislocation density accelerating the kinetics of RX and to more pronounced strain inhomogeneities generating nucleation sites, which might influence the DRX mechanisms [Hum95]. On the other hand the heat generation from the deformation increases causing higher T_P . In [Mur03] an increasing d_g with increasing R was reported in an AZ31 alloy, while in [Uem06] a decreasing d_g with increasing R was reported in AZ alloys. Gall [Gal12] observed a minor decrease of the d_g in case of an AZ31 alloy if the R was increased from $R = 92 : 1$ to $R = 123 : 1$.

Fig 2.11 exhibits schematic drawings of typical extrusion textures. While pure Mg and conventional Mg alloys usually exhibit $\langle 10\bar{1}0 \rangle$, $\langle 11\bar{2}0 \rangle$ or $\langle 10\bar{1}0 \rangle / \langle 11\bar{2}0 \rangle$ fiber textures the addition of RE elements introduces an additional RE texture component ($\langle 11\bar{2}1 \rangle$) weakening the overall texture [Yi04, Agn05, Sta08b, Sta08c, Als10, Boh10, Hup10a, Hup10b, Sta10b, Sta11, Brö11, Ill14].

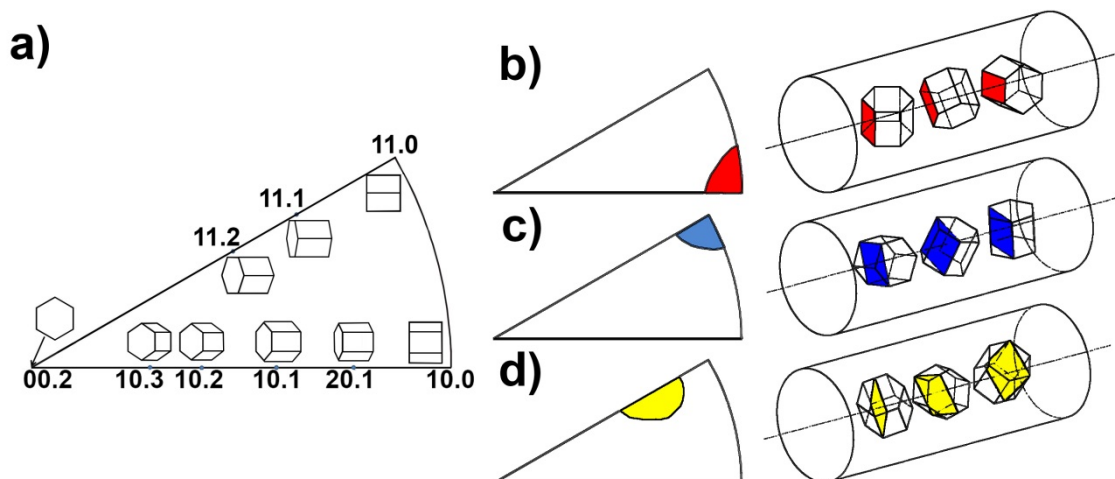


Fig 2.11: Schematic drawing of typical extrusion textures (\parallel ED): a) Visualization of crystals within the stereographic triangle, b) $\langle 10\bar{1}0 \rangle$ fiber texture, c) $\langle 11\bar{2}0 \rangle$ fiber texture, d) RE texture between $\langle 11\bar{2}1 \rangle$ and $\langle 11\bar{2}2 \rangle$.

Based on this texture development extruded Mg bars usually exhibit an anisotropic deformation behavior. Fig 2.12 a) demonstrates an example of the tension – compression asymmetry of an extruded ME21 bar, while Fig 2.12 b) exhibits SF distributions, which were calculated by Muransky et al. [Mur08] for tensile testing of an extruded AZ31 alloy. If compression tests are conducted parallel to the extrusion direction (ED), TTW-ing is readily activated, while its uniaxiality prevents its activation in tension tests. As TTW-ing usually features a low CRSS and little work hardening [Kel58, Bar07a, Lou09] the compression yield strength (CYS) is usually lower than the tensile yield strength (TYS) (e.g. [Swi06, Mül07, Hup10a, Hup10b, Ill14]). Furthermore, the activation of TTW-ing results in a typical sigmoidal-shape compression flow curve.

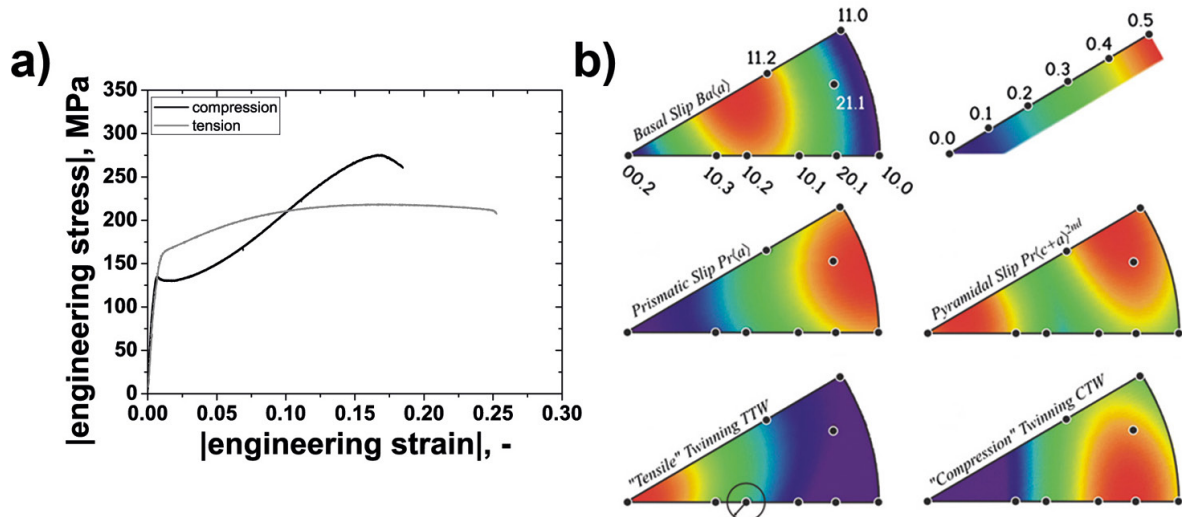


Fig 2.12: a) Tension – compression asymmetry of an ME21 extrusion, b) SF distribution calculated for uniaxial tension of extruded bars [Mur08].

In order to quantify the yield asymmetry the strength differential effect (SDE) is frequently used [Sto04, Mül07, Hup10a, Hup10b]:

$$SDE = 2 \cdot \frac{|CYS| - |TYS|}{|CYS| + |TYS|} \quad (2.3)$$

Huppmann et al. reported an SDE in the range of -0.10 to -0.70 in case of AZ31 [Hup10a] and -0.14 to -0.26 in case of ME21 [Hup10b].

2.4 Influence of alloying elements

Since the first industrial applications of Mg alloys in the early 20th century there has been considerable effort to influence the properties of pure Mg through alloying. The main mechanisms affecting the mechanical properties are solid solution hardening and precipitation hardening, where solid solution hardening is based on the difference in atomic radii and precipitation hardening on the reduced solubility at low temperatures enabling precipitation of intermetallic phases. Effective precipitation hardening requires a high precipitate density, an ideal distribution and precipitate size [Kam00, Kai03]. The following sections describe the influence of alloying elements, which are relevant for this study.

2.4.1 ME21

Within this study an ME21 alloy containing 2 wt% Mn and 0.7 wt% Ce mischmetal was investigated. Fig 2.13 exhibits the binary phase diagrams corresponding to the investigated ME21 alloy. The addition of Mn increases the strength, if the concentration is higher than 1.5 wt%. In addition, alloying with Mn improves the corrosion resistance by lowering the

solubility of iron, refines the grain structure and contributes to the weldability [Kai03]. Due to its low solubility Ce is usually observed to form $Mg_{12}Ce$ precipitates. In the investigated ME21 alloy micrometer-sized $Mg_{12}Ce$ precipitates and nanometer-sized Mn precipitates occur simultaneously [Hup10a, Hup11, Brö11, Li11, Gal12].

Several authors have reported a significant increase of the ductility of Ce containing alloys, which was usually attributed to texture modifications introducing an additional RE texture component with favorable orientation for the activation of $\langle a \rangle$ basal slip [Sta08b, Sta08c, Hup10a, Brö11, Len13]. Chino et al. [Chi08] reported an enhanced ductility and stretch formability of an Mg 0.2 wt% Ce alloy compared to pure Mg, which was attributed to a higher activity of non-basal slip especially $\langle a \rangle$ prismatic slip. It was supposed that the addition of Ce increases the SFE indicating that non-basal slip modes can be activated to a significant extent in Ce containing Mg alloys. In [Li11] and [Hir13] it is suggested that Ce addition changes the relative CRSS of several slip systems compared to AZ31 indicating solid solution hardening and softening effects on slip and twin modes despite the presence of the aforementioned precipitates.

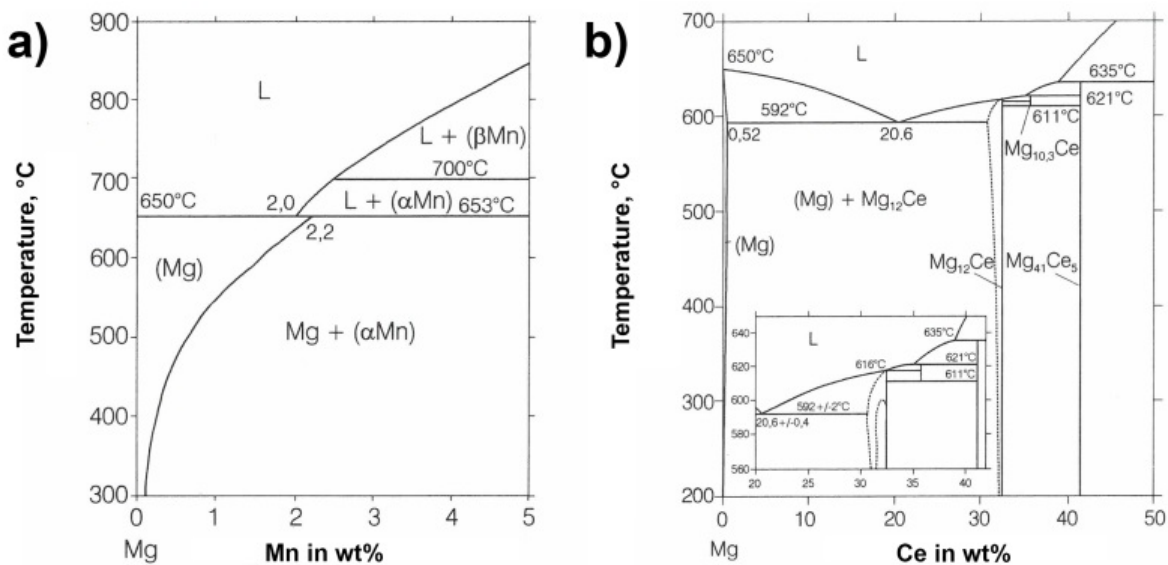


Fig 2.13: Binary phase diagrams: a) Mg-Mn, b) Mg-Ce [Kam00].

2.4.2 WE54

The WE54 alloy contains 5 wt% Y and 4 wt% heavy RE metals, predominantly Nd. Based on the solubility of the alloying elements at high temperatures and the limited solubility at lower temperatures age-hardening is possible in this alloy (Fig 2.14, [Kam00, Nie00, Kai03]).

Agnew et al. [Agn01] showed that the solid solution of Y enhances the activity of the $\langle c+a \rangle$ pyramidal slip system, which helps the accommodation of c -axis compression, via VPSC modeling. This result is supported by studies of Sandlöbes et al. [San11, San12, San13] using TEM experiments and density functional theory (DFT) calculations to analyze pure Mg and binary Mg-Y alloys. According to their studies the SFE of the sessile stacking fault I_1 decreases with Y addition. As this stacking fault acts as a heterogeneous nucleation source for $\langle c+a \rangle$ pyramidal dislocations, a high activity of $\langle c+a \rangle$ dislocations gliding on 1st and 2nd order pyramidal planes was observed [San11, San12, San13, Agn15]. Very recently, Stanford et al. [Sta15] showed that high Y solute concentrations result in a reduced $\{10\bar{1}2\}$ TTW-ing activity and the appearance of $\{11\bar{2}1\}$ twins. They ([Sta15]) suggest that the large

atomic radius of Y ($r_Y = 0.181$ nm; $r_{Mg} = 0.160$ nm [Sha05]) hinders the atomic shuffling process which accompanies the twinning shear in TTW-ing.

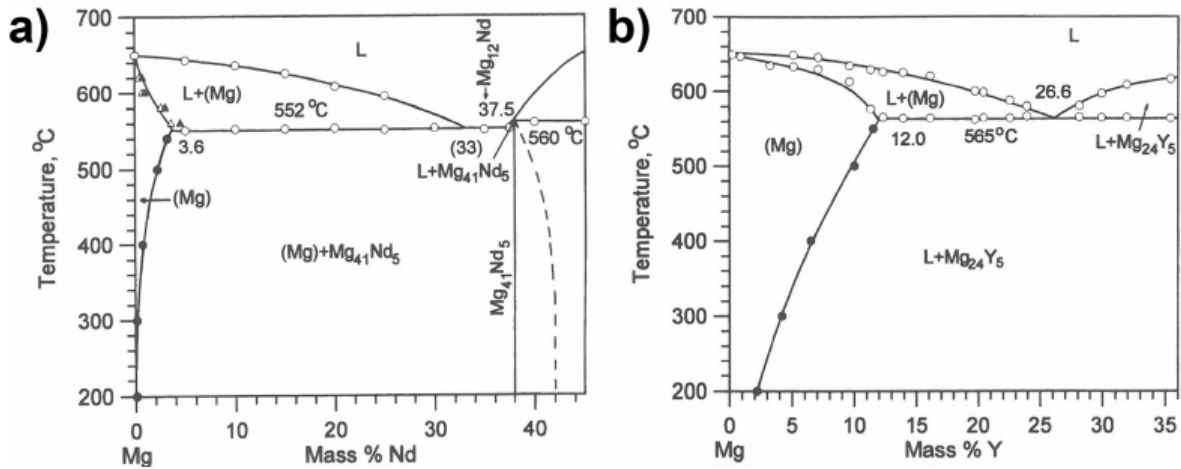


Fig 2.14: Binary phase diagrams: a) Mg-Nd, b) Mg-Y [Roh03].

Hidalgo-Manrique et al. [Hid14] observed a strong influence of Nd solute atoms and precipitates on the yield stress asymmetry in an MN11 alloy and proposed that solute Nd constitutes a strong obstacle for basal dislocation. Similar results were found by Dudamell et al. [Dud13]. Zhang et al. [Zha12] applied DFT calculations to investigate the influence of RE elements on the stacking faults of Mg solid solutions. According to their study the SFEs of the I_1 and I_2 stacking faults decrease with Nd addition. In [San12] it was shown that I_1 stacking faults can promote $\langle c+a \rangle$ pyramidal slip. A decreased I_2 SFE could reduce the cross-slip probability for basal dislocations, which could result in a less mobile basal dislocation structure causing a relatively higher activation of non-basal deformation modes [San12]. Based on the investigations of Stanford et al. [Sta15] and the very similar atomic radii of Nd ($r_{Nd} = 0.182$ nm [Sha05]) and Y, it is likely that Nd hinders the atomic shuffling process, which is required during TTW-ing, analogous to Y.

The precipitation sequence of Mg-Y-Nd alloys has been investigated several times ([Nie99, Nie00, Ant03, Gao12]). It is summarized in the review article [Nie12] and illustrated in Fig 2.15. According to [Nie12] the following precipitation sequence occurs:

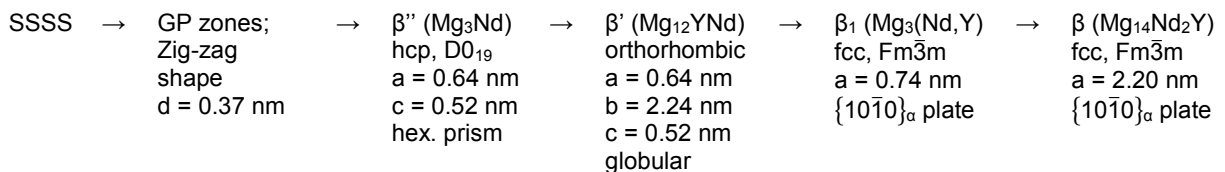


Fig 2.15: Precipitation sequence of Mg-Y-Nd alloys.

Gao et al. [Gao12] developed a phase field model of β_1 precipitation indicating stress concentrations at rim of the β_1 disk, which favor nucleation and growth of β' particles. In [Agn13] the effect of age-hardening on the relative activity of deformation modes is investigated in a cast WE43 alloy using in-situ neutron diffraction and EPSC simulations. The simulations reveal that plate-shaped precipitates on $\{10\bar{1}0\}_\alpha$ planes, which are generated during age-hardening, effectively hinder $\langle a \rangle$ basal slip, while $\langle a \rangle$ prismatic slip and TTW-ing are not affected as much as basal slip. Interestingly, the study indicates that the CRSS of TTW-ing is lower in the aged samples than in the solutionized samples.

Fig 2.16 depicts β' , β_1 and β phases, which were observed in a WE54 alloy after different 250 °C heat treatments [Nie00].

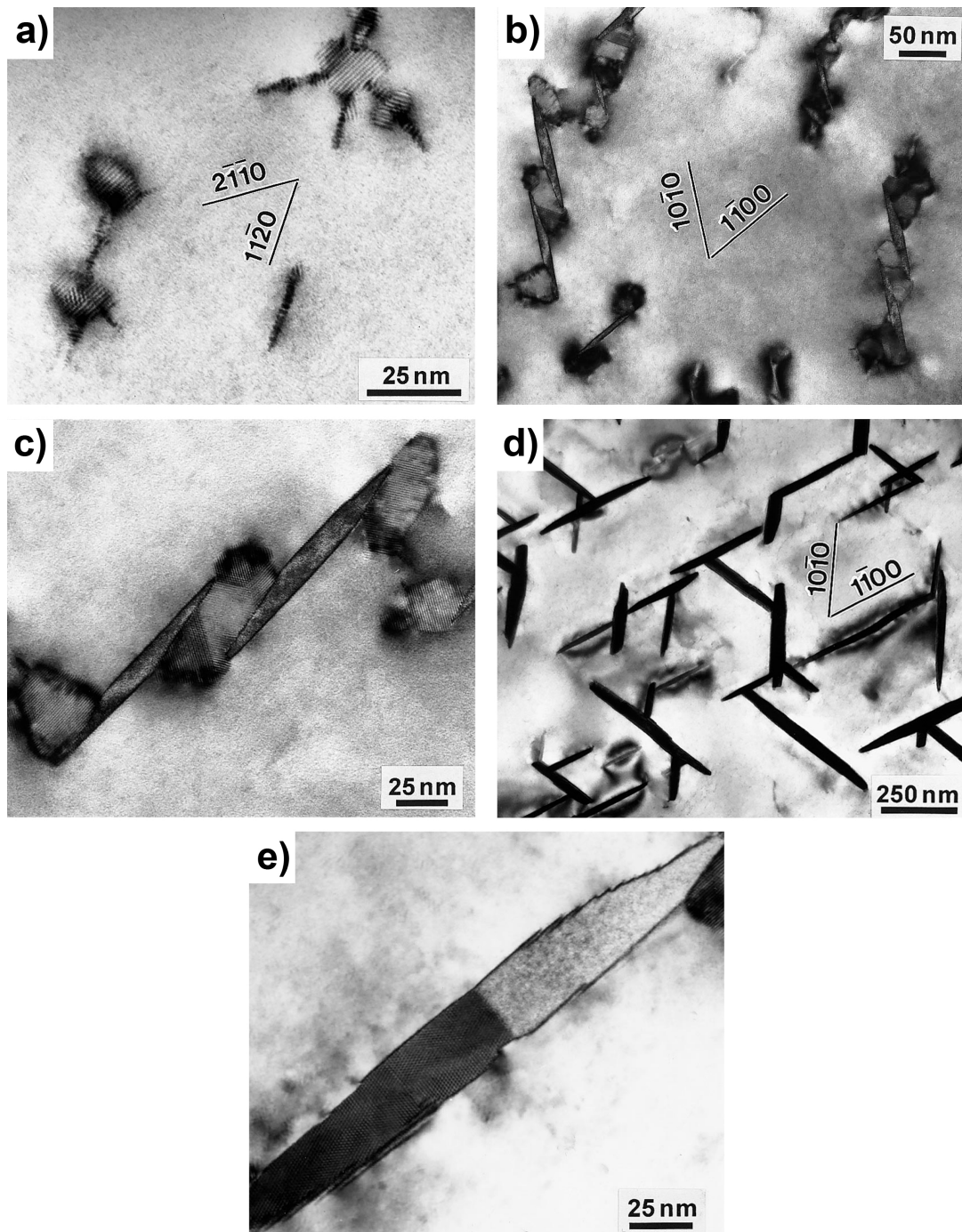


Fig 2.16: Precipitation in WE54 aged at 250 °C (ZA [0001]). a) 4 h - $\{11\bar{2}0\}$ platelets and globular β' precipitates; b) and c) 48 h - globular β' precipitates and $\beta_1 \{10\bar{1}0\}$ platelets; d) 2400 h - equilibrium $\beta \{10\bar{1}0\}$ plates; e) 48 h - β_1 to β transition [Nie00].

2.4.3 L4 and LA41

Within this study the Mg-Li alloys L4 (4 wt% Li) and LA41 (4 wt% Li and 1 wt% Al) were investigated. Due to its low density alloying with Li enables a further reduction of the density of Mg alloys. At ambient temperature Li is retained in solid solution (< 15 at%) causing an increased ductility. Hauser et al. [Hau56] have reported a decreasing c/a ratio with increasing Li concentrations in such alloys. At higher Li concentrations the β bcc phase forms resulting in a dual phase microstructure (15 - 30 at%) or a single phase β microstructure (> 30 at%). The corresponding phase diagram is shown in Fig 2.17 a). Although, a further decrease of the density is attractive for light-weight applications, several disadvantages such as an increased reactivity, negative effects on burning and vapor behavior of the melt and a worse

corrosion behavior limit the application of such alloys [Kam00, Kai03]. Nevertheless, there has been significant effort in designing Mg-Li based alloys and suitable processing [San96, Haf00, Agn01, Agn02, Bac03, Son04, Agn06b, Als08a, Als09, Cou09].

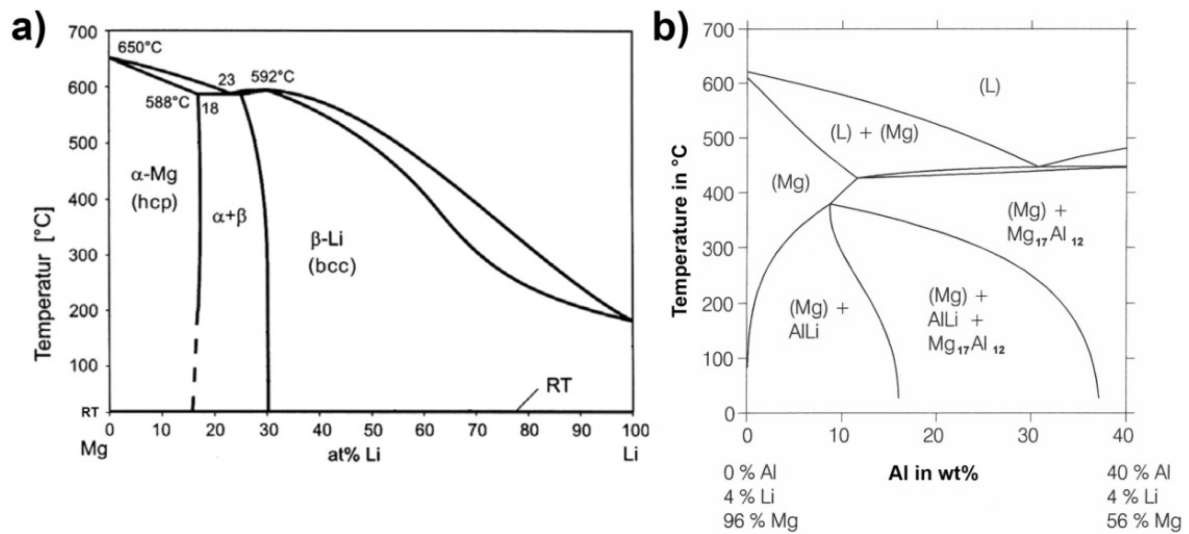


Fig 2.17: a) Binary Mg-Li phase diagram, b) section through the Mg-Li-Al phase diagram (a) based on [Als09], b) based on [Kam00].

Several early studies indicate hardening of $\langle a \rangle$ basal slip and softening of $\langle a \rangle$ prismatic slip in Mg-Li alloys [Ahm65, Qui62, Kel68]. An early investigation by Kelley and Hosford [Kel68] showed that the addition of 4 wt% Li to Mg single crystals lowers the CRSS of $\langle a \rangle$ prismatic slip, while $\langle a \rangle$ basal slip and TTW-ing are hardened. In [Agn01] VPSC simulations and mechanical testing were applied revealing significantly improved elongations to failure caused by an increase of $\langle c+a \rangle$ pyramidal slip activity in Mg-Li alloys. These results were confirmed [Agn02] via TEM dislocation analysis of deformed Mg 15 at% Li samples containing a higher amount and more uniform distributed $\langle c+a \rangle$ dislocations than pure Mg samples, which indicates a promoting effect of Li additions on the activation of $\langle c+a \rangle$ pyramidal slip. As this slip mode provides 5 independent slip systems and enables c -axis deformation it was suggested that its promotion causes the enhancement of the ductility of hcp solid solution Mg-Li alloys [Agn01, Agn02]. Al-Samman [Als09] analyzed the deformation behavior of an Mg 4wt% Li alloy in comparison to an AZ31 alloy and reported a significantly enhanced ductility of the Mg-Li alloy. This study suggests that $\langle c+a \rangle$ pyramidal slip is enhanced at room temperature, while elevated temperature renders $\langle a \rangle$ prismatic slip more active than $\langle c+a \rangle$ pyramidal slip [Als09]. DFT calculations by Han et al. [Han11] and Muzyk et al. [Muz12] indicate that the basal SFE is increased by Li alloying. This would decrease the tendency of $\langle c+a \rangle$ dislocations to decompose into the basal plane and promote prismatic cross-glide of $\langle a \rangle$ dislocations [Agn02]. Presently, there is less information on the effect of Li on the CRSS of TTW-ing. In [Muz12] the ratio of the twinning energy and the unstable SFE of the $\langle a \rangle$ prismatic slip system was used to assess the effect of alloying elements on twin formation. Their study indicates that Li addition increases this ratio compared to pure Mg decreasing the possibility of twin formation during deformation. Similar results were obtained by Shang et al. [Sha14] using first-principles calculations to analyze the SFEs and the propensity to twin (so called twinnability) of dilute Mg alloys and revealed that Li additions tend to lower the twinnability.

Through the addition of Al to Mg-Li alloys AlLi precipitates and Mg₁₇Al₁₂ precipitates can be generated providing a significant increased strength and embrittlement [Kam00]. An increased Al solute content reduces the DRX d_g in AZ alloys [Wat01] and according to Shang et al. [Sha14] Al addition lowers the twinnability.

3. Aim

In order to exploit the full weight-saving capacity of Mg parts, wrought alloys are required as they usually exhibit improved mechanical properties such as higher strength and ductility than cast alloys [Pek13]. However, the application of Mg wrought alloys is currently restricted by their limited room temperature formability and a pronounced anisotropy of the products.

For a given alloy each processing step introduces changes of the microstructure including alterations of the grain size, the texture, the precipitate size and distribution as well as solute contents. Each of these microstructural parameters in turn influences the mechanical properties of a (semi-finished) product. Here, a profound understanding of the correlations between processing parameters and the generated product's microstructure is required to enable failure-free processes and tailored materials for specific applications or forming processes. The aim of the present study is to contribute to the understanding of processing - microstructure as well as microstructure - mechanical property correlations investigating four Mg alloys (ME21, WE54, L4 and LA41).

Therefore, the extrusion process starting from the cast material and including post extrusion heat treatments is selected exemplary to investigate the effect of different processing parameters on the microstructural development. Here, the effect of different billet temperatures, extrusion ratios and cooling conditions as well as the effect of heat treatment parameters temperature and dwell time are of particular interest as they enable the variation of the above mentioned microstructural parameters within a wide range. The alloy selection was chosen to enable the investigation of grain size effects (ME21, WE54, L4 and LA41), solute effects (WE54, L4 and LA41), precipitate effects (ME21 and WE54) as well as texture effects (ME21 and WE54).

In order to enable the analysis of Hall-Petch effects the grain size was modified. Low billet temperatures and high cooling rates enable the generation of fine grained materials, while high billet temperatures and air cooling as well as post extrusion heat treatments cause coarse grained materials. The solid solution alloys L4 and LA41 enable the investigation of Li solute concentrations on the active deformation modes, while the WE54 alloy features high Y and Nd concentrations, which are expected to affect the deformation behavior, significantly. The latter mentioned alloy allows the controlled generation of precipitates through post extrusion heat treatments, which enable the investigation of precipitation hardening and at the same time reduce the solute concentrations. Thereby, the effect of changing solute concentrations on the deformation behavior can be analyzed in a single alloy. In addition, the ME21 and the WE54 alloys are expected to generate extrusion textures, which deviate from the conventional $\langle 10\bar{1}0 \rangle$, $\langle 11\bar{2}0 \rangle$ or $\langle 10\bar{1}0 \rangle / \langle 11\bar{2}0 \rangle$ extrusion textures through the addition of rare earth elements, enabling the investigation of texture effects on the deformation behavior.

4. Materials and characterization techniques

4.1 Alloys and metallographic sample preparation

In this study the alloys Mg-4wt%Li (L4), Mg-4wt%Li-1wt%Al (LA41), Mg-2wt%Mn-0.7wt%Ce mischmetal (ME21) and Mg-5wt%Y-4wt%Nd mischmetal (WE54) were investigated. The investigated alloys were obtained from the “Institut für Werkstoffkunde – Leibniz Universität Hannover” (Mg-Li based alloys), “Stolfig Group - Geisenfeld” (ME21) and “Magnesium Elektron – Manchester” (WE54). The chemical compositions of the alloys are given in Table 4.1.

Table 4.1: Chemical compositions of the investigated alloys (wt%). In case of the Mg-Li based alloys the concentrations of the accompanying elements correspond to the used high purity Mg. The ME21 alloy is equivalent to the alloy investigated in [Hup10a, Hup11, Gal12].

	Li	Al	Zn	Si	Cu	Mn	Fe	Ni	Ca
L4	4.0	0.01	<0.01	0.01	<0.01	0.03	<0.01	<0.01	0.02
	Li	Al	Zn	Si	Cu	Mn	Fe	Ni	Ca
LA41	4.0	1.0	<0.01	0.01	<0.01	0.03	<0.01	<0.01	0.02
	Mn	Ce	Al	Nd	Pr	Si	Th	Y	Zn
ME21	2.1	0.7	<0.01	<0.02	<0.01	<0.02	0.14	0.04	<0.02
	Y	Nd	HRE+Nd	Zr	Zn	Si	Cu	Mn	Others
WE54	5.0	1.6	2.6	0.5	0.01	<0.01	<0.01	0.01	<0.01

All samples were prepared by standard metallographic methods including grinding, mechanical and chemical polishing. Here, a solution of 12 ml hydrochloric acid (37 %), 8 ml nitric acid (65 %) and 100 ml ethanol was applied. For optical microscopy investigations the samples were etched using the etching solutions given in Table 4.2. The etching time varied between 2 s and 5 s. The d_g of the samples were determined via optical microscopy using the software “a4i Analysis” (aquinto) and “ImageJ” [Abr04].

Table 4.2: Applied etching solutions.

L4 & LA41	L4 & LA41 (polarized light)	ME21	WE54 as-extruded	WE54 aged
5 g citric acid	4.2 g picric acid	4.2 g picric acid	4.2 g picric acid	5 g citric acid
95 ml distilled water	10 ml acetic acid	10 ml acetic acid	10 ml acetic acid	95 ml distilled water
	10 ml water	10 ml water	10 ml water	
	70 ml ethanol	70 ml ethanol	70 ml ethanol	

For electron backscatter diffraction (EBSD) analysis etching was skipped. The samples were removed from the embedding compound and chemically polished. For transportation to the scanning electron microscope (SEM) the samples were either kept in ethanol or in an evacuated steel cylinder.

The thin foils required for TEM analysis were prepared by cutting, polishing and electrolytically thinned using a TENOPOL-3 (Struers). Initially, a perchloric acid solution (1000 ml ethanol + 50 ml perchloric acid) was used for electrolytical thinning, which provides reasonable results in case of the ME21 alloy. However, this solution was not suitable for the preparation of Mg-Li based alloys and the WE54 alloy, which were thinned using a solution of 5.3 g lithium chloride, 11.16 g magnesium perchlorate, 500 ml methanol and 100 ml 2-butoxy-ethanol. Typically, cross-sections were used for TEM analysis. However, the analysis of twinning required samples from the longitudinal sections as these provide suitable grain orientations of the parent and the twin based on the initial texture of the extruded bars.

4.2 Extrusion and heat treatments

The indirect extrusion trials were performed at the Extrusion Research and Development Center at Technische Universität Berlin using a horizontal extrusion press with a maximum capacity of 8 MN. The billet dimension was $\varnothing = 123 \text{ mm}$, $l = 150 \text{ mm}$ for all trials, while the T_B , the R (25 : 1, 41 : 1, 71 : 1) and the cooling medium (air / water) were varied. A product speed of 1.7 m/min was typically used. The following homogenization procedures were applied:

- L4: 4 h at 300 °C or none
- LA41: none
- ME21: 12 h at 400 °C
- WE54: 8 h at 525 °C

Post extrusion heat treatments were performed using Heraeus furnaces M110 and K1252 for high temperature annealing ($\geq 475 \text{ °C}$) or T6060 for age-hardening ($\leq 250 \text{ °C}$). The samples were quenched in water after high temperature annealing, while air cooling was applied for age-hardened samples.

4.3 Mechanical testing

Laboratory mechanical testing was performed using a servo-hydraulic “MTS 810” universal testing machine and a strain rate $\dot{\epsilon} = 2.5 \times 10^{-4} \text{ s}^{-1}$. The flow curves were recorded using the software “MTS TestStar (TestWare-SX)” and an extensometer “MTS 634.12F-34”. The specimen geometry of the standard samples and of specimens used for in-situ synchrotron studies (cf. section 4.5) are shown in Fig 4.1. In order to analyze the microstructural development during deformation, samples were deformed to predefined strain levels and analyzed using EBSD and X-ray diffraction based texture measurements.

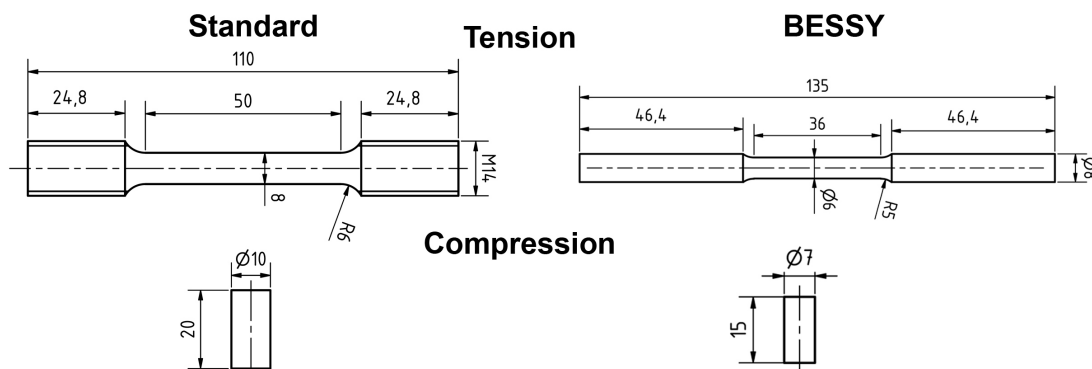


Fig 4.1: Specimen geometry: Standard laboratory samples (left), synchrotron samples (right).

4.4 Electron microscopy

According to the Rayleigh criterion $\Delta x \approx 0.6 \lambda / \sin \alpha$ the maximum resolution is proportional to the wavelength of the applied light, which limits the resolution of optical microscopes to $\approx 0.3 \mu\text{m}$. However, de Broglie proposed that particles such as electrons or neutrons possess a wavelike character, where $\lambda = h/(mv)$ with h being the Planck's constant, m the mass and v the speed of the particle. Consequently, sufficiently accelerated electrons enable much higher spatial resolution ($\approx 0.2 \text{ nm}$ using a modern TEM and an acceleration voltage of 200 keV) [Ege05].

4.4.1 Scanning electron microscopy

In scanning electron microscopy the electron beam is scanned across the specimen in two directions (x and y). Although, the spot size is in the range of 1 nm to 10 nm the resolution of

an SEM is lower due to the interaction of the beam and the sample. Within the interaction volume a variety of electron - specimen interactions can occur, which give rise to manifold signals, which can be exploited using suitable detectors to analyze the materials properties. Within this study secondary electrons (SE), backscattered electrons (BSE) and emitted characteristic X-ray radiation are relevant. When primary electrons interact with the specimen weakly bound outer shell electrons can be released. Such SEs feature a low kinetic energy (commonly < 100 eV). Most SEs are brought to rest within the interaction volume, however, those secondary electrons escaping into the vacuum provide a topographical contrast of the surface area. BSEs are primary electrons, which have been ejected from a solid by scattering through an angle > 90°. Most BSEs escape from the sample with energies not far below those of primary electrons. The fraction of primary electrons that escape as BSEs depends on the atomic number and hence, BSE detectors provide a contrast due to variations in the chemical composition. Furthermore, primary electrons can be scattered inelastically exciting sample atoms. When other atomic electrons fill the inner-shell vacancies characteristic X-ray photons are emitted enabling the characterization of the chemical composition of phases within the sample using energy-dispersive X-ray spectroscopy (EDS) [Ege05].

In addition, individual grain orientations can be determined via EBSD enabling local texture (aka microtexture) measurements, point-to-point orientation correlations and phase identifications within the SEM environment. EBSD relies on the evaluation of Kikuchi pattern, which are generated through the combined effect of diffuse scattering of primary electrons and elastic scattering fulfilling the Bragg equation [Ran00]:

$$2d_{hkl} \sin \theta = n\lambda \quad (4.1)$$

where d_{hkl} is the lattice plane spacing, 2θ the angle between incident and diffracted beam and λ the wavelength of the applied monochromatic radiation and n an integer defining the order of diffraction [Koc00, Ran00, Spi09].

When the electron beam enters the specimen it is diffusely scattered in all directions and hence, there must always be some electrons fulfilling the Bragg equation, which can undergo elastic scattering and give a strong reinforced beam. As the diffraction of electrons through the Bragg angle occurs in all directions a cone is generated, which extends about the normal of the reflecting lattice planes. If a detector is positioned to intercept the diffraction cones, a pair of conic sections results which appears as straight parallel lines (so-called Kikuchi lines). Kikuchi patterns arise from the superimposition of Kikuchi lines corresponding to different crystallographic planes. These patterns can be evaluated to determine the grain orientation [Ran00]. Fig 4.2 illustrates the generation of Kikuchi pattern and the typical EBSD geometry used in SEM.

The SEM investigations were carried out using:

- a SEM-Hitachi S-4000, which is equipped with an energy dispersive X-ray detector and an Oxford Instruments EBSD detector Nordlys II (TU Berlin – ZELMI),
- a Zeiss DSM 982 GEMINI SEM equipped with an EDAX Hikari camera for EBSD data acquisition (TU Berlin – ZELMI),
- a Zeiss Ultraplus SEM equipped with an Oxford Instruments EBSD detector NordlysNano (Helmholtz Zentrum Berlin).

In-situ EBSD measurements during compression tests were conducted using the Zeiss DSM 982 GEMINI SEM and a Kammrath & Weiss tensile / compression module 5 kN (Fig 4.2 b)).

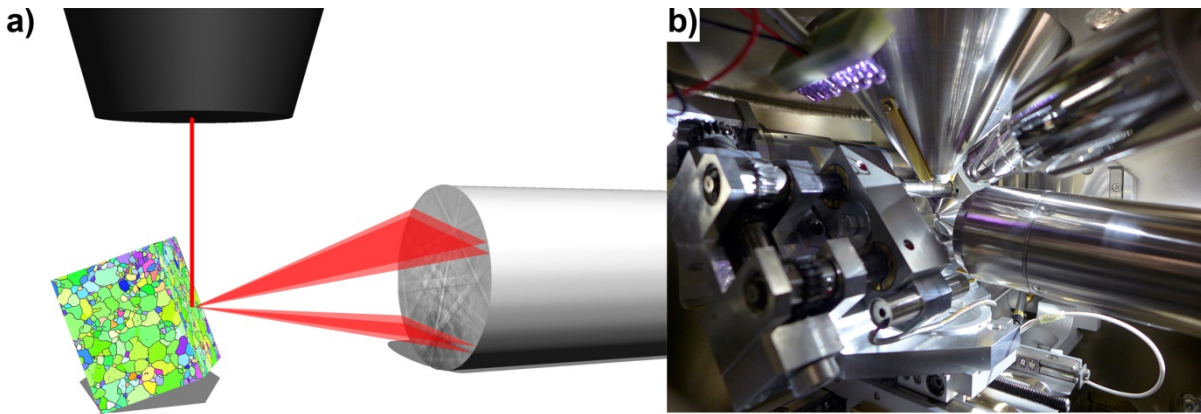


Fig 4.2: Schematic drawing of an EBSD setup and a view of the Kammrath & Weiss tensile / compression module installed in a Zeiss DSM982 GEMINI SEM.

4.4.2 Transmission electron microscopy

While the spatial resolution of a SEM is limited to the interaction volume of the primary electron beam, the application of TEMs enable spatial resolution on atomic scale ($\approx 0.2 \text{ nm}$) [Ege05]. Therefore, much higher acceleration voltages (200 keV - 300 keV) are applied to analyze thin foils in transmission providing insight on manifold materials properties such as the chemical composition of small scale precipitates via phase contrasts and EDS, dislocation arrangements and densities, the lattice of phases via Laue diffraction, point-to-point orientation relations, etc. A major advantage of the TEM is the ability to combine diffraction and imaging methods easily [Czi06]. However, the preparation of TEM thin foils is much more challenging than specimen preparation for SEM analysis. Fig 4.3 illustrates the thin-lens ray diagram of an imaging system of a TEM in diffraction and imaging mode.

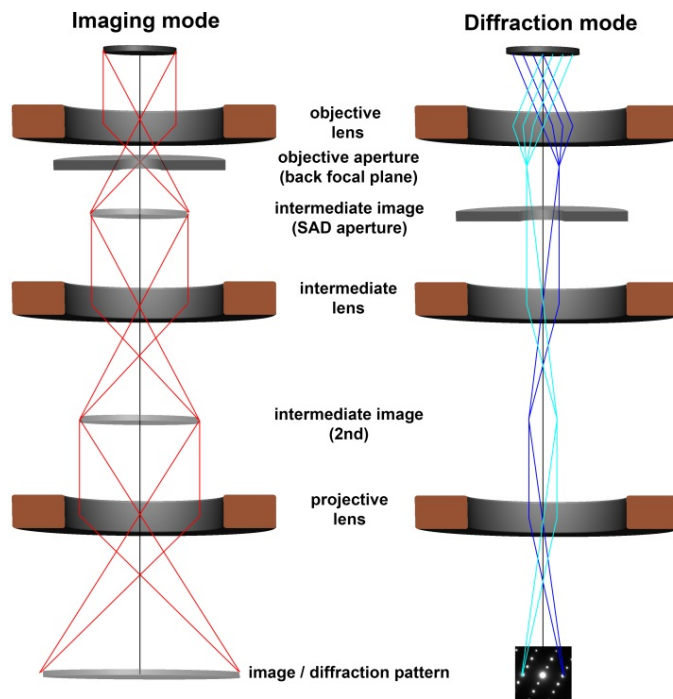


Fig 4.3: Schematic of a TEM in imaging mode and diffraction mode.

In the imaging mode the image of the real space, formed on the image plane of the objective lens, is projected onto the fluorescence screen or detector, while in the diffraction mode the diffraction pattern, generated on the back focal plane, is projected on the screen. In order to analyze the diffraction pattern of a specific area (e.g. large scale precipitates) an aperture for selected area diffraction (SAD) is inserted at the image plane of the objective lens. In the

imaging mode the SAD aperture is removed and an objective aperture is inserted in the back focal plane selecting the direct beam (bright-field image) or a diffracted beam (dark-field image). In case of high-resolution TEM (HR-TEM) the objective aperture is removed to form an image collecting many diffraction beams including diffracted beams featuring large $|\vec{g}|$ values (where \vec{g} to a reflection is normal to the corresponding hkl plane and $|\vec{g}| = d_{hkl}^{-1}$), which contain information of small-scale structures of the sample [Czi06]. Point-to-point orientation correlations and misorientation correlations can be determined on the basis of Laue diffraction and indexing of Kikuchi pattern analogous to EBSD in SEM.

In this study conventional TEM and HR-TEM investigations were conducted using a Philips CM-30 with a Voyager EDS-system applying an acceleration voltage of 250 keV and a FEI Titan 80-300 Berlin Holography Special TEM using 300 keV. In conventional TEM investigations orientation relations were determined through indexing of Kikuchi pattern using the software TOCA [Zae00].

4.5 Diffraction

Diffraction methods enable a series of investigations of crystalline materials such as crystal structure determination, phase analysis, lattice strain measurements for stress analysis and texture analysis. Within this study laboratory X-ray diffraction and time-of-flight (TOF) neutron diffraction are applied for texture analysis, while energy-dispersive X-ray synchrotron diffraction (EDXRSD) is used to measure the elastic lattice strain (ε_{hkl}) evolution during loading. These techniques are based on the Bragg equation, which is valid for X-ray and neutron diffraction (Eq. 4.1). For a given λ changes of 2θ result from changes of the lattice parameters and therefore, enable the calculation of ε_{hkl} , while texture analysis is based on changes of the reflection intensity as a function of the sample position (azimuthal angle φ and polar angle Ψ) [Koc00, Ran00, Spi09].

4.5.1 Laboratory X-ray texture measurements

X-ray texture measurements rely on the contribution of each crystallite, which fulfills the Bragg equation, within the gauge volume to the reflection intensity [Spi09]. Consequently, the measured intensity and the volume fraction of crystallites fulfilling the Bragg condition are coupled and can be measured as a function of the sample position. Laboratory X-ray texture analysis is usually performed using a 4-circle diffractometer. The goniometer moves the detector with respect to the X-ray beam into an appropriate 2θ position and subsequently, the sample is positioned relative to the X-ray beam by two rotations φ and Ψ . While φ and Ψ are scanned in a regular mesh (e.g. in 5° steps) the intensity is recorded for each angle combination providing the intensity distribution of a reflection. Based on the intensity distribution of several reflections (at least 5 in case of hcp crystals) the orientation distribution function (ODF) respectively the texture can be calculated applying several corrections (e.g. background, defocussing correction) [Koc00, Spi09].

In this study monochromatic Co- K_α radiation was used to measure the intensity distribution of the reflections $(10\bar{1}0)$, (0002) , $(10\bar{1}1)$, $(10\bar{1}2)$ and $(11\bar{2}0)$. In some cases the $(10\bar{1}3)$ reflection was measured, additionally, to back up the ODF calculation. The orientation distribution function was determined from the experimental data using the ODF program system [Bun93] and the Matlab software package MTEX [Bac10]. The recalculated textures are displayed in the form of inverse pole figures (IPF) using equal angular projections. Due to the generation of laboratory X-ray radiation using X-ray tubes, the penetration depth and the flux are currently limited. Therefore, bulk measurements and in-situ experiments require the use of other forms of radiation such as X-ray synchrotron radiation or neutron radiation.

4.5.2 Time-of-flight neutron diffraction for texture analysis

In contrast to X-rays, neutrons interact with the nuclei of the atoms. The application of neutron diffraction for bulk texture analysis has several advantages compared to X-rays particularly low absorption, high angular resolution and large beam cross sections. Complete pole figures can be obtained without special sample preparation and the measured pole figures can be used for ODF calculations after background corrections. However, the neutron flux is significantly lower than the photon flux in synchrotron diffraction resulting in longer required exposure times [Koc00, Wen03, Rei08].

In this study the time-of-flight (TOF) diffractometer HIPPO (High-Pressure-Preferred Orientation) at LANSCE (Los Alamos Neutron Science Center) was used to conduct in-situ texture measurements during high temperature heat treatments of the alloy ME21. In order to compensate the lower flux HIPPO is equipped with five banks of detector panels, which are arranged on rings (Fig 4.4) [Wen03]. A detailed description on the instrument and on the Rietveld texture analysis from TOF neutron diffraction data using the software MAUD (Materials Analysis Using Diffraction) can be found in [Wen03, Wen10].

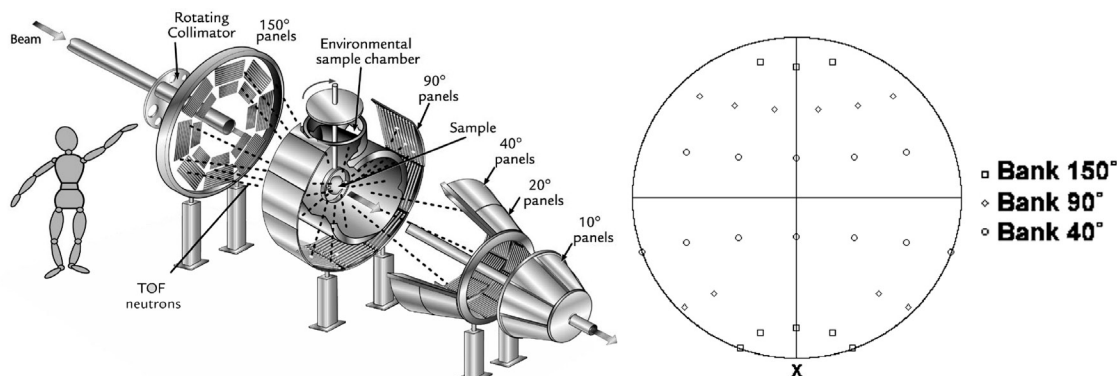


Fig 4.4: Schematic of the HIPPO diffractometer with five banks of detector panels arranged on rings and pole figure coverage with 30 detectors for $2\theta = 150^\circ$, 90° and 40° without sample rotations [Wen03].

In this study as-extruded ME21 samples ($l = 20$ mm, $\varnothing = 10$ mm) were heated in a vacuum furnace (standard ILL furnace from AS Scientific) up 475°C , 500°C , 525°C and 550°C using a heating rate of 20 K/min. As the vapor pressure of Mg increases significantly at the analyzed temperatures, sublimation of the sample is expected in vacuum [Kam00]. Therefore, the samples were encapsulated in a steel tube. The pole figure data collection started as soon as the desired annealing temperature was reached. Three sample rotations ($\omega = 0^\circ$; -67.5° ; -90°) were used to compute one pole figure. The exposure time was 2 min for each rotation which results in a time resolution of ≈ 8 min. In order to confirm that the short exposure times did not introduce artifacts during ODF calculations, additional measurements were performed prior to heating using exposure times of 10 min and 2 min. The obtained diffraction patterns were analyzed using the software MAUD (e.g. [Wen03, Wen10]), which applies the Rietveld method [Rie69], and the EWIMV texture method [Wen03, Wen10]. The first texture was refined manually for each temperature. Subsequently, the obtained parameters were used as starting parameters for successive measurements, which were evaluated using batch processing. Pole figures were recalculated based on the determined ODFs and visualized in form of IPFs using MTEX [Bac10].

4.5.3 In-situ energy-dispersive X-ray synchrotron diffraction

Based on its wide energy spectrum, brilliance, brightness and the orders of magnitude higher photon flux compared to conventional X-ray source, synchrotron radiation has become a powerful probe for the analysis of materials [Gen07]. In this study EDXRS is used to

evaluate the ε_{hkl} evolution during tensile or compression loading. The experiments were conducted at the energy-dispersive diffraction beamline EDDI at the Berlin synchrotron BESSY II. The setup of the EDDI beamline and the experimental setup of the loading experiments are depicted in Fig 4.5, a detailed description of the beamline can be found in [Gen07]. In contrast to monochromatic laboratory radiation, the EDDI beamline provides a white beam with a usable energy range in between about 15 keV and 150 keV [Gen07].

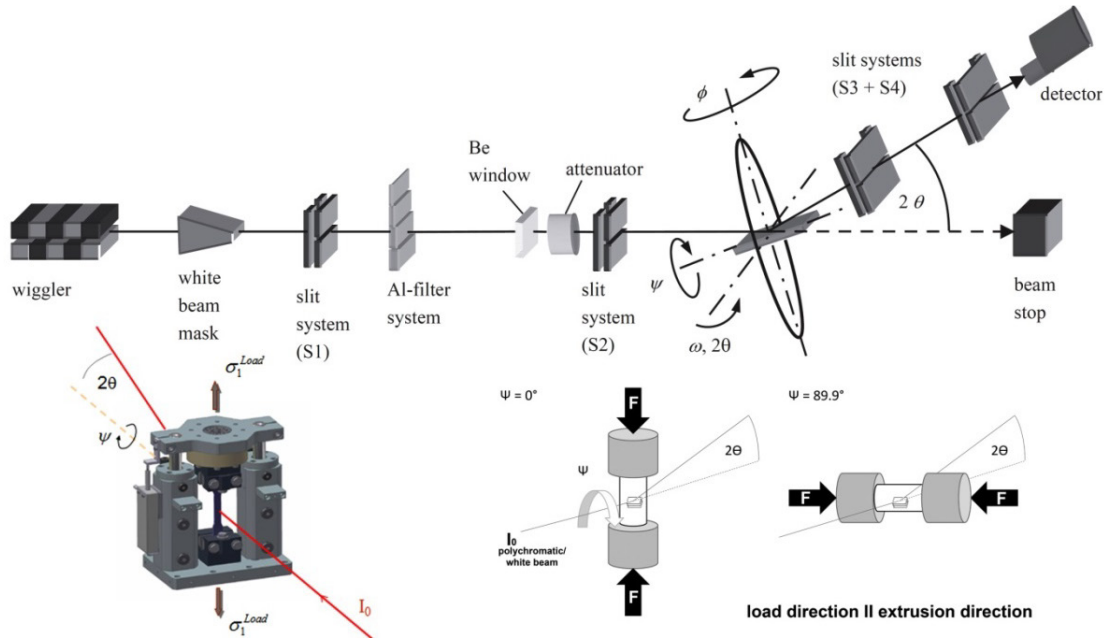


Fig 4.5: Setup of the EDDI beamline and schematic drawings of the tension / compression test station [Gen07, Hup11, Len13].

Using a fixed $\omega - 2\theta$ geometry and $E = h\nu = hc\lambda^{-1}$ the Bragg equation can be rewritten:

$$d_{hkl} = \frac{hc}{2 \sin \theta} \cdot \frac{1}{E_{hkl}} \text{ with } \frac{hc}{2 \sin \theta} = \text{const.} \quad (4.2)$$

where h is the Planck's constant, c the velocity of light, E_{hkl} the diffraction line corresponding to d_{hkl} . Based on this equation the elastic lattice strain $\varepsilon_{hkl,\varphi\Psi}$ can be determined [Gen07]:

$$\varepsilon_{hkl,\varphi\Psi} = \frac{d_{hkl,\varphi\Psi}}{d_{hkl,\varphi\Psi}^0} - 1 = \frac{E_{hkl,\varphi\Psi}}{E_{hkl,\varphi\Psi}^0} - 1 \quad (4.3)$$

As the present study analyzes elastic lattice strains resulting from an external load, $d_{hkl,\varphi\Psi}^0$ corresponds to the lattice plane spacing and $E_{hkl,\varphi\Psi}^0$ to the diffraction line position prior to loading. The applied experimental setup is summarized in Table 4.3; the specimen geometry is given in Fig 4.1:

Table 4.3: Applied experimental parameters.

General settings	Discontinuous lattice strain setup	Continuous intensity and lattice strain setup
Transmission mode	2 - 11 Ψ -angles	Continuous loading using a displacement rate of 0.001 mms^{-1}
Energy range 20 - 70 keV	60 s exposure	5 s or 10 s exposure
$2\theta = 10.3^\circ$ or 9.72°	Texture scans (assuming rotational symmetry)	
S1 and S2 were selected depending on the grain size	19 Ψ -angles	
S1 = S2 = $1 \times 1 \text{ mm}^2$ or	30 s exposure	
S1 = S2 = $1 \times 2 \text{ mm}^2$		
S3 = S4 = $0.1 \times 7 \text{ mm}^2$		

While X-ray synchrotron radiation provides a high spatial resolution, the maximum spot size as well as the penetration depth are limited in comparison to neutrons.

4.6 Elastoplastic self-consistent modeling

EPSC is a computer code, which simulates the thermo-mechanical deformation behavior of polycrystalline aggregates. The original EPSC model is a small strain formulation predicting the evolution of internal stresses in polycrystal during deformation in the elastoplastic regime. The code takes the single crystal elastic, plastic and thermal properties as well as hardening of slip systems into account and enables direct comparison of the predicted evolution of elastic strains in subsets of grains oriented for contributing to diffraction along specific directions and measurements made using X-ray or neutron diffraction methods [Tom10]. The EPSC model was developed by Turner and Tomé [Tur94] and applies the Eshelby inclusion formalism to represent the interaction of each grain with the homogeneous effective medium, which represents the average properties of the bulk material. Neil et al. [Nei10] extended the originally small strain model to finite strains, including texture development due to slip, and thereby the model allows the prediction of the texture evolution by twinning and slip, the ε_{hkl} evolution and the flow curve.

In order to predict the deformation behavior and ε_{hkl} evolution of Mg alloys during loading hardening models and twinning models are required. Within this study an empirical Voce hardening law [Tom84, Tom10] (ME21) and a dislocation based hardening law [Bey08, Kne13] were applied (WE54, L4, LA41). Furthermore, different twinning models, which will be introduced in sections 4.6.2 and 4.6.4, were used.

4.6.1 Voce hardening law

The extended Voce hardening law developed by Tomé et al. [Tom84] calculates the CRSS (τ^s) using the following equation [Cla08, Tom10]:

$$\tau^s = \tau_0^s + (\tau_1^s + \theta_1^s \Gamma) \left(1 - \exp\left(-\frac{\theta_0^s \Gamma}{\tau_1^s}\right) \right) \quad (4.4)$$

with θ_0^s and θ_1^s being the initial and the final hardening rate, Γ is the accumulated shear strain on the deformation mode and $(\tau_0^s + \tau_1^s)$ is the back-extrapolated intercept of the final hardening rate at $\Gamma = 0$ [Mur08, Tom10]. This empirical hardening model allows describing the high hardening rate observed at the onset of plasticity and its decrease towards a constant rate at large strains. Fig 4.6 illustrates the hardening for different parameter combinations [Tom10].

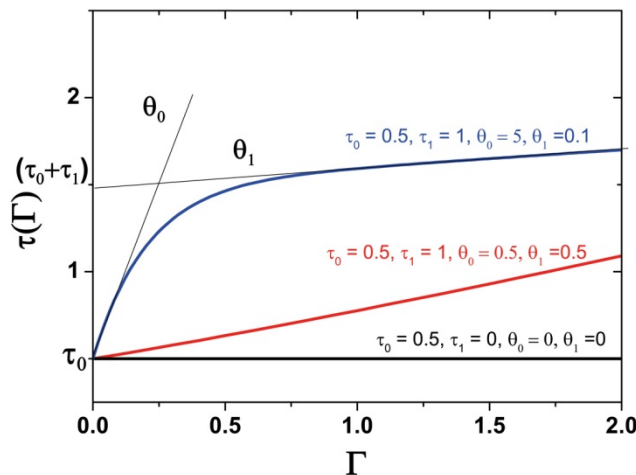


Fig 4.6: Illustration of the effect of the hardening parameters on the hardening rate as a function of the accumulated strain. Redrawn using Eq. 4.4 [Tom10].

The empirical Voce hardening law has the advantage that it allows easy interpretation of the used parameters and is widely-used in numerous publications dealing with deformation behavior of Mg alloys (e.g. [Agn01, Agn03, Agn06a, Cla08, Mur08, Mur10a, Wan10, Agn13]).

4.6.2 Finite initial fraction and continuity twin model

Clausen et al. [Cla08] developed two twinning schemes namely a ‘continuity’ approach and the ‘FIF’ (finite initial fraction) assumption. The continuity assumption applies continuity conditions for strains ε and stresses σ across the twin boundary:

$$\varepsilon_{11}^{\text{el,parent}} = \varepsilon_{11}^{\text{el,twin}}, \quad \varepsilon_{22}^{\text{el,parent}} = \varepsilon_{22}^{\text{el,twin}}, \quad \varepsilon_{12}^{\text{el,parent}} = \varepsilon_{12}^{\text{el,twin}} \quad (4.5)$$

$$\sigma_{33}^{\text{parent}} = \sigma_{33}^{\text{twin}}, \quad \sigma_{23}^{\text{parent}} = \sigma_{23}^{\text{twin}}, \quad \sigma_{13}^{\text{parent}} = \sigma_{13}^{\text{twin}} \quad (4.6)$$

where the local coordinate system is defined with axis 1 along the shear direction of the twin system and the 3 direction along the twin plane normal. The ‘FIF’ scheme assumes that twin nucleation is accompanied by twin growth up to a finite initial fraction resulting in an excess of plastic strain, which generates a back-stress between the parent and the twin. Thereby, this model is capable of modeling the repeatedly observed back-stress in the measured ε_{hkl} . Both implemented twin schemes allow the EPSC code to predict the texture evolution by twinning and slip, the ε_{hkl} evolution and the flow curve [Cla08].

4.6.3 Dislocation based hardening law

Within the dislocation based hardening model the evolution of slip resistance is calculated using the equation:

$$\tau^s = \tau_{0,f}^s + \tau_{HP}^s + \tau_{for}^s + \tau_{sub}^s \quad (4.7)$$

where $\tau_{0,f}^s$ is the friction stress (dependent on the Peierls stress, precipitates and the initial content of dislocation debris), τ_{HP}^s a barrier effect term (dependent on d_g , discussed in section 4.6.4), τ_{for}^s a forest dislocation interaction stress (dependent on a spatial random distribution of stored dislocations) and τ_{sub}^s a dislocation substructure interaction stress (dependent on non-random or ordered distribution of stored dislocations). The evolution of τ_{for}^s and τ_{sub}^s is determined by the evolution of the forest dislocation ρ_{for}^s and the substructure ρ_{sub}^α dislocation densities [Bey08, Kne13]. The effect of ρ_{for}^s can be calculated by a Taylor law [Mec81, Bey08, Kne13]:

$$\tau_{for}^s = \chi^s b^s \mu^s \sqrt{\rho_{for}^s} \quad (4.8)$$

with $\chi^s = 0.9$ being a dislocation interaction parameter, b^s the magnitude of the Burgers vector and μ^s the shear modulus. The contribution of ρ_{sub} to the hardening can be calculated via

$$\tau_{sub}^s = k_{sub} b^s \mu^s \sqrt{\rho_{sub}} \log\left(\frac{1}{b^s \rho_{sub}}\right) \quad (4.9)$$

where $k_{sub} = 0.086$ is an empirical parameter that recovers the Taylor law for low substructure dislocation densities [Mad02, Bey08, Kne13]. The evolution of ρ_{for}^s results from the competition between the rate of storage $\frac{\partial \rho_{gen,for}^s}{\partial \gamma^s}$ and the rate of dynamic recovery $\frac{\partial \rho_{rem,for}^s}{\partial \gamma^s}$:

$$\frac{\partial \rho_{for}^s}{\partial \gamma^s} = \frac{\partial \rho_{gen,for}^s}{\partial \gamma^s} - \frac{\partial \rho_{rem,for}^s}{\partial \gamma^s} = k_1^s \sqrt{\rho_{for}^s} - k_2^s(\dot{\varepsilon}, T) \rho_{for}^s, \quad (4.10)$$

$$\Delta\rho_{for}^s = \frac{\partial\rho_{for}^s}{\partial\gamma^s} |\Delta\gamma^s|$$

with γ^s being the shear, k_1^s a rate-insensitive coefficient for dislocation storage by statistical trapping of gliding dislocations by forest obstacles and k_2^s a rate-sensitive coefficient that accounts for dynamic recovery by thermally activated mechanisms [Bey08, Kne13]. According to Beyerlein et al. [Bey08] k_2^s can be calculated by:

$$\frac{k_2^s}{k_1^s} = \frac{\chi^s b^s}{g^s} \left(1 - \frac{kT}{D^s b^3} \ln\left(\frac{\dot{\epsilon}}{\dot{\epsilon}_0}\right)\right) \quad (4.11)$$

where k is the Boltzmann constant, $\dot{\epsilon}_0 = 1 \times 10^7 \text{ s}^{-1}$ a reference strain rate, g^s an effective activation enthalpy and D^s a drag stress [Bey08, Kne13]. In the model the rate of substructure development is coupled with rate of recovery of all active dislocations:

$$\Delta\rho_{sub} = \sum_s q^s b^s \frac{\partial\rho_{rem,for}^s}{\partial\gamma^s} |\Delta\gamma^s| \quad (4.12)$$

where q^s is a dislocation recovery rate coefficient defining the fraction of dislocations that do not annihilate and become substructure [Kne13].

4.6.4 Composite grain based twinning model and related barrier effects

Within the dislocation based hardening model twinning is described by the composite grain model [Pro07] using the FIF (= 0.015) assumption, where the twin system with the highest shear-rate among all active twin systems is identified in each grain and selected as predominant twin system (PTS = 0.05). Subsequently, the grain is subdivided into a stack of ellipsoids having the crystallographic orientation of the predominant twin and of the matrix, respectively. If more shear is realized by the twin, volume fraction is transferred from parent to twin and the ellipsoids representing the twin thickening and the parent shrinking [Pro07, Kne13]. In case of twinning τ^t is calculated via:

$$\tau^t = \tau_0^t + \mu^t \sum_t C^{st} b^t b^s \rho_{for}^s + \tau_{HP}^t \quad (4.13)$$

where μ^t , C^{st} and $b^t = 5.54 \times 10^{-11} \text{ m}$ are the elastic shear modulus on the system, the latent hardening matrix and the magnitude of the Burgers vector of a given twin [Opp12, Kne13]. The barrier effects τ_{HP}^t and τ_{HP}^s are calculated using HP like equations:

$$\tau_{HP}^s = \mu^s HP^s \sqrt{\frac{b^s}{d_g}} \quad \text{without twins} \quad (4.14)$$

$$\tau_{HP_mfp}^s = \mu^s HP^{st} \sqrt{\frac{b^s}{d_{mfp}^{s,PTS}}} \quad \text{with twins} \quad (4.15)$$

$$\tau_{HP}^t = \frac{HP^{tt}}{\sqrt{d_g}} \quad \text{without twin} \quad (4.16)$$

$$\tau_{HP_mfp}^t = \frac{HP^{tt}}{\sqrt{d_{mfp}^{s,PTS}}} \quad \text{with twins} \quad (4.17)$$

where HP are Hall-Petch terms, d_g the initial grain size and d_{mfp} the mean free path calculated based on the separation between twin lamellas [Bey08, Opp12]. In Mg TTW boundaries are not expected to introduce effective barriers for dislocations [Cap09a, Kne10, Opp12] and hence, were not considered as barriers in the simulations.

5. Results

5.1 ME21

5.1.1 Extrusion billets

Fig 5.1 displays a macrosection and a micrograph of a homogenized ME21 extrusion billet, which illustrate the d_g and precipitates, respectively. The billet features a coarse grain microstructure and precipitates of two different size scales. According to [Hup10a] and [Gal12] the coarse precipitate fraction predominantly corresponds to the $Mg_{12}Ce$ phase, while the fine precipitates are Mn.

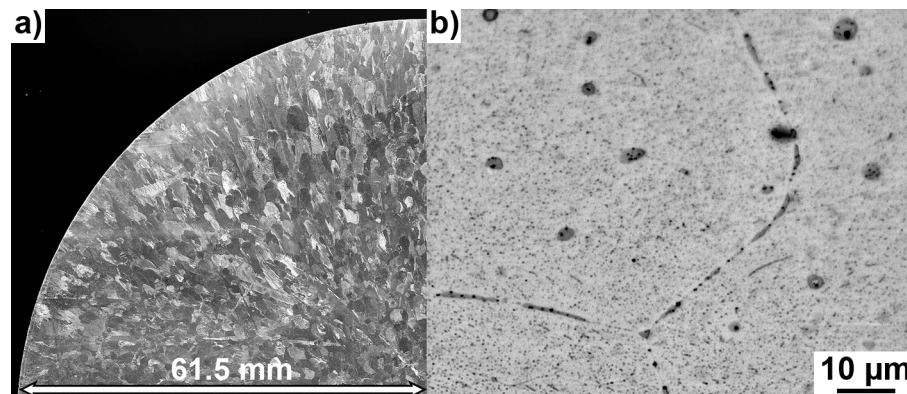


Fig 5.1: a) Macrosection of a homogenized ME21 cast billet, b) micrograph illustrating coarse $Mg_{12}Ce$ and fine Mn precipitates within the billet.

5.1.2 Extrusion products

Within this study several extrusion trials were conducted to analyze the effect of the T_B , the R and the cooling conditions on the microstructure, texture and mechanical properties (cf. Table 5.1). All billets were homogenized using a temperature of 400 °C and a dwell time of 12 h. The resulting microstructure and texture will be shown below.

Table 5.1: Summary of the applied extrusion parameters.

Extrusion	T_B , °C	R	Product speed, m/min	Cooling	Peak force, MN
A	450	41 : 1	1.7	air	4.1
B	450	41 : 1	1.7	water	4.1
C	500	41 : 1	1.7	air	3.3
D	500	41 : 1	1.7	water	3.3
E	500	25 : 1	1.7	air	2.5
F	550	41 : 1	1.7	air	2.6
G	500	71 : 1	1.7	air	2.6
H	450	71 : 1	1.7	air	4.6

5.1.2.1 Microstructure and texture

The ME21 extrusions feature a recrystallized largely homogeneous microstructure. Very occasionally larger grains were observed, which are elongated parallel to the ED (Fig 5.2). Fig 5.3 and Table 5.2 summarize the effect of different extrusion parameters on the average d_g of the ME21 extrusions. Increasing T_B and air cooling result in increasing average d_g . However, increasing R do not show an unambiguous trend. The comparison of the extrusions C, E and F (500 °C, air cooling) displays a minimal average d_g using R 41 : 1. The smallest d_g was obtained using $T_B = 450$ °C, R 41 : 1 and air cooling.

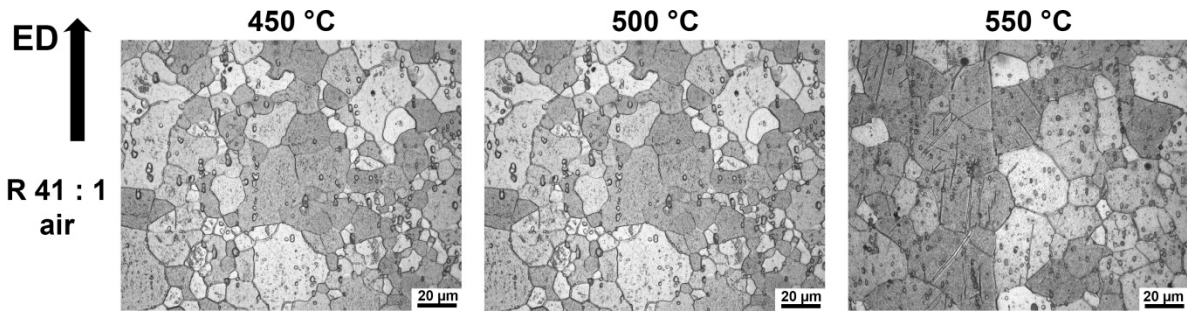


Fig 5.2: Exemplary micrographs illustrating the effect of extrusion parameters on the d_g .

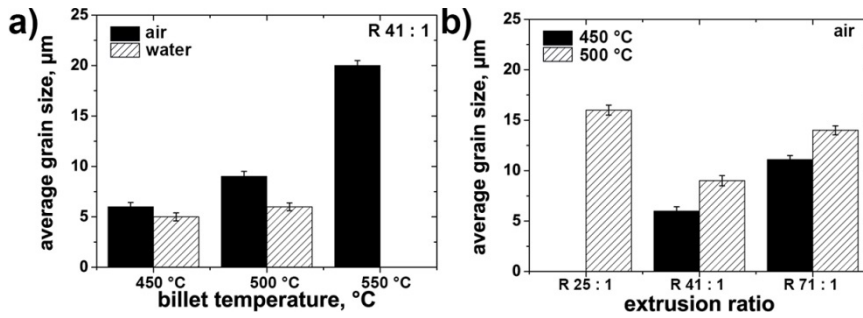


Fig 5.3: Histograms showing the effect of the extrusion parameters on d_g : a) Effect of T_B , b) effect of R.

Table 5.2: Applied extrusion parameters and resulting average d_g (μm). The standard deviation of the log-normal distribution is approximately $0.5 \mu\text{m}$.

T_B , cooling	ME21		
	R 25 : 1	R 41 : 1	R 71 : 1
450 °C, air	-	6	11
450 °C, water	-	5	-
500 °C, air	16	9	14
500 °C, water	-	6	-
550 °C, air	-	20	-

The observed textures are similar to previously reported ME21 extrusion textures [Hup10a, Hup11] and summarized in Fig 5.4:

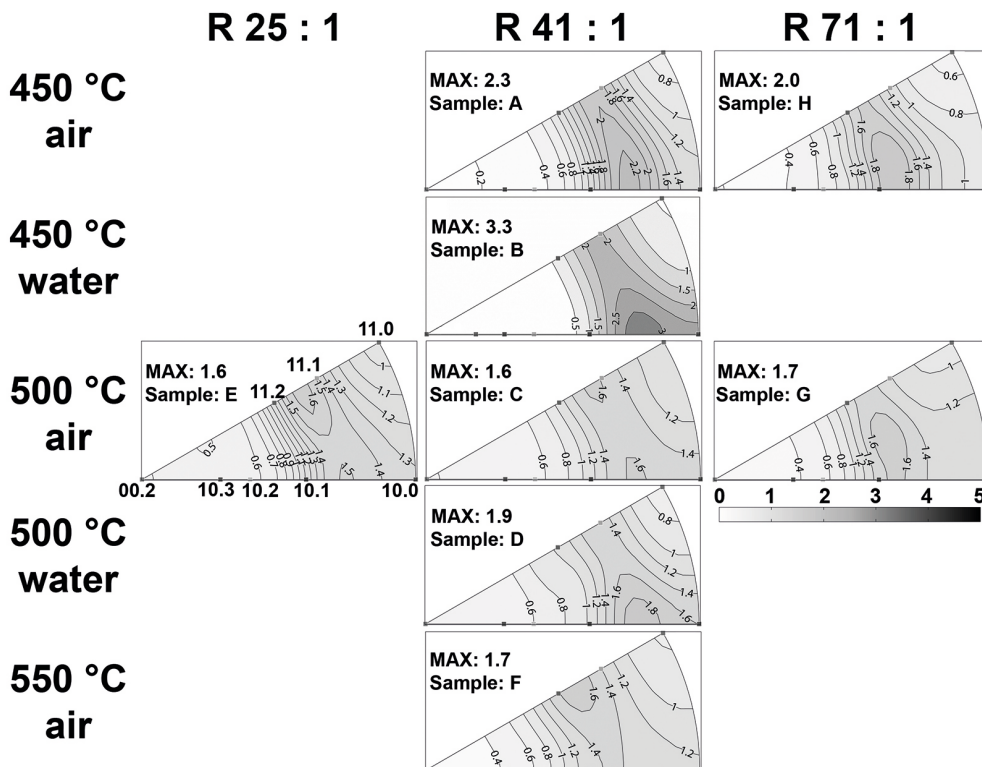


Fig 5.4: Measured extrusion texture (IPF || ED).

In contrast to conventional Mg alloy extrusions, which usually feature $\langle 10\bar{1}0 \rangle$, $\langle 11\bar{2}0 \rangle$ or $\langle 10\bar{1}0 \rangle / \langle 11\bar{2}0 \rangle$ fiber textures, the investigated alloy exhibits weak textures containing RE texture components. High R result in a shift of the maximum intensity towards the $\langle 10\bar{1}1 \rangle$ component, while increasing T_B and reduced cooling rates promote $\langle 11\bar{2}1 \rangle$ and $\langle 11\bar{2}2 \rangle$ orientations. Water cooling sharpens the texture.

5.1.3 Heat treatments

Based on the investigation of Brömmelhoff et al. [Brö11], which indicates a remarkable increase of the elongation to failure in uniaxial compression tests of heat treated ($T > 475$ °C) ME21 extrusions the following high temperature heat treatments were conducted using the extruded bar B, which features the smallest d_g (Table 5.2).

- 5 min to 24 h at 475 °C
- 5 min to 10 h at 500 °C
- 5 min to 10 h at 525 °C
- 5 min to 10 h at 550 °C

5.1.3.1 In-situ TOF neutron diffraction

In order to investigate the kinetics of the texture evolution in-situ TOF neutron diffraction experiments were conducted. The texture evolution is illustrated in Fig 5.5, which reveals a fast transition to an enhanced RE texture component at the time scale of minutes, if the annealing temperature ≥ 475 °C. At temperatures ≥ 500 °C the maximum density has shifted to the RE texture component during the data collection of the first evaluable data set (using only one ω rotation). Subsequently, there are no qualitative changes of the texture and minor changes of the maximum intensity.

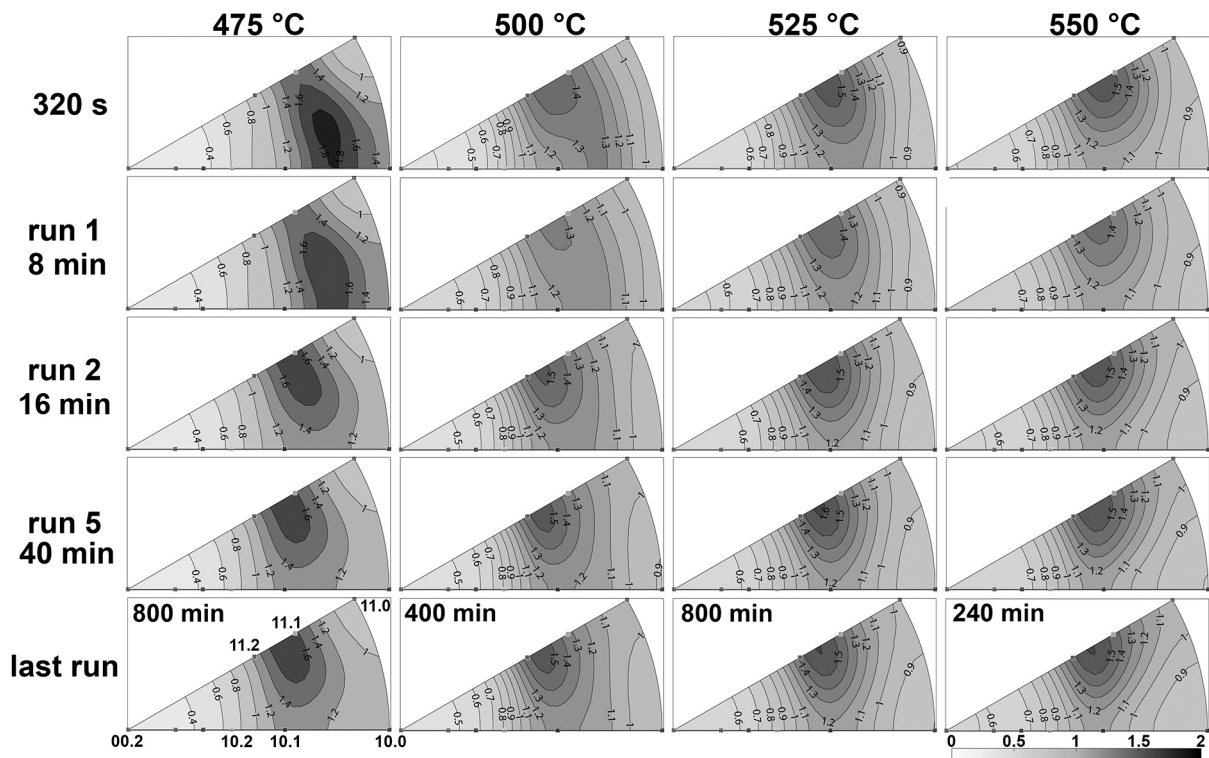


Fig 5.5: Time resolved analysis of the texture development (IPF || ED) determined via TOF neutron diffraction.

At 475 °C the texture evolution is decelerated. Here, a gradual shifting of the maximum density towards the RE texture component is observed. Between 320 s and 8 min the maximum density spreads out towards the RE texture component, which becomes dominant at dwell

times ≥ 16 min. While previous studies [Brö11, Len13] examined dwell times ≥ 1 h, the present results show that significantly shorter dwell times are required to obtain equivalent textures. However, it was shown that a homogeneous microstructure is required in addition to the favorable texture to generate optimal elongations to failure [Len13]. Therefore, EBSD measurements were conducted to analyze microstructure and microtexture evolution.

5.1.3.2 Microstructure and texture

Post-mortem EBSD investigations were conducted after 5 min and 10 h annealing. The corresponding EBSD maps are displayed in Fig 5.6 and Fig 5.7, while Fig 5.8 analyses the changes of the d_g distribution using histograms. Fig 5.9 illustrates the corresponding macrotextures, which were extracted from the EBSD maps. The determined IPFs confirm the above TOF neutron diffraction results. These results will be discussed below.

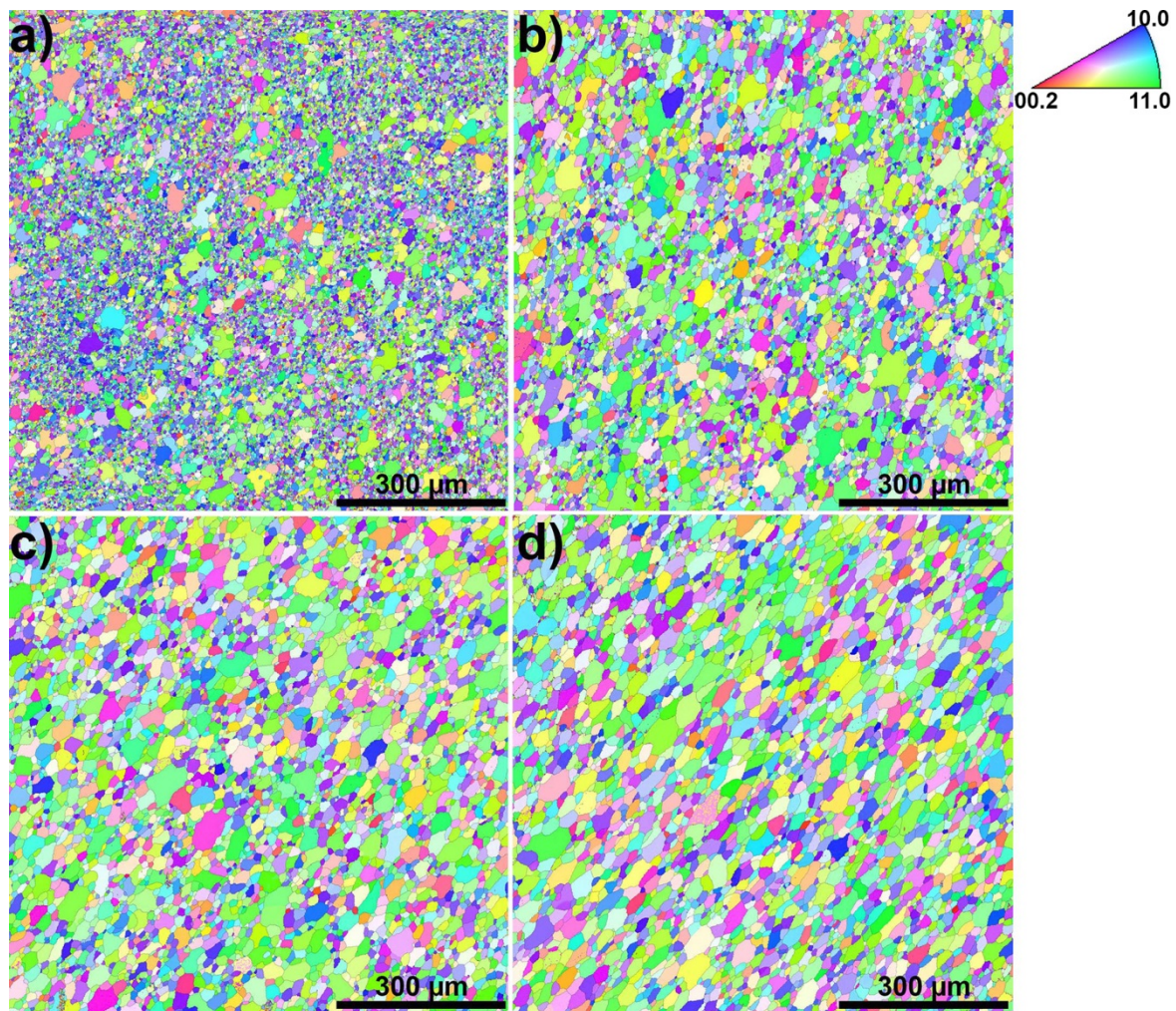


Fig 5.6: EBSD maps showing the microstructure after 5 min annealing (cross-section): a) 475 °C, b) 500 °C, c) 525 °C, d) 550 °C.

As might be expected from the TOF neutron diffraction results the grain growth rate decreases significantly using annealing temperature below 500 °C. In addition, Fig 5.6 a) and Fig 5.7 a) reveal a bimodal microstructure, which also has been reported in [Brö11, Len13], where a part of the grains grows significantly, while the majority of the grains feature a very low d_g . The comparison of Fig 5.6 and Fig 5.7 indicates that abnormal grain growth (AGG) occurs during the early stage of the annealing treatments, which is quantified using histograms in Fig 5.8. After 5 min coarse grains have formed being surrounded by a matrix of fine grains. These coarse grains reveal AGG, which proceeds up to 10 h annealing (Fig 5.7), where a variety of very coarse grains has formed, while the fine grained (FG) fraction fea-

tures a much lower growth rate. Here, it should be noted that the abnormal growth is not limited to grains of a single orientation.

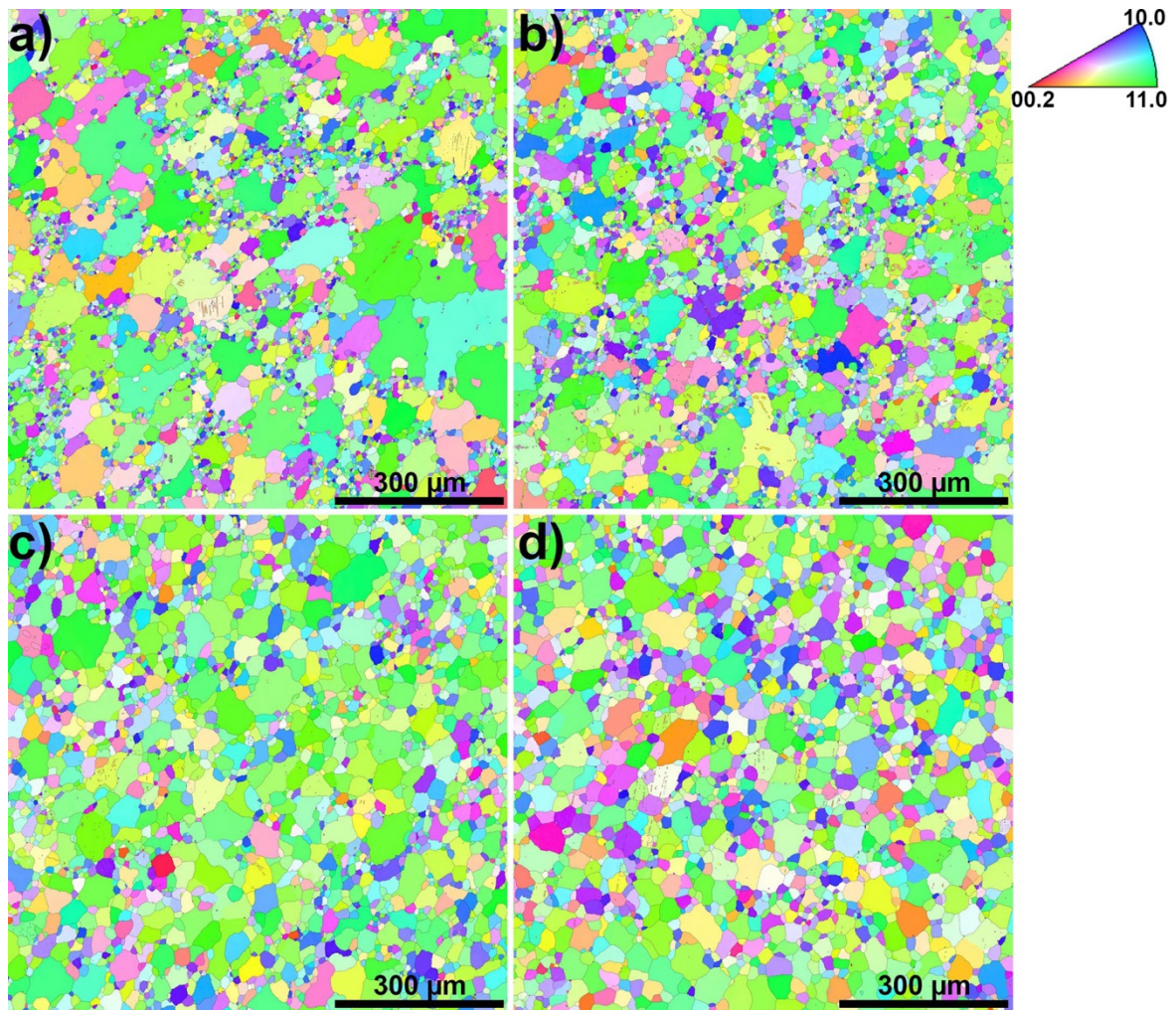


Fig 5.7: EBSD maps showing the microstructure after 10 h annealing (cross-section): a) 475 °C, b) 500 °C, c) 525 °C, d) 550 °C.

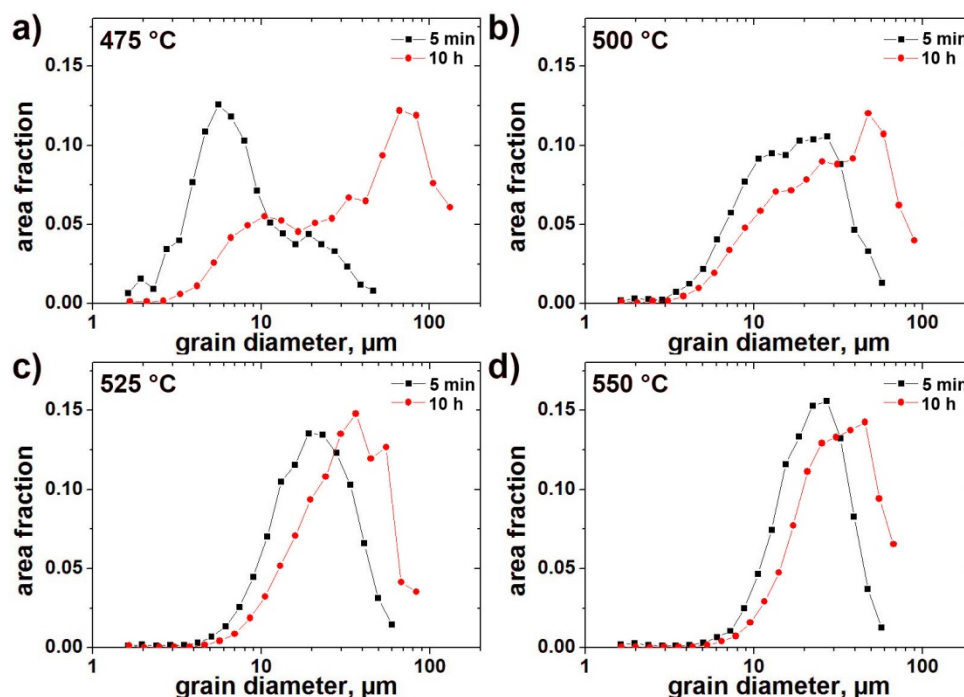


Fig 5.8: Histograms of the d_g : a) 475 °C, b) 500 °C, c) 525 °C, d) 550 °C.

Increasing annealing temperatures cause an acceleration of the grain growth, which is correlated to the swiftness of the texture evolution at temperatures ≥ 500 °C. Even more important, the AGG is gradually replaced by continuous grain growth (CGG) producing a more homogeneous microstructure. At 500 °C AGG and CGG are competing mechanisms; the d_g is more uniform than at 475 °C, although two d_g fractions were observed. At 525 °C CGG is more pronounced than AGG. The microstructure is relatively homogeneous in the early and the final stage of the annealing treatment. However, the d_g distribution (Fig 5.8 c) remains relatively broad indicating different growth rates within the sample. Using an annealing temperature of 550 °C CGG is dominant. This temperature results in a high grain growth rate generating a homogeneous d_g distribution within 5 min. Due to the increased grain growth rate and the more homogeneous growth a largely stable microstructure is formed. The grain growth between 5 min and 10 h is limited and hence appears to saturate. The obtained histogram (Fig 5.8 d) exhibits a much narrower d_g distribution than the other samples (particularly 475 °C and 500 °C). Furthermore, the final average d_g is similar to those at lower annealing times and smaller than the large grain fraction of the 475 °C annealed samples.

Post-mortem EBSD analysis of the heat treated samples did not reveal any correlation between the grain orientation or particular misorientation relations and abnormal growth of grains. To gain insight into the generation of AGG quasi-in-situ EBSD experiments were performed, where the same sample area was investigated before and after a 45 min 475 °C heat treatment (Fig 5.10).

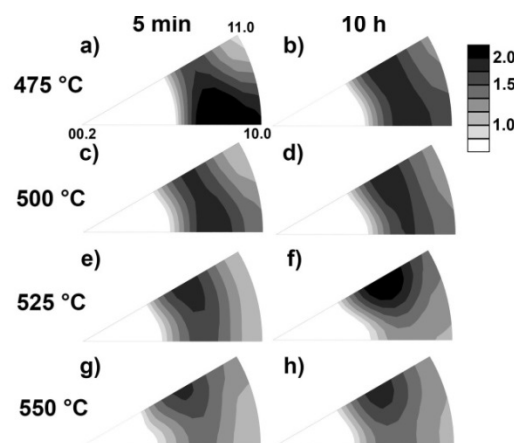


Fig 5.9: Texture evolution determined from the recorded EBSD data (cf. Fig 5.6, Fig 5.7).

Fig 5.10 a) and b) illustrate the procedure, which was used to relocate the mapped area after the heat treatment, as an external furnace was used for the heat treatment. After the heat treatment the sample was chemically polished to enable reliable EBSD pattern acquisition. In addition, to the visible hardness indent a further mark was placed at one edge of the sample (not shown) to realign the cylindrical sample within the SEM. After the first EBSD measurement contamination was visible demarking the mapped area. This contamination endured the heat treatment as well as subsequent chemical polishing and enabled an accurate realignment within the SEM. Fig 5.10 c) and d) display the corresponding EBSD maps, where Fig 5.10 c) exhibits the as-extruded microstructure and d) the same area after the heat treatment. Fig 5.10 e) and f) depict Fig 5.10 c) in terms of the recrystallized fraction and internal misorientation. A small x - y translation between the two maps could not be avoided. Therefore, several grains are marked using numbers to facilitate the interpretation.

The comparison of Fig 5.10 c) and d) reveals that AGG cannot be solely attributed to a size advantage favoring the growth of preexisting large grains. Grain 1 and grain 2 are larger than the surrounding grains, however, the EBSD analysis reveals growth of grain 2 while the area

of grain 1 is reduced. In addition, many larger grains feature CGG. As has been stated above neither grain orientation nor special intergranular misorientation relations could be associated to AGG. Fig 5.10 e) reveals that the microstructure contains a significant fraction of substructured grains, although DRX has consumed the deformed cast microstructure and has produced a fine microstructure. In addition, Fig 5.10 f) reveals significant internal misorientations within several grains particularly in grain 3. The comparison of Fig 5.10 c) - d) shows that AGG occurs within grain 3 and its surroundings.

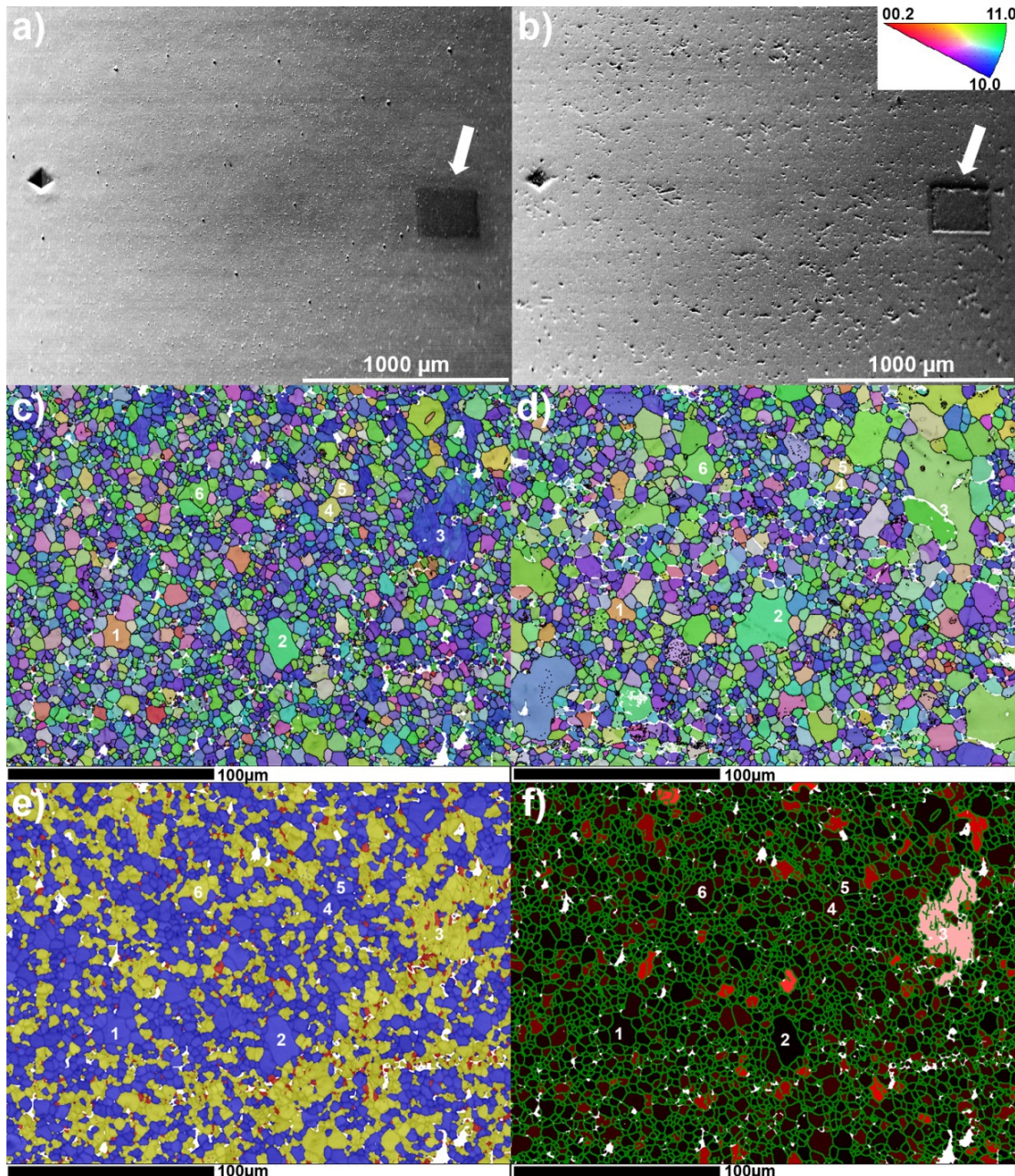


Fig 5.10: Quasi-in-situ EBSD analysis of a 45 min 475 °C heat treatment. a), b) SEM images illustrating the mapped area: a) after data collection, b) after annealing and chemical polishing. White arrows mark the mapped area. The hardness indent was used to relocate the mapped area and to align the sample within the SEM. c) IPF map (as-extruded), d) IPF map (annealed). e) EBSD map representing recrystallized (blue), substructured (yellow) and deformed (red) grains (as-extruded); f) internal misorientation map (as-extruded). High angle grain boundaries ($> 10^\circ$) = green. The brightness of the red color is proportional to the internal misorientation. Numbers are used to label various grains before and after annealing.

In order to analyze the deformation behavior of extruded and annealed samples in detail an as-extruded (extrusion B), a 24 h 475 °C and a 1 h 550 °C sample were analyzed using in-situ EDXRD and EPSC simulations, whose microstructure is analyzed below.

The initial microstructure of the as-extruded and the heat treated samples is represented in the longitudinal section in Fig 5.11. The as-extruded material is dominated by a FG recrystallized microstructure. However, some large grains appear in the micrographs, which are elongated parallel to ED. As expected from the above described results and [Brö11], the 24 h 475 °C sample features a bimodal microstructure, while the 550 °C sample exhibits a rather homogeneous d_g . In order to evaluate effects of the heat treatments on precipitates SEM (Fig 5.12) and TEM (Fig 5.13) investigations were conducted. As reported by Huppmann et al. [Hup10a] the precipitates are dominated by a relatively coarse $Mg_{12}Ce$ phase and substantially finer precipitates consisting mainly of Mn.

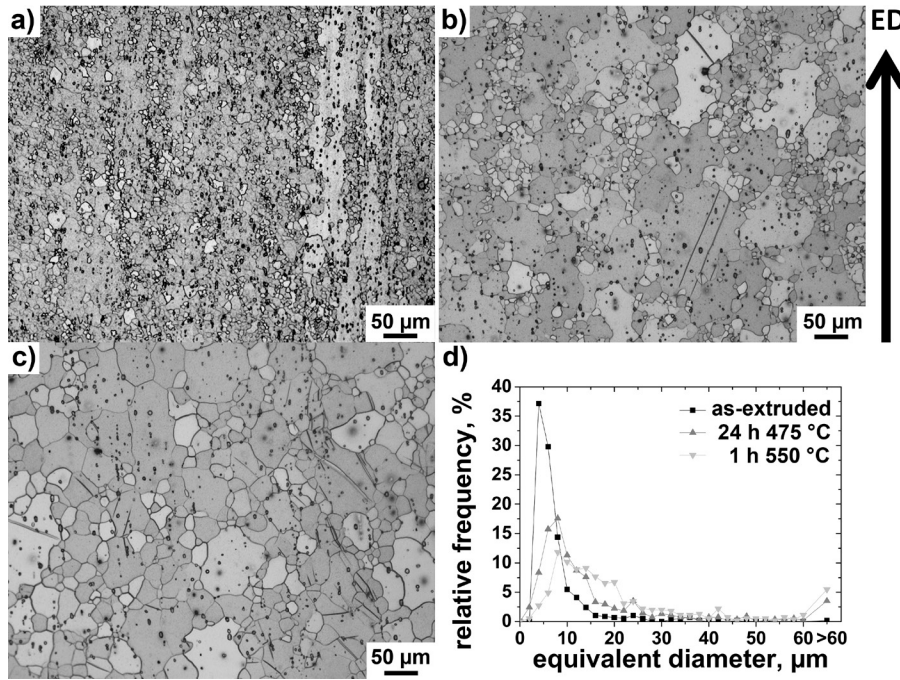


Fig 5.11: Longitudinal section of the initial microstructure: a) as-extruded, b) 24 h 475 °C, c) 1 h 550 °C, d) d_g distribution [Len13].

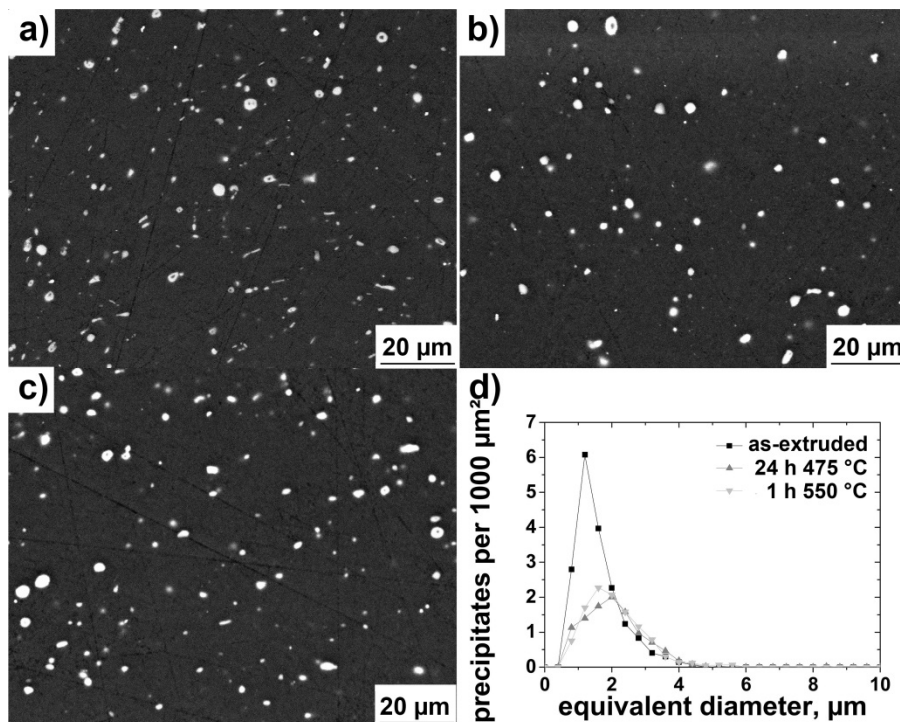


Fig 5.12: SEM images of the coarse precipitate fraction (mainly $Mg_{12}Ce$): a) as-extruded, b) 24 h 475 °C, c) 1 h 550 °C, d) comparison of the precipitation density and size [Len13].

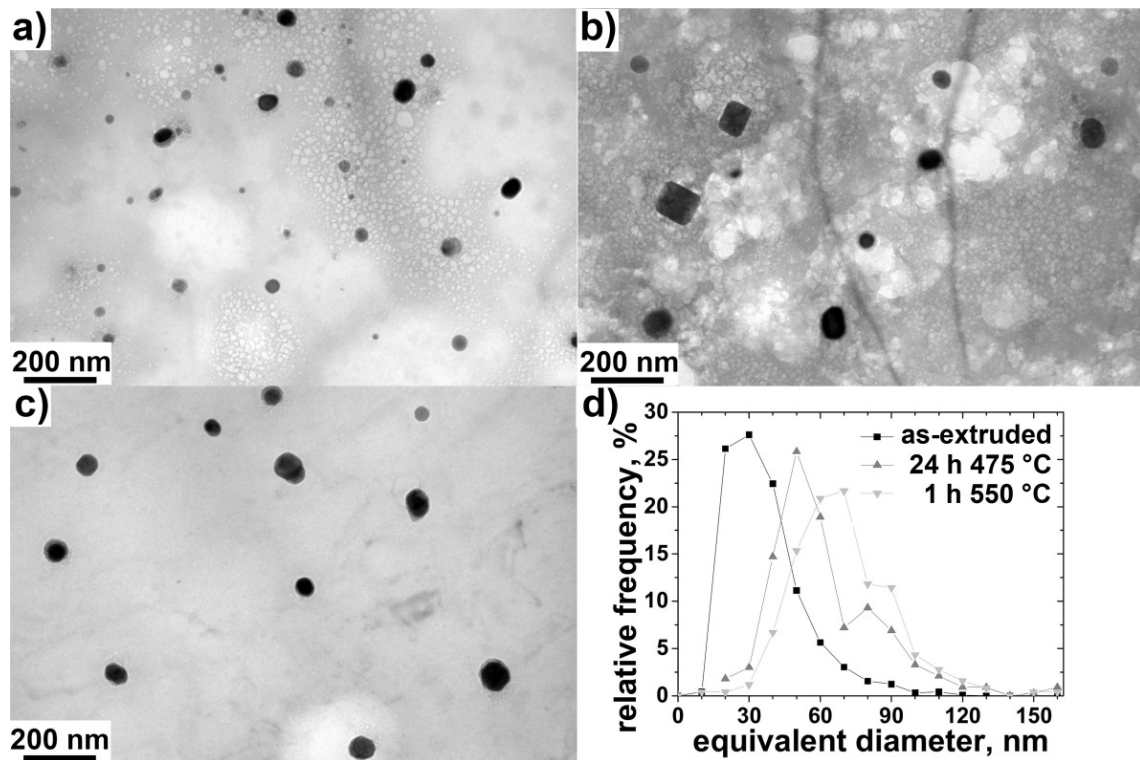


Fig 5.13: TEM images of the fine precipitate fraction: a) as-extruded, b) 24 h 475 °C, c) 1 h 550 °C, d) comparison of the precipitate size distribution [Len13].

Both heat treatments result in very similar size distributions of the large precipitates lowering the number of precipitates by dissolution as well as shifting it to slightly higher equivalent diameters. The TEM (Fig 5.13) investigations show that the size distribution and the density of the fine Mn containing precipitates are strongly affected by the heat treatments. The maximum of the size distribution is shifted to approximately 2 times higher equivalent diameters. Furthermore, both heat treatments cause a significant decrease of number densities of the small scale precipitates. The texture evolution is consistent with the above described evolution, however, in case of the 24 h 475 °C sample the $\langle 11\bar{2}0 \rangle$ texture component is more enhanced than the $\langle 11\bar{2}1 \rangle$ texture component.

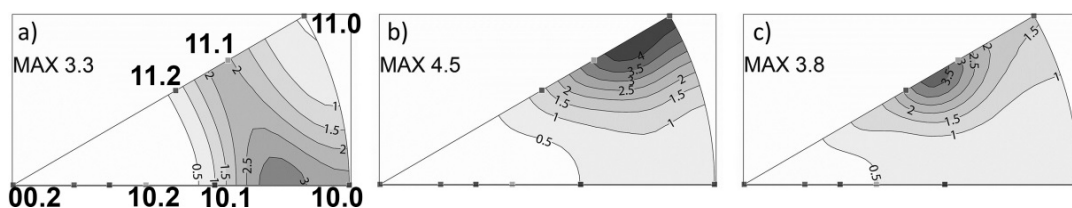


Fig 5.14: Comparison of the extrusion and annealing textures: a) as-extruded, b) 24 h 475 °C c) 1 h 550 °C.

5.1.4 Mechanical properties

The above described microstructural modifications generate significant changes of the mechanical properties, which will be analyzed in terms of the macroscopic flow curves, the microstructural and texture development during deformation and EPSC simulations.

5.1.4.1 Flow curves

In order to analyze the effect of the microstructure on the mechanical properties and the deformation behavior, uniaxial tension and compression tests were conducted. The corresponding flow curves are displayed as a function of the extrusion parameters in Fig 5.15 and Fig 5.16, while the resulting CYS, TYS and SDE are summarized in Table 5.3. Here, it should be noted that d_g effects and texture effects on the mechanical properties are superimposed complicating a direct correlation to the mechanical properties.

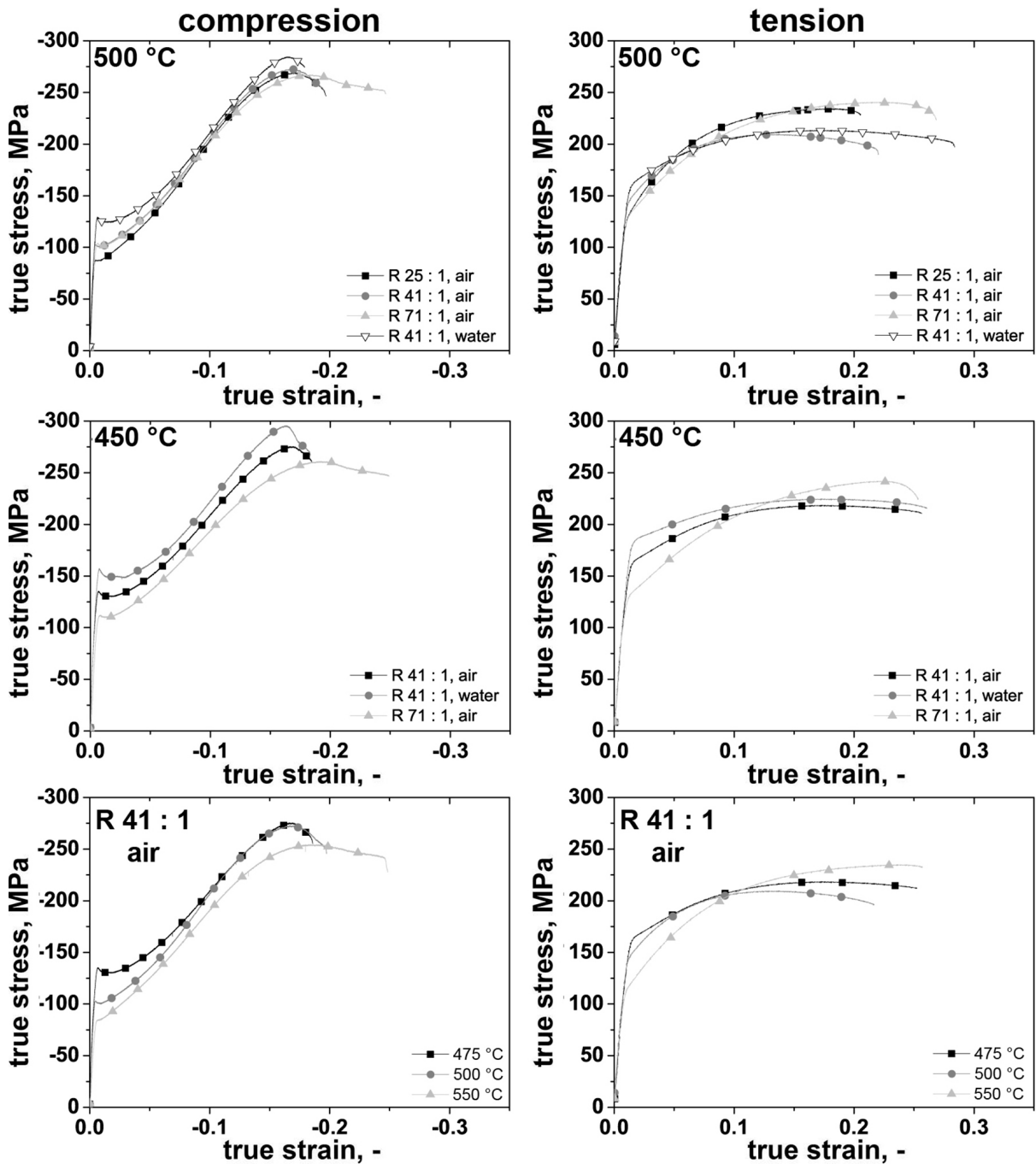


Fig 5.15: Flow curves of the extruded bars tested in uniaxial compression and tension.

The initial textures result in a significant yield asymmetry (SDE), where the CYS is generally lower than the TYS (cf. Table 5.3). In compression the samples feature the well-known sigmoidal shape, which is associated to the extensive activation of TTW-ing [Kel68, Kha11, Len14a], while the tension flow curves display no signs of twinning. It will be shown in section 5.1.4.2 that TTW-ing is indeed activated to a large extent during compression. As expected, the comparison of Table 5.2 and Table 5.3 reveals a significant d_g dependence of both CYS and TYS, where large average d_g result in low yield stresses. In addition, small d_g appear to lower the yield anisotropy generating lower SDE values. The highest strength was observed in the FG extrusion B (450 °C, R = 41 : 1 and water cooling).

Fig 5.16 illustrates the remarkable effect of high temperature heat treatments on the mechanical properties of extruded ME21 alloys. While short term heat treatments (Fig 5.16 a)) predominantly lower the strength and generate only minor improvements of the ductility, a

1 h 550 °C heat treatment results in a remarkable increase of the elongation to failure in compression. However, in tension the elongation to failure is in the same range like the as-extruded materials (Fig 5.15). Here, it should be noted that the 24 h 475 °C annealed sample features a particular low elongation to failure in tension.

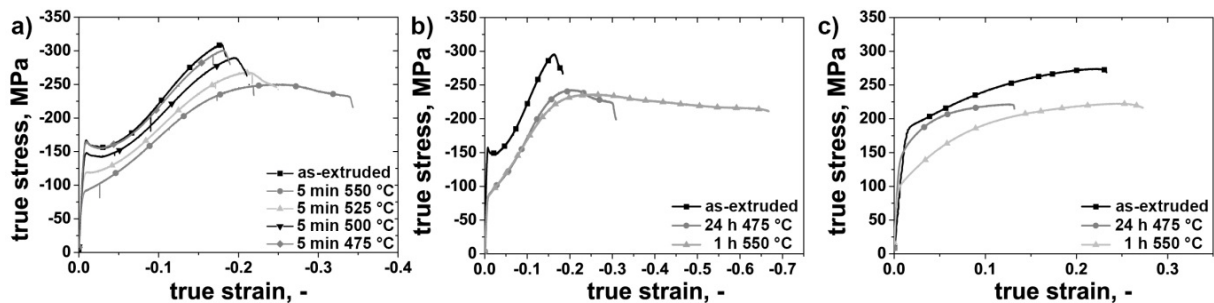


Fig 5.16: Flow curves of heat treated extrusion B: a, b) compression; c) tension. (a) displays the effect of short term heat treatments, while b) and c) illustrate the effect of long dwell times).

Table 5.3: Tension compression yield asymmetry specified by the CYS, TYS and SDE of the extruded bars. The error of CYS and TYS is below 5 MPa.

T_B , cooling	ME21								
	R 25 : 1			R 41 : 1			R 71 : 1		
	CYS, MPa	TYS, MPa	SDE, -	CYS, MPa	TYS, MPa	SDE, -	CYS, MPa	TYS, MPa	SDE, -
450 °C air	-	-	-	-135	159	-0.16	-113	115	-0.02
450 °C water	-	-	-	-159	180	-0.12	-	-	-
500 °C air	-88	124	-0.34	-103	143	-0.33	-105	125	-0.17
500 °C water	-	-	-	-130	154	-0.17	-	-	-
550 °C air	-	-	-	-85	108	-0.24	-	-	-
24 h 475 °C	-	-	-	-85	140	-0.49	-	-	-
1 h 550 °C	-	-	-	-82	100	-0.20	-	-	-

In order to analyze the underlying deformation mechanism causing the flow curves the deformed microstructure was analyzed using optical microscopy, EBSD and XRD texture analysis.

5.1.4.2 Deformed microstructure

Fig 5.17 exemplary displays the microstructural evolution during uniaxial compression of extrusion F. At low strains ($\epsilon_e = -5\%$) the deformation behavior is dominated by TTW-ing. The majority of the grains contain at least one TTW. These appear as red lamella in the EBSD maps. Furthermore, TTW boundaries are highlighted (red) in the band contrast (BC) maps. Those few grains, which do not contain any TTW correspond to orientations featuring a low SF for TTW-ing and a high SF for $\langle a \rangle$ basal slip (e.g. $\langle 11\bar{2}2 \rangle$). The importance of TTW-ing in this stage of deformation is further illustrated in Fig 5.18 using the MDFs; the vast majority of the high angle grain boundaries corresponds to TTW boundaries (Fig 5.18 a)).

During further compression the parent microstructure is successively overtaken by the TTWs, which manifests in the predominance of the red color in the IPF maps, the decreasing

number of TTW boundaries, the enhancement of the $\langle 0002 \rangle$ texture component, the decreasing relative frequency of the $\approx 86^\circ$ grain boundaries and the increasing relative frequency of TTW-TTW intersections (Fig 5.18 c).

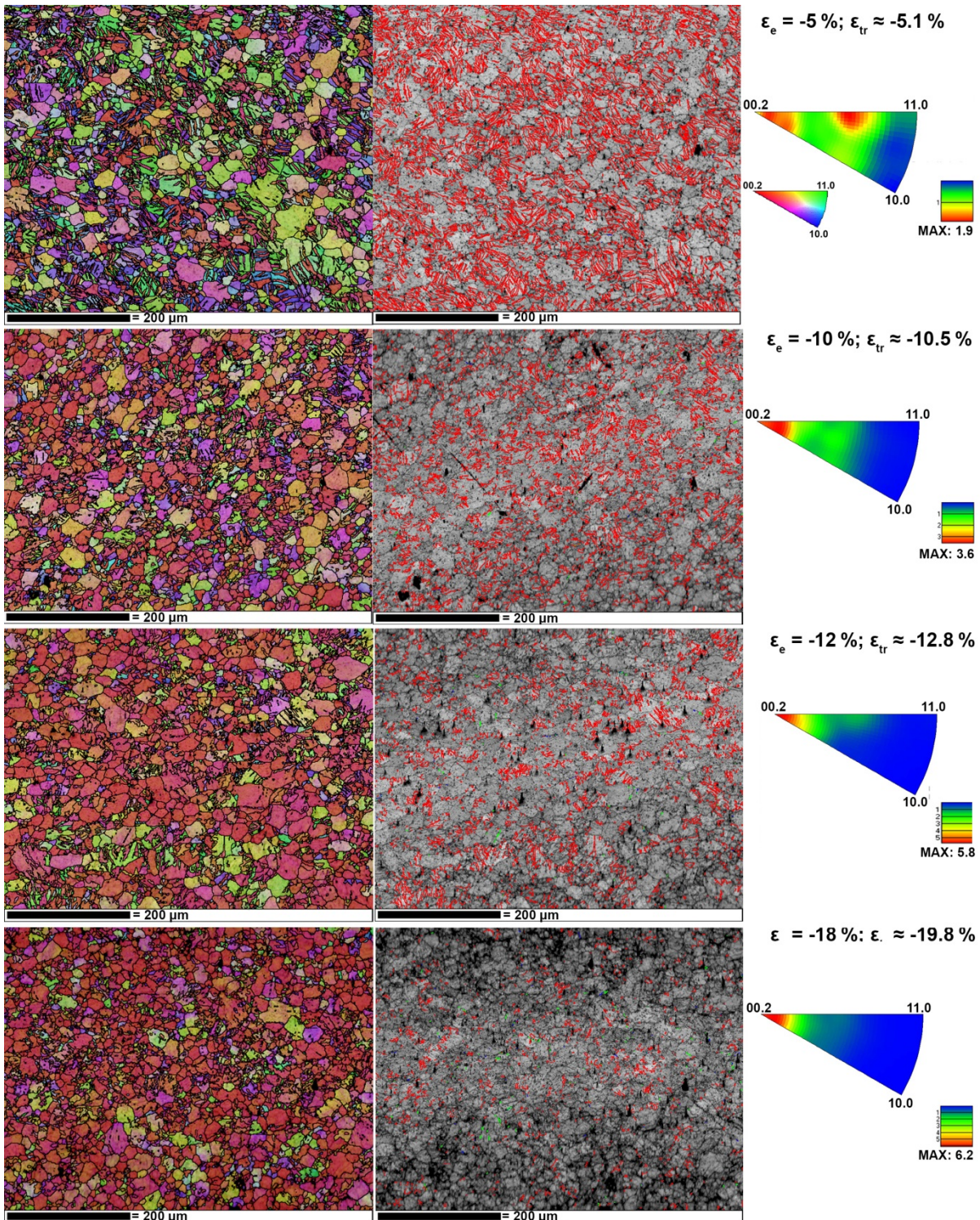


Fig 5.17: EBSD maps, BC maps highlighting twin boundaries ($86^\circ \langle 11\bar{2}0 \rangle = \text{red}$, $56^\circ \langle 11\bar{2}0 \rangle = \text{yellow}$, $38^\circ \langle 11\bar{2}0 \rangle = \text{green}$, $30^\circ \langle 11\bar{2}0 \rangle = \text{blue}$) and IPFs of compression samples (extrusion F) [Len14c].

However, as the parent microstructure is overtaken by TTW-ing, this deformation mode is increasingly exhausted and hence, other deformation modes are required for strain accommodation. The comparison of $\epsilon_e = -10\%$, $\epsilon_e = -12\%$ and $\epsilon_e = -18\%$ maps indicate that TTW-ing is largely exhausted between $\epsilon_e = -10\%$ and $\epsilon_e = -12\%$. Subsequently, no significant twin-

ning activity (including CTW-ing and DTW-ing) was observed. Therefore, the deformation has to be realized by slip modes.

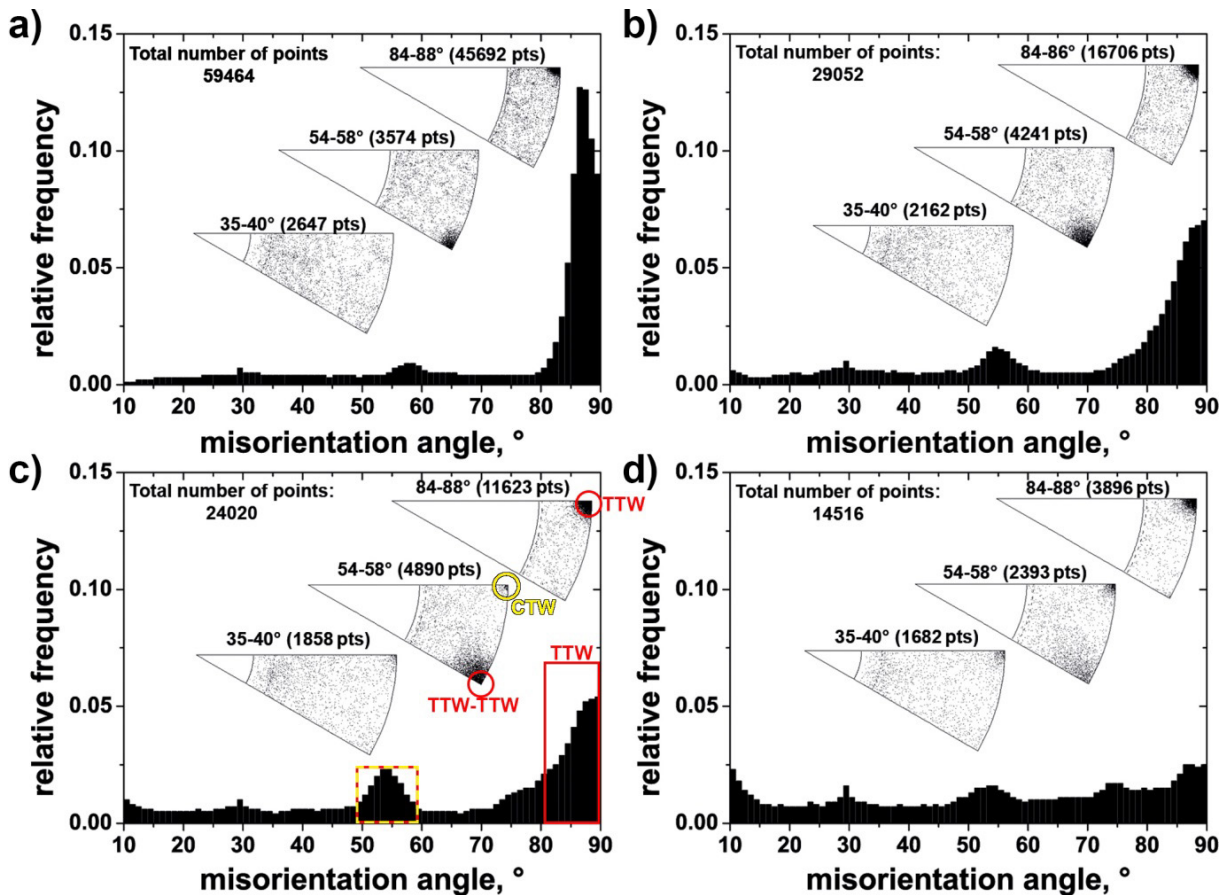


Fig 5.18: MDFs: a) strain (ϵ) = -5 %, b) ϵ = -10 %, c) ϵ = -12 %, d) ϵ = -18 %. The insets show the distribution of the rotation axis for characteristic angular ranges. $86^\circ <11\bar{2}0>$ = red, $56^\circ <11\bar{2}0>$ = yellow [Len14c].

In order to analyze the deformation behavior of heat treated samples a combination of optical microscopy and XRD texture analysis was applied. Fig 5.19 illustrates the deformed microstructure in terms of optical micrographs, while Fig 5.20 exhibits the corresponding IPFs. In agreement with the above EBSD investigation, the as-extruded and the heat treated samples feature a high TTW-ing activity. The optical micrographs reveal many TTW lamellas, which can be correlated to TTWs by the sudden appearance of the $<0002>$ texture component. The $<0002>$ intensity is generated by a $\approx 86^\circ$ rotation about $<11\bar{2}0>$ axes of the parent grains (predominantly $<10\bar{1}0>$ and $<11\bar{2}0>$ texture components). An important feature of the micrographs at $\epsilon_e = -6\%$ is that several grains are extensively twinned while other surrounding grains do not show any signs of TTW-ing. This feature is most noticeable in case of the heat treated samples and reflects the enhancement of the slip activity due to the promoted RE texture component. The activity of slip systems becomes visible by the gradual shift of the RE texture component to the inside close to the $<11\bar{2}2>$ texture component ($\epsilon_e = -6\%$). At higher strain some residual TTWs were observed, however, secondary twinning was not observed in a notable amount. Consequently, the further texture evolution is solely based on grain rotation due to crystallographic slip and hence, limited.

Likewise, texture changes are gradual and more continuous in case of tension tests, where TTW-ing is omitted due to the initial texture. Here, crystallographic slip results in the enhancement of the $<10\bar{1}0>$ or $<11\bar{2}0>$ texture fibers.

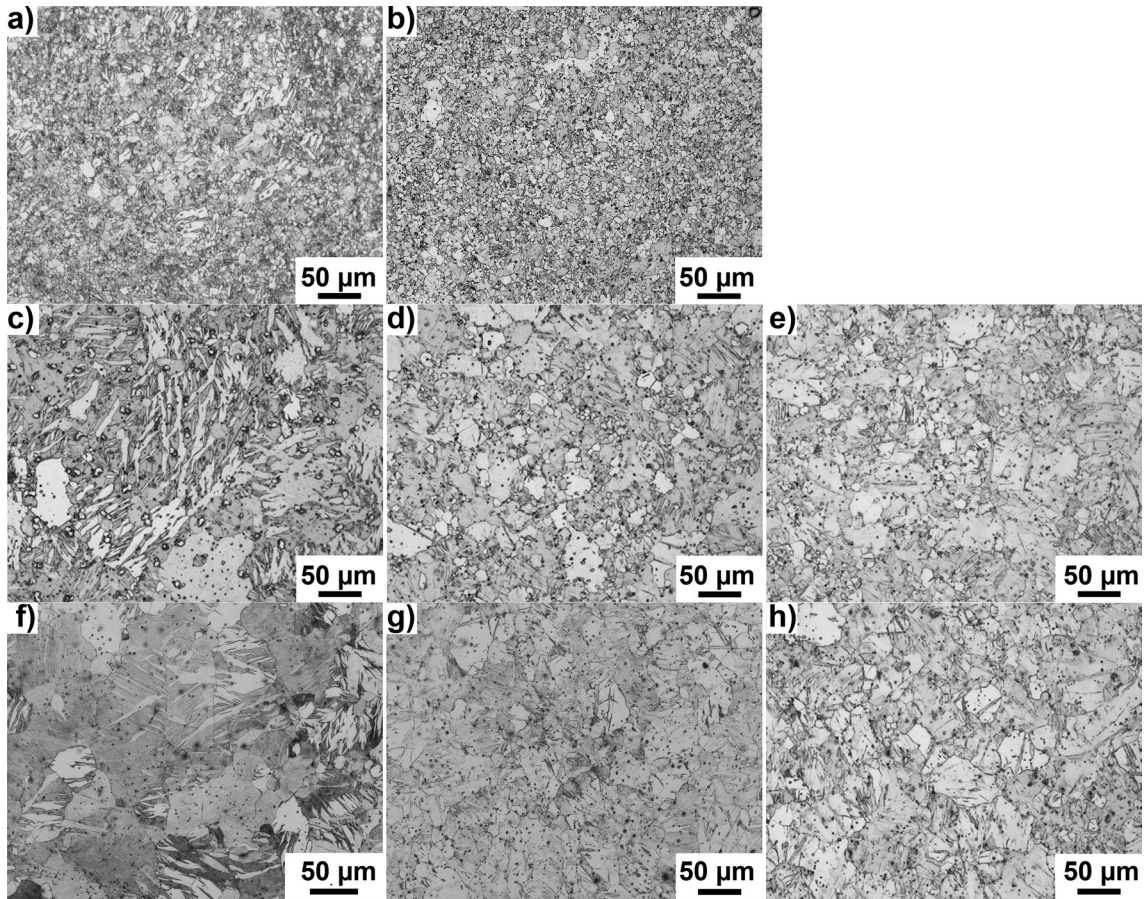


Fig 5.19: Cross sections of compression samples: as-extruded (extrusion B): a) $\epsilon = -6\%$, b) $\epsilon_{fr,c}$; 24 h 475 °C: c) $\epsilon = -6\%$, d) $\epsilon = -20\%$, e) $\epsilon_{fr,c}$; 1 h 550 °C: f) $\epsilon = -6\%$, g) $\epsilon = -27\%$, h) $\epsilon_{fr,c}$ [Len13].

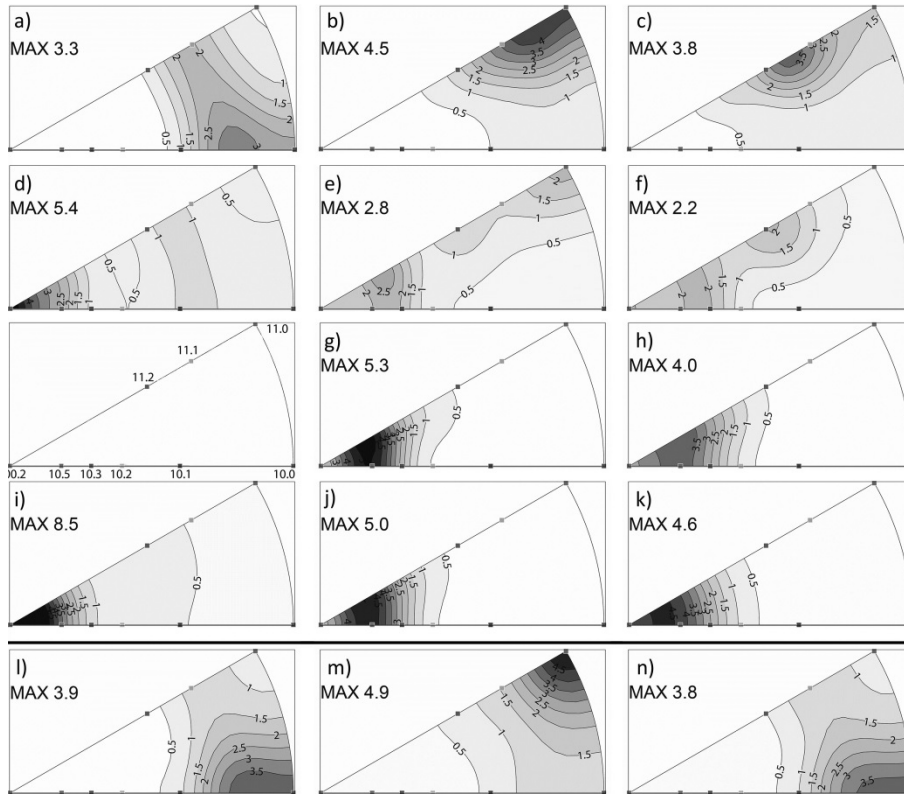


Fig 5.20: IPFs as a function of the strain: a) as-extruded (extrusion B), b) 24 h 475 °C, c) 1 h 550 °C, d) as-extruded: $\epsilon = -6\%$, e) 24 h 475 °C: $\epsilon = -6\%$, f) 1 h 550 °C: $\epsilon = -6\%$, g) 24 h 475 °C: $\epsilon = -20\%$, h) 1 h 550 °C: $\epsilon = -27\%$, i) as-extruded: elongation to failure – compression ($\epsilon_{fr,c}$), j) 24 h 475 °C: $\epsilon_{fr,c}$, k) 1 h 550 °C: $\epsilon_{fr,c}$, l) as-extruded: elongation to failure – tension ($\epsilon_{fr,t}$), m) 24 h 475 °C: $\epsilon_{fr,t}$, n) 1 h 550 °C: $\epsilon_{fr,t}$ [Len13].

5.1.4.3 EPSC simulations

In order to determine the active deformation modes underlying the remarkably improved formability of 1 h 550 °C annealed samples, in-situ EDXRD experiments were conducted during uniaxial compression and tension tests. The acquired data was evaluated using the EPSC model and applying the Voce hardening law. The applied hardening parameters (Table 5.4) were obtained from modelling the flow curves, the ε_{hkl} evolution and the texture evolution. Fig 5.21 displays the experimental and the simulated flow curves and ε_{hkl} as well as the predicted deformation mode activity during compression, while Fig 5.22 illustrates the corresponding tension data. Fig 5.23 exhibits the predicted texture evolution, which is in good agreement with the measured texture evolution (Fig 5.20).

The applied hardening parameters (Table 5.4) are in the order of those previously used for Mg alloys (Table 2.3). As expected the applied τ_0^s generally increase in the order $\langle a \rangle$ basal $\langle a \rangle$ prismatic $\langle c+a \rangle$ pyramidal slip. While a larger d_g results in a lower τ_0^s the work hardening increases in coarse grained (CG) materials. The CRSS of TTW-ing is in the range of $\langle a \rangle$ prismatic slip and the hardening parameters τ_1^s , θ_0^s and θ_1^s of TTW-ing were set to zero, as it is generally assumed that TTW-ing requires a higher stress for nucleation than for growth in case of Mg alloys.

Table 5.4: Hardening parameter of the Voce hardening law (FIF = 0.001) [Len13].

Deformation mode	As-extruded				24 h 475 °C				1 h 550 °C			
	τ_0^s	τ_1^s	θ_0^s	θ_1^s	τ_0^s	τ_1^s	θ_0^s	θ_1^s	τ_0^s	τ_1^s	θ_0^s	θ_1^s
$\langle a \rangle$ -basal	15	5	10	0	1	10	65	0	1	10	40	0
$\langle a \rangle$ -prismatic	72	38	135	0	35	36	420	0	42	48	360	0
$\langle c+a \rangle$ -pyramidal	85	130	900	0	52	102	1350	0	54	117	1950	0
TTW-ing	76	0	0	0	41	0	0	0	38	0	0	0

As the hardening parameters are by far the lowest for the $\langle a \rangle$ basal slip systems the ε_{hkl} of the (10 $\bar{1}$ 1) and the (10 $\bar{1}$ 2) orientated grains, which are favorably orientated for $\langle a \rangle$ basal slip show the lowest ε_{hkl} . The (10 $\bar{1}$ 0) and the (11 $\bar{2}$ 0) reflections representing grains, which are favorably orientated for TTW-ing and $\langle a \rangle$ prismatic slip, show significantly higher ε_{hkl} as these deformation modes require higher CRSS to be activated. Based on the diffraction geometry and the initial texture the (0002) reflection is not present during tension tests, however, in compression the activation of TTW-ing orientates grains in such a way that they fulfill the Bragg condition generating a (0002) reflection. Consequently, the ε_{hkl} can be evaluated once a sufficient amount of TTWs has formed. The absence of the reflection prior to deformation results in a large uncertainty of the absolute value of the ε_{hkl} of the twinned grains. Nevertheless, the qualitative evolution of the measured ε_{hkl} is in good agreement with the simulation. As the grains represented by the (0002) reflection are aligned with their c-axes parallel to the compression axis, $\langle c+a \rangle$ pyramidal slip (the hardest deformation mode) has to be activated to a significant extent within these TTWs resulting in pronounced (geometric) hardening and high ε_{hkl} . In case of the heat treated samples TTW-ing of the RE texture component generate an additional (10 $\bar{1}$ 3) reflection, which features a higher SF for $\langle a \rangle$ basal slip than grains corresponding to the (0002) reflection and hence the (10 $\bar{1}$ 3) ε_{hkl} are lower.

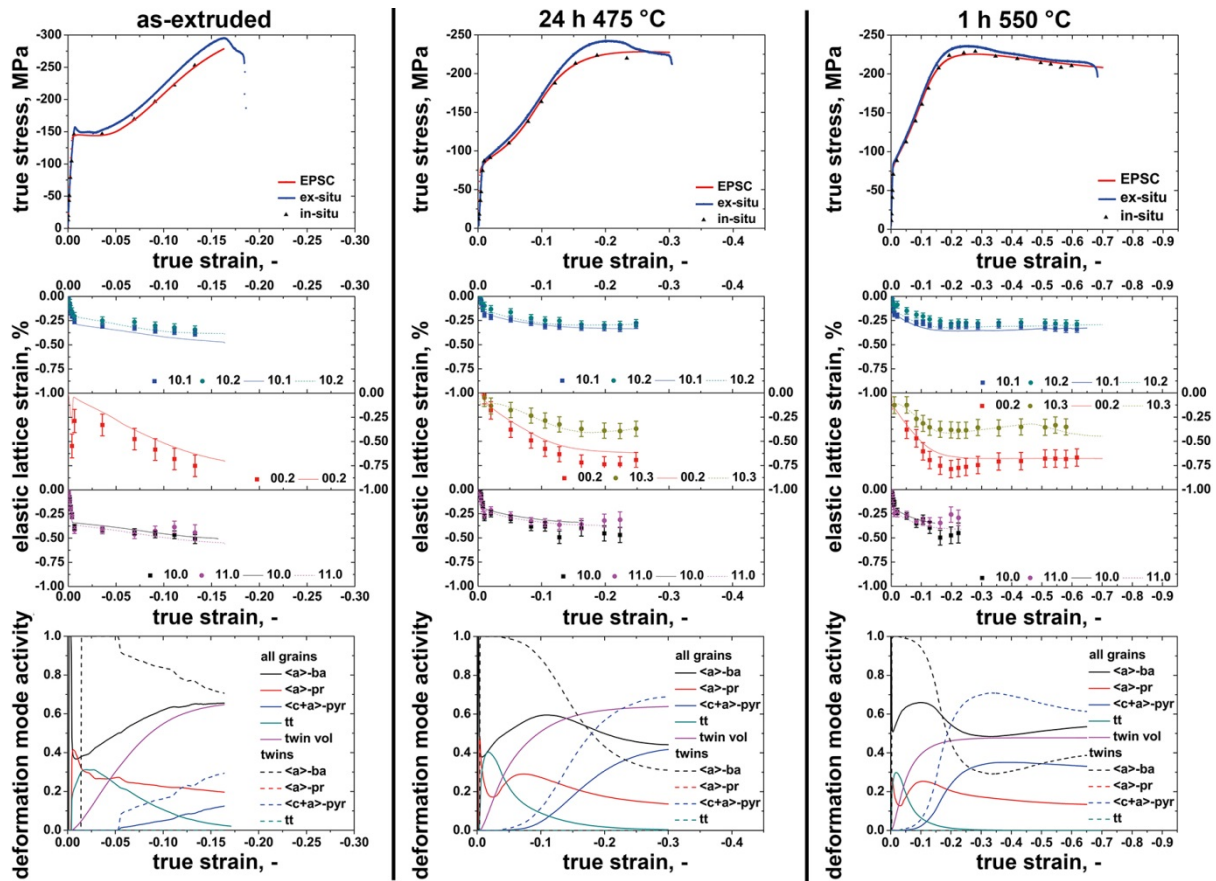


Fig 5.21: EPSC simulation of the flow curve, lattice strains and deformation mode activity (compression). As-extruded and heat treated conditions correspond to extrusion B [Len13].

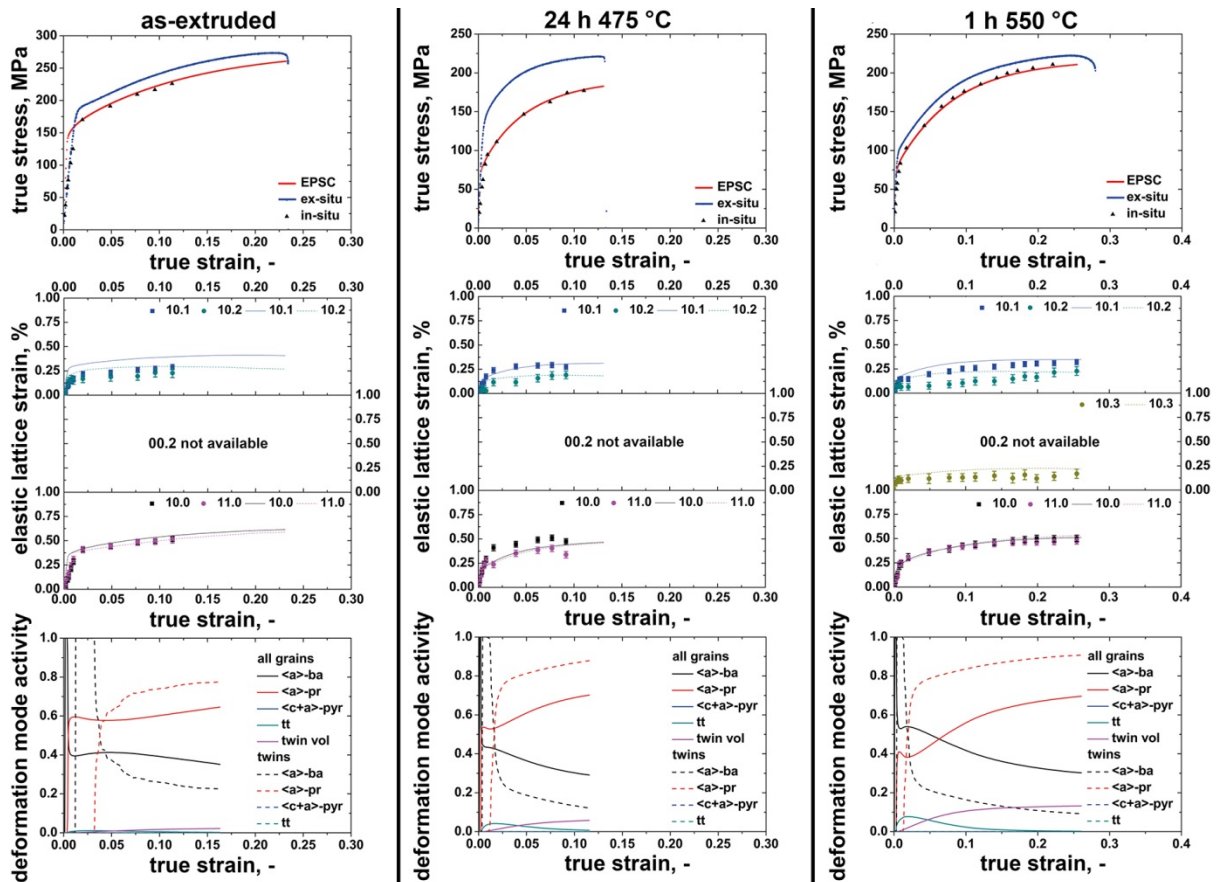


Fig 5.22: EPSC simulation of the flow curve, lattice strains and deformation mode activity (tension). As-extruded and heat treated conditions correspond to extrusion B [Len13].

Considering the compression flow curves, the as-extruded material features a plateau during initial deformation, which is absent in the heat treated samples. This plateau is caused by pronounced TTW-ing and a low hardening rate of $\langle a \rangle$ prismatic slip. The comparison of the deformation mode activities reveals that the remarkable elongation to failure of the 1 h 550 °C annealed sample is correlated to the combined activation of $\langle c+a \rangle$ pyramidal slip and $\langle a \rangle$ basal slip.

A remarkable feature of the ε_{hkl} evolution of the compression test is that the ε_{hkl} are almost constant or slightly decreasing at strains higher than -0.2. This indicates that none of the deformation modes hardens significantly beyond this point being consistent with the final hardening rate $\theta_1^s = 0$ for all deformation modes, which means that neither hardening nor softening should occur at this point. Nevertheless, the compression flow curve clearly shows that the material is softening. Consequently, the softening is correlated to the texture evolution and is likely to contribute to the high elongation to failure. In addition, the TTW volume fraction is reduced in this material condition. In order to explain the reduced TTW volume fraction additional simulations were conducted, which will be discussed at the end of this section. The tensile deformation is predominantly realized through the activation of $\langle a \rangle$ prismatic and $\langle a \rangle$ basal slip.

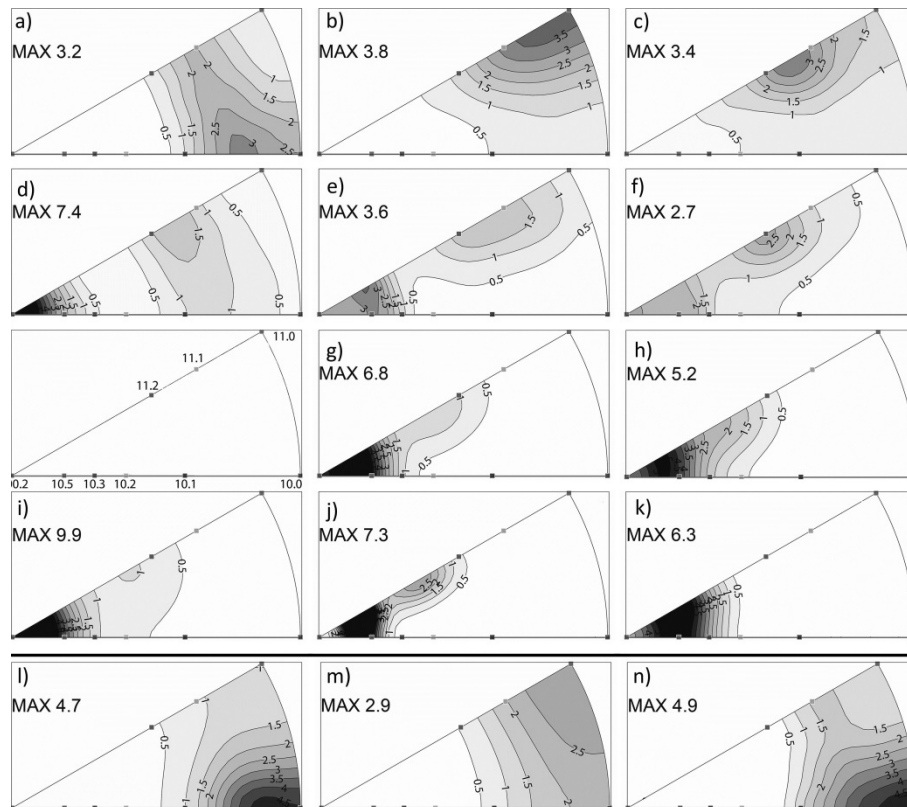


Fig 5.23: Simulated IPFs as a function of the strain: a) as-extruded, b) 24 h 475 °C, c) 1 h 550 °C, d) as-extruded: $\varepsilon = -6\%$, e) 24 h 475 °C: $\varepsilon = -6\%$, f) 1 h 550 °C: $\varepsilon = -6\%$, g) 24 h 475 °C: $\varepsilon = -20\%$, h) 1 h 550 °C: $\varepsilon = -27\%$, i) as-extruded: $\varepsilon_{fr,c}$, j) 24 h 475 °C: $\varepsilon_{fr,c}$, k) 1 h 550 °C: $\varepsilon_{fr,c}$, l) as-extruded: $\varepsilon_{fr,t}$, m) 24 h 475 °C: $\varepsilon_{fr,t}$, n) 1 h 550 °C: $\varepsilon_{fr,t}$ [Len13]. The corresponding experimental IPFs are displayed in Fig 5.20.

In order to evaluate texture effects separately, additional simulations were conducted using the hardening parameters of the as-extruded condition and the different starting textures (Fig 5.24). Fig 5.24 a) indicates that the CYS is very little influenced by the observed texture changes. However, an important impact of the initial texture on the subsequent deformation behavior is predicted. According to the simulation the as-extruded sample and the 475 °C annealed sample feature initial textures, which promote extensive TTW-ing causing TTW volume fractions of 0.6 to 0.7. The higher TTW volume fraction results in an increased acti-

vation of $\langle c+a \rangle$ pyramidal slip causing pronounced hardening. At strains higher than -0.25 the hardening has saturated and the $\langle a \rangle$ basal and the $\langle c+a \rangle$ pyramidal slip system balance each other resulting in a slight softening.

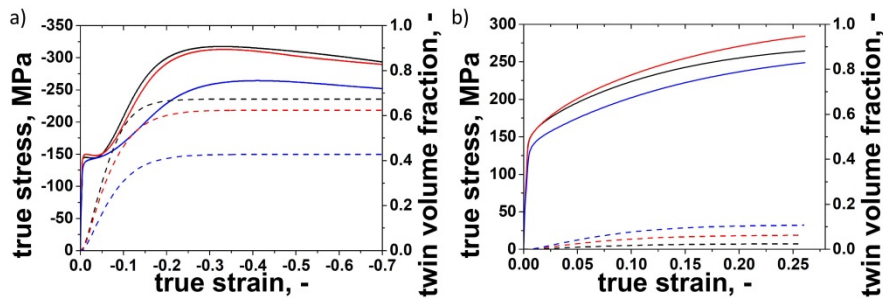


Fig 5.24: Simulation of the effect of the texture on the flow curves and the TTW volume fraction (dashed lines): a) compression, b) tension; black = as-extruded texture, red = 24 h 475 °C texture, blue = 1 h 550 °C texture [Len13].

In contrast the 550 °C annealing texture promotes the activation of slip systems particularly the $\langle a \rangle$ basal slip system causing a lower TTW volume fraction. The texture evolution is more gradual in this case and a reduced TTW volume fraction results in reduced geometric hardening. This is also related to a shift of the onset of softening to strains in the range of -0.35. The predicted tensile flow curves exhibit a bigger difference in the TYS of approximately 30 MPa (Fig 5.24 b)). Here, TTW-ing and $\langle c+a \rangle$ pyramidal slip are negligible due to the texture and the high initial CRSS of pyramidal slip. Therefore, the changes of the flow curve have to be attributed to the activities of the $\langle a \rangle$ slip systems. The deviations of the TYS is coupled to the higher SF of the $\langle a \rangle$ basal slip system in case of the RE texture component. Consequently, the TYS is reduced if the RE texture component is enhanced. During tensile deformation the activation of the $\langle a \rangle$ slip systems enhances the $\langle 10\bar{1}0 \rangle$ texture component, causing a decreasing SF of $\langle a \rangle$ basal slip. Therefore, the $\langle a \rangle$ prismatic slip system has to support the plastic deformation to a larger extent during the ongoing plastic deformation leading to a continuous hardening.

5.2 WE54

5.2.1 Extrusion billets

Fig 5.25 displays a micrograph of a homogenized WE54 cast billet featuring homogeneously distributed equiaxed grains. An average d_g of 180 μm was determined, where the d_g varies within the range from 100 μm to 500 μm . Due to the homogenization of the cast billet being a solution annealing, the number of precipitates is very limited. The observed precipitates predominantly are Y-rich and occasionally Zr-rich phases. In order to enable the extrusion trials the hot working behavior of this alloy was investigated using hot compression and processing maps. This analysis can be found in [Len14d].

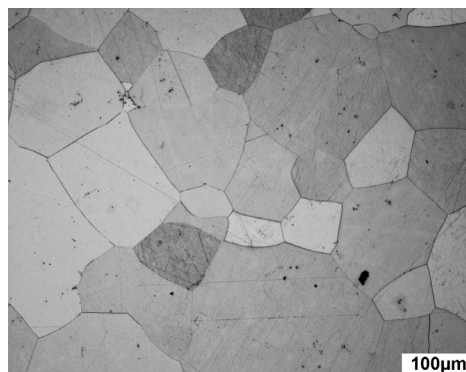


Fig 5.25: Micrograph of a homogenized WE54 cast billet [Len14d].

5.2.2 Extrusion products

Within this study six extrusion trials were successfully conducted to analyze the effect of the T_B and the R on the microstructure, texture and mechanical properties (cf. Table 5.5). All billets were homogenized using a temperature of 525 °C and a dwell time of 8 h.

Table 5.5: Summary of the applied extrusion parameters.

Extrusion	T_B , °C	R	Product speed, m/min	Cooling	Peak force, MN
A	500	25 : 1	1.7	air	2.8
B	500	41 : 1	1.7	air	2.9
C	500	71 : 1	1.7	air	3.3
D	450	41 : 1	1.7	air	5.3
E	450	41 : 1	1.7	water	5.3
F	450	71 : 1	1.7	water	5.5

5.2.2.1 Microstructure and texture

The WE54 extrusions feature a very homogeneous recrystallized microstructure, which is illustrated via exemplary micrographs in Fig 5.26. The microstructure consists of equiaxed grains, no elongated grains were observed. The average d_g is displayed in Fig 5.27 and summarized in Table 5.6 as a function of the extrusion parameters. Comparing equivalent extrusion parameters (500 °C, air cooling) the d_g is generally higher than in the ME21 extrusions (cf. Table 5.2). However, adjusting the extrusion parameters to $T_B = 450$ °C and water cooling generates FG material. Fig 5.27 reveals a clear trend, where increasing R and water cooling produce finer average d_g , while increasing T_B result in larger grains. Water cooling appears to be the most effective parameter in grain refinement during extrusion.

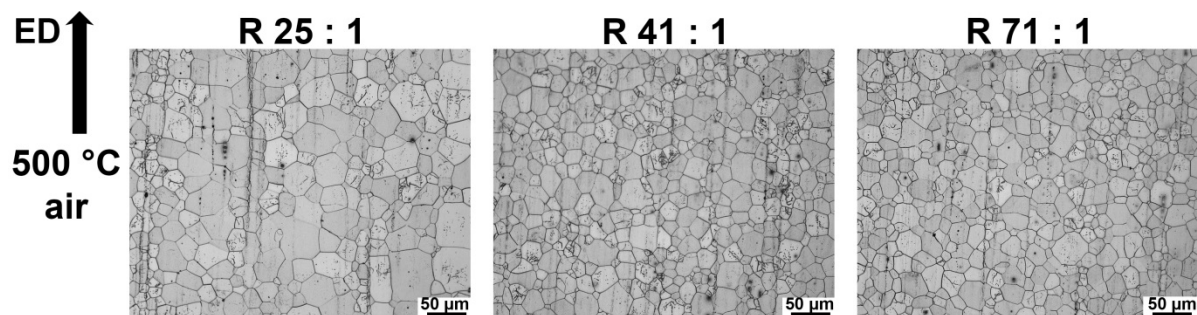


Fig 5.26: Optical micrographs showing the microstructure in the extruded bars.

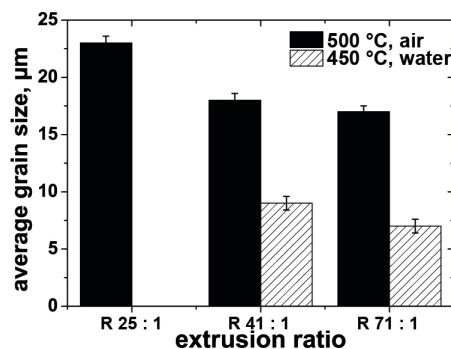


Fig 5.27: Histogram showing the effect of the extrusion parameters on the d_g .

Table 5.6: Applied extrusion parameters and resulting average d_g (µm). The standard deviation of the log-normal distribution is approximately 0.6 µm.

T_B , cooling	WE54		
	R 25 : 1	R 41 : 1	R 71 : 1
500 °C, air	23	18	17
450 °C, air	-	17	-
450 °C, water	-	9	7

In as-extruded conditions the WE54 material contains minor amounts of large Y-rich or Zr-rich precipitates (Fig 5.28). Using TEM smaller precipitates were observed occasionally, but in very limited amounts.

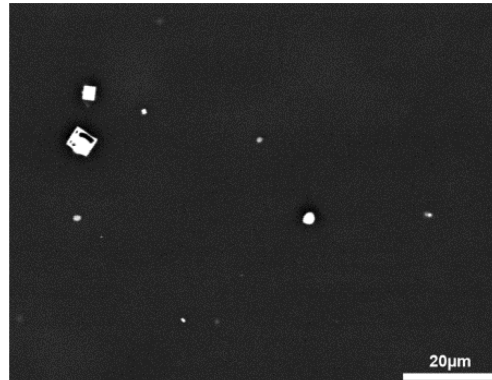


Fig 5.28: Y-rich precipitates in an extruded WE54 bar.

Fig 5.29 summarizes the WE54 extrusion textures. As has been previously reported [Bal94] the alloy tends to generate very weak extrusion textures, which are close to random. The maximum observed intensity was 1.8. Altering the extrusion parameters results in very minor changes of the textures.

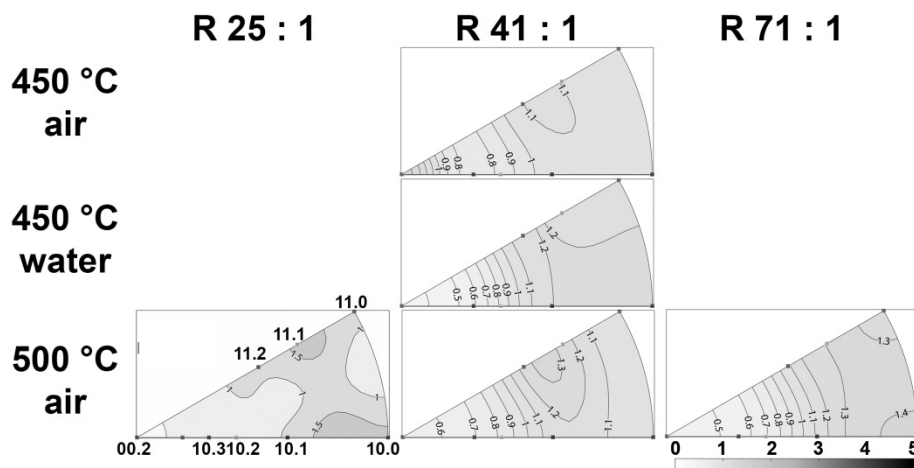


Fig 5.29: Measured extrusion texture (IPFs || ED).

5.2.3 Heat treatments

In case of the WE54 alloy age-hardening experiments at 250 °C and annealing experiments at 400 °C were conducted using extrusion C to generate precipitates within the grains and at grain boundaries:

- 16 h at 250 °C
- 500 h at 250 °C
- 24 h at 400 °C

Thereby, a case study of precipitate effects on the deformation behavior is enabled.

5.2.3.1 Microstructure and texture

Fig 5.30 illustrates the effect of the above mentioned heat treatments on the microstructure using optical micrographs. The heat treatments introduce very limited grain growth, where the average d_g spread in the range from 17 μm (as-extruded, extrusion C) to 20 μm (24 h 400 °C). In addition, the micrographs reveal differences of the precipitation behavior, where fine precipitates are formed within the grains using age-hardening at 250 °C and coarse pre-

precipitates are generated during a 400 °C annealing. These precipitates are further analyzed using SEM (Fig 5.31) and TEM (Fig 5.32).

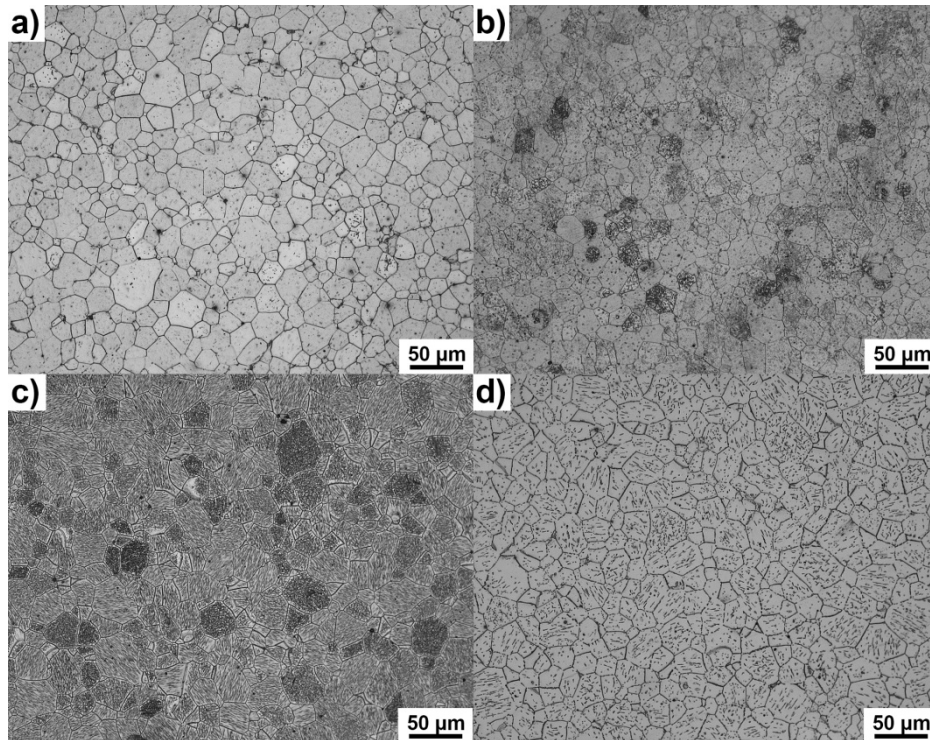


Fig 5.30: Micrographs showing the microstructure in a) as-extruded material, and material heat treated for: b) 16 h at 250 °C, c) 500 h at 500 °C, d) 24 h at 400 °C [Len15b].

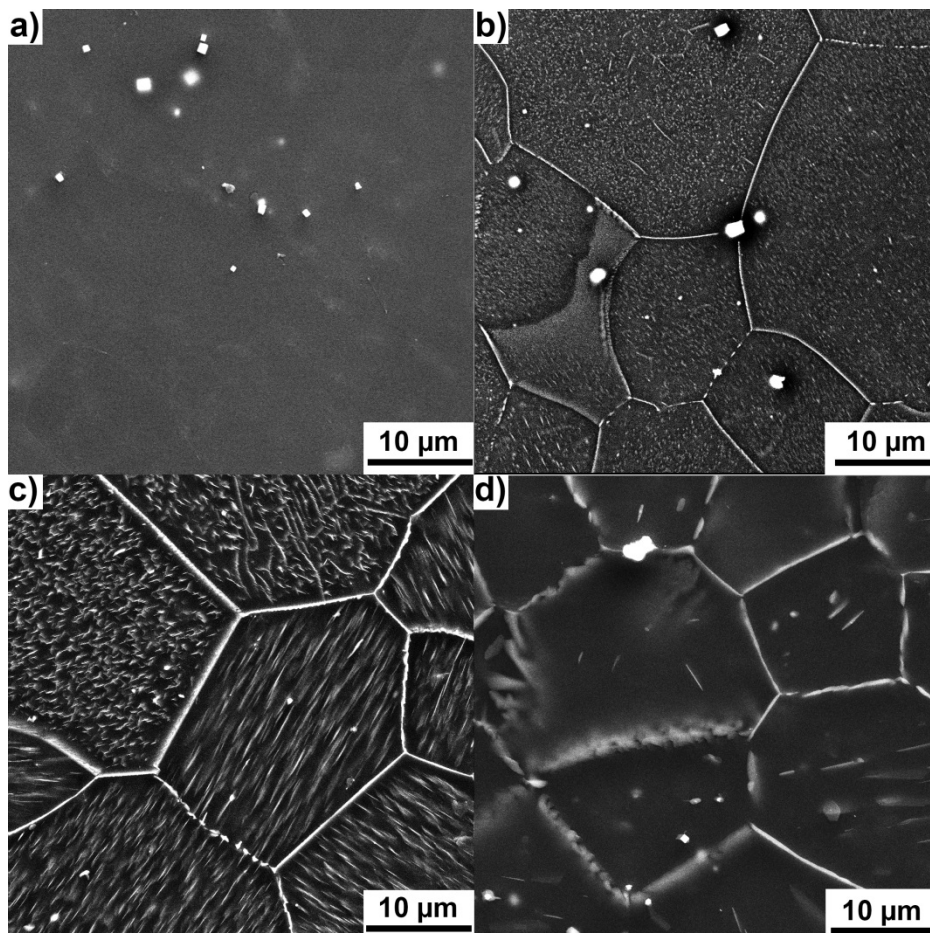


Fig 5.31: SEM images showing precipitates in a) as-extruded material, and material heat treated for: b) 16 h at 250 °C, c) 500 h at 500 °C, d) 24 h at 400 °C [Len15b].

As has been mentioned above, the as-extruded material contains very limited amounts of Y-rich precipitates (Fig 5.28, Fig 5.31 a)). Age-hardening at 250 °C generates precipitates within the grains (16 h: Fig 5.31 b), Fig 5.32 a) and c); 500 h: Fig 5.31 c), Fig 5.32 b) and c)). The observed precipitates were identified using the references [Nie99, Nie00, Nie12], and the fast Fourier transforms of the HR-TEM images, which were recorded using the FEI Titan 80-300 Berlin Holography Special TEM (ZELMI, TU Berlin). The 16 h age-hardening results in the formation of prismatic plate-shaped (β_1) and globular precipitates (β'), while the 500 h age-hardened sample only contains prismatic plate-shaped precipitates (β).

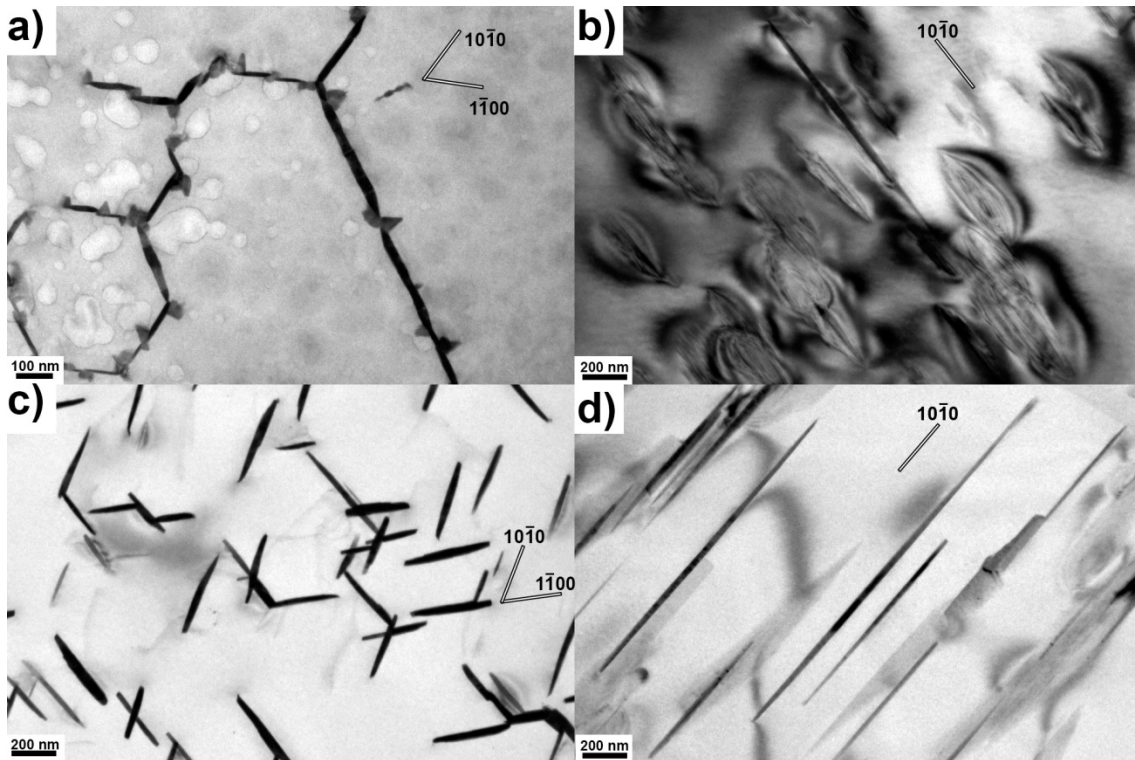


Fig 5.32: TEM images of precipitates in the heat treated material a) 16 h 250 °C; <00.2> ZA, b) 16 h 250 °C; <11.0> ZA, c) 500 h 250 °C; <00.2> ZA d) 500 h 250 °C; <11.0> ZA [Len15b].

In contrast to the 250 °C samples, the 400 °C annealed samples form precipitates in the grain boundaries and very few precipitates within the grains. Due to the low precipitation density within the grains, no significant precipitation hardening is expected, but the precipitates at the grain boundaries would, at the same time, mean a reduced amount of solutes within the grains. The reduced solute concentrations were confirmed using electron probe microanalysis. Line scans of a (1 h 400 °C) sample revealed decreasing Nd (from 1.8 wt% to 0.8 wt%) and Y (from 5.3 wt% to 5.0 wt%) concentration within the grain interiors due to precipitation at grain boundaries.

As might be expected from the very limited grain growth during the heat treatments, the texture of the alloy does not change significantly during the heat treatments. Fig 5.33 exhibits the effect of the conducted heat treatments on the texture. The IPFs were determined from large scale EBSD maps (1800 x 700 μm^2 , not shown).

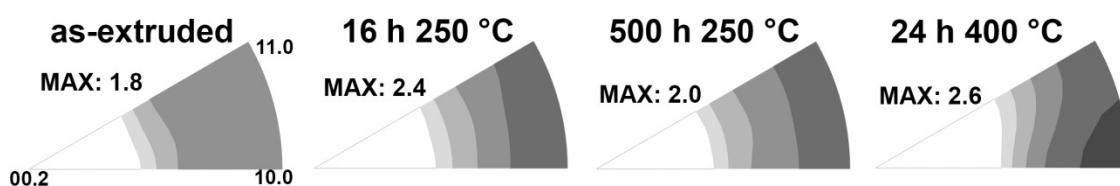


Fig 5.33: Effect of heat treatments on the texture (determined from the recorded EBSD data) [Len15b].

5.2.4 Mechanical properties

The above described changes of the d_g , the precipitates and the solute concentrations affect the mechanical properties, which will be investigated using the macroscopic flow curves, the microstructural and texture development during deformation and EPSC simulations.

5.2.4.1 Flow curves

The effect of the microstructure on the mechanical properties and the deformation behavior was analyzed via uniaxial tension and compression tests. The corresponding flow curves are displayed in Fig 5.34 and Fig 5.35. In Table 5.7 the resulting CYS, TYS and SDE are summarized.

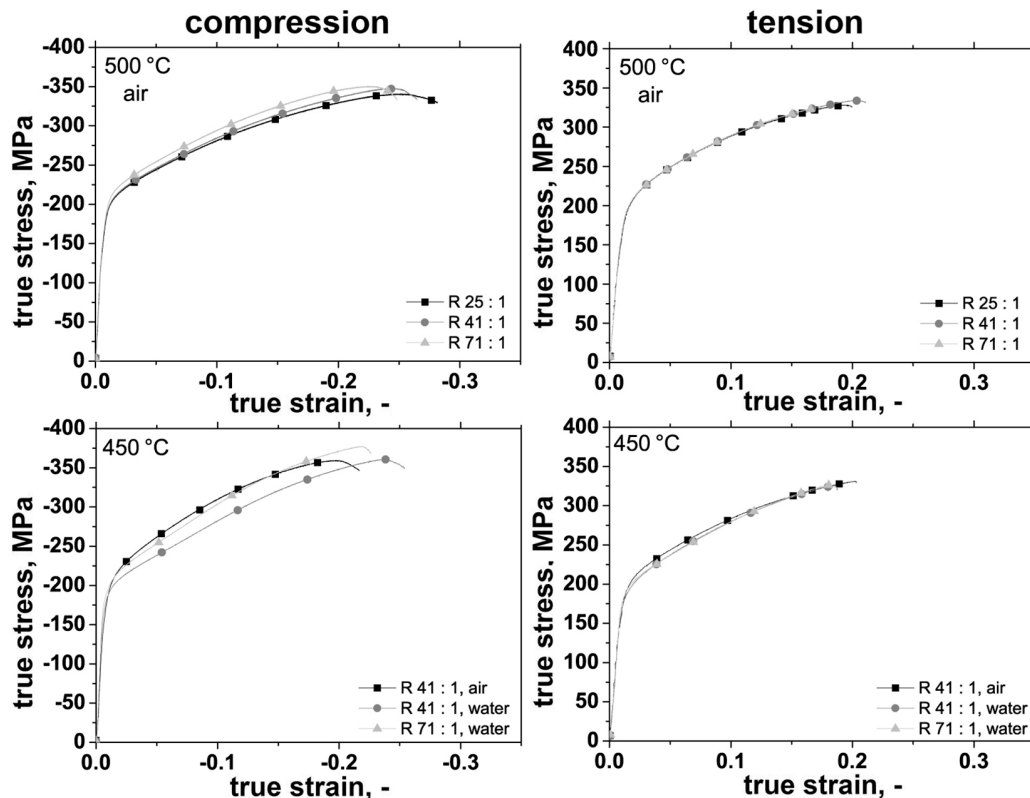


Fig 5.34: Flow curves of the extruded bars tested in uniaxial compression and tension.

In comparison to the ME21 extrusions three major differences are evident: 1. The alloy features a significantly higher strength, 2. the yield asymmetry and the plastic anisotropy are negligible and the SDE is close to 0 regardless of the d_g and texture, and 3. the compression flow curve of the extrusions do not feature a sigmoidal shape or any other signs of an important TTW-ing activity.

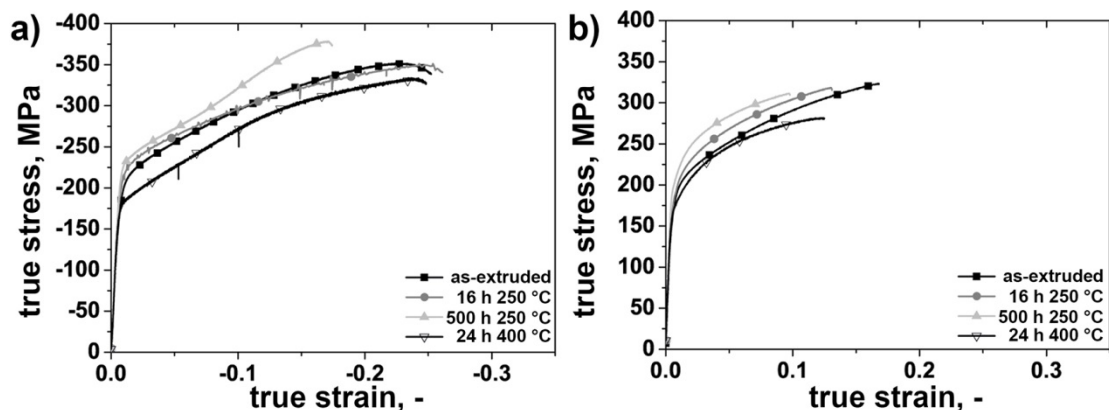


Fig 5.35: Effect of heat treatments on the flow curves a) compression, and b) tension [Len15b].

Interestingly, the 500 h age-hardening and the 24 h 400 °C annealing appear to render TTW-ing more active. The corresponding compression flow curves exhibit a slight, but clearly visible, sigmoidal shape being characteristic of a notable contribution of TTW-ing to the deformation (Fig 5.35 a). From Fig 5.35 and Table 5.7 it is apparent, that age-hardening increases both CYS and TYS. At the same time the elongation to failure is reduced particularly in tension. The 24 h 400 °C annealing results in decreasing strength and elongations to failure.

Table 5.7: Tension compression yield asymmetry specified by the CYS, TYS and SDE of the extruded bars. The error of CYS and TYS is below 5 MPa.

T_B , cooling	WE54								
	R 25 : 1			R 41 : 1			R 71 : 1		
	CYS, MPa	TYS, MPa	SDE, -	CYS, MPa	TYS, MPa	SDE, -	CYS, MPa	TYS, MPa	SDE, -
450 °C air	-	-	-	-169	166	0.02	-	-	-
450 °C water	-	-	-	-174	170	0.02	-183	179	0.02
500 °C air	-170	157	0.08	-171	166	0.03	-182	169	0.07
16 h 250 °C	-	-	-	-	-	-	-199	179	0.11
500 h 250 °C	-	-	-	-	-	-	-219	199	0.10
24 h 400 °C	-	-	-	-	-	-	-173	166	0.04

In order to analyze the underlying deformation mechanism causing the flow curves, the deformed microstructure was analyzed using EBSD.

5.2.4.2 Deformed microstructure

Fig 5.36 exhibits the EBSD analysis of deformed compression samples (extrusion A) at the engineering strain levels: $\epsilon_e = -5\%$, $\epsilon_e = -10\%$, $\epsilon_e = -12\%$ and $\epsilon_e = -18\%$, while Fig 5.37 displays the corresponding MDFs. The comparison of Fig 5.17 and Fig 5.36 reveals a significantly lower TTW-ing activity in the WE54 extrusion than in the ME21 extrusion.

At $\epsilon_e = -5\%$ TTWs nucleate and grow readily in the ME21 alloy (Fig 5.17), while their number is significantly reduced in the WE54 alloy (Fig 5.36). In WE54 the TTWs tend to be thin and needle-like and TTW-ing is limited to grains, which feature a very high SF for TTW-ing. In case of the WE54 alloy TTW-ing and the corresponding IPFs exhibit a relatively low $\langle 0002 \rangle$ density compared to ME21. Here, grains that correspond to the $\langle 10\bar{1}0 \rangle / \langle 11\bar{2}0 \rangle$ double fiber are retained to a higher extend. These findings are supported by the correlated MDFs (Fig 5.18 and Fig 5.37) showing a lower frequency of TTW boundaries in case of the WE54 alloy (the maximum at $\approx 86^\circ$ is more pronounced). Additionally, the local maximum at $\approx 58^\circ$ about the $\langle 10\bar{1}0 \rangle$ axis, which can be correlated to the intersection of different TTW variants, is absent in the WE54 indicating lower nucleation and growth rates in this alloy.

In between $\epsilon_e = -10\%$ and $\epsilon_e = -12\%$ TTW-ing is exhausted in ME21 (Fig 5.17), while several grains contain no TTWs in case of the WE54 alloy. However, those grains, which contain at least one TTW, have not been overtaken. The limited growth of the TTWs is further supported by limited changes of the relative frequency of TTW boundaries in the strain range from $\epsilon_e = -10\%$ to $\epsilon_e = -18\%$. The additional peaks, which were observed at $\epsilon_e = -18\%$, at $\approx 28^\circ$ and at $\approx 74^\circ$ could not be correlated to a particular twin mode. Highlighting these

angular ranges in the BC maps reveals that these peaks are associated to noise, that is introduced by the high deformation of the sample.

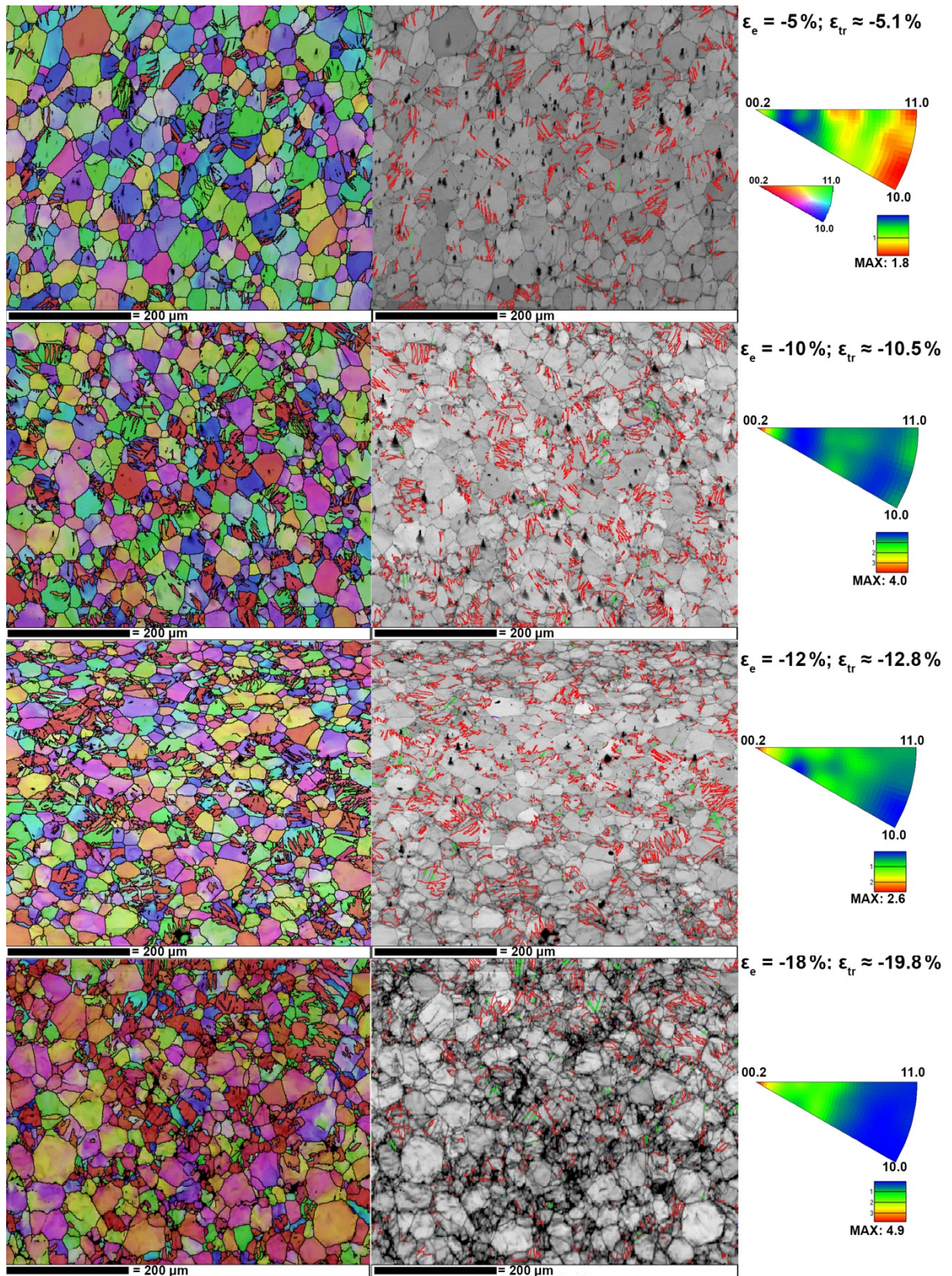


Fig 5.36: EBSD maps, BC maps highlighting twin boundaries ($86^\circ \langle 11\bar{2}0 \rangle = \text{red}$, $56^\circ \langle 11\bar{2}0 \rangle = \text{yellow}$, $38^\circ \langle 11\bar{2}0 \rangle = \text{green}$, $30^\circ \langle 11\bar{2}0 \rangle = \text{blue}$) and IPFs of compression samples (extrusion A) [Len14c].

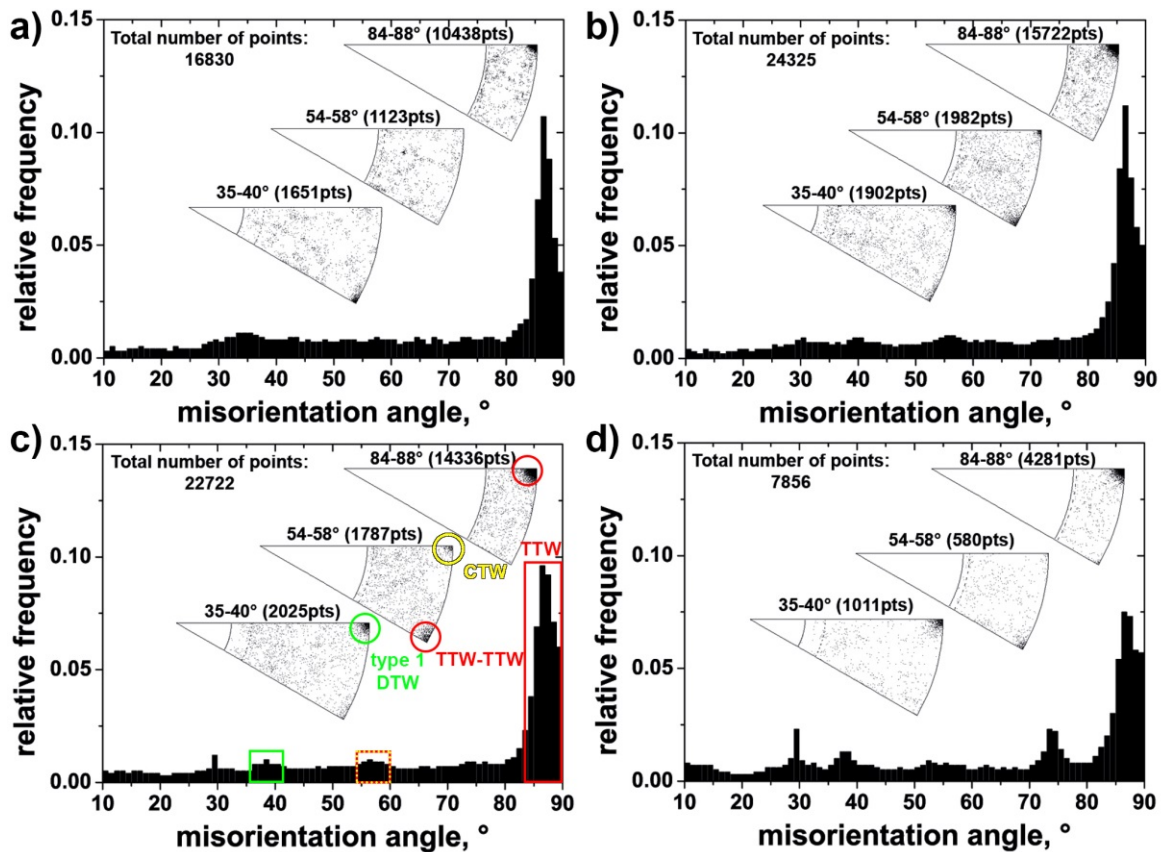


Fig 5.37: MDFs of compression samples (extrusion A): a) $\epsilon_e = -5\%$, b) $\epsilon_e = -10\%$, c) $\epsilon_e = -12\%$, d) $\epsilon_e = -18\%$. Insets show the distribution of the rotation axis for characteristic angular ranges. $86^\circ <11\bar{2}0>$ = red, $56^\circ <11\bar{2}0>$ = yellow [Len14c].

Here, it should be emphasized that TTW-ing does not overtake the parent grains even at $\epsilon_e = -18\%$. In addition, the WE54 alloy tends to resist texture changes during compression, which is observed through the weak $<0002>$ texture and the large orientation spread at high strains.

In order to investigate the effects of precipitates and solutes on the deformation behavior and the corresponding microstructure and texture evolution further EBSD investigations were conducted using as-extruded (extrusion C), 250 °C age-hardened and 400 °C annealed samples. In Fig 5.35 a slight sigmoidal shaped compression flow curve was observed in case of the 500 h age-hardened and the 400 °C annealed sample suggesting an enhancement of TTW-ing through precipitation hardening or the reduction of the solute content. Below it will be shown via EBSD analysis that TTW-ing is indeed enhanced in these samples.

Fig 5.38 illustrates the collected EBSD maps, while Fig 5.39 displays the MDFs at $\epsilon_e = -5\%$. The final textures correspond to samples, which were investigated via in-situ EDXRS. The corresponding flow curves and strains are displayed in Fig 5.41 and will be discussed in section 5.2.4.3. As has been shown in the foregoing EBSD analysis of extrusion A, the as-extruded material (extrusion C) features very few TTWs, which appear as red lamella, at $\epsilon_e = -5\%$. While the 16 h 250 °C age-hardened does not alter the number or the size of the TTWs significantly, the 500 h 250 °C age-hardened and the 24 h 400 °C annealed sample exhibit a major increase of the number of TTWs. Here, many grains contain at least one TTW, many of which contain multiple TTW lamellae and wider TTWs. The difference in TTW-ing activity is quantified statistically in Fig 5.39. The relative frequency of TTW boundaries and therefore, the TTW-ing activity increases in the following order: as-extruded (Fig 5.39 a) < 16 h 250 °C (Fig 5.39 b) < 24 h 400 °C (Fig 5.39 d) < 500 h 250 °C (Fig 5.39 c).

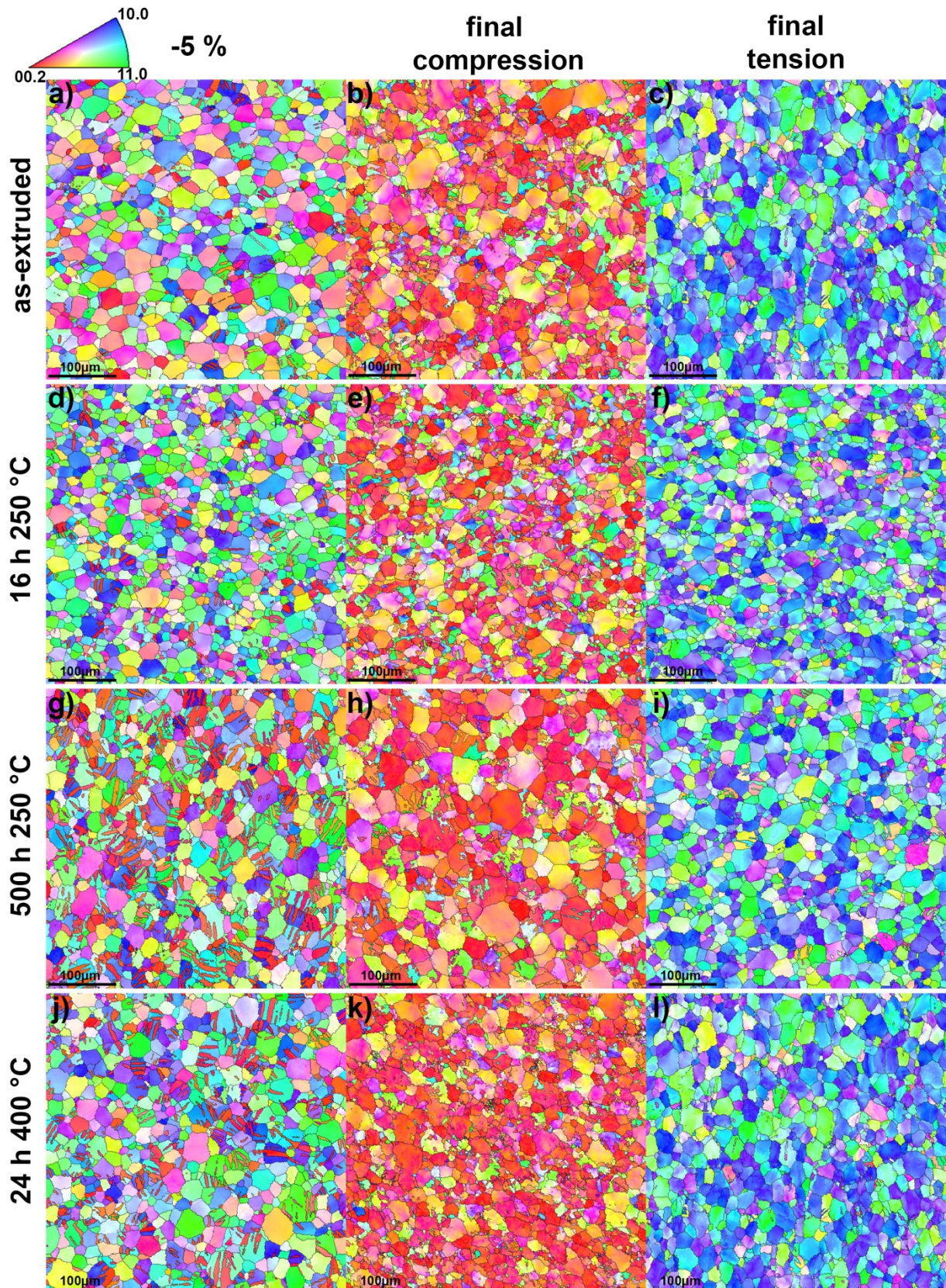


Fig 5.38: EBSD maps of deformed samples (based on extrusion C): a), d), g), j) at -5 % compression; b), e), h), k) after final load step - compression; c), f), i), l) after final load step – tension [Len15b].

All samples, but in particular the as-extruded and the 16 h age-hardened samples, contain partially twinned grains at this high strain level. Hence, TTW-ing proceeds uncommonly slow in comparison to other Mg alloys, where TTWs grow readily and overtake the parent grains quickly. Fig 5.38 c), f), i) and l) exhibit the EBSD maps of the tension samples (final load

step). During tensile loading, negligible amounts of twins are formed, and the grains predominantly feature a $\langle 10\bar{1}0 \rangle$ orientation.

The above described evolution is confirmed by the corresponding texture evolution (Fig 5.40). The limited TTW-ing activity is observed through the very weak $\langle 0002 \rangle$ texture component in compression. An enhanced $\langle 0002 \rangle$ texture component reflects pronounced TTW-ing of the parent grains featuring $\langle 10\bar{1}0 \rangle$ and $\langle 11\bar{2}0 \rangle$ texture components. A very weak enhancement of the $\langle 0002 \rangle$ density is indeed observed in case of the 500 h age-hardened sample. Further compression results in the rotation of grains towards the $\langle 0002 \rangle$ texture component via crystallographic slip, particularly by the activation of $\langle a \rangle$ basal slip. In contrast to the ME21 alloy the maximum intensity is significantly shifted away from the $\langle 0002 \rangle$ texture component. This maximum corresponds to the RE texture component, which has been rotated towards the $\langle 0002 \rangle$ pole due to the activation of slip systems. However, the rotation towards the $\langle 0002 \rangle$ texture component is slow in comparison to other Mg alloys, which indicates the enhanced activation of non-basal slip modes.

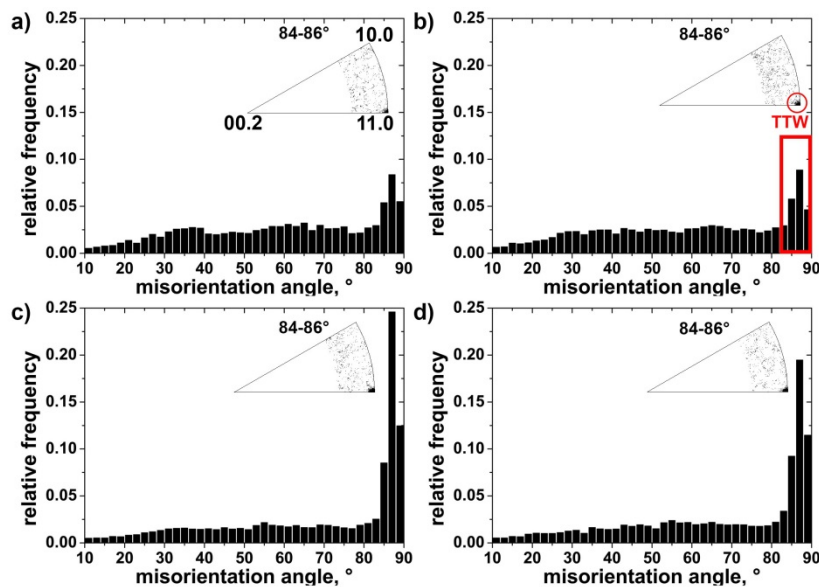


Fig 5.39: Histograms showing MDFs at -5 % strain in a) as-extruded and material heat treated for: b) 16 h at 250 °C, c) 500 h at 250 °C, d) 24 h at 400 °C [Len15b].

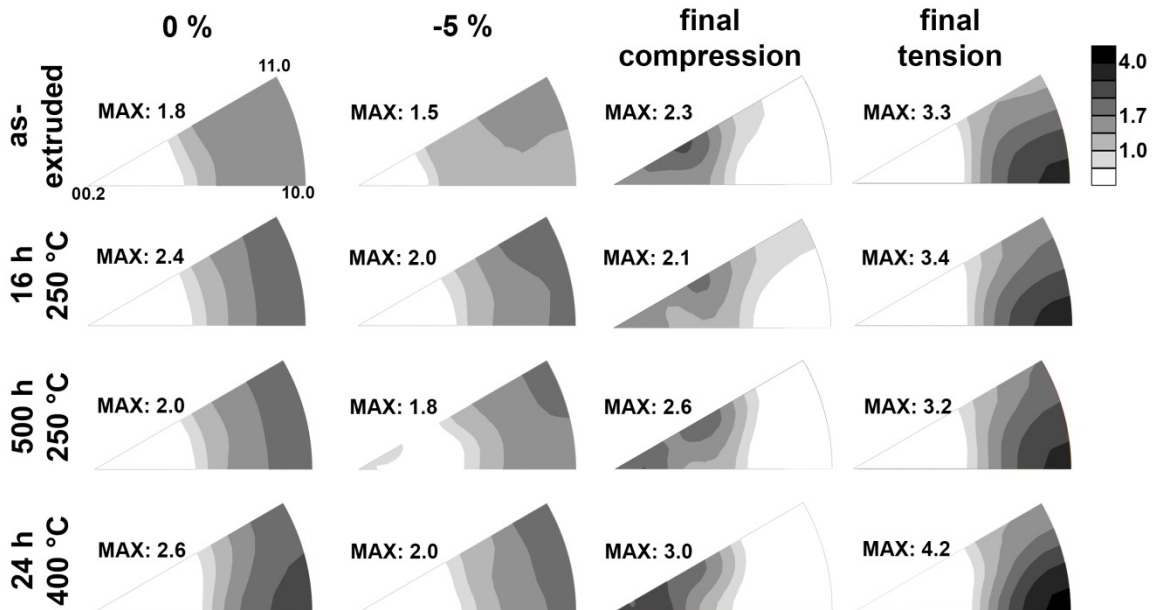


Fig 5.40: IPFs showing texture development during deformation [Len15b].

5.2.4.3 EPSC simulations

In order to uncover the underlying deformation mechanism and the effect of the heat treatments on the hardening behavior of the individual deformation modes in-situ EDXRSD experiments during loading and EPSC simulations have been conducted. In order to characterize the model parameters the flow curves (Fig 5.41), the ϵ_{hkl} (Fig 5.42 and Fig 5.43) and the texture evolution (Fig 5.44) were evaluated and will be discussed in turn below. The applied hardening parameters for slip and TTW-ing are summarized in Table 5.8 and Table 5.9. The spread in d_g of 17 μm to 20 μm was too small to evaluate the HP coefficients accurately. Therefore, HP coefficients, which were determined in Mg-Li(-Al) alloys featuring a wide spread in d_g (sections 5.3.3.3 and 5.4.3.3, [Len15a]), were used. Unfortunately, the strength increment between the as-extruded and the 16 h age-hardened sample is too small to detect changes in the hardening parameters. However, several important findings could be obtained:

First, as might be expected for Mg alloys the slip activation stresses $\tau_{0,f}^s$ (Table 5.8) increase in the following order regardless of the formation of precipitates: $\langle a \rangle$ basal $< \langle a \rangle$ prismatic $< \langle c+a \rangle$ pyramidal slip. In agreement with Agnew et al. [Agn13], the age-hardening has a significant effect on $\langle a \rangle$ basal slip, which is evident by the relative increase of 50 % in $\tau_{0,f}^s$ between the as-extruded and the 500 h age-hardened samples compared to the very slight changes in $\tau_{0,f}^s$ for $\langle a \rangle$ prismatic and $\langle c+a \rangle$ pyramidal slip.

Table 5.8: Hardening parameters for slip [Len15b].

Parameter	As-extruded			16 h 250 °C		
	$\langle a \rangle$ prism	$\langle a \rangle$ basal	$\langle c+a \rangle$ pyr	$\langle a \rangle$ prism	$\langle a \rangle$ basal	$\langle c+a \rangle$ pyr
$\tau_{0,f}^s$ (MPa)	80	10	115	80	10	115
k_1^s (m^{-1})	1.5E+08	1.0E+08	2.5E+09	1.5E+08	1.0E+08	2.5E+09
D^s (MPa)	3.5E+03	3.5E+03	8.5E+03	3.5E+03	3.5E+03	8.5E+03
g^s	5.0E-03	5.0E-03	9.5E-03	4.0E-03	4.0E-03	9.5E-03
ρ_0 (m^{-2})	1.5E+12	1.5E+12	1.5E+12	1.5E+12	1.5E+12	1.5E+12
HP^s	160	90	20	160	90	20
C^{st}	50	50	400	50	50	400

Parameter	500 h 250 °C			24 h 400 °C		
	$\langle a \rangle$ prism	$\langle a \rangle$ basal	$\langle c+a \rangle$ pyr	$\langle a \rangle$ prism	$\langle a \rangle$ basal	$\langle c+a \rangle$ pyr
$\tau_{0,f}^s$ (MPa)	82	15	115	60	8	105
k_1^s (m^{-1})	1.5E+08	1.0E+08	8.5E+09	1.5E+08	1.0E+08	15.5E+09
D^s (MPa)	3.5E+03	3.5E+03	8.5E+03	3.5E+03	3.5E+03	8.5E+03
g^s	4.0E-03	4.0E-03	11.5E-03	4.0E-03	4.0E-03	7.5E-03
ρ_0 (m^{-2})	1.5E+12	1.5E+12	1.5E+12	1.5E+12	1.5E+12	1.5E+12
HP^s	160	90	20	160	90	20
C^{st}	50	50	400	50	50	400

Table 5.9: Hardening parameters for TTW-ing [Len15b].

Parameter	As-extruded	16 h 250 °C	500 h 250 °C	24 h 400 °C
τ_0^t (MPa)	115	115	98	78

Second, the limited TTW-ing activity in the as-extruded and 16 h age-hardened conditions (e.g. Fig 5.38) is correlated with a remarkably high τ_0^t in these samples, where τ_0^t is in the order of $\tau_{0,f}^s$ for $\langle c+a \rangle$ pyramidal slip. Here, it is important to emphasize that τ_0^t is considerably lowered by the 500 h age-hardening and the 400 °C annealing, where the solute concentration has dropped.

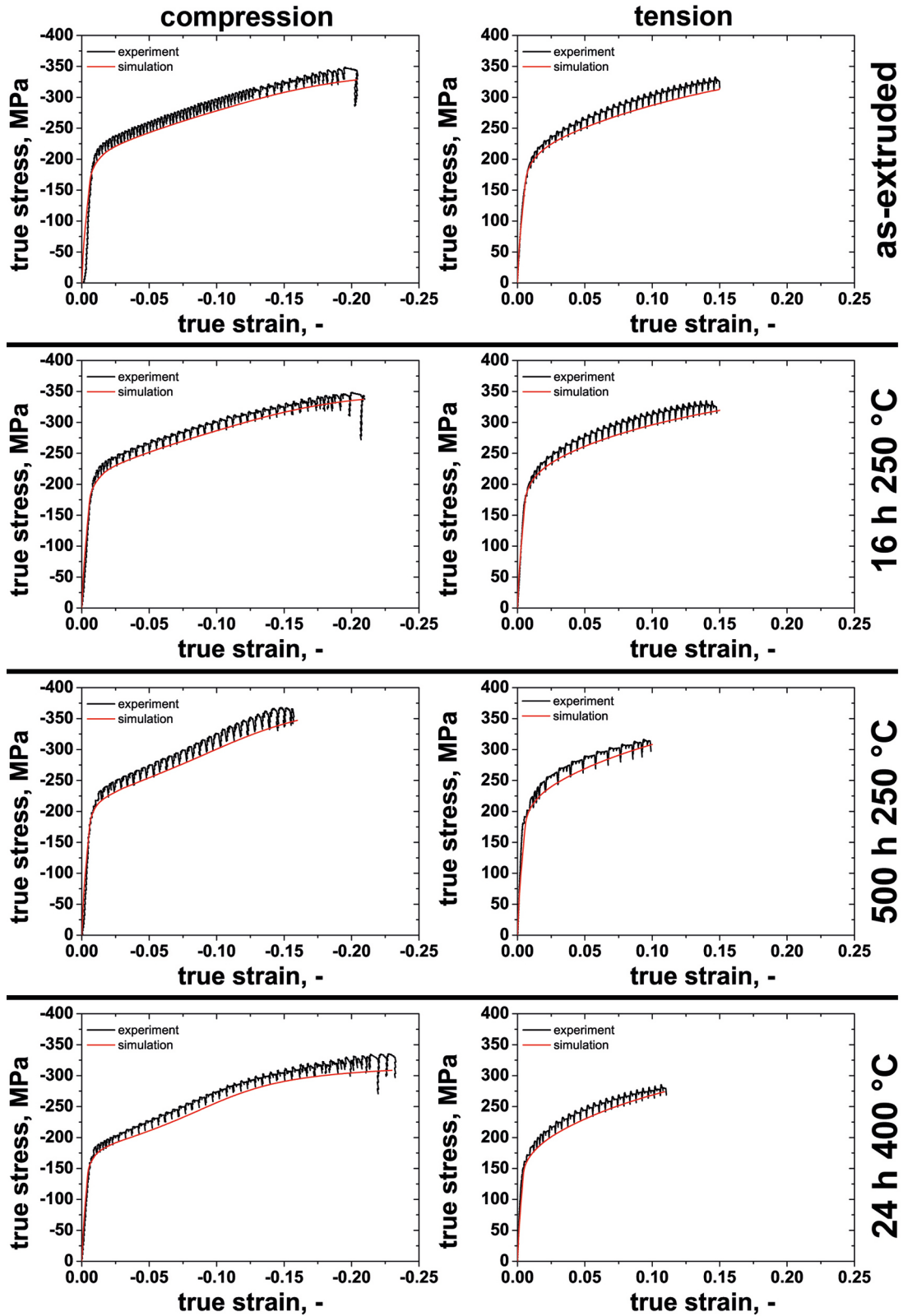


Fig 5.41: Comparison of the experimental and simulated flow curves [Len15b].

Third, $\tau_{o,f}^S$ decreases for all slip modes in the 400 °C annealed sample, which features a reduced solute content and precipitates at the grain boundaries. The reduction of the solute concentration results in weaker solute hardening and the grain boundary precipitates are ineffective in terms of hindering dislocation movement. Fig 5.42 and Fig 5.43 display the evolution of axial and transversal ϵ_{hkl} of the $(10\bar{1}0)$, (0002) , $(10\bar{1}1)$, $(10\bar{1}2)$, $(11\bar{2}0)$, $(10\bar{1}3)$, $(11\bar{2}2)$ and $(20\bar{2}1)$ reflections during compression and tension tests.

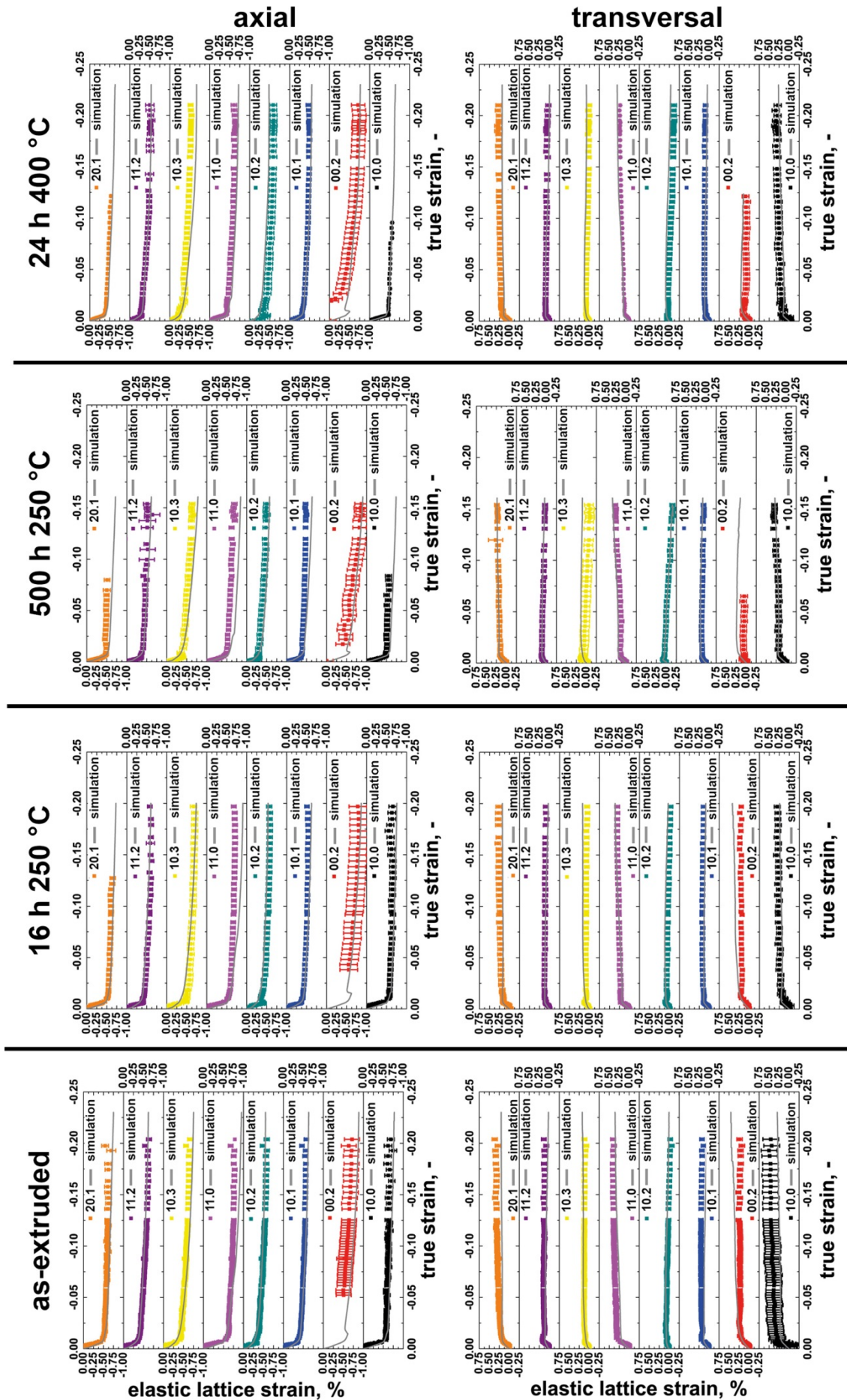


Fig 5.42: Comparison of the measured and predicted ϵ_{hkl} during compression [Len15b].

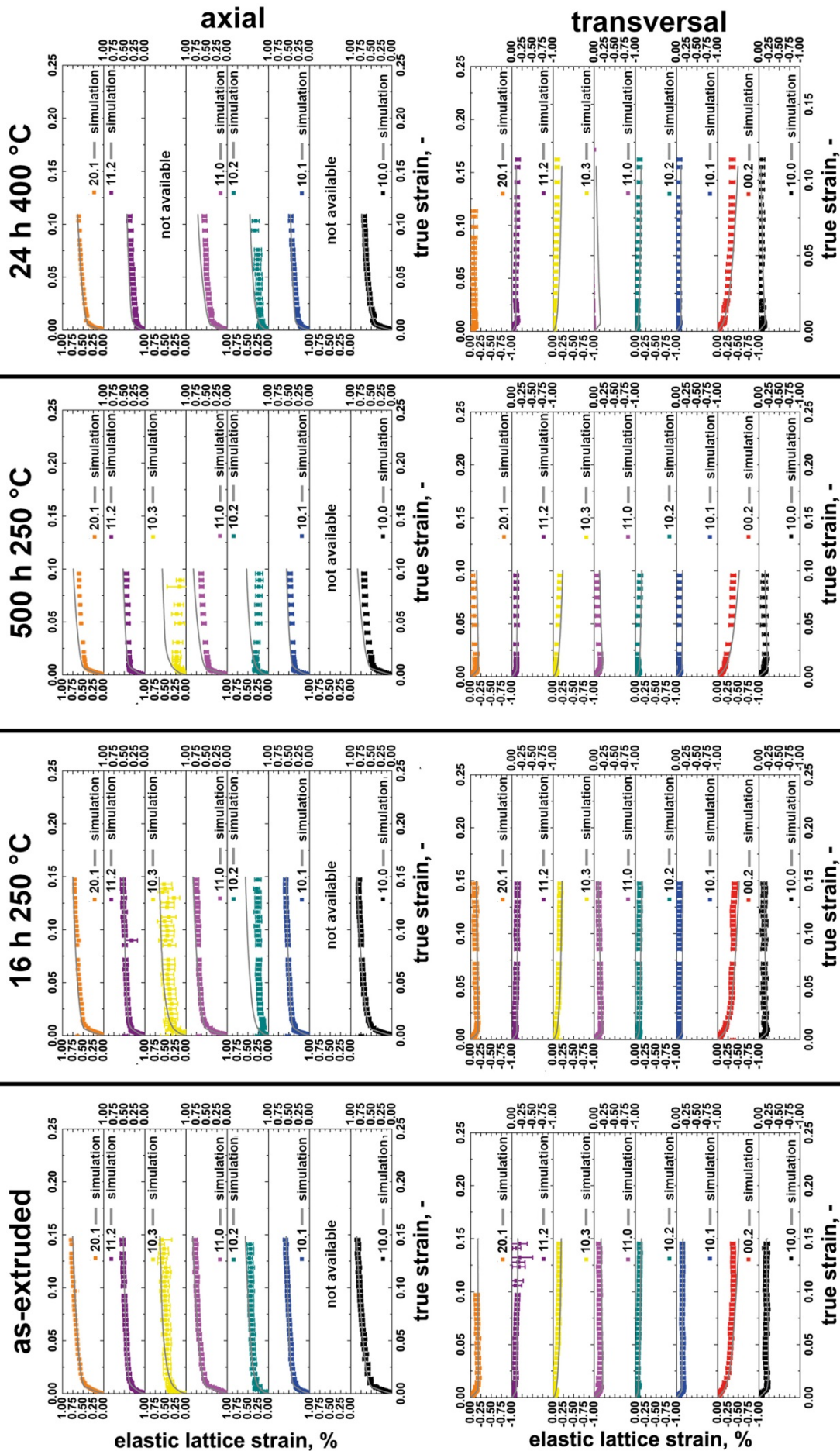


Fig 5.43: Comparison of the measured and predicted ϵ_{hkl} during tension [Len15b].

Each reflection corresponds to a subset of grains, which feature a common orientation. Grains featuring a $(10\bar{1}1)$, $(10\bar{1}2)$, $(10\bar{1}3)$ or $(11\bar{2}2)$ orientations possess high SFs for $\langle a \rangle$ basal slip and relatively high SFs for $\langle a \rangle$ prismatic slip. These slip modes have the lowest $\tau_{o,f}^s$ and consequently, these reflections feature the lowest axial and transversal ϵ_{hkl} in tension and compression tests.

The axial $(10\bar{1}0)$, $(11\bar{2}0)$ and $(20\bar{2}1)$ as well as the transversal (0002) reflections correspond to the $\langle 10\bar{1}0 \rangle / \langle 11\bar{2}0 \rangle$ texture components and hence possess high SF for $\langle a \rangle$ prismatic and $\langle c+a \rangle$ pyramidal slip as well as TTW-ing in case of compression loading parallel to ED. However, the SF for $\langle a \rangle$ basal slip is close to zero in these grains. In most Mg alloys, where TTW-ing is readily activated when the compression direction is perpendicular to the crystallographic c-axis, such grains would deform by $\langle a \rangle$ prismatic slip and TTW-ing during compression parallel to ED generating a tension compression yield asymmetry since the TTW-ing is only activated in compression. However, the conducted EPSC simulations reveal that TTW-ing features a very high activation threshold stress τ_o^t in case of the WE54 alloy, and therefore, would likely occur after large strains. Hence, the initial deformation should be realized by slip, which is confirmed by the late occurrence of the axial (0002) reflection particularly in the as-extruded and the 16 h 250 °C sample. This reflection corresponds to twinned grains, which have been reoriented by TTW-ing (86° rotation about an $\langle 11\bar{2}0 \rangle$ axis). The (0002) reflection is observed at lower strains in case of the 500 h 250 °C and the 24 h 400 °C compression samples, where TTW-ing is less hindered. Usually, the relative activity of $\langle c+a \rangle$ pyramidal slip is high within the TTWs causing pronounced hardening, which results in a sigmoidal compression flow curve and a significant increase of the ϵ_{hkl} . However, such features were not observed in the present WE54 alloy, where the (0002) reflection exhibits very limited hardening indicating that $\langle c+a \rangle$ pyramidal slip occurs at a relatively low CRSS.

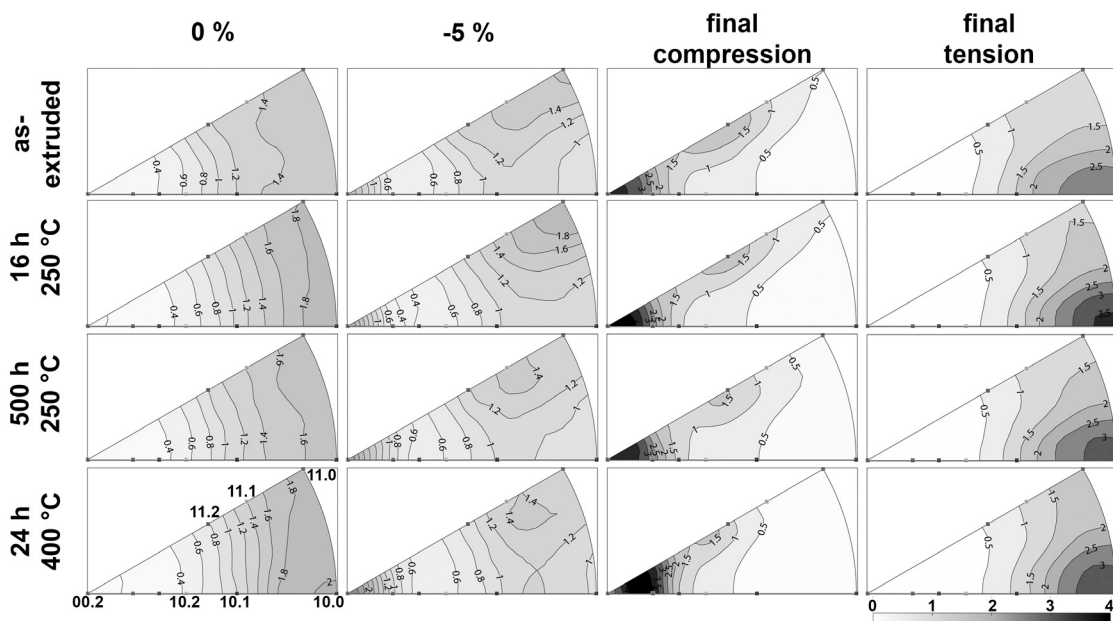


Fig 5.44: IPFs showing the simulated textures (\parallel ED = load direction) [Len15b].

Based on the conducted experiments and EPSC simulations, the relative deformation mode activities associated with the observed texture development have been extracted (Fig 5.45). A comparison of the simulated (Fig 5.44) and the experimental textures (Fig 5.40) displays good agreement considering the limitation of the self-consistent homogenization scheme in accounting for grain-to-grain interactions only in an average sense without explicit neighboring effects. Nevertheless, minor deviations, such as the simulated IPFs showing a $\langle 0002 \rangle$

texture component unlike the measured IPFs, are visible. Notably, however, the predicted TTW volume fractions are in good agreement with measured TTW volume fractions, showing sufficiently accurate prediction of the TTW-ing activity. Therefore and because of the good agreement of the flow curves and the ϵ_{hkl} , the model is considered reliable for interpreting the deformation behavior of the studied samples.

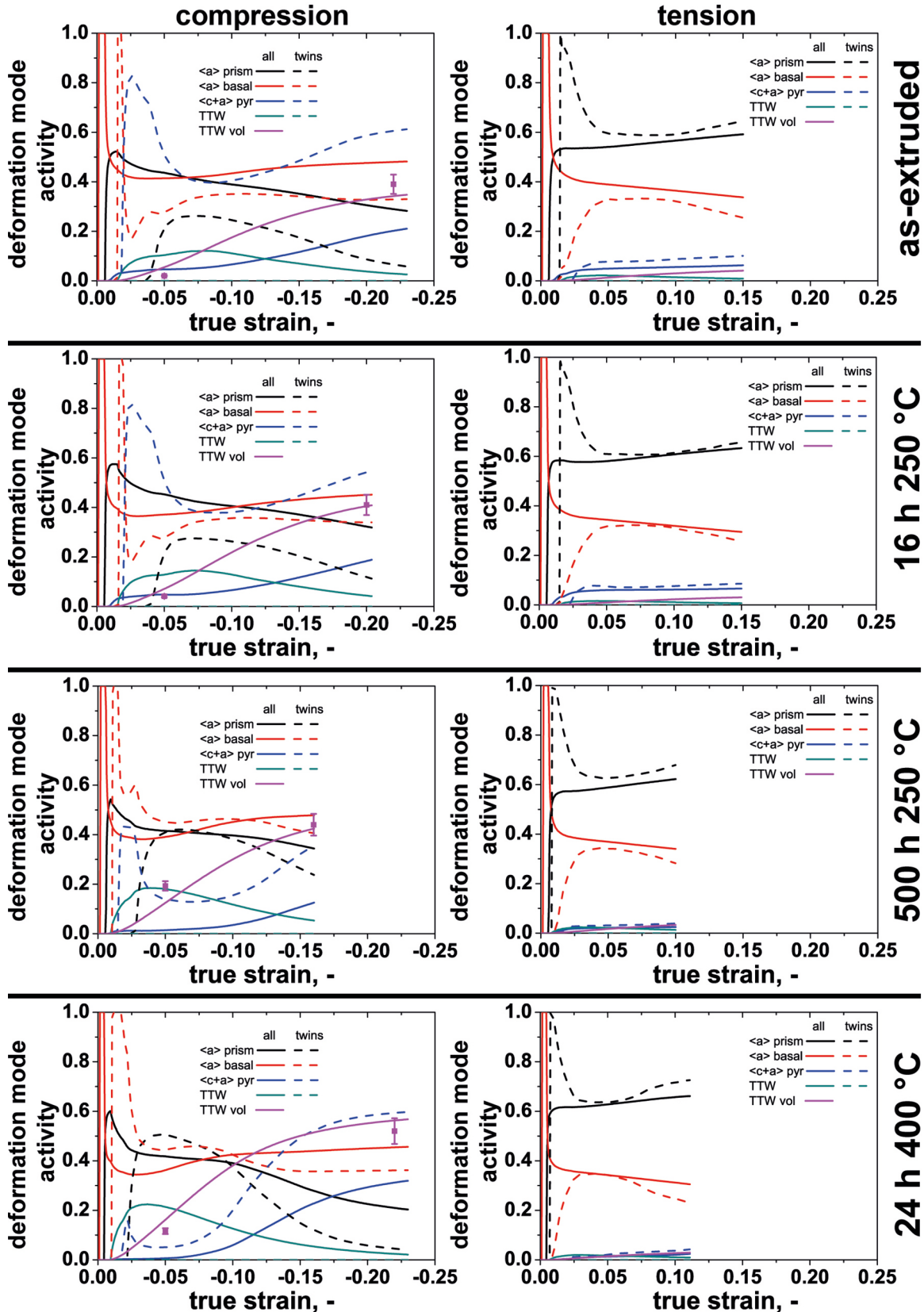


Fig 5.45: Relative activities of the active deformation modes predicted by the EPSC model [Len15b].

Fig 5.45 illustrates the relative deformation mode activity as a function of the applied strain path and strain. It is evident that TTW-ing is significantly hindered compared to other Mg alloys, such as ME21 (Fig 5.21), particularly in the as-extruded and the 16 h age-hardened samples. The reduced TTW activity is compensated by the enhanced activation of slip. Here, an enhancement of the activity of $\langle a \rangle$ prismatic and $\langle a \rangle$ basal slip was observed, while an enhancement of $\langle c+a \rangle$ pyramidal slip at low compressive strains is only predicted in the as-extruded and the 16 h 250 °C samples. The 500 °C age-hardened and the 400 °C annealed samples feature an increased TTW-ing activity in comparison to the other materials conditions and consequently, a reduced initial activity of $\langle c+a \rangle$ pyramidal slip. Tensile deformation is predominantly realized by $\langle a \rangle$ slip systems causing the enhancement of the $\langle 10\bar{1}0 \rangle$ texture component. In addition, a small relative activity of the $\langle c+a \rangle$ pyramidal slip system is predicted in tension.

5.3 L4

5.3.1 Extrusion billets

Fig 5.46 displays a micrograph of a L4 cast billet featuring equiaxed grains. d_g varies within the range from several 100 μm to about 1 mm. In comparison to the ME21 and the WE54 billets, the L4 billets exhibit a relatively large porosity, where the size of the voids was up to several millimeters. In addition, the alloy contained (Al)-Si rich precipitates and Mg oxides, which were not expected in this binary alloy and were probably introduced during casting.

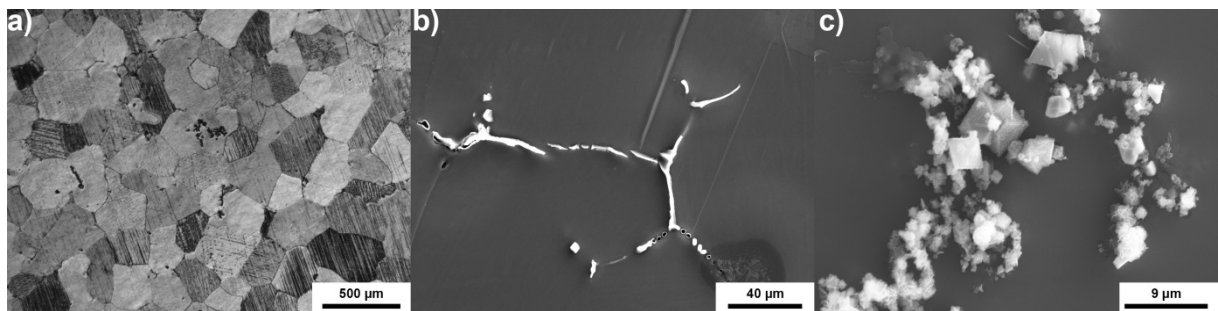


Fig 5.46: Micrograph of a L4 cast billet: a) grain structure, b) Si-rich phase, c) Al-Si rich phase.

5.3.2 Extrusion products

Within this study several extrusion trials were performed to analyze the effect of T_B , R and the cooling conditions on the microstructure, texture and mechanical properties. Here, as-cast and homogenized extrusion billets (4 h at 300 °C) were used.

Table 5.10: Summary of the applied extrusion parameters.

Extrusion	Homogenization	T_B , °C	R	Product speed, m/min	Cooling	Peak force, MN
A	4 h / 300 °C	300	25 : 1	1.7	air	3.2
B	4 h / 300 °C	300	41 : 1	1.7	air	3.5
C	4 h / 300 °C	300	71 : 1	1.7	air	4.0
D	4 h / 300 °C	200	41 : 1	1.7	air	5.0
E		200	25 : 1	1.7	air	5.9
F		200	41 : 1	1.7	air	5.9
G		200	71 : 1	1.7	air	6.9
H		200	25 : 1	1.7	water	7.1
I		200	41 : 1	1.7	water	-
J		200	71 : 1	1.7	water	7.3
K		250	41 : 1	1.7	air	4.7
L		300	41 : 1	1.7	air	3.7

5.3.2.1 Microstructure and texture

Fig 5.47 displays representative micrographs of longitudinal sections of the extrusions. The extruded bars exhibit an almost fully recrystallized microstructure, apart from some, relatively large grains, elongated parallel to the ED. The influence of the extrusion parameters on the generated average d_g is illustrated in Fig 5.48 and summarized in Table 5.11. Increasing T_B and air cooling result in increased average d_g as has been reported above for ME21 and WE54 extrusion. Like the WE54 alloy, the L4 extrusions feature decreasing average d_g , if R is increased. In addition, the saturation of grain growth at $T_B > 250\text{ }^\circ\text{C}$ (Fig 5.48 a) and the limited effect of water cooling at R 71 : 1 are worth mentioning. The smallest d_g ($\approx 5\text{ }\mu\text{m}$) was obtained using the extrusion parameters $T_B = 200\text{ }^\circ\text{C}$, R 71 : 1 and either water or air cooling.

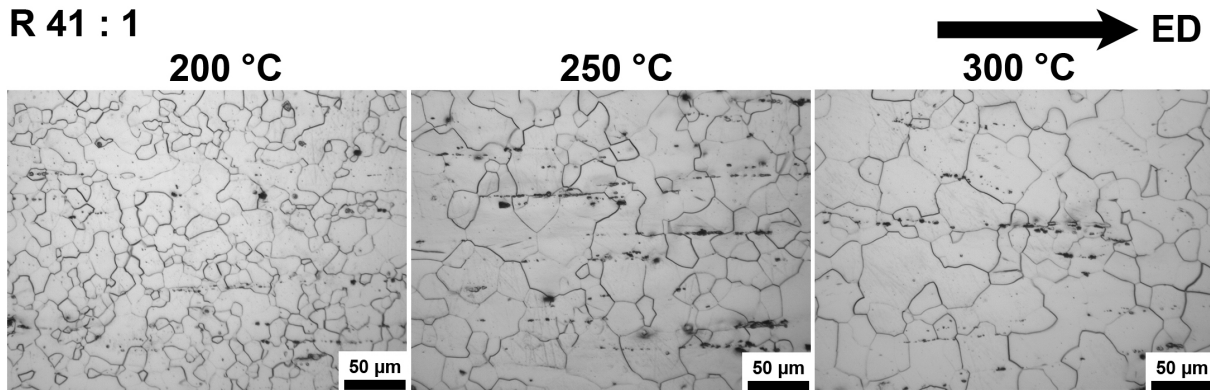


Fig 5.47: Microstructure of extrusions, which were processed using R 41 : 1 and air cooling [Len15a].

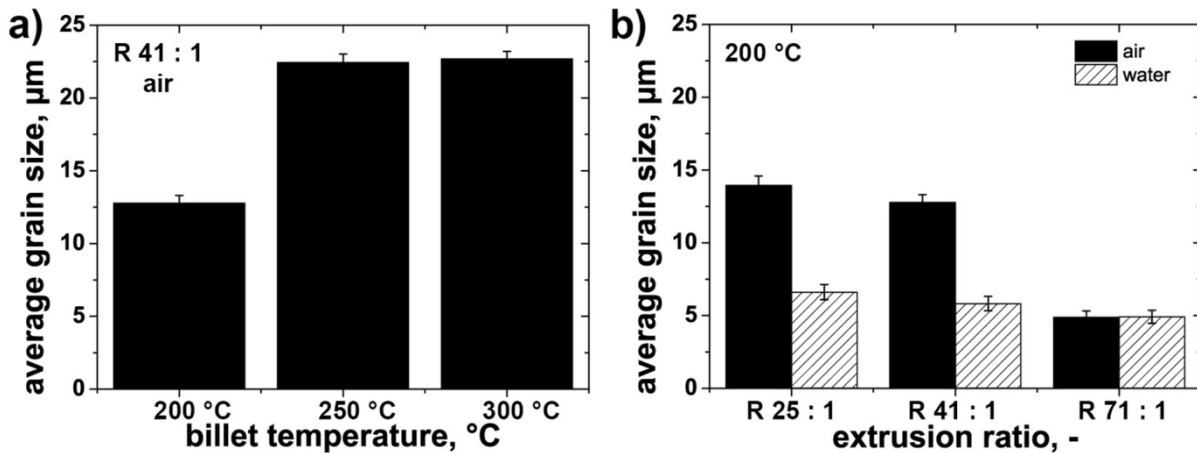


Fig 5.48: Histograms showing the effect of the extrusion parameters on d_g [Len15a].

Table 5.11: Applied extrusion parameters and resulting average d_g (μm) [Len15a]. The standard deviation of the log-normal distribution is below $0.5\text{ }\mu\text{m}$.

T_B , cooling	L4		
	R 25 : 1	R 41 : 1	R 71 : 1
200 °C, air	14	13	5
200 °C, water	7	6	5
250 °C, air	-	23	-
300 °C, air	30	23	-

All extruded bars contained a significant amount of (Al-)Si rich phases, which appear as necklace structures parallel to the ED and were likely introduced during the cast process (Fig 5.49). Due to their size and distribution, it is assumed that these precipitates do not affect the CRSS or the hardening of the deformation modes. However, they might influence the formability of the alloys. Using TEM no evidence of further precipitates of a smaller size was observed.

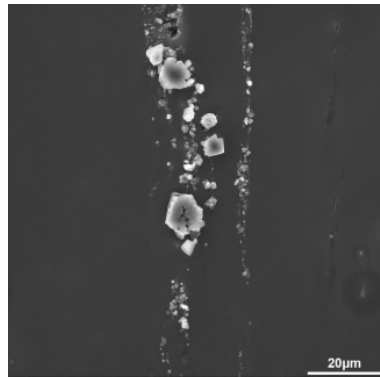


Fig 5.49: SEM images showing (Al-)Si-rich phases (ED↑) [Len15a].

In addition, to the effects of the extrusion parameters on the d_g , they also influence the texture of the extruded bars (Fig 5.50). Generally all samples feature the common extrusion fiber textures such as $\langle 10\bar{1}0 \rangle$ or $\langle 10\bar{1}0 \rangle / \langle 11\bar{2}0 \rangle$. More interestingly the $\langle 11\bar{2}0 \rangle$ texture component is enhanced in extrusions, which feature a medium to coarse d_g , while $\langle 10\bar{1}0 \rangle$ fiber textures are generated in the FG samples. This difference indicates that the $\langle 11\bar{2}0 \rangle$ texture component is predominantly formed during GC. Consequently, high R and water cooling result in sharp $\langle 10\bar{1}0 \rangle$ textures.

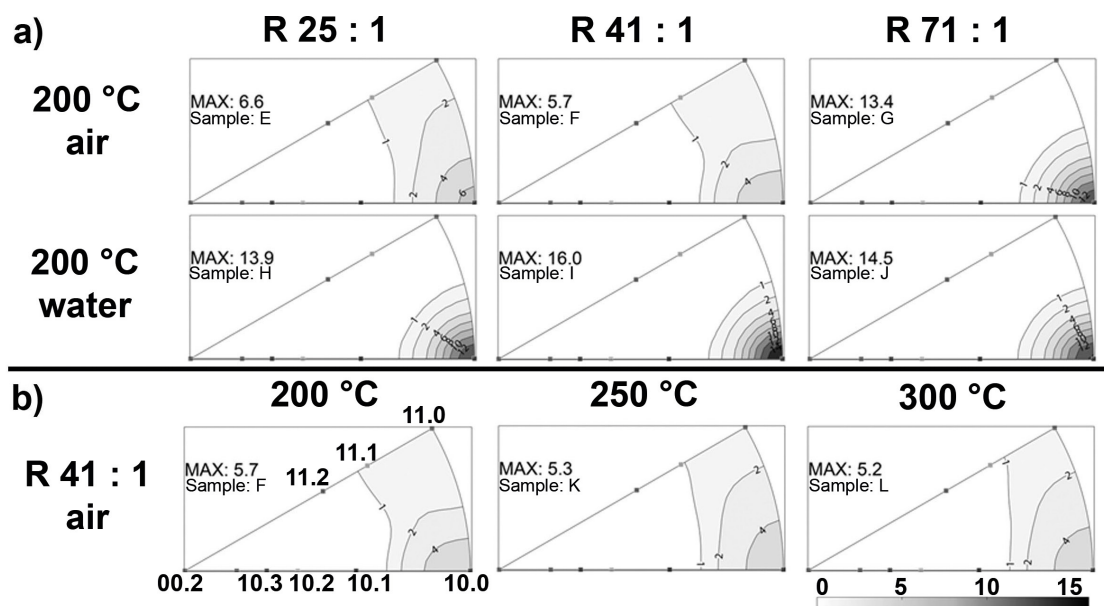


Fig 5.50: IPFs showing the effect of extrusion parameters on the texture development (II ED). a) Effect of R and the cooling conditions, b) effect of the T_B using a constant R 41 : 1 and air cooling. [Len15a].

5.3.3 Mechanical properties

The above described changes of the d_g influence the mechanical properties, which will be investigated using the macroscopic flow curves, the microstructural and texture development during deformation and EPSC simulations.

5.3.3.1 Flow curves

Fig 5.51 presents the flow curves of the extruded bars, the CYS, TYS and SDE of the samples are given in Table 5.12. Interestingly, in all tested samples - independent of d_g or texture effects - the CYS is slightly, but consistently, higher than the TYS and hence the SDE is small and positive. Although not pronounced, the finding of a positive SDE is a remarkable result as most conventional alloys exhibit a much more pronounced negative SDE, where the CYS is significantly lower than the TYS [Hup10a, Hup10b]. Apart from this particularity the extrusions feature typical flow curves, where the compression flow curve exhibits a pro-

nounced sigmoidal shape, while the tension flow curves do not display any signs of important twinning activity. As might be expected from above shown microstructure and texture, the grain refinement is the dominant microstructural parameter influencing the strength of the alloy (Table 5.12).

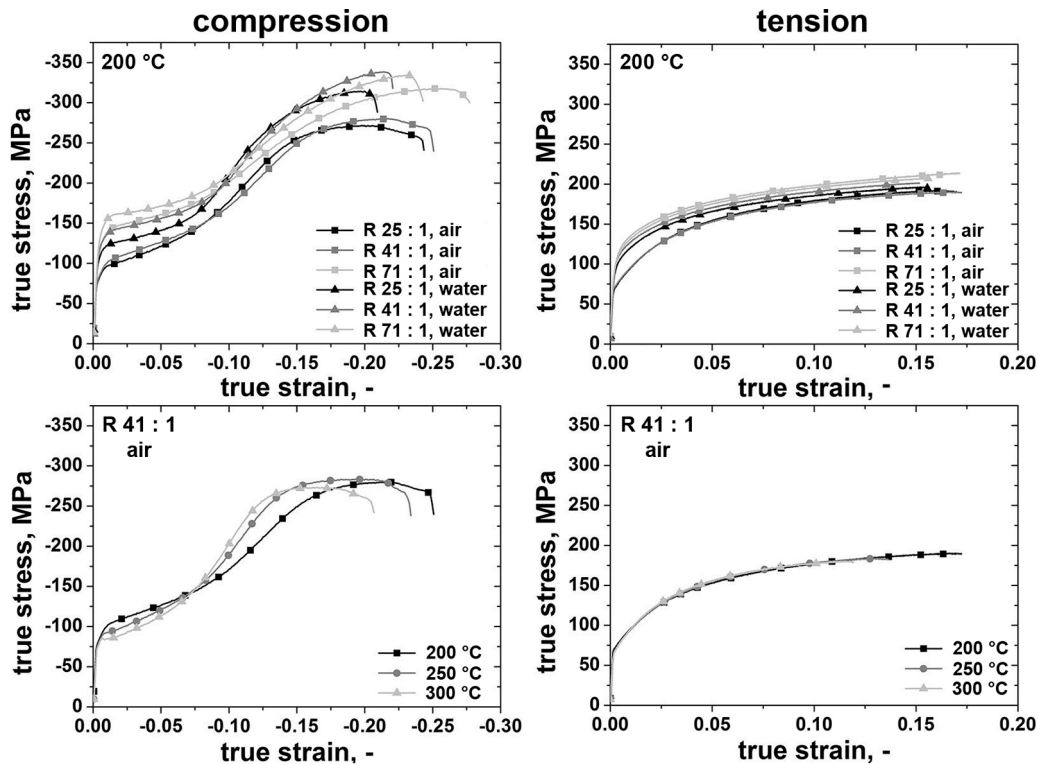


Fig 5.51: Flow curves of the extruded bars tested in uniaxial compression and tension [Len15a].

Table 5.12: Tension compression yield asymmetry specified by the CYS, TYS and SDE of the extruded bars. The error of CYS and TYS is below 5MPa [Len15a].

T _B , cooling	L4								
	R 25 : 1			R 41 : 1			R 71 : 1		
	CYS, MPa	TYS, MPa	SDE, -	CYS, MPa	TYS, MPa	SDE, -	CYS, MPa	TYS, MPa	SDE, -
200 °C air	-81	76	0.06	-83	77	0.08	-123	114	0.08
200 °C water	-108	103	0.05	-120	114	0.05	-137	130	0.05
250 °C air	-	-	-	-80	74	0.08	-	-	-
300 °C air	-77	72	0.07	-79	73	0.08	-	-	-

In order to analyze the underlying deformation mechanism causing the flow curves, the deformed microstructure was analyzed using EBSD and TEM.

5.3.3.2 Deformed microstructure

Fig 5.52 shows the EBSD orientation maps, BC maps highlighting the twin boundaries, and IPFs corresponding to strains of $\epsilon_e = -5\%$, $\epsilon_e = -10\%$, $\epsilon_e = -12\%$, and $\epsilon_e = -18\%$ strain (extrusion A). At $\epsilon_e = -5\%$ the maps reveal a very high activity of TTW-ing. TTW-ing takes place in almost every grain and reorients the grains of the initial fiber texture by $\approx 86^\circ$ to the $\langle 0002 \rangle$ pole. However, twin growth varies depending on the orientation of the parent grain. A primary TTW volume fraction of $\approx 33\%$ was determined.

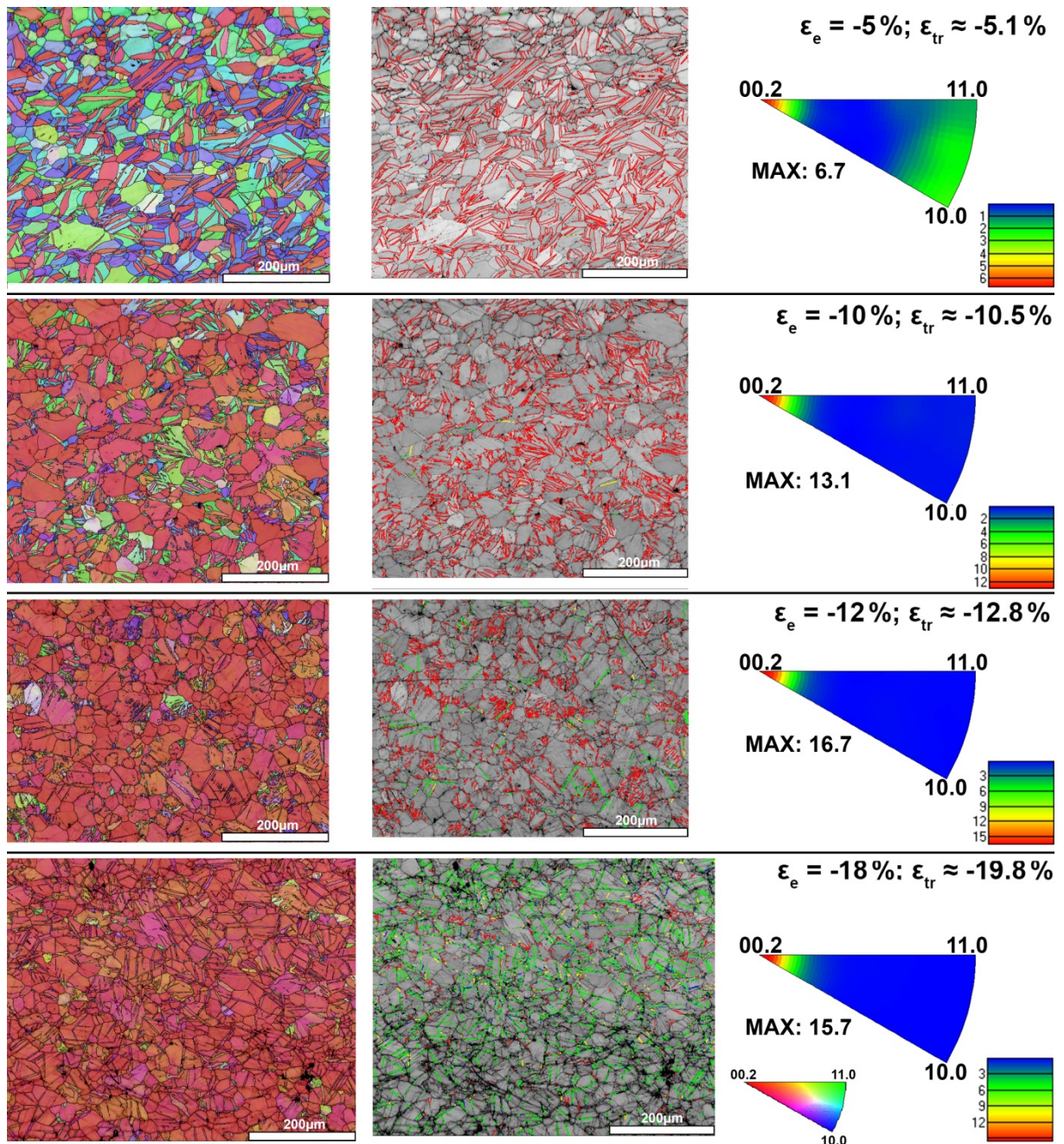


Fig 5.52: Sequential activation of TTW-ing, CTW-ing and DTW-ing represented by EBSD maps and BC maps highlighting twin boundaries ($86^\circ \langle 11\bar{2}0 \rangle = \text{red}$, $56^\circ \langle 11\bar{2}0 \rangle = \text{yellow}$, $38^\circ \langle 11\bar{2}0 \rangle = \text{green}$, $30^\circ \langle 11\bar{2}0 \rangle = \text{blue}$) and IPFs (load direction = ED) [Len14a].

At $\epsilon_e = -10\%$ strain, TTW-ing has overtaken the majority of the grains causing a pronounced $\langle 0002 \rangle$ texture component (TTW volume fraction $\approx 70\%$). Consequently, TTW-ing is almost exhausted, although the grains are not entirely overtaken by primary TTW-ing as is evident by the high amount of TTW boundaries in the BC map. Here, most grains are aligned with their c-axis parallel to the load and hence load is now applied parallel to the c-axis enabling the activation of secondary CTW-ing. Consequently, secondary CTWs and tertiary type 1 DTWs were observed, occasionally, in addition to the TTW boundaries. At $\epsilon_e = -12\%$, TTW-ing has overtaken the majority of the grains completely causing an increased TTW volume fraction of $\approx 83\%$. Nevertheless, some remainders of the parent grains are visible. While the amount of secondary CTW-ing did not increase significantly, the number of type 1 DTWs has increased in comparison to the $\epsilon_e = -10\%$ compressed sample.

At $\epsilon_e = -18\%$ strain, the microstructure is dominated by type 1 DTW boundaries, although type 2 DTWs were observed occasionally. Nevertheless, the volume fraction of the DTWs is too low to introduce significant changes of the texture and hence the volume fraction of the DTWs and the CTWs was not determined. Residuals of primary TTWs and secondary CTWs were sporadically observed. As primary TTW-ing is largely exhausted the TTW volume fraction does not increase significantly ($\approx 86\%$).

To evaluate the variants associated with these twins the MDFs were extracted from these EBSD maps (Fig 5.53). The MDFs enable a more accurate quantitative description of the twin boundaries. The insets illustrate the distribution of the rotation axes for the misorientations characteristic of TTW, CTW and DTW boundaries.

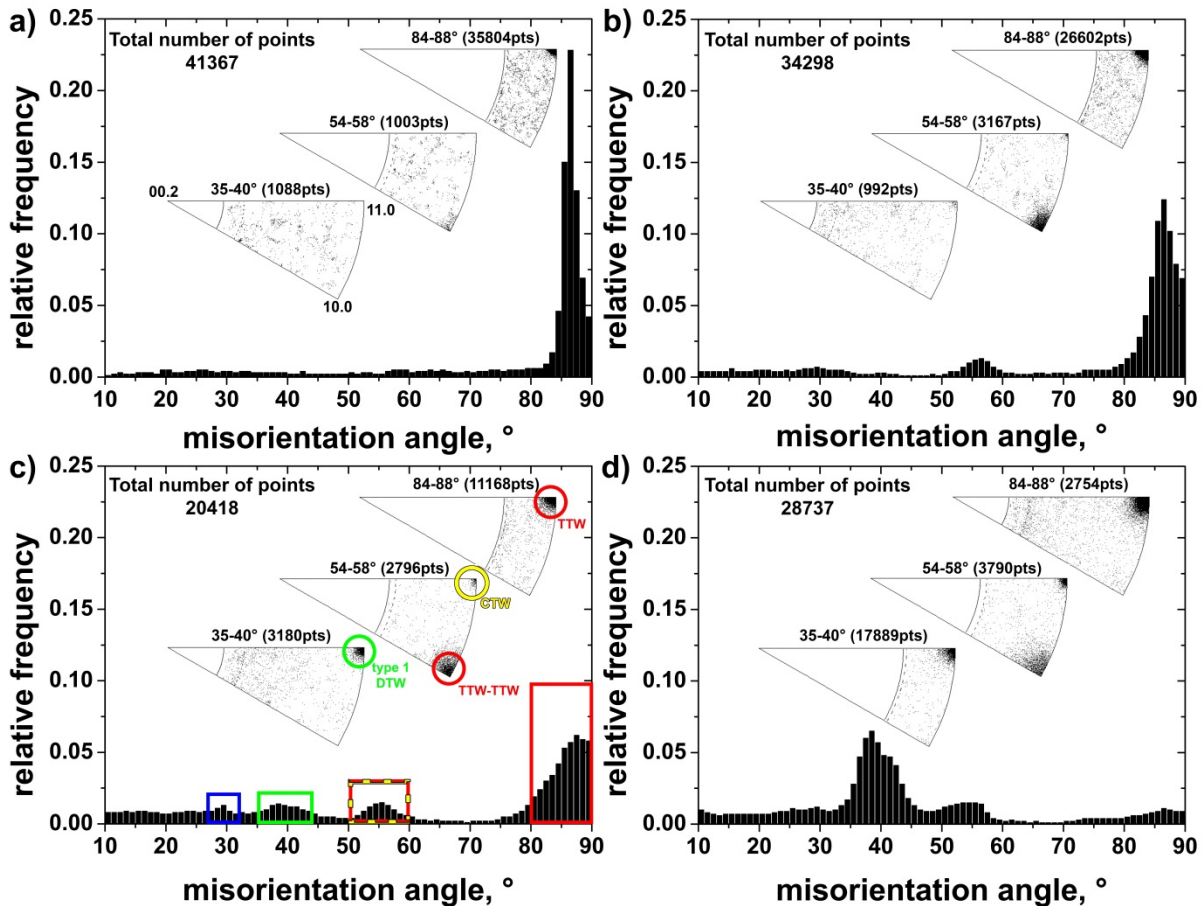


Fig 5.53: MDFs: a) strain (ϵ) = -5 %, b) $\epsilon = -10\%$, c) $\epsilon = -12\%$, d) $\epsilon = -18\%$ (extrusion A). Insets show the distribution of the rotation axis for characteristic angular ranges. $86^\circ \langle 11\bar{2}0 \rangle = \text{red}$, $56^\circ \langle 11\bar{2}0 \rangle = \text{yellow}$, $38^\circ \langle 11\bar{2}0 \rangle = \text{green}$, $30^\circ \langle 11\bar{2}0 \rangle = \text{blue}$ [Len14a].

At $\epsilon_e = -5\%$, the most frequently observed high angle boundaries are TTWs with a misorientation of $\approx 86^\circ$ about the $\langle 11\bar{2}0 \rangle$ axis. Hence, the twins are predominantly primary TTWs. At $\epsilon_e = -10\%$ strain the relative frequency of TTW boundaries has decreased, while a local maximum in misorientation occurs in the angular range of $50^\circ - 60^\circ$. Within this angular rotation range, the $\langle 10\bar{1}0 \rangle$ rotation axis is dominant and the $\langle 11\bar{2}0 \rangle$ rotation axis less frequent. The former angle-axis pair corresponds to TTW-TTW boundaries, which form when two distinct TTW variants intersect [Nav04, Mu12], while the latter corresponds to a secondary CTW. These results suggest that at $\epsilon_e = -10\%$, the TTWs have grown and coalesced. In addition first CTWs have formed. At $\epsilon_e = -12\%$ strain the relative frequency of TTW boundaries is significantly lower. At the same time a small increase in the relative frequencies within the angular range of $35^\circ - 40^\circ$ was observed. Within this range, the

$\langle 11\bar{2}0 \rangle$ rotation axis is most frequent corresponding to the type 1 DTW variant. This finding marks the onset of DTW-ing. Within the angular range from 50° - 60° no significant changes were observed, and hence, the number of CTW boundaries did not change significantly. At $\epsilon_e = -18\%$ strain, the amount of type 1 DTW boundaries has multiplied four-fold, while the relative frequencies of TTW, TTW-TTW and CTW boundaries did not change significantly. In addition, the frequencies of the other DTW variants 2 ($\approx 30.1^\circ$), 3 ($\approx 66.5^\circ$) and 4 ($\approx 69.9^\circ$) are negligible, which is a strong indication of a type 1 DTW-ing predominance. In summary, the sequential activation of primary TTW-ing, secondary CTW-ing and tertiary DTW-ing has been observed according to Fig 2.6 and Fig 2.7.

As mentioned in section 2.1.4, the predominance of the type 1 DTW variant has been reported in prior studies on other Mg alloys [Bar04, Mar10]. Many explanations for this strong preference have been proposed but to date the underlying mechanism has yet to be clarified. Insight can be gained by evaluating the CTW-DTW transition in detail via in-situ EBSD and TEM investigations. In-situ EBSD experiments using a compression test device were conducted to monitor the CTW-DTW transition, locally. A sample was pre-deformed to $\epsilon_e \approx -17.5\%$ strain prior to the in-situ experiment to generate a secondary CTW, which is in the process of a CTW-DTW transition. Using a $150 \times 150 \mu\text{m}^2$ overview scan on the longitudinal section, areas containing the CTW-DTW transition were detected. Subsequently, the sample was compressed in -1% strain steps using the compression test device within the SEM and displacement control in order to observe the progression of the CTW-DTW transition.

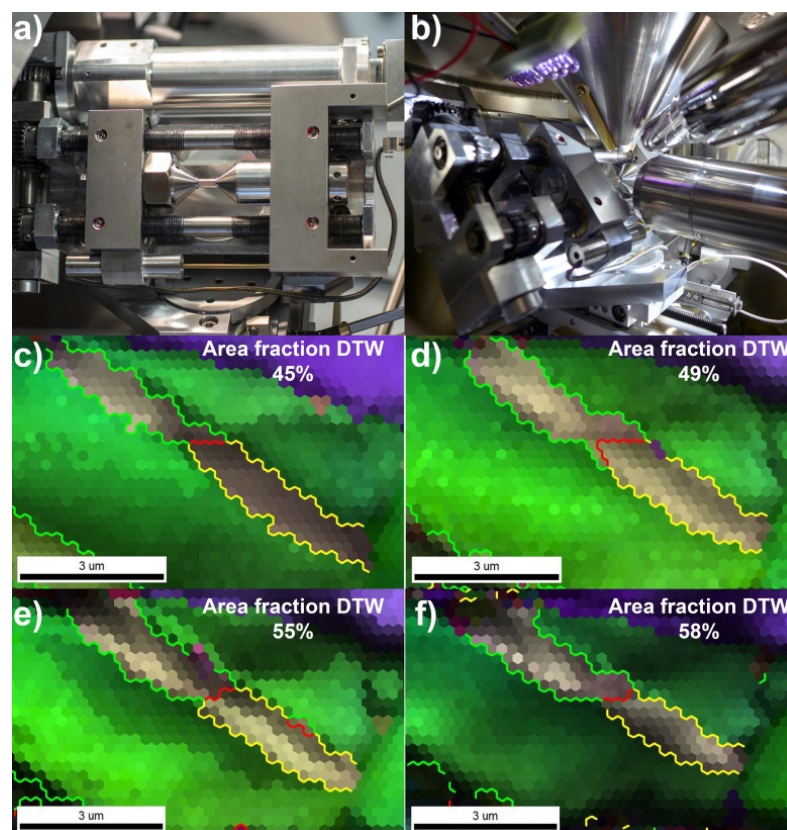


Fig 5.54: a, b) experimental setup of the in-situ EBSD analysis; c-f) CTW-DTW transition. c) $\epsilon = -17.5\%$, d) $\epsilon = -18.5\%$, e) $\epsilon = -19.5\%$, f) $\epsilon = -20.5\%$. Boundary colorcoding: TTW = red, CTW = yellow, DTW = green. [Len14a].

Fig 5.54 depicts the CTW-DTW transition using EBSD maps highlighting the twin boundaries. The DTW propagation is tracked through the movement of a tertiary TTW boundary within a preexisting CTW. Here, a type 1 DTW has already formed within a secondary CTW. The growth of the type 1 DTW is observed by the movement of the internal TTW boundary

through the CTW in Fig 5.54 c) - f). The ongoing transition manifests through the increasing area fraction of the DTW from 45 % to 58 %. During loading no significant thickening of the secondary CTW was observed. To the author's knowledge this is the first time that an ongoing CTW-DTW transition has been visualized dynamically indicating a higher mobility of the internal TTW boundary compared to the preexisting CTW boundary. Thereby, the conducted in-situ experiment confirms the suggestions of a high lateral growth rate of the internal twin by Cizek et al. [Ciz08] and Barnett et al. [Bar08a]. Here, it should be noted that the stress-state changes from the bulk material (triaxial) to the surface (biaxial), causing a deceleration of twin propagation and the CTW-DTW transition.

To analyze the mechanisms involved in the CTW-DTW transition, post-mortem TEM investigations (Fig 5.55) were carried out to examine the local microstructure as well as the slip activity in the vicinity of a DTW. This analysis relies on the identification of a CTW-DTW transition and the determination of the orientation matrices of the primary TTW, the secondary CTW and the tertiary DTW, which were determined using two independent techniques:

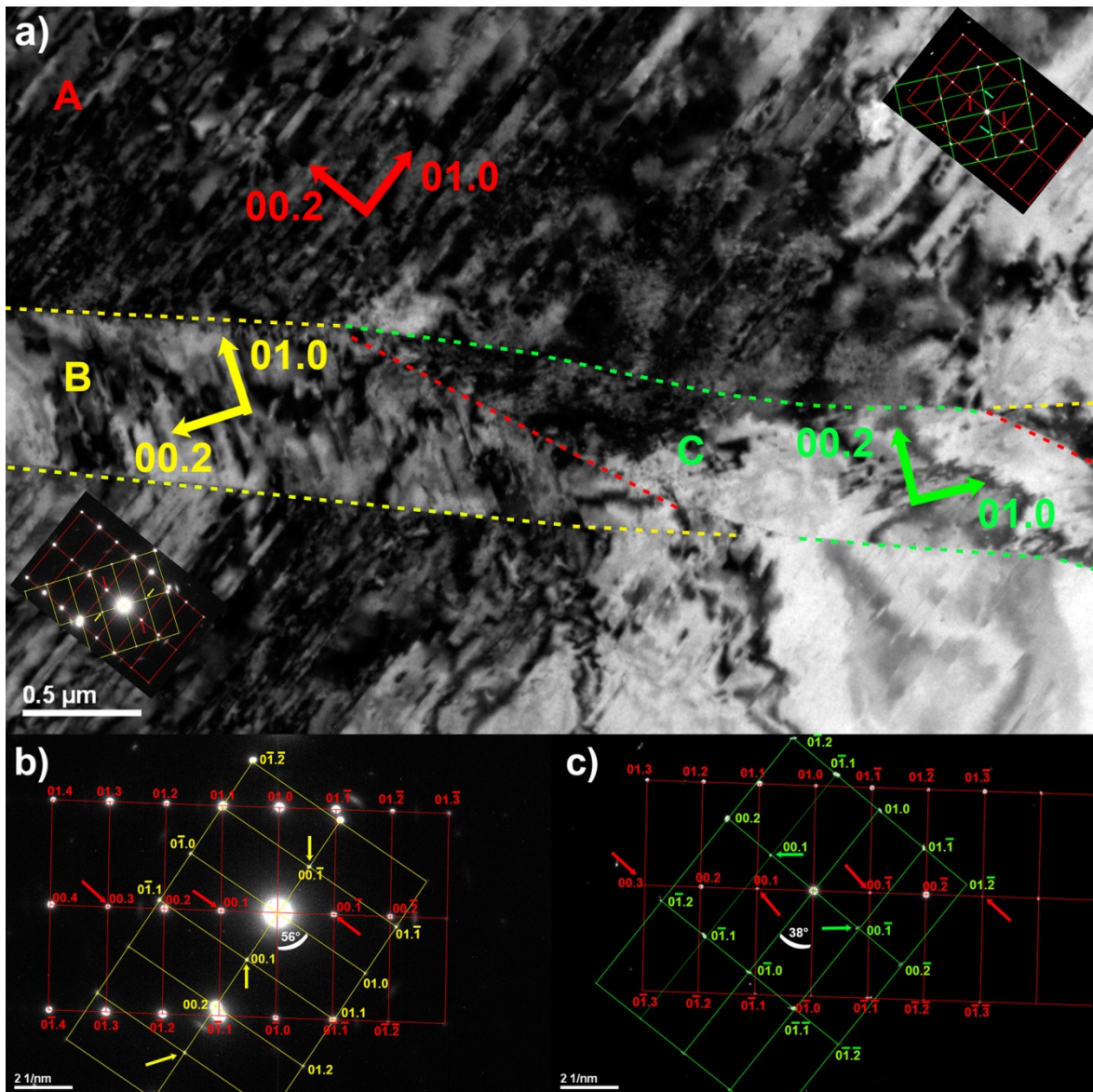


Fig 5.55: a) Bright field image at the $[2\bar{1}\bar{1}0]$ ZA showing a primary TTW (A, red) and the transition from secondary CTW (B, yellow) to a tertiary type 1 DTW (C, green). The indexed Laue patterns b) and c) are shown in their correct orientation relative to the crystal in the insets. b) SAD of the TTW (red) and the CTW (yellow), c) SAD of the CTW (yellow) and the DTW (green). Boundary colorcoding: TTW = red, CTW = yellow, DTW = green. ($\epsilon = -18\%$) [Len14a].

As type 1 and type 2 DTWs share the same $\langle 11\bar{2}0 \rangle$ ZA with the preexisting CTW (cf. Fig 2.8), their misorientation relation can be directly determined evaluating the rotation of the Laue patterns recorded by SAD selecting a $\langle 11\bar{2}0 \rangle$ ZA (Fig 5.55 b) and c)). In contrast type 3 and type 4 DTWs have ZAs that do not lie in the basal plane of the preexisting CTW (cf. Fig 2.8) complicating the analysis of the Laue pattern. Therefore, a second general applicable technique was applied, additionally: The evaluation of Kikuchi patterns using the TOCA software [Zae00]. This software enables the determination of the orientation matrix through indexing the Kikuchi patterns (analogous to EBSD) allowing the identification of the orientation matrix at any crystal orientation that provides sufficient Kikuchi bands (e.g. any ZA). In addition, the TOCA software allows calculating line directions in the image plane as well as the cross product of these line directions and the beam direction. Using the cross product the twin plane can be calculated when the twin planes are edge-on. In this case the Burgers vectors of the observed twin systems are lying in the image plane and the line directions along the twin planes are parallel to these Burgers vectors.

Fig 5.55 exhibits a TEM bright field image of a $\epsilon_e = -18\%$ compressed sample, containing three different crystallographic domains. Each of the domains contains a characteristic pattern of straight parallel lines. The direction of the incident beam is parallel to the $[2\bar{1}\bar{1}0]$ ZA and hence, the twin planes and the basal glide plane (0001) of type 1 or type 2 DTWs are simultaneously in the edge-on position.

Fig 5.55 b) displays the orientation relation between the domains A and B, while Fig 5.55 c) reveals the orientation relation between the domains A and C. The interface between A and B exhibits a misorientation angle of $\approx 56^\circ$ about the $[2\bar{1}\bar{1}0]$ ZA. The yellow $(0\bar{1}\bar{1}\bar{1})$ spot coincides with the red $(01\bar{1}1)$ spot specifying the twin plane $\pm (01\bar{1}1)$. Consequently, this interface is a CTW boundary. The red and the green diffraction patterns do not contain common diffraction spots. Therefore, the interface between the domains A and C is incoherent. The misorientation angle between the two diffraction pattern is $\approx 38^\circ$ about the $[2\bar{1}\bar{1}0]$ ZA and hence, corresponds to a type 1 DTW. Here, it is important to mention that the Laue pattern contain $0002n+1$ reflections ($n = 0, \pm 1, \dots$) that do not correspond to the hcp diffraction pattern (marked with arrows). Interestingly, the Laue pattern of each domain contained these forbidden reflections.

The misorientation relations were established more precisely using the TOCA software to calculate the orientation matrices of the areas A, B and C. The orientation matrices of A and B reveal that the yellow marked interface is $(01\bar{1}1)[0\bar{1}\bar{1}2]$, a CTW. Analogous evaluation of the domains A and C identified the red marked interface as a $(01\bar{1}2)[0\bar{1}\bar{1}1]$ TTW. However, the interface between the domains A and C was identified as a $\approx (01\bar{1}\bar{5})$ plane and therefore, does not correspond to a common twin mode. Based on the determined orientation matrices of the three twins the local coordinate systems were plotted into Fig 5.55 a) showing that the straight parallel lines are aligned perpendicular to the basal plane normals of each twin.

In order to examine the possible mechanisms of strain accommodation at the different boundaries of the observed twins, HR-TEM investigations were conducted. All images were recorded using the common $[2\bar{1}\bar{1}0]$ ZA of the primary TTW, the secondary CTW and the tertiary type 1 DTW. HR-TEM images of the interfaces between the three twins are displayed in Fig 5.56 (TTW-CTW: Fig 5.56 a); CTW-DTW: Fig 5.56b); primary TTW-DTW: Fig 5.56 c) and d)). Here, the characteristic angle-axis relations of the twin modes are directly observed through the selected ZA and the misorientation angles between the basal planes in the ad-

joining domains. Fig 5.56 c) and d) exhibit the characteristic type 1 DTW misorientation angle of $\approx 38^\circ$ about the common $[2\bar{1}10]$ ZA, which is created by tertiary TTW-ing within the secondary CTW. As a consequence, the interface between the primary TTW and the tertiary DTW does not correspond to a common Mg twin plane ($\{10\bar{1}2\}\langle 10\bar{1}\bar{1}\rangle$, $\{10\bar{1}1\}\langle 10\bar{1}\bar{2}\rangle$, $\{10\bar{1}3\}\langle 30\bar{3}\bar{2}\rangle$), although the sequential activation of CTW-ing and internal TTW-ing creates a characteristic angle-axis pair. As a result very thin residual CTWs separate the tertiary DTW and the primary TTW at the atomic scale. Apparently, there is no direct connection between the primary TTW and the DTW.

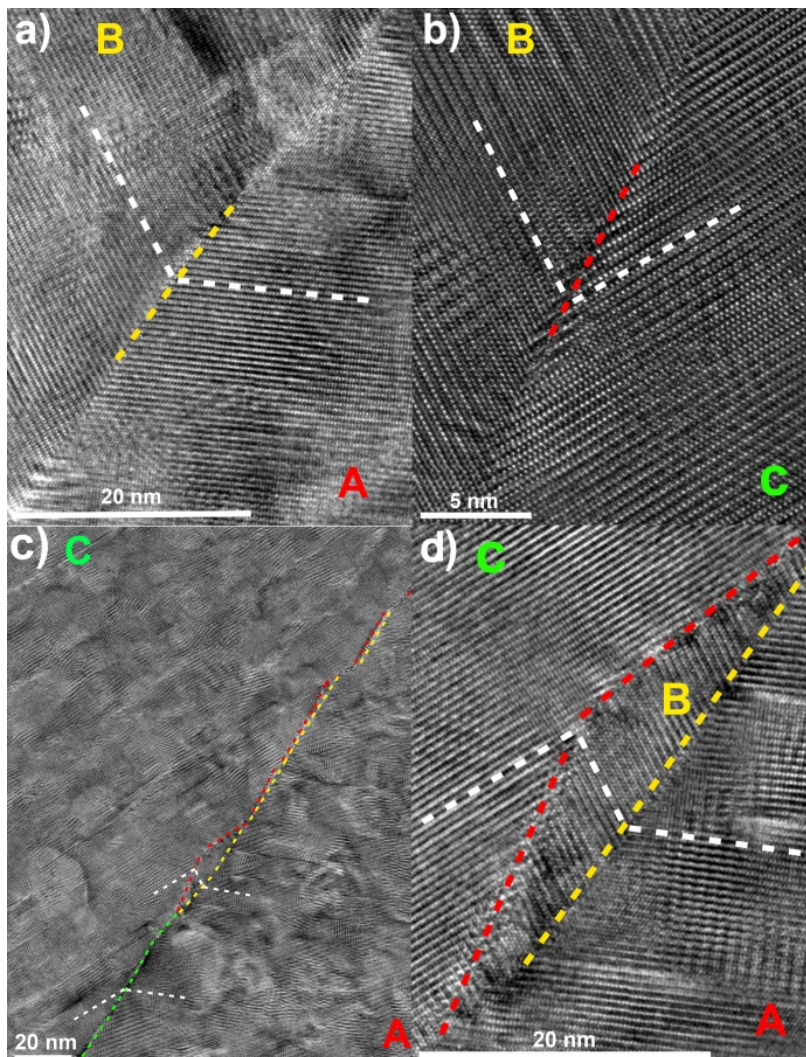


Fig 5.56: HR-TEM analysis of the a) primary TTW (A) – secondary CTW (B) interface, b) secondary CTW (B) – tertiary DTW interface (C), c) primary TTW – tertiary DTW interface, d) higher magnification of c). The white dashed lines correspond to the basal planes [Len14a].

Fig 5.57 and Fig 5.58 reveal the atomic order and disorder within the vicinity of the TTW-CTW-DTW triple point. Here, the lattice is highly distorted and hence, Fourier filtering was applied using the 0002 and $0\bar{1}10$ spots of the three twinned domains. Thereby, the respective lattice planes appear as straight lines, while all other directions are omitted. Hence, the (0002) and the $(0\bar{1}10)$ planes, which are tilted on edge can be analyzed separately. Fourier filtering was successfully applied, although the separation of the 0002 and the $0\bar{1}10$ spots of the CTW and the DTW is complicated by the $\approx 86^\circ$ rotation, which causes a very small distance between the corresponding spots. Fig 5.57 displays the filtered (0002) planes and Fig 5.58 exhibits the filtered $(0\bar{1}10)$ planes. Both figures contain several dislocations, which are marked with black arrows.

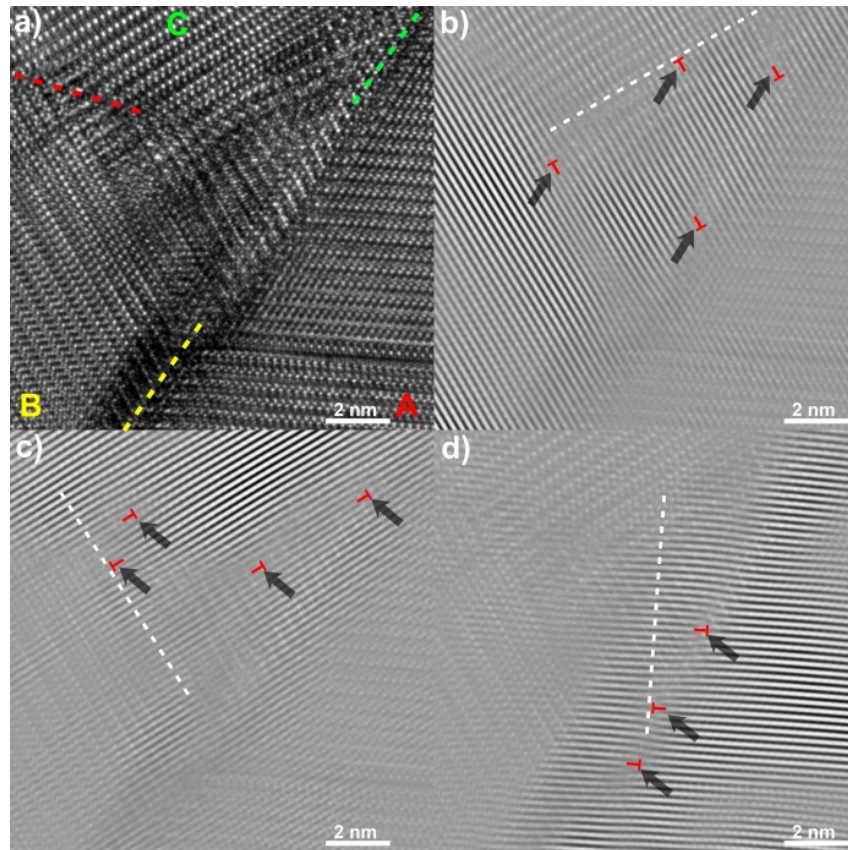


Fig 5.57: HR-TEM and inverted FFT using the 0002 spots: a) HR-TEM, b) (0002) planes of the CTW (B), c) (0002) planes of the DTW (C), d) (0002) planes of the TTW (A). Black arrows mark dislocations. Boundary colorcoding: TTW = red, CTW = yellow, DTW = green. White dashed lines show $(01\bar{1}0)$ planes [Len14a].

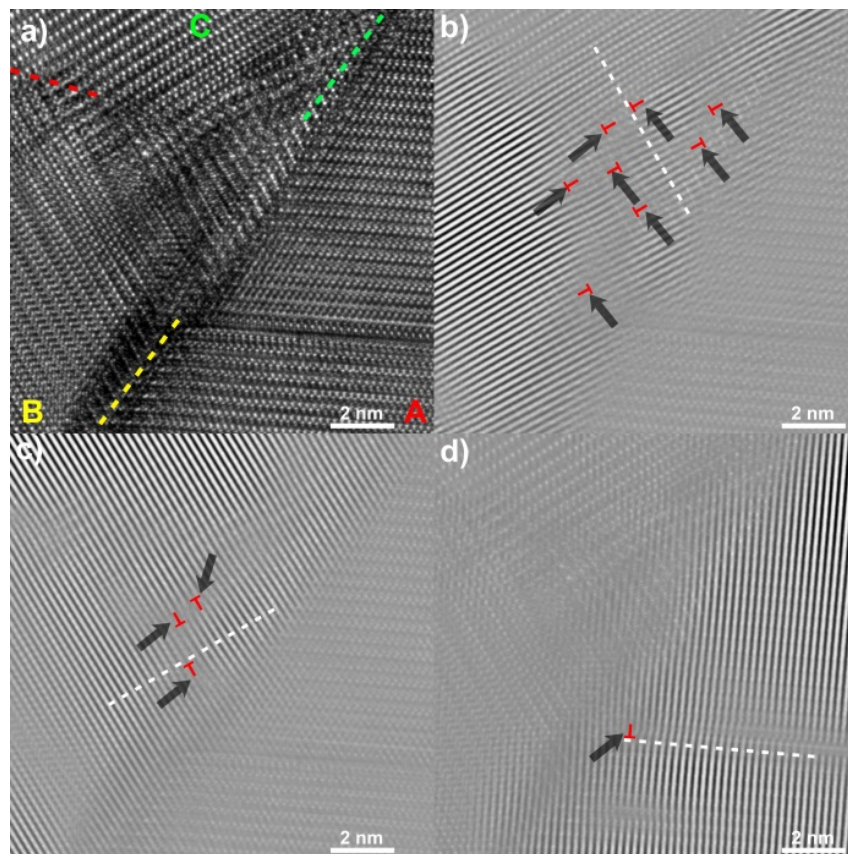


Fig 5.58: HR-TEM and inverted FFT using the $01\bar{1}0$ spots: a) HR-TEM, b) $(01\bar{1}0)$ planes of the CTW (B), c) $(01\bar{1}0)$ planes of the DTW (C), d) $(01\bar{1}0)$ planes of the TTW (A). Black arrows mark dislocations. Boundary colorcoding: TTW = red, CTW = yellow, DTW = green. White dashed lines show (0002) planes [Len14a].

Regarding these dislocations, there are two interesting findings. First, several $\langle 0001 \rangle$ dislocations were observed within the TTW-CTW interface (Fig 5.57 d)) and in the distorted area of the triple point (Fig 5.57 b), c)). Dislocations of this type occur in all twins and were observed within the twin boundaries or their vicinity. Second, Fig 5.58 exhibits many basal dislocations within the different twins with respect to the $(01\bar{1}0)$ planes. These are either projections of $\langle a \rangle$ or $\langle 0\bar{1}10 \rangle$ partial dislocations generated by the dissociation of $\langle a \rangle$ dislocations via the dislocation dissociation $\frac{1}{3}[\bar{1}210] = \frac{1}{3}[0\bar{1}10] + \frac{1}{3}[1\bar{1}00]$ (e.g. [Par67, Pek13]). The majority of the basal dislocations were observed within the $(01\bar{1}0)$ planes of the CTW, while fewer dislocations were detected in the DTW and the TTW lattice. Interestingly, the comparison of Fig 5.58 a) and d) visualizes a basal dislocation within the previously observed line pattern.

Given that the predominantly observed DTW variant (type 1), which is also dominant in the present alloy, has been correlated to the onset of flow localization, void formation and fracture, as the activity of $\langle a \rangle$ basal slip is significantly enhanced within the narrow DTW [Won67, Bar07b, Ciz08], it is important to identify ways to suppress the activation of DTW-ing. Here, grain refinement is a promising approach to minimize the DTW-ing activity as it is known to hinder twinning in many classes of metals (e.g. [Hul61, Lin63, Eco83, Chr95, Mey01, Bar04, Cer07, Bar08b, Jai08]) and is generally applicable. In order to analyze d_g effects on three generations of twins, samples of extrusions A and J were compressed to $\varepsilon_e = -15\%$ and analyzed using EBSD (Fig 5.59). These extrusions feature the largest available spread of the average d_g , while the textures only differ mildly in intensity. This enables the analysis of d_g effects, decoupled from strain, strain rate, and texture effects.

As can be seen by the red color (Fig 5.59 a) and b)), the analysis indicates that almost all parent grains are entirely overtaken by TTWs in case of the CG sample (extrusion A). Here, it should be noted that the parent grains are overtaken by one primary TTW variant causing equivalent d_g of the parent and the TTW. In contrast the FG sample (extrusion J) contains several grains that have not been overtaken by TTW-ing completely or have not twinned at all. The volume fraction of the primary TTWs was determined from the EBSD data by evaluating the fiber volume of the $\langle 0002 \rangle$ texture component. Therefore, the interval $\psi = 60^\circ - 90^\circ$ and $\varphi = 0^\circ - 360^\circ$, was assigned to primary TTW-ing. The TTW volume fractions are 81 % (CG, extrusion A) and 65 % (FG, extrusion J) and the MDFs computed from the entire maps (Fig 5.59 c) and d)) reveal a higher relative frequency of TTW boundaries ($\approx 86^\circ$) in case of the FG sample. These results are consistent with the previously reported HP effect in TTW-ing [Bar04, Bar08b, Jai08].

Even more importantly, a significantly reduced number of CTWs and DTWs was observed in case of the FG sample. While the CG (Fig 5.59 a)) contains numerous type 1 DTWs and occasional CTWs, the FG sample (Fig 5.59 b)) exhibits a very limited number of DTWs. In this sample, the sum of the CTWs and the DTWs is less than 5 in the entire $248\ \mu\text{m} \times 248\ \mu\text{m}$ map (not shown). This result is supported by the comparison of the corresponding MDFs (Fig 5.59 c) and d)). In case of the CG three maxima were observed. The insets provide a more accurate quantitative description of these maxima through plotting the distribution of the rotation axis distributions. Thereby, the maxima can be correlated to the activity of twin modes (cf. Fig 2.7): Within the angular range from $35^\circ - 40^\circ$ the most frequent rotation axis is $\langle 2\bar{1}\bar{1}0 \rangle$ identifying type 1 DTWs. Within $54^\circ - 58^\circ$ the predominant rotation axes are $\langle 10\bar{1}0 \rangle$ axes and less frequent $\langle 2\bar{1}\bar{1}0 \rangle$ axes. The former mentioned angle-axis pair is generated, when different TTW variants [Nav04, Mu12] intersect, while the latter is characteristic for CTW boundaries. Within misorientation angle range $84^\circ - 86^\circ$, the dominant

rotation axis is $\langle 2\bar{1}\bar{1}0 \rangle$. This angle-axis pair is characteristic for TTW boundaries. Fig 5.59 c) indicates that DTWs are the most frequent high angle grain boundaries in the CG sample, while the number of CTW and DTW boundaries is too low to generate a local maximum in the MDF in case of the FG sample (Fig 5.59 d)). Thereby, it was shown that CTW-ing and DTW-ing can be largely eliminated by reducing the mean d_g from $\approx 30 \mu\text{m}$ to $\approx 5 \mu\text{m}$ in this alloy confirming a pronounced HP effect on these deformation modes.

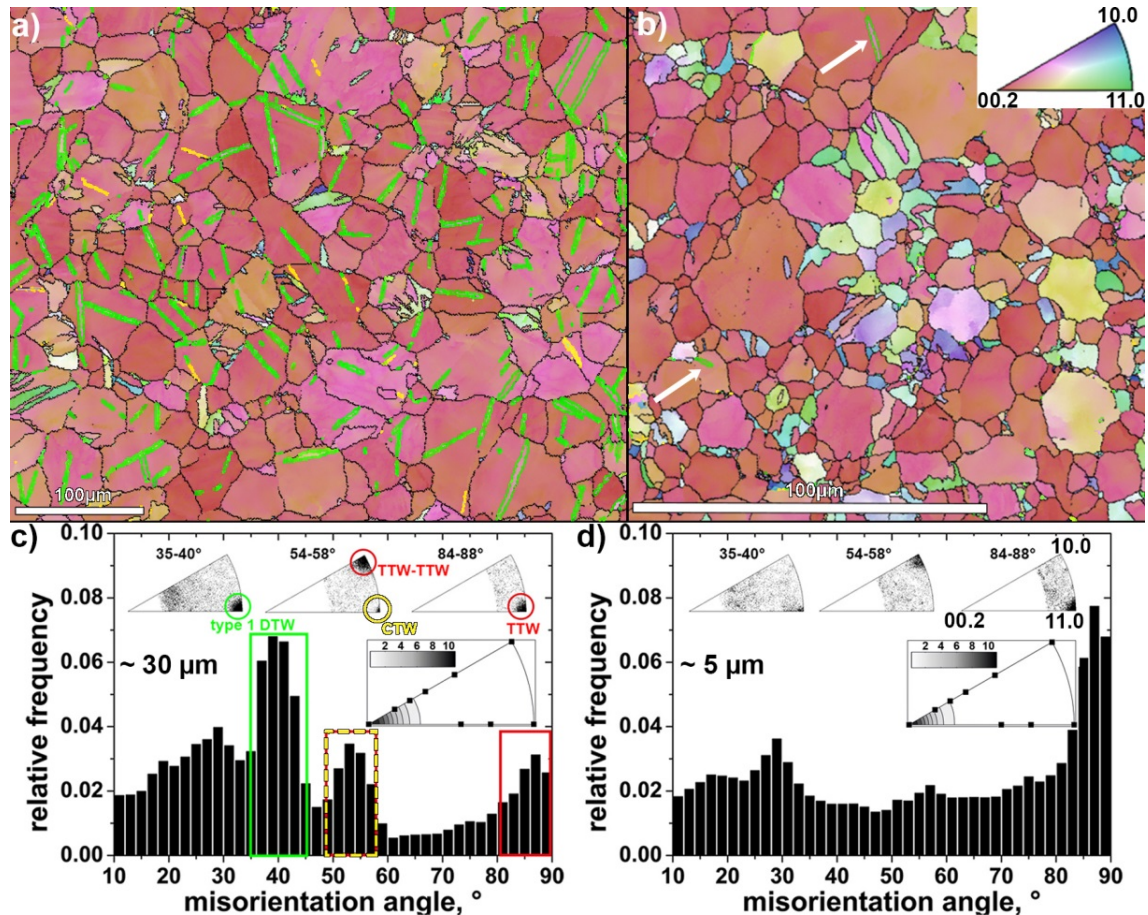


Fig 5.59: a) and b) EBSD maps highlighting CTW (yellow) and type 1 DTW (green); a) extrusion A, b) extrusion J (detail of a $248 \mu\text{m} \times 248 \mu\text{m}$ map). White arrows mark DTWs in the FG samples. c) and d) correlated MDF: c) extrusion A; CG, d) extrusion J; FG. Please note the different scale bars [Len14b].

5.3.3.3 EPSC simulations

To reveal the underlying deformation mechanisms, their individual activation stresses and hardening characteristics of the above describe microstructural development during loading a combination of in-situ EDXRD and EPSC modeling was employed. Flow curves were used to characterize the model material parameters. Fig 5.60 compares the simulated and the measured flow curves. As has been shown in the above section the L4 alloy exhibits complex deformation behavior involving twinning and several slip modes, each hardening and interacting with one another differently. Considering such complexities, and the fact that the simulated flow curves, texture evolutions, and ϵ_{hkl} agree satisfactory with experimental data, the model is considered reliable for interpreting the deformation. The observed discrepancies are most likely related to the limitation of the self-consistent homogenization scheme, which accounts for grain-to-grain interactions only in an average sense without explicit neighboring effects. Here, it should be noted that the tensile ϵ_{hkl} of the FG sample (extrusion J) have not been measured due to the restricted availability of beamtime. Hence, a laboratory tension flow curve was used as reference for the simulation. The corresponding single-set of hardening parameters for the slip and twinning modes are given in Table 5.13 and Table 5.14.

With these parameters, the textures, ε_{hkl} evolution, and relative slip and TTW-ing activity were predicted. Fig 5.61 compares the measured and the simulated textures using of IPFs parallel to the ED (= load direction). Fig 5.62 provides the comparison of the measured and the predicted ε_{hkl} evolution, while Fig 5.64 illustrates the predicted relative deformation mode activities. These data are discussed in turn below.

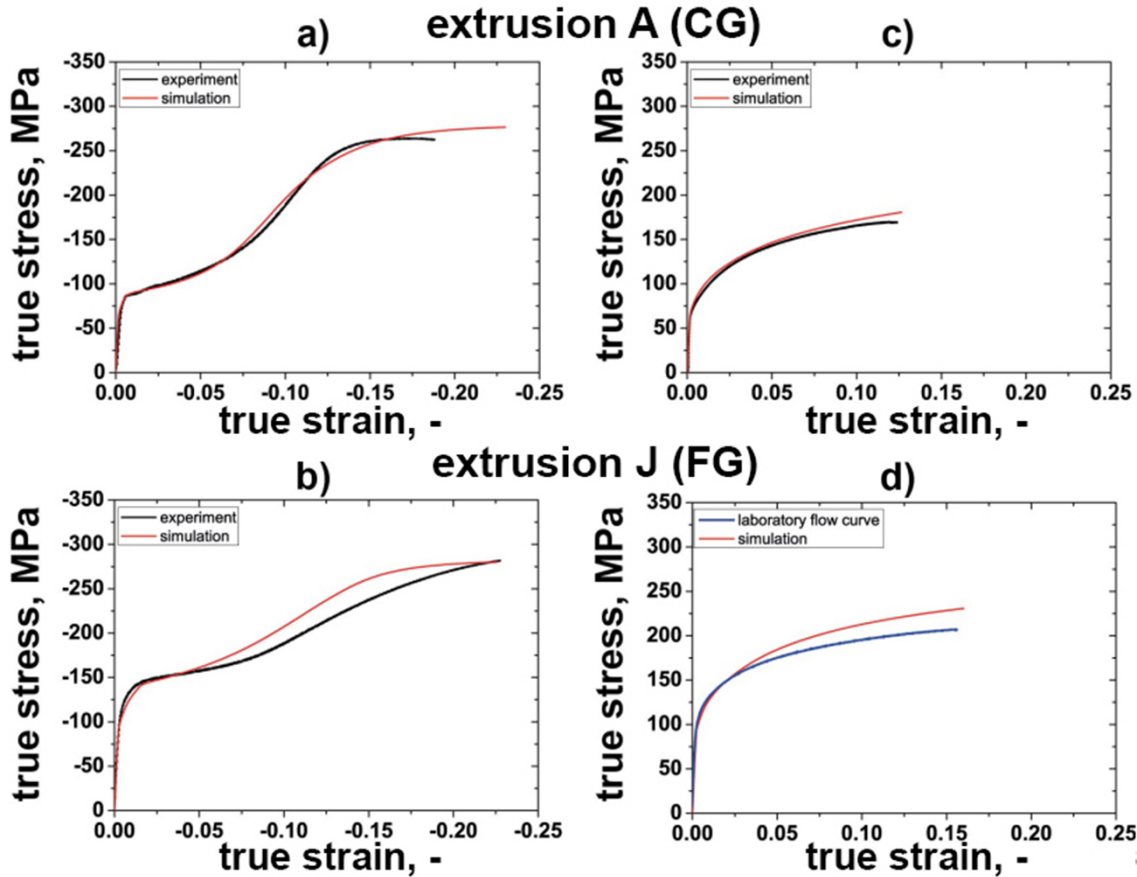


Fig 5.60: Comparison of the experimental and simulated flow curves: a), b) compression, c), d) tension. Lower elongations to failure in tension might be attributed to downscaled samples and sample mounting for in-situ EDXRS experiments [Len15a].

Table 5.13: Hardening parameters for slip systems [Len15a].

Parameter	L4		
	<a> prism	<a> basal	<c+a> pyr
$\tau_{0,f}^s$ (MPa)	14	5	52
k_1^s (m^{-1})	2.5E+08	1.5E+08	5.5E+09
D^s (MPa)	2.5E+03	3.5E+03	3.3E+03
g^s	3.3E-03	3.3E-03	9.0E-03
ρ_0 (m^{-2})	1.5E+12	1.5E+12	1.5E+12
HP^s	160	90	20
C^{st}	50	50	450

Table 5.14: Hardening parameters for TTW-ing [Len15a].

Parameter	L4
τ_0^t (MPa)	25
HP^t	145

As presented in Table 5.13 and Table 5.14, the simulation allowed the characterization of the slip and twin activation stresses and energies separately from d_g effects. Two important findings emerged:

- As shown in Table 5.13, the slip activation stresses $\tau_{0,f}^S$ increase in the order: $\langle a \rangle$ basal $< \langle a \rangle$ prismatic $< \langle c+a \rangle$ pyramidal slip. This order is the same as that observed in other Mg alloys (e.g. [Agn06a, Cla08, Kne10, Bey11b, Opp12]).
- The twin activation stresses τ_0^t for TTW-ing is higher than $\tau_{0,f}^S$ for $\langle a \rangle$ prismatic (Table 5.13 and Table 5.14, Fig 5.63), deviating from the usually observed order for other Mg alloys [Agn06a, Cla08, Kne10, Bey11b, Opp12].

As has been shown in sections 5.3.3.1 and 5.3.3.2 grain refinement significantly increases the yield strength of the samples. To evaluate how each slip mode may have contributed to this d_g effect, the HP coefficients given in Table 5.13, Table 5.14 (cf. Eq. 4.14) were adopted within the conducted simulations. Here, TTW boundaries were not considered as barriers in the simulation, in contrast to grain boundaries. In Mg TTWs propagate very quickly and hence, TTW boundaries are not expected to introduce effective barriers for dislocations [Cap09a, Kne10, Opp12]. The analysis suggests that $\langle a \rangle$ prismatic slip and TTW-ing are more sensitive to grain refinement than $\langle a \rangle$ basal and $\langle c+a \rangle$ pyramidal slip (Table 5.13 and Table 5.14, Fig 5.63). This result is generally consistent with previous reports of higher macroscopic HP coefficients for twinning than for slip in other Mg alloys [Mey01, Bar04, Bar08a]. In particular the enhanced sensitivity of TTW-ing to d_g found for the present alloy indicates that a significant reduction of TTW-ing is expected as d_g decreases, which has been shown indeed using EBSD in section 5.3.3.2 (Fig 5.59).

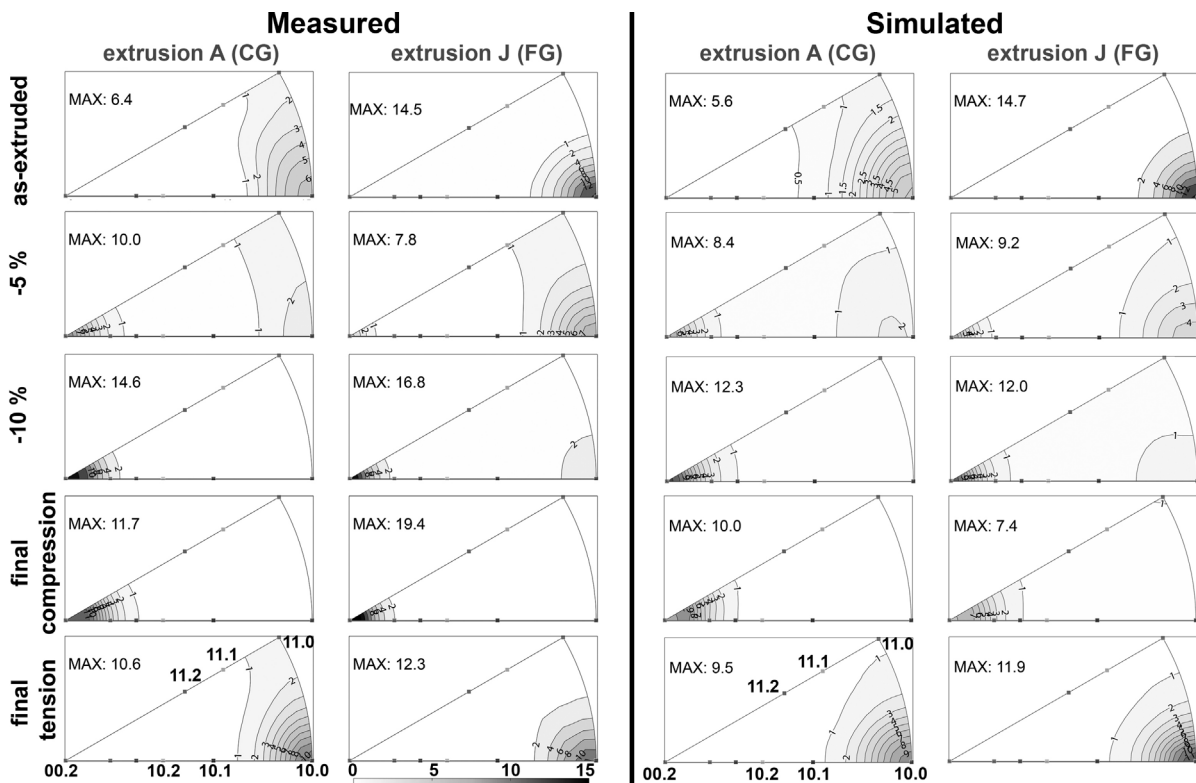


Fig 5.61: Comparison of the measured and simulated texture evolution (IPFs ||ED) [Len15a].

Fig 5.62 compares the measured and the simulated ϵ_{hkl} evolution of the $(10\bar{1}0)$, (0002) , $(10\bar{1}1)$, $(11\bar{2}0)$ and $(20\bar{2}1)$ reflections. Generally, grains, which belong to the $(10\bar{1}1)$ reflection display the lowest ϵ_{hkl} . Such grains feature a high SF for $\langle a \rangle$ basal slip, which is the softest deformation mode in Mg alloys. The reflections $(10\bar{1}0)$, $(11\bar{2}0)$ and $(20\bar{2}1)$ correspond to grains, which exhibit a high SF for $\langle a \rangle$ prismatic slip, and in compression tests, a high SF for TTW-ing and a low SF for $\langle a \rangle$ basal slip. These ϵ_{hkl} are consistently higher than the $(10\bar{1}1)$ ϵ_{hkl} , being in good agreement with previous investigations of other Mg alloys (e.g. [Agn06a,

Cla08, Mur10a, Len13]) and with the present simulations predicting a higher CRSS ($\tau_{o,f}^S$) for <a> prismatic slip and TTW-ing than that for <a> basal slip.

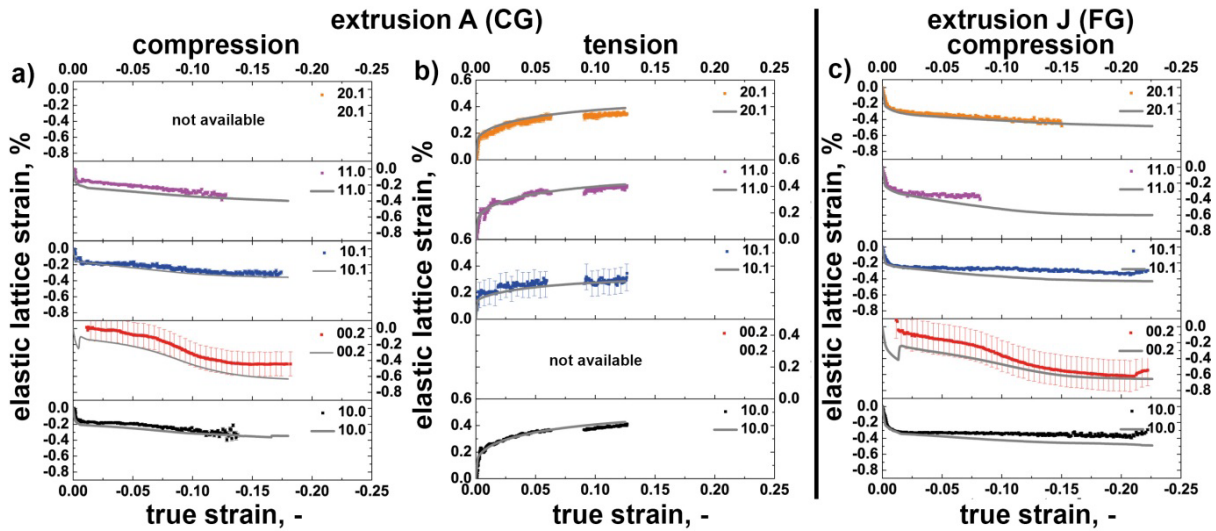


Fig 5.62: Comparison of the experimental ϵ_{hkl} data (colored) and simulation (gray lines) results: a, c) compression and b) tension. Due to texture effects some reflections could not be accurately measured and hence were not evaluated. In this case the label “not available” was added. The tensile ϵ_{hkl} of the FG sample have not been measured due to the restricted availability of beamtime [Len15a].

Overall, the ϵ_{hkl} of grains corresponding to $(10\bar{1}0)$, $(10\bar{1}1)$, $(11\bar{2}0)$ and $(20\bar{2}1)$ reflections increase only slightly during plastic deformation, which means limited hardening of <a> basal and <a> prismatic slip. This finding is captured by the model, as can be seen in Fig 5.63 for the average CRSS evolution during compression tests. Based on the initial texture, the (0002) reflection is not present initially, but generated during compression via TTW-ing. Therefore, the (0002) reflection corresponds to the TTWs and the (0002) ϵ_{hkl} evolution becomes measureable as soon as a sufficient volume fraction of TTWs has formed. The initial absence of the (0002) reflection prevents the determination of E_0^{0002} from the pre-loading diffraction pattern introducing a higher uncertainty in the absolute value of the (0002) ϵ_{hkl} . However, the measurement shows significant hardening of the TTWs, which is associated to the strain accommodation via <c+a> pyramidal slip as will be shown below.

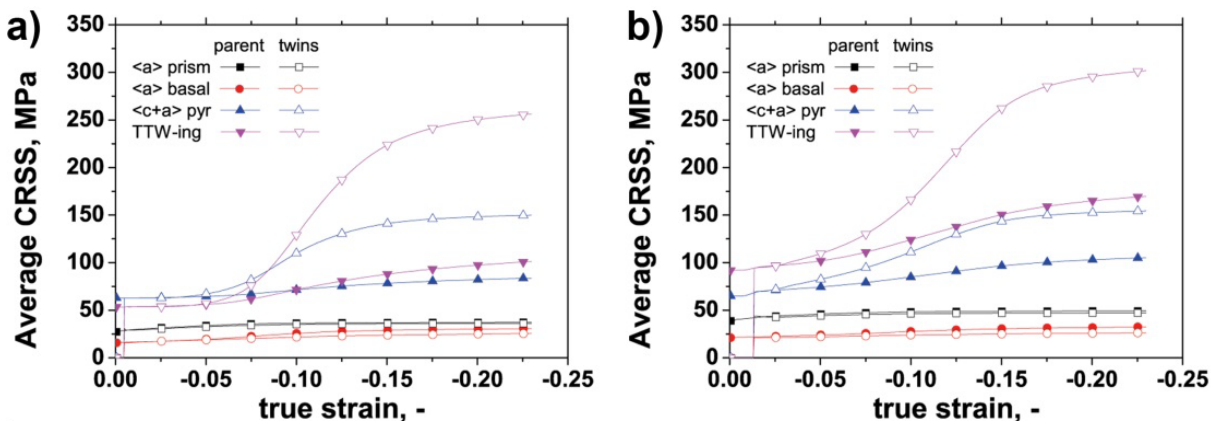


Fig 5.63: Evolution of the average CRSS during compression within the parent grains and the TTWs: a) CG, extrusion A; b) FG, extrusion J.

The c-axis of the generated TTWs are spread about the (compression) load axis, which results in low but non-negligible SFs for the <a> basal and <a> prismatic slip. The EPSC model predicts a high activity of these <a> slip modes during the initial deformation of the TTWs. This finding is supported by the TEM analysis in [Len14a] (Fig 5.55 and Fig 5.58), which provides evidence for extensive basal slip and basal stacking faults within the primary TTWs (as

well as in secondary and tertiary twins)². During the deformation the grains reorient further causing the activation of the hard $\langle c+a \rangle$ pyramidal slip mode. The activation of $\langle c+a \rangle$ pyramidal slip causes pronounced hardening as well as a sigmoidal shape of the (0002) ε_{hkl} . The observed ε_{hkl} evolution and the negligible effect of twin boundaries on the hardening indicate that the sigmoidal shape of the macroscopic flow curve is predominantly generated through the activation of pyramidal $\langle c+a \rangle$ slip within the TTW domains.

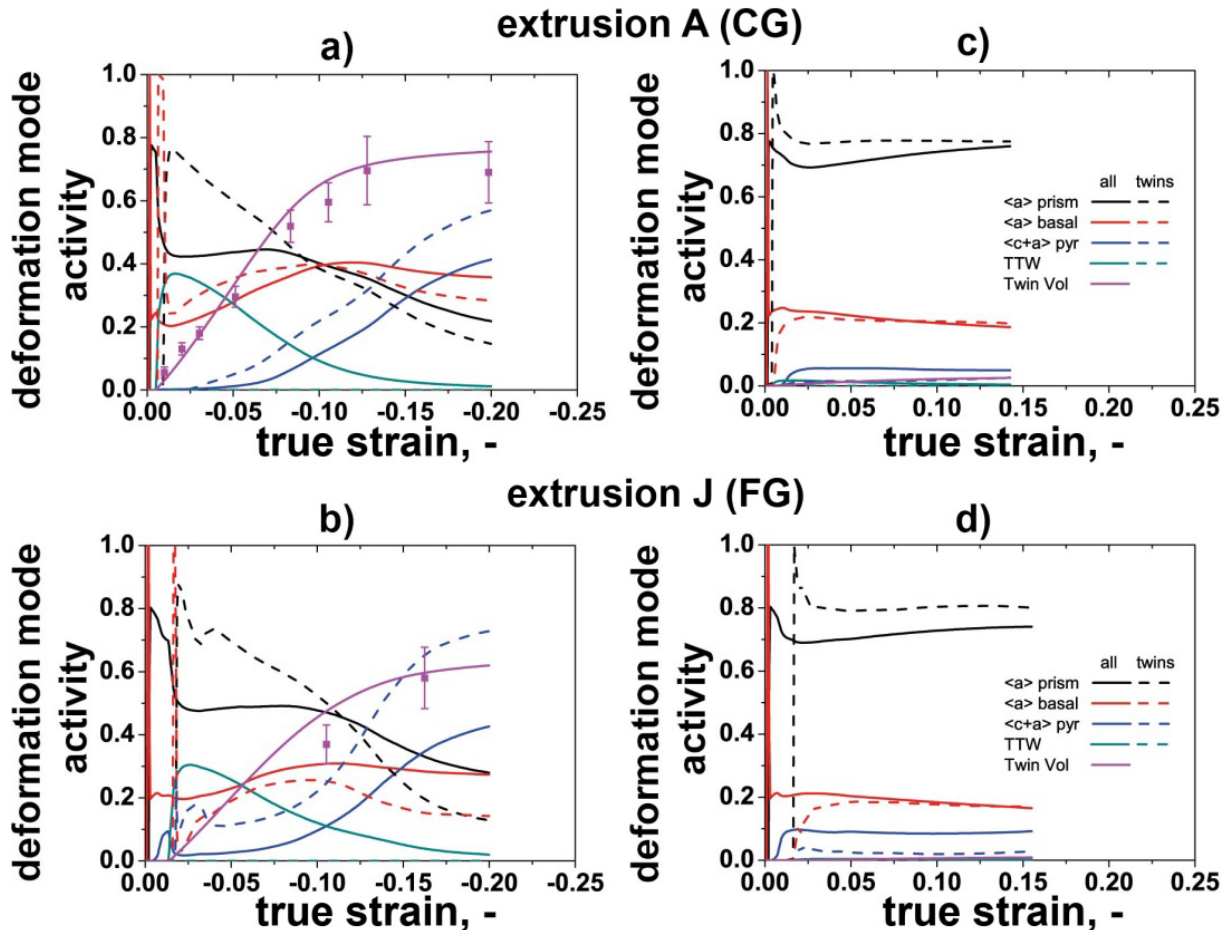


Fig 5.64: Relative activities of the active deformation modes predicted by the EPSC model: a), b) compression, c), d) tension [Len15a].

Fig 5.64 displays the EPSC prediction of the deformation mode activity as a function of the applied strain in: a), b) compression and c), d) tension. The calculations for the compression tests support above described findings. In compression, the model suggests that the initial deformation is realized mainly by $\langle a \rangle$ prismatic slip and TTW-ing and to a minor extent by $\langle a \rangle$ basal slip. As TTW-ing continues to overtake the parent grains the TTW-ing activity decreases. The reorientation generated by TTW-ing and additionally the grain rotation via $\langle a \rangle$ basal slip rotates grains, which results in an alignment of the c -axis with the load direction at strains $> -10\%$ (Fig 5.61). Thereby, an enhanced activity of the hard $\langle c+a \rangle$ pyramidal slip is generated. Fig 5.64 b) displays a significantly reduced TTW volume fraction due to grain refinement. This result is in good agreement with above described EBSD results. The simulations further indicate that the reduced TTW-ing activity is compensated by an increased relative activity of $\langle c+a \rangle$ pyramidal slip. This prediction can be supported through careful examination of the compression flow curve of the FG sample within the vicinity of the CYS. Here, it is observed that yielding occurs before the plateau characteristic of active TTW-ing is reached. This indicates that dislocation slip occurs prior to the activation of TTW-

² This finding will be derived in section 6.4.2.4.

ing. Taken together, these results suggest a more pronounced d_g effect on TTW-ing than on dislocation slip, which has been conjectured for Mg alloys [Bar04, Bar08b]. The EPSC model predictions for the tensile tests in Fig 5.64 c) and d) indicate that tensile deformation is realized mainly via $\langle a \rangle$ prismatic slip with some $\langle a \rangle$ basal slip activity. More significantly, $\langle c+a \rangle$ pyramidal slip is activated in both specimens, confirming previous studies reporting an enhancement of $\langle c+a \rangle$ pyramidal slip in Mg-Li alloys (e.g. [Agn01, Agn02, Als09]).

5.4 LA41

5.4.1 Extrusion billets

Fig 5.65 displays a micrograph of a LA41 cast billet. The grains are larger than in the other alloys, where the d_g is within the range from 300 μm to 1 mm. Like the L4 billets, the LA41 billets featured a relatively large porosity, where the size of the voids was up to several millimeters, as well as (Al-)Si rich precipitates and Mg oxides, which were not expected in this alloy.

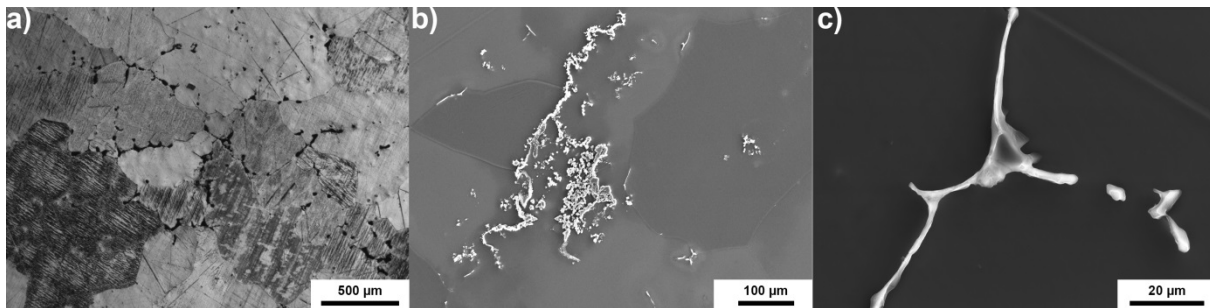


Fig 5.65: Micrograph of a LA41 cast billet: a) grain structure, b) Mg oxide, c) Si-rich phase.

5.4.2 Extrusion products

Within this study five extrusion trials (Table 5.15) were carried out to analyze the effect of T_B , R and the cooling conditions on the microstructure, texture and mechanical properties. In contrast to the L4 alloy, additional trials using $T_B = 200\text{ }^\circ\text{C}$, higher R (41 : 1 or 71 : 1) and water cooling could not be conducted due to the higher strength of this alloy. Here, the required extrusion force would exceed the available capacity of the used extrusion press.

Table 5.15: Summary of the applied extrusion parameters.

Extrusion	T_B , $^\circ\text{C}$	R	Product speed, m/min	Cooling	Peak force, MN
A	200	25 : 1	1.7	air	7.0
B	200	41 : 1	1.7	air	7.7
C	200	25 : 1	1.7	water	8.1
D	250	41 : 1	1.7	air	6.0
E	300	41 : 1	1.7	air	5.0

5.4.2.1 Microstructure and texture

Fig 5.66 displays exemplary micrographs of the LA41 extrusion illustrating the effect of the T_B on the microstructure. The extruded bars exhibit a widely recrystallized microstructure, apart from occasional large grains, elongated parallel to the ED. The influence of the extrusion parameters on the generated average d_g is illustrated in Fig 5.67 and summarized in Table 5.16. In agreement with the above reported results for ME21, WE54 and L4 extrusions, increasing T_B and air cooling result in increased average d_g . Water cooling appears to be most effective in reducing the average d_g of this alloy. Comparing equivalent extrusion parameter sets the LA41 extrusions consistently exhibit smaller average d_g than the L4 alloy indicating a

grain refining effect of the Al addition. The comparison of Fig 5.48 and Fig 5.67 shows that grain growth saturates faster in the L4 alloy than in the LA41 alloy. An increase of the T_B from 250 °C to 300 °C caused an increasing average d_g of the LA41 alloy, while the d_g of the L4 alloy did not show a further increase.

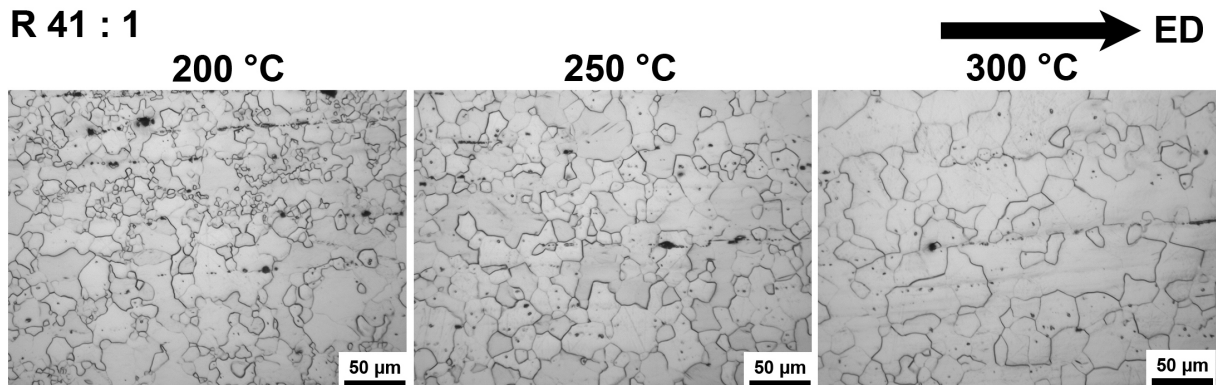


Fig 5.66: Microstructure of extrusions, which were processed using R 41 : 1 and air cooling [Len15a].

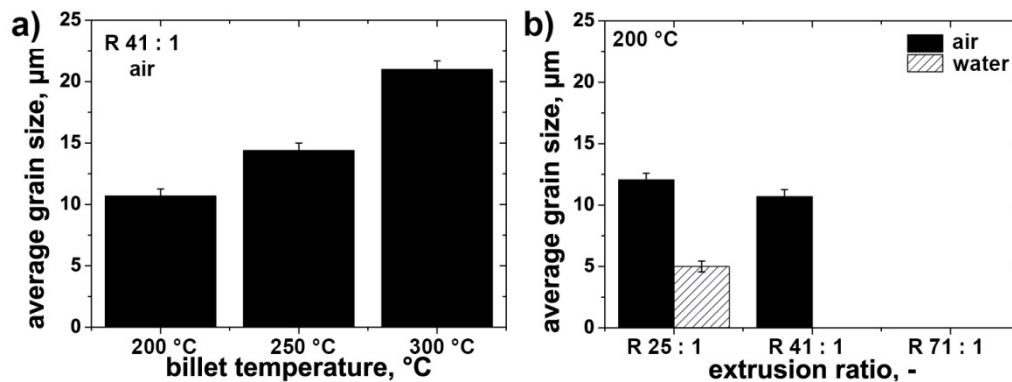


Fig 5.67: Histograms showing the effect of the extrusion parameters on the d_g [Len15a].

Table 5.16: Applied extrusion parameters and resulting average d_g (μm) [Len15a]. The standard deviation of the log-normal distribution is approximately 0.6 μm.

T_B , cooling	LA41	
	R 25 : 1	R 41 : 1
200 °C, air	12	11
200 °C, water	5	-
250 °C, air	-	14
300 °C, air	-	21

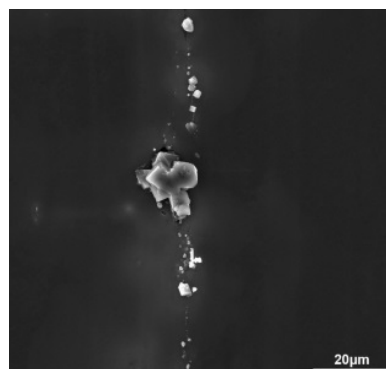


Fig 5.68: SEM images showing (Al-)Si-rich phases (ED↑) [Len15a].

In addition, all extruded bars contained (Al-)Si rich phases, which appear as necklace structures parallel to the ED and were likely introduced during casting. Fig 5.68 displays a typical example of these phases. Using TEM no evidence of finer precipitates was found.

Moreover, the extrusion parameters had some influence on texture development (Fig 5.69). The extrusions feature typical $\langle 10\bar{1}0 \rangle$ or $\langle 10\bar{1}0 \rangle / \langle 11\bar{2}0 \rangle$ extrusion fiber textures, where changing T_B and R introduce only very slight deviations of the maximum intensity, while water cooling sharpens the texture significantly generating a pronounced $\langle 10\bar{1}0 \rangle$ fiber texture.

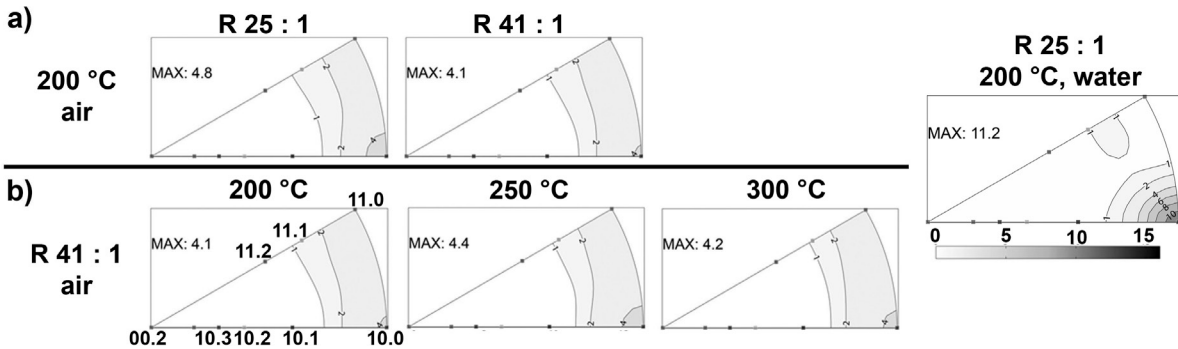


Fig 5.69: IPFs showing the effect of the extrusion parameters on the texture development (\parallel ED): a) Effect of R and the cooling conditions, b) effect of the T_B using a constant R 41 : 1 and air cooling [Len15a].

5.4.3 Mechanical properties

The shown grain refinement influences the mechanical properties, which will be depicted in the following sections using the macroscopic flow curves, the microstructural and texture development during deformation and EPSC simulations.

5.4.3.1 Flow curves

Fig 5.70 displays the flow curves of the extruded bars, the yield strengths and SDE of the samples are given in Table 5.17.

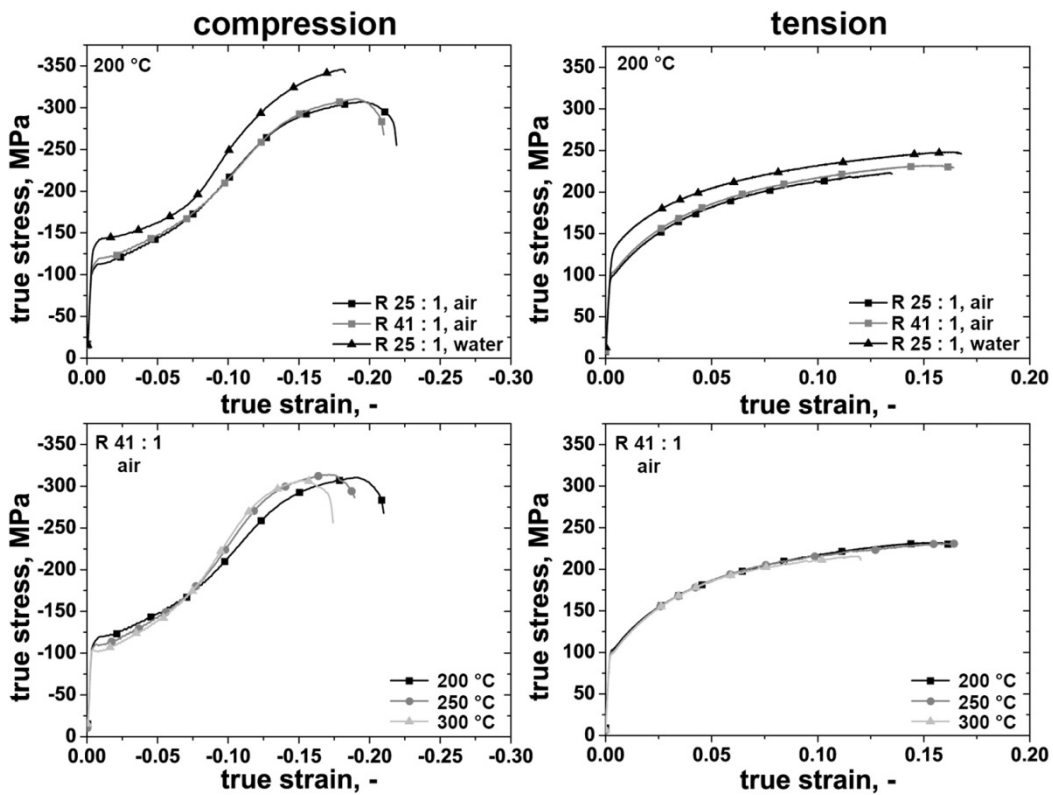


Fig 5.70: Flow curves of the extruded bars tested in uniaxial compression and tension [Len15a].

As has been reported for the L4 alloy (section 5.3.3.1) all tested samples feature a slightly higher CYS than TYS and a small and positive SDE deviating from common Mg alloys. Like the L4 alloy, the LA41 extrusion feature typical flow curves, where the compression flow curve exhibits a pronounced sigmoidal shape, while the tension flow curves do not display

any signs of important twinning activity. Again, grain refinement is the dominant parameter influencing the strength of this alloy analogous to the L4 alloy (Table 5.17). As might be expected the strength of the LA41 extrusions is higher in case of the LA41 extrusions than for the L4 alloy. Surprisingly, both alloys feature significantly lower elongations to failure than previously reported (e.g. [Als09]).

Table 5.17: Tension compression yield asymmetry specified by the TYS, CYS and SDE of the extruded bars. The error of CYS and TYS is below 5 MPa [Len15a].

T_B , cooling	LA41					
	R 25 : 1			R 41 : 1		
	CYS, MPa	TYS, MPa	SDE, -	CYS, MPa	TYS, MPa	SDE, -
200 °C air	-106	101	0.05	-112	105	0.06
200 °C water	-136	132	0.03	-	-	-
250 °C air	-	-	-	-108	102	0.06
300 °C air	-	-	-	-104	100	0.04

5.4.3.2 Deformed microstructure

In case of the LA41 alloy the microstructural development during deformation is analogous to the L4, which has been depicted in detail in section 5.3.3.2. Therefore, an abbreviated description of deformed microstructure will be presented. The texture development will be displayed in conjunction with the EPSC simulations.

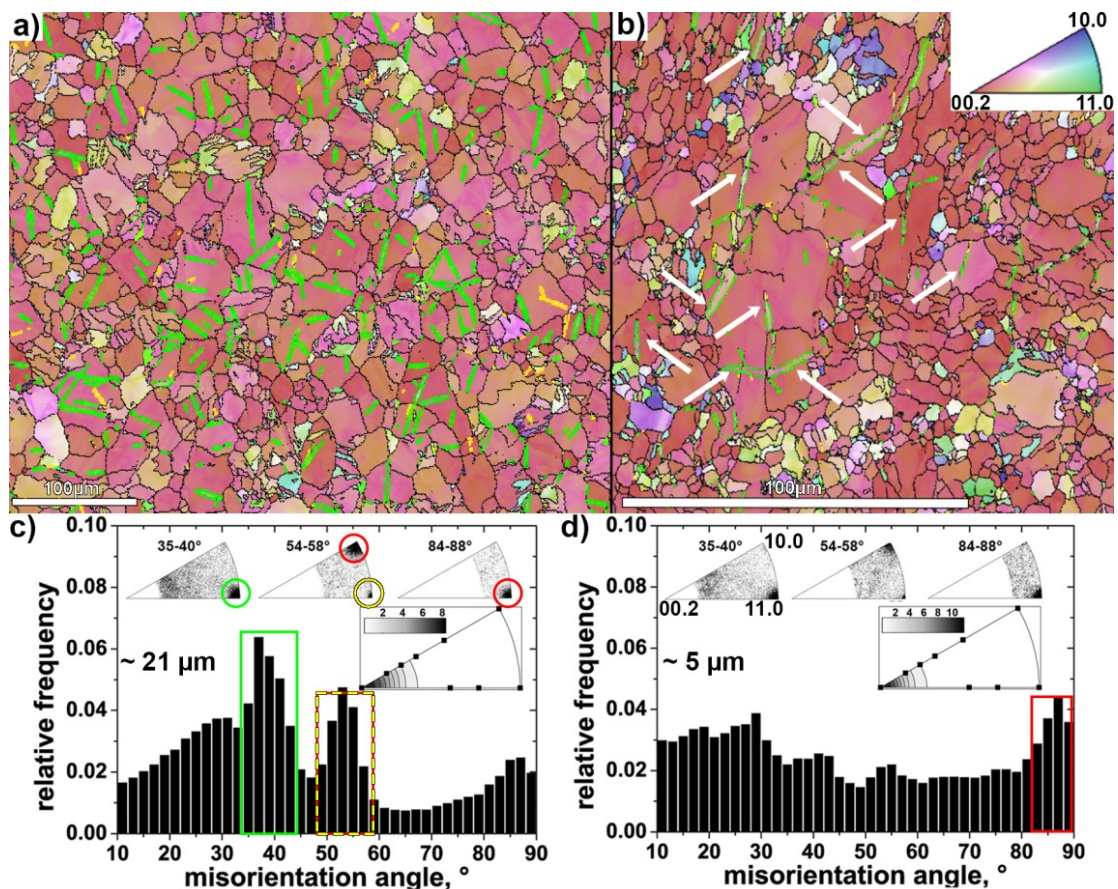


Fig 5.71: a) and b) EBSD maps highlighting CTWs (yellow) and type 1 DTWs (green); a) extrusion E (MG), b) extrusion C (FG) (detail of a 248 x 248 μm^2 map). White arrows mark DTWs in the FG samples. c) and d) correlated MDF: c) extrusion E (MG), d) extrusion C; FG. Please note the different scale bars [Len14b].

A sequential activation of primary TTW-ing, secondary CTW-ing and tertiary DTW-ing was observed, where the DTWs are almost exclusively type 1 DTWs. Thereby, the pronounced variant selection in DTW-ing was confirmed. Analogous to Fig 5.59, Fig 5.71 displays EBSD maps and MDFs of a medium grained (MG; extrusion E) and a FG sample (extrusion C), which were compressed to $\epsilon_e = -15\%$. The TTW volume fractions are 76 % (MG) and 73 % FG, confirming the HP effect of TTW-ing. In addition, the analysis confirms a significantly reduced amount of DTWs within the FG sample, confirming a more pronounced HP effect on CTW-ing and DTW-ing than on TTW-ing. However, the microstructure of FG LA41 sample is less homogeneous than the FG L4 sample enabling the investigation of d_g effects on CTWs and DTWs within one sample providing additional insights. Several DTWs were observed, but only within the larger grains, and have been marked using white arrows. The FG fraction does not contain significant amounts of CTWs or DTWs supporting the previously observed HP effect on these deformation modes. In addition, the contraction twins (including CTWs and DTWs) correspond almost exclusively to type 1 DTWs in both the MG and the FG, although the amount of twins and hence the statistic dataset are very limited in the FG samples. This indicates that the CTW-DTW transition takes place readily regardless of the d_g .

5.4.3.3 EPSC simulations

To analyze the underlying deformation mechanisms, their individual activation stresses and hardening characteristics causing the above described mechanical properties and deformation behavior a combination of in-situ EDXRSD and EPSC modeling was employed. Flow curves (Fig 5.72), texture development (Fig 5.73) and ϵ_{hkl} (Fig 5.74) were used to extract the required parameters. Fig 5.72 provides a comparison of the simulated and the measured flow curves.

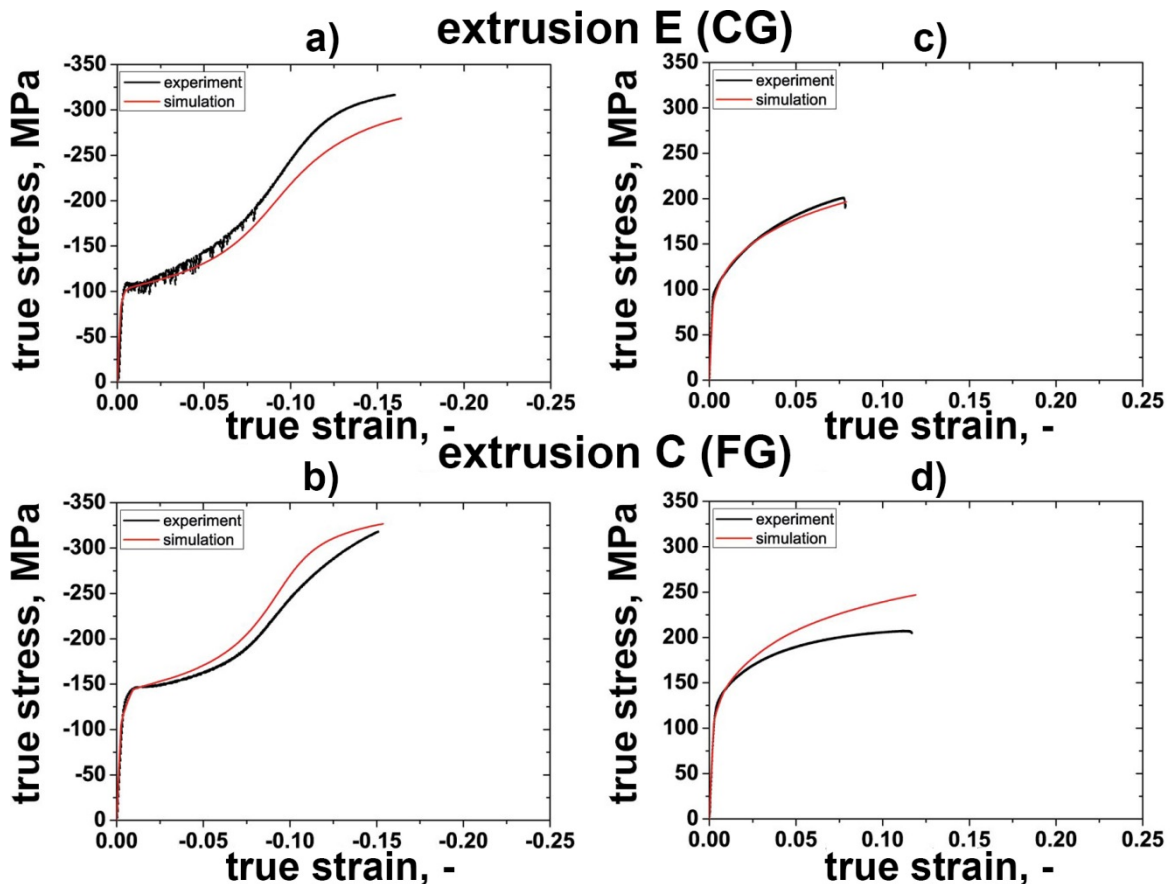


Fig 5.72: Comparison of the experimental and simulated flow curves: a), b) compression, c), d) tension. Lower elongations to failure in tension might be attributed to downscaled samples and sample mounting for in-situ EDXRSD experiments [Len15a].

Considering the above described complex deformation behavior the predicted flow curves, texture evolutions, and ϵ_{hkl} exhibit sufficient agreement with the experimental measures to enable the interpretation of the deformation. As has been mentioned above the discrepancies between the measured and simulated flow curves are most likely caused by the limitation of the self-consistent homogenization scheme considering grain-to-grain interactions only in an average sense without explicit neighboring effects. The applied single-set of hardening parameters for the slip and TTW-ing are given in Table 5.18 and Table 5.19. Within these tables the parameters, which deviate from the parameters used to model the deformation of the L4 extrusions are highlighted.

Table 5.18: Hardening parameters for slip systems [Len15a].

Parameter	LA41		
	<a> prism	<a> basal	<c+a> pyr
$\tau_{0,f}^s$ (MPa)	20	9	60
k_1^s (m ⁻¹)	2.5E+08	1.5E+08	5.5E+09
D^s (MPa)	2.5E+03	3.5E+03	3.3E+03
g^s	3.3E-03	3.3E-03	9.8E-03
ρ_0 (m ⁻²)	1.5E+12	1.5E+12	1.5E+12
HP^s	160	90	20
C^{st}	50	50	450

Table 5.19: Hardening parameters for TTW-ing [Len15a].

Parameter	LA41
τ_0^t (MPa)	22
HP^t	145

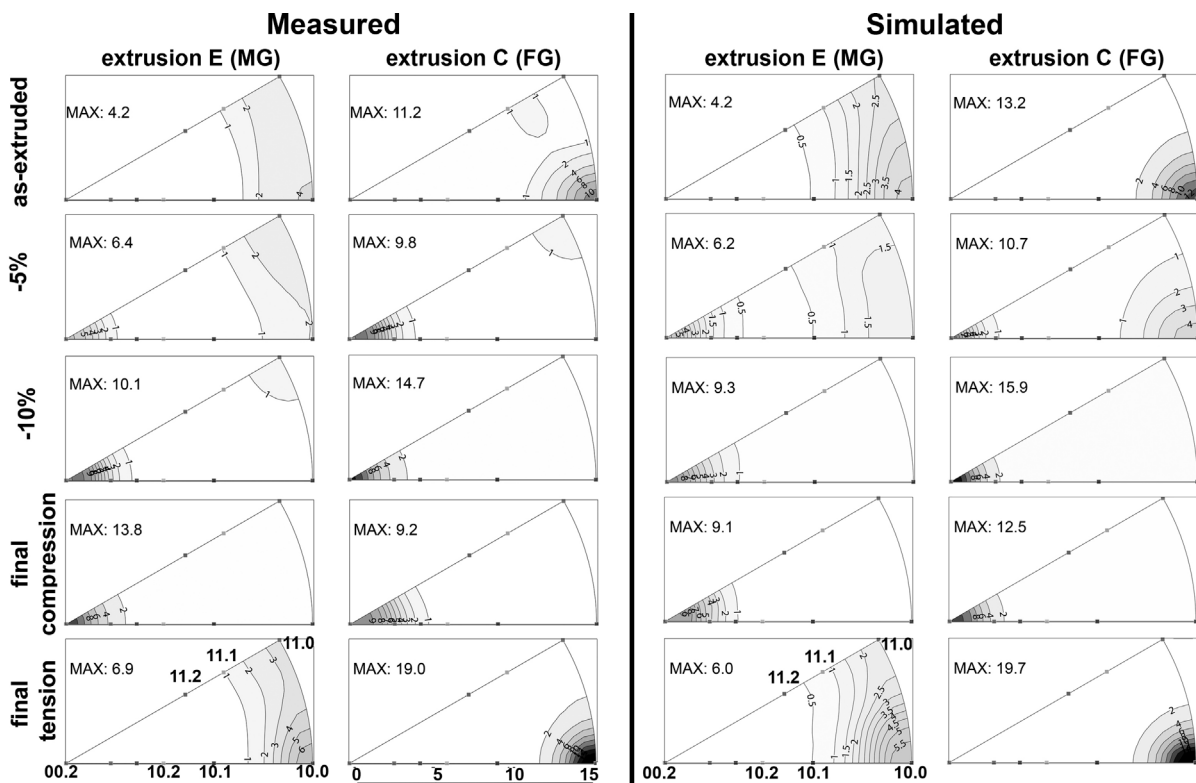


Fig 5.73: Comparison of the measured and simulated texture evolution (IPFs ||ED) [Len15a].

As has been shown above for the L4 alloy the slip activation stresses $\tau_{0,f}^s$ increase in the following order: <a> basal < <a> prismatic < <c+a> pyramidal slip. In addition, as might be anticipated, alloying with Al increases the $\tau_{0,f}^s$ of all slip modes. Like in the L4 alloy the twin

activation stress τ_0^t for TTW-ing is higher than $\tau_{0,f}^s$ for $\langle a \rangle$ prismatic slip, although the Al additions appears to increase the athermal stresses for slip, it lowers the activation stress for TTW-ing τ_0^t . Even though this finding might be surprising, it can be supported by recent first-principles calculations, which will be discussed in section 6.4.2.5. Furthermore, the calculations suggest that alloying with Al increases the activation energy g^s of $\langle c+a \rangle$ pyramidal slip. In order to capture hardening through grain refinement the same HP coefficients like in the L4 alloy were used. The texture development (Fig 5.73), the ϵ_{hkl} (Fig 5.74) and the CRSS evolution (Fig 5.75) as well as the relative deformation mode activities (Fig 5.76) evolve in accordance with the description given in section 5.3.3.3 and therefore, will be introduced only briefly.

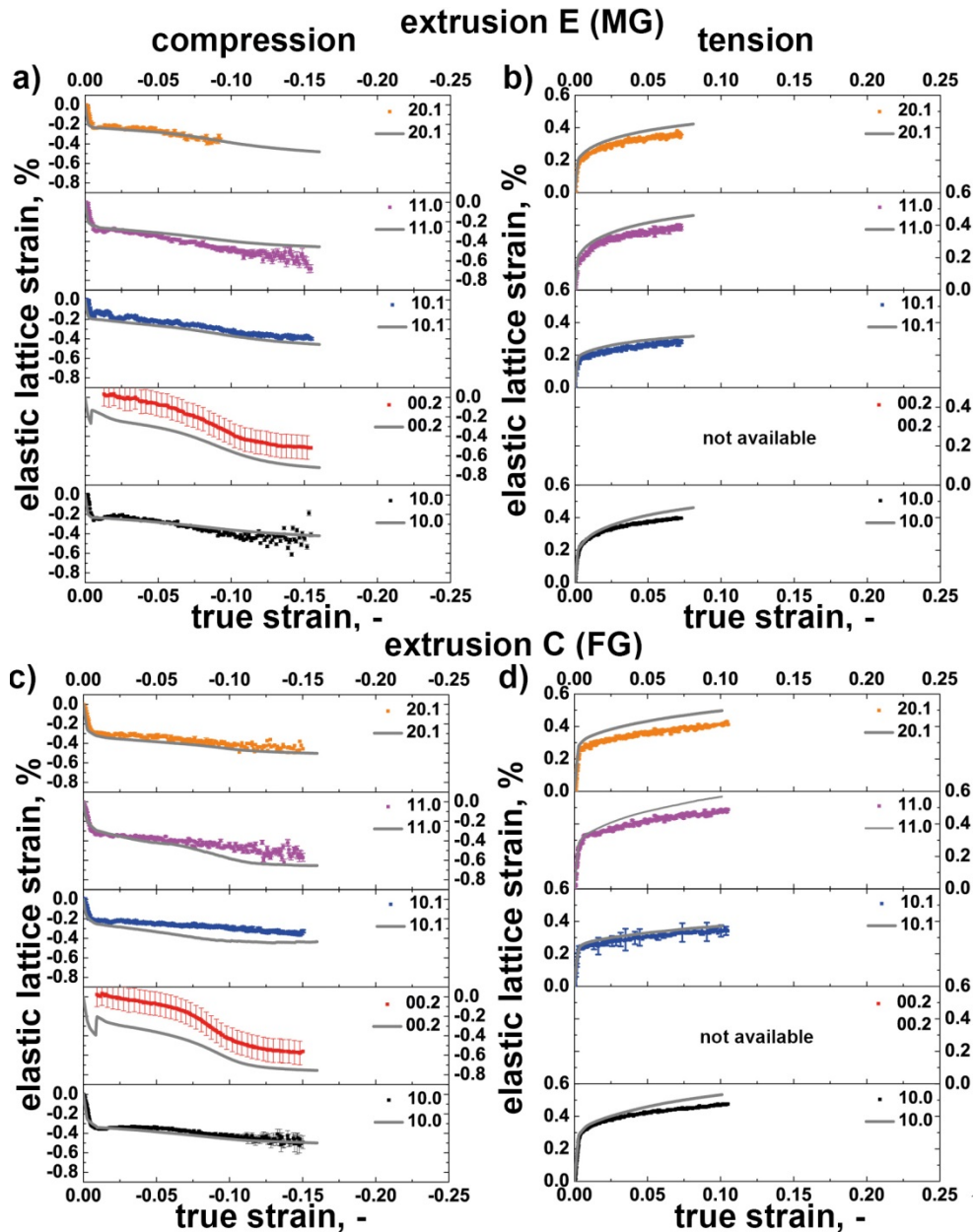


Fig 5.74: Comparison of the experimental ϵ_{hkl} data (colored) and simulation (gray lines) results: a, c) compression b, d) tension. Due to texture effects some reflections could not be accurately measured and hence were not evaluated. In this case the label “not available” was added [Len15a].

In compression the texture evolution is initially dominated by TTW-ing resulting in a sudden reorientation of the $\langle 10\bar{1}0 \rangle / \langle 11\bar{2}0 \rangle$ texture components (Fig 5.73 and Fig 5.76). The twins deform initially by $\langle a \rangle$ slip systems, while the hard $\langle c+a \rangle$ pyramidal slip mode becomes in-

creasingly active with increasing strains. In tension, TTW-ing is omitted due to the crystallographic texture; the texture development is governed by the activation of $\langle a \rangle$ slip system. However, the predicted relative deformation mode activities reveal a non-negligible contribution of $\langle c+a \rangle$ pyramidal slip during tensile deformation (Fig 5.76).

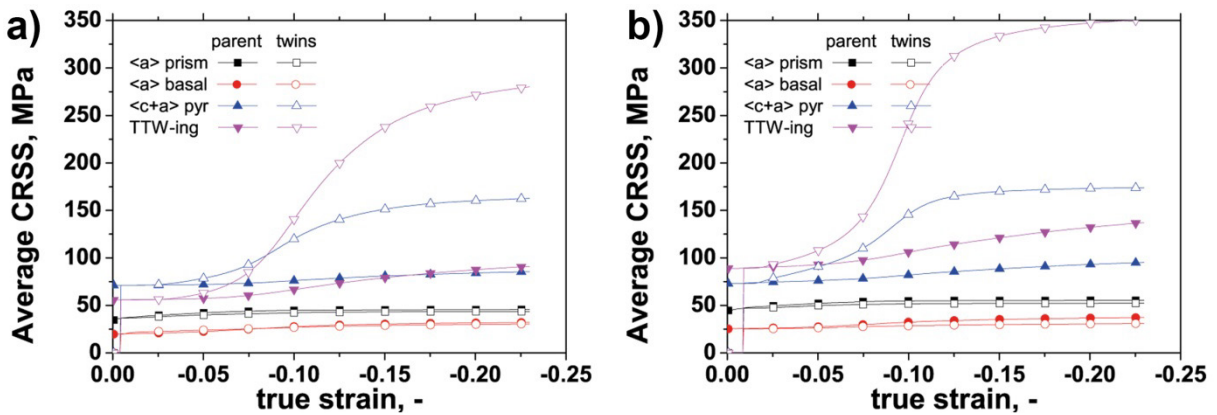


Fig 5.75: Evolution of the average CRSS during compression within the parent grains and the TTWs: a) extrusion E (MG), b) extrusion C (FG).

Again, grains deforming predominantly by $\langle a \rangle$ basal slip feature the lowest ϵ_{hkl} (e.g. $(10\bar{1}1)$), while those grains, which require the activation of non-basal slip systems and TTW-ing, exhibit higher ϵ_{hkl} . TTWs corresponding to the (0002) reflection exhibit pronounced hardening, which is associated to the substantial activation of $\langle c+a \rangle$ pyramidal slip, while the $(10\bar{1}0)$, $(10\bar{1}1)$, $(11\bar{2}0)$ and $(20\bar{2}1)$ ϵ_{hkl} increase only moderately indicating limited hardening of $\langle a \rangle$ basal and $\langle a \rangle$ prismatic slip. This finding is confirmed by the simulations (Fig 5.75).

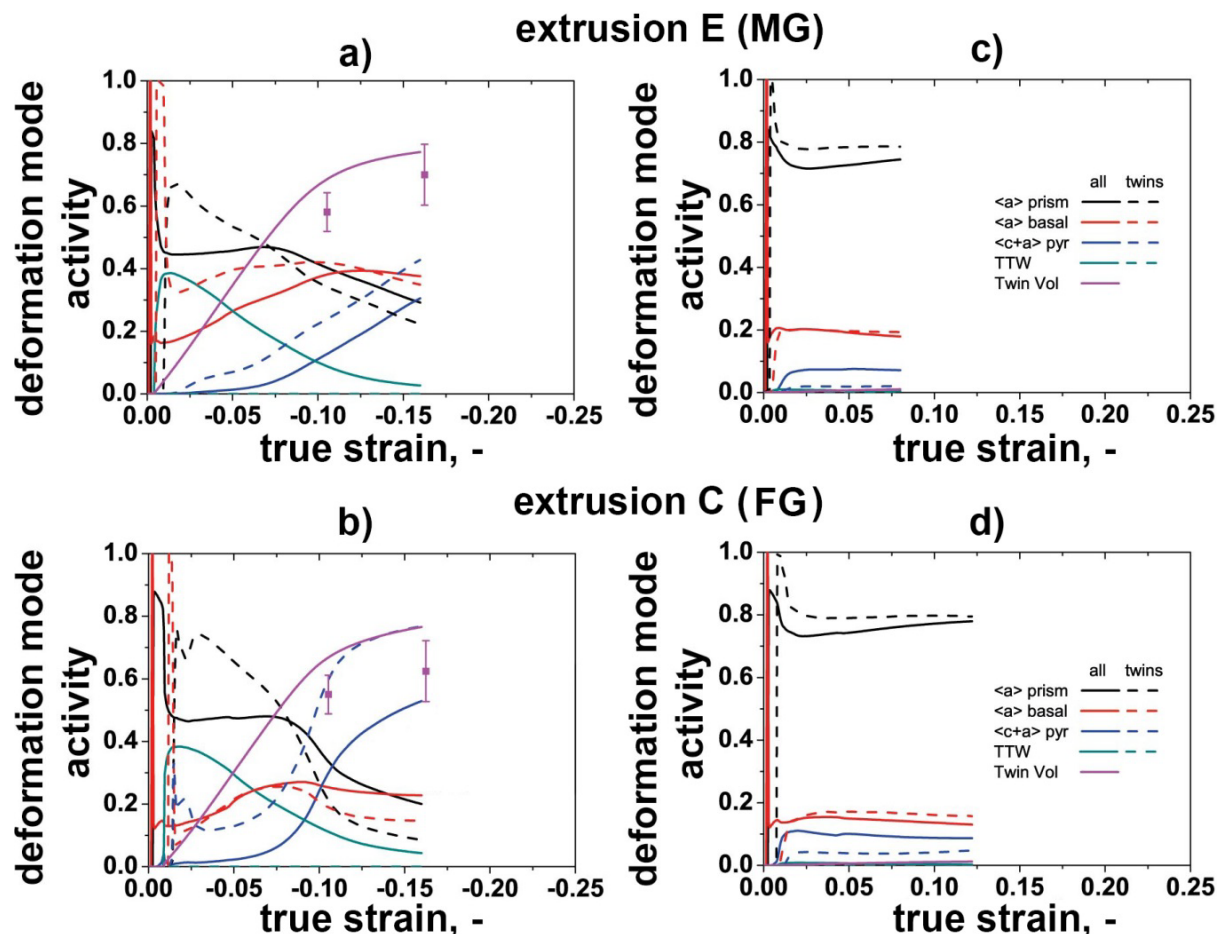


Fig 5.76: Relative activities of the active deformation model predicted by the model: a), b) compression, c), d) tension [Len15a].

6. Discussion

6.1 Cast billets

As shown in Fig 5.1 the ME21 cast billet features coarse grains as well as precipitates, which form due to the low solubility of Mn and Ce in Mg at ambient temperature (Fig 2.13). In particular Ce features a low maximum solubility of ≈ 0.5 wt% causing a high density of coarse $Mg_{12}Ce$ precipitates, which have been previously reported (e.g. [Hup10a, Hup11, Li11, Gal12]). In contrast Mn exhibits a maximum solubility of ≈ 2.2 wt% at ≈ 650 °C. However, the homogenization was conducted at 400 °C. At this temperature the solubility of Mn in Mg is low causing a high precipitate density of fine Mn-rich precipitates. TEM-EDS was used to determine their chemical composition (of extruded conditions) and revealed that these precipitates consist almost exclusively in Mn. Based on the binary Mg-Mn phase diagram (Fig 2.13 a)) it can be assumed that the fine precipitates correspond to the α -Mn phase.

In contrast the WE54 alloy features a considerably smaller d_g (Fig 5.25) and a very limited number of precipitates. Here, the homogenization was conducted at 525 °C, a temperature which enables high solute concentrations of Y and Nd (Fig 2.14). At this temperature the solubilities of Y and Nd in Mg are higher than the elements concentration within the investigated alloys. In fact the applied homogenization has been previously used in [Nie99, Nie00, Ant03] to solutionize these elements in WE43 and WE54 alloys to enable the investigation of the precipitation sequence in these Mg-Y-Nd alloys. Although, the applied air cooling resulted in comparatively slow cooling rates the kinetics of precipitation in this alloy appear to be sufficiently slow to retain Y and Nd almost completely in solid solution generating a SSSS. Nevertheless, occasional precipitates were observed, which contained predominantly Y or Zr. Zr is a very effective grain refiner used in Mg alloys, which do not contain Al, Mn, Si or Fe [StJ05, Fri06]. Soluble and insoluble Zr contents contribute to grain refinement [StJ05] and to the generation of the homogeneous microstructure of the WE54 cast billets.

While the ME21 and the WE54 alloys are commercial alloys, which are cast using industrial processes, the L4 and the LA41 alloys are experimental alloys, which were cast on laboratory scale. In addition, Li-containing melts feature a high reactivity regarding oxygen and humidity requiring shielding gas atmosphere during melting and casting [Kam00]. As shown in Fig 5.46 and Fig 5.65 the microstructure of the cast billets features relatively fine grains as well as various precipitates and inclusion including Mg oxides and (Al-)Si-rich phases, which were not expected based on the alloy composition. The origin of these precipitates is not entirely clear. Mg oxides form during the melting process if the molten Mg reacts with oxygen, when the melt is exposed to the atmosphere [Lun13]. The (Al)-Si rich phases might be caused by impurities of the master alloys or from refractory material. However, as these impurities are contained in intermetallic phases, they do not significantly alter the active deformation modes. Unfortunately, these phases are detrimental for the ductility and the elongation to failure, which will be discussed in section 6.4.2.4.

6.2 Effect of the extrusion parameters on RX, microstructure and texture

As has been shown in section 5, modifications of the extrusion parameters T_B , R and cooling medium cause significant changes of the d_g as well as texture modifications. Generally, increasing T_B result in increased average d_g , while water cooling reduces the d_g (Fig 5.3, Fig 5.27, Fig 5.48, Fig 5.67, Table 5.2, Table 5.6, Table 5.11, Table 5.16). In addition,

increasing R appear to reduce the d_g with the exception of the ME21 alloy. Considering the investigated extrusion parameters, water cooling is most effective reducing the d_g .

6.2.1 ME21

The effect of the extrusion parameters on the microstructure and texture of the ME21 extrusions is illustrated in section 5.1.2. As has been reported in [Hup10a], the ME21 alloy generally features a homogeneous relatively FG microstructure, where large elongated grains are observed only very occasional compared to the most commonly used AZ31 alloy (e.g. [Boh05, Hup10b, Hup11]). Comparing equivalent extrusion parameter sets, the ME21 extrusions feature significantly smaller average d_g than the WE54 extrusions. In [Sta10b] and [Mis08] it is shown that Ce is an effective grain refiner. In addition, the presence of the fine Mn precipitates is likely to decelerate GC. According to [Doh97], closely spaced particles pin grain boundaries (Zener pinning). Robson et al. [Rob11b] showed that the presence of a fine Mn particle dispersion allows retaining a largely unrecrystallized microstructure after hot rolling in Mg-Mn alloys. Gall [Gal12] observed smaller DRX d_g in extruded ME21 sheets than in AZ31 extrusions, which was attributed to a Zener pinning effect of the Mn precipitates and to grain refining effects of the Ce addition.

Fig 5.3 a) displays very low $d_g \approx 5 \mu\text{m}$ using $T_B = 450 \text{ }^\circ\text{C}$ or $T_B = 500 \text{ }^\circ\text{C}$ and water cooling. Using these extrusion parameters, the T_P is relatively low and therefore, the grain boundary mobility is low limiting GC. In contrast $T_B = 550 \text{ }^\circ\text{C}$ resulted in a significant increase of the average d_g to $\approx 20 \mu\text{m}$. The higher T_B caused a higher T_P , which in turn enhances the grain boundary mobility and GC. This explanation is supported by post extrusion annealing experiments [Brö11] revealing a very low grain growth rate at $400 \text{ }^\circ\text{C}$, where the average d_g increased from $5.6 \mu\text{m}$ to $7 \mu\text{m}$ within 24 h, and pronounced GC at $550 \text{ }^\circ\text{C}$.

In contrast to T_B and cooling medium effects on d_g the effect of R is not unambiguous. Fig 5.3 b) exhibits a minimal d_g using $R 41 : 1$. This minimum is generated, because R is correlated to two opposing trends, which superimpose each other. R is coupled to the true strain (φ) via $\varphi = \ln(R)$. Consequently, an increased R corresponds to a higher strain being related to a higher stored dislocation density. According to [Hum95] the stored energy is proportional to the dislocation density: $\sim 0.5\rho Gb^2$, with ρ , G and b being the dislocation density, the shear modulus and the Burgers vector. Therefore, an increased dislocation density increases the driving force for RX accelerating the kinetics of DRX. In addition, more pronounced strain inhomogeneities are generated adding nucleation sites, which might influence the DRX mechanisms [Hum95]. Following this line of thought a decreasing average d_g would be expected, if R is increased. However, the plastic deformation results in increasing T_P , where the temperature increment ΔT can be estimated using [Bau01]:

$$\Delta T = \frac{k_f \varphi}{\rho c_p} \quad (6.1)$$

with k_f , φ , ρ , c_p being the yield stress, true strain, density and specific heat capacity. The increased T_P promotes GC through higher grain boundary mobility. The conducted extrusion trials show that $R 41 : 1$ provides an optimum combination of the superimposing effects for the generation of a small d_g .

The generated extrusion textures (Fig 5.4) are similar to those previously reported by [Hup10a, Hup11, Brö11]. From Fig 5.4 several important findings emerge:

1. The maximum density is shifted towards the $\langle 10\bar{1}1 \rangle$, $\langle 11\bar{2}1 \rangle$ or $\langle 11\bar{2}2 \rangle$ texture component, in contrast to conventional Mg extrusion featuring pronounced $\langle 10\bar{1}0 \rangle$, $\langle 11\bar{2}0 \rangle$ or $\langle 10\bar{1}0 \rangle / \langle 11\bar{2}0 \rangle$ textures.
2. The RE texture component is enhanced if high T_B and low cooling rates are applied, indicating that the RE texture component is related to GC.
3. Higher R appear to enhance the shift of the maximum density from $\langle 10\bar{1}0 \rangle / \langle 11\bar{2}0 \rangle$ towards $\langle 10\bar{1}1 \rangle / \langle 11\bar{2}2 \rangle$.

The origin of the RE texture component has been analyzed in many studies investigating various RE elements and considering PSN (e.g. [Ba194]), SBN [Sta08a, Sen08, Han10, Hup10a, Gal12, Had12, Bas13, Bas14, Han14] and solute segregations at grain boundaries [Boh10, Sta10a, Als11, Sta11, Had12, Hir13]. In agreement with previous studies [Hup10a, Gal12] PSN, GBN, SBN and nucleation at twin boundaries (TBN) were observed analyzing the front-ends of the extrusions, which feature a lower true strain and therefore, are partially recrystallized (Fig 6.1). The percentage of each nucleation mechanism varied between the extruded bars. For example extrusion B featured an uncommonly high contribution of PSN, while extrusion D displayed predominantly SBN. However, the resulting textures of both extruded bars are very similar varying only in the maximum intensity, indicating that the nucleation mechanism might not be determining the texture. Similar results were found by Basu et al. [Bas13] comparing rolled Mg 1 wt% Ce and Mg 1 wt% Gd alloys. Although, the RX behavior of both alloys was governed by SBN, the Mg-Gd alloy displayed significant texture modification, while the Mg-Ce alloy showed no potential for rolling texture modification. The observation that the RE texture component is enhanced during GC indicates that the texture modification might be related to selective GC as has been suggested in [Brö11] and was observed in section 5.1.3. The importance of selective GC with respect to texture development will be elaborated further in section 6.3.1.

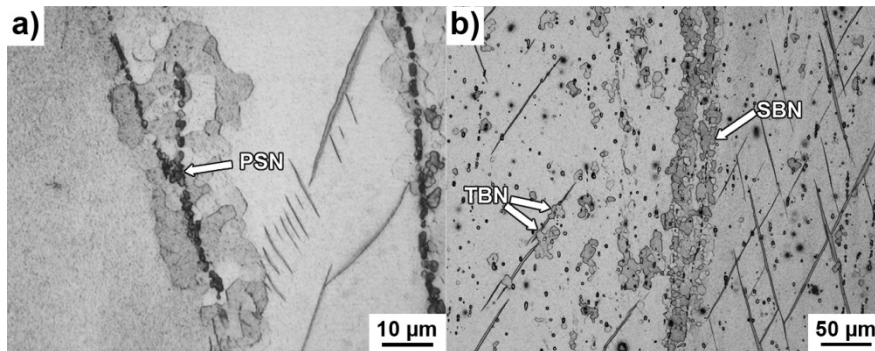


Fig 6.1: Micrographs of the front-ends of ME21 extrusion: PSN (extrusion B), b) SBN (extrusion D).

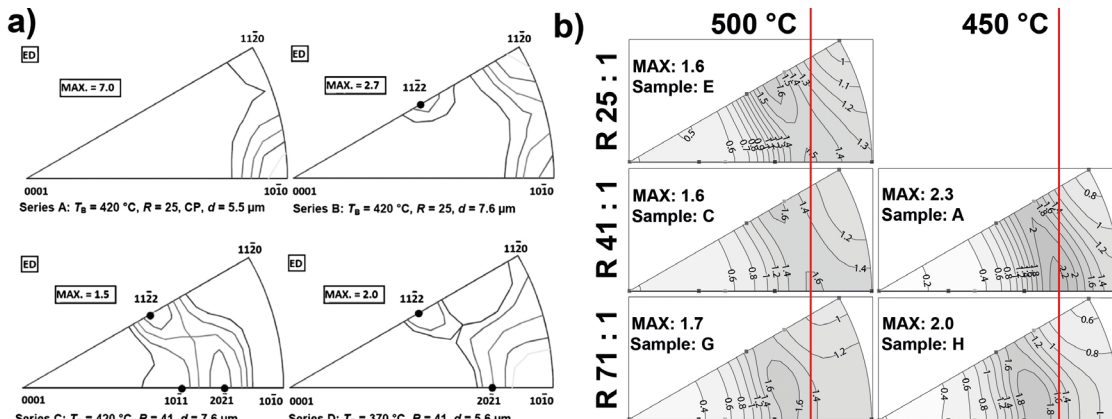


Fig 6.2: IPFs (||ED) illustrating the shifting maximum density as a function of the applied R. a) [Hup10a], b) present study.

In terms of texture randomization and of promoting $\langle a \rangle$ basal slip, the shift of the maximum intensity towards the $\langle 10\bar{1}1 \rangle$ pole is of great importance. In [Hup10a] a conventional $\langle 10\bar{1}0 \rangle / \langle 11\bar{2}0 \rangle$ fiber texture was observed in ME21 extrusions, if low T_B ($= 420$ °C) and low R ($25 : 1$) were applied, while an increased R ($41 : 1$) showed a shift of the maximum intensity between $\langle 10\bar{1}1 \rangle$ and $\langle 20\bar{2}1 \rangle$ being in good agreement with the present results. Fig 6.2 illustrates the shifting maximum intensity as a function of the applied R comparing the results of [Hup10a] (Fig 6.2 a)) and of the present study (Fig 6.2 b)).

These IPFs reveal a pronounced effect of R and hence the true strain on the generated texture. Hadorn et al. [Had13] investigated hot rolled (400 °C) Mg-Ce alloys using TEM and intragranular misorientation analysis (IGMA). They observed an increased amount of $\langle c+a \rangle$ pyramidal dislocations and non-basal $\langle a \rangle$ dislocations within the most concentrated alloy (0.49 at% Ce), which also featured the weakest texture indicating a possible impact of the active deformation modes on texture randomization. During the extrusion of round bars the deformation is dominated by compression along the radial direction. In uniaxial single crystal compression the slip plane normal tends to align with the load direction [Abb09]. Hence, the activation of the softest deformation mode $\langle a \rangle$ basal slip contributes to the formation of the $\langle 10\bar{1}0 \rangle / \langle 11\bar{2}0 \rangle$ double fiber. However, the activation of non-basal slip modes particularly $\langle c+a \rangle$ pyramidal slip would alter the deformation texture and most likely effect the DRX. Given that the extrusion trials were performed at high temperatures and high R causing high plastic strains, a significant activation of non-basal slip modes including $\langle c+a \rangle$ pyramidal slip is possible and would explain the shifting maximum density, although the assumption of uniaxial single crystal deformation and the neglected DRX provide a rough estimate only. A more accurate discussion of the texture effects would require crystal plasticity simulations including a possible as-cast texture, grain-grain interaction and RX simulation, which is beyond the scope of this study.

6.2.2 WE54

Analogous to the ME21 alloy the extrusion parameters affect the average d_g (Fig 5.26, Table 5.6), where higher T_B promote GC via increased T_P , while water cooling reduces the average d_g by suppressing GC. Here, higher R result in smaller average d_g indicating that the effect of a higher dislocation density through higher true strains is more important than the increasing ΔT .

As has been mentioned above the WE54 extrusions (Table 5.6) generally feature larger average d_g than the ME21 extrusions (Table 5.2). Due to the homogenization, which corresponds to a solution heat treatment (e.g. [Nie00]), the amount of precipitates within the WE54 cast billet is very low. In addition, the solubility of Nd and particularly Y are high at the applied $T_B \geq 450$ °C and therefore, precipitation during the extrusion process is avoided. Consequently, precipitate effects including PSN and Zener pinning are negligible, while solute effects, which appear to be less effective in terms of grain refinement than the precipitates in ME21, are more likely to occur. Hantzsche et al. [Han10] observed a grain refining effect of Y and Nd solutes in hot rolled and annealed binary alloys, where an addition of ≈ 0.05 at% of the alloying elements generated a significant grain refinement, while increasing solute concentrations did not cause a further decrease in d_g . In addition, they found a texture randomizing effect through the promotion of twins (CTW, DTW), which introduce nucleation sites featuring new orientations. Hadorn et al. [Had12] observed Y solute segregation at grain boundaries reducing the grain boundary mobility and decelerating GC. Using IGMA they showed an enhancement of non-basal $\langle a \rangle$ slip through the addition of Y stabilizing shear banding, twinning and SBN.

Fig 5.29 displays the very weak extrusion textures of the WE54 alloy, which are close to random. Similar results were found by Ball and Prangnell [Bal94], who attributed the randomization to PSN. However, within the present material the density of the precipitates is very low. Therefore, it is unlikely that PSN introduces drastic texture randomization. Via hot compression tests using various strain rates and temperatures SBN, twin boundary nucleation (TBN) and GBN, were observed in the homogenized WE54 cast billet, while PSN was found to be negligible [Len14d]. Using these hot compression samples the effect of SBN and GBN on texture randomization was investigated using EBSD (Fig 6.3). In agreement with previous studies (e.g. [Sta08a]) SBN was found to introduce a more pronounced texture randomization than GBN.

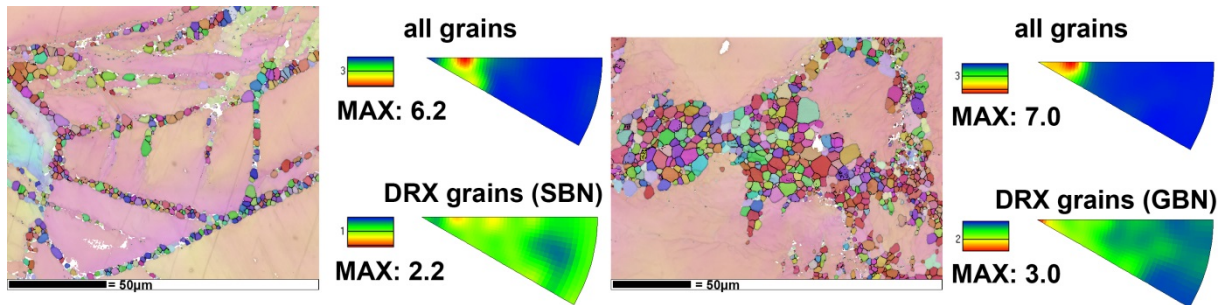


Fig 6.3: Effect of SBN (left) and GBN (right) on texture randomization.

The combination of this result and the investigations of Hadorn et al. [Had13] and Hantzsche et al. [Han10] suggests that the texture randomization is attributed to SBN, TBN, solute segregation and an enhanced activity of non-basal slip modes. The assumed higher activity of non-basal slip modes is also supported by [Agn01, San11, San12, San13] suggesting an enhanced $\langle c+a \rangle$ pyramidal slip activity in Mg-Y alloys as well as decreasing I_1 SFE through Y and Nd solutes [San14].

6.2.3 L4 and LA41

The effect of the extrusion parameters on the microstructure and texture of the L4 (Fig 5.48, Table 5.11) and the LA41 (Fig 5.67, Table 5.16) extrusions are in agreement with the aforementioned discussion, where higher T_B and air cooling promote GC and cause higher average d_g . Higher R being equivalent to a higher shear strain generate higher dislocation densities and additional nucleation sites for DRX generating lower d_g , while the increased ΔT appears to be an inferior effect like in the WE54 extrusions (cf. section 6.2.2, Table 5.6). Although the extrusion trials were conducted at substantially lower T_B , the average d_g are high in comparison to the ME21 alloy. Both alloys (L4 and LA41) feature negligible amounts of precipitates apart from the (Al-)Si rich phases and MgO inclusions. Based on their size and distribution, these phases do not hinder GC significantly and therefore, no effective obstacles retarding GC are available. Comparing equivalent extrusion parameter sets for the L4 and the LA41 alloys reveals decreasing d_g in case of the LA41 alloy. The reduced d_g might result from a deceleration of GC via the solute Al or by an increased nucleation rate in the LA41 alloy. In addition, GC saturates faster in the L4 alloy than in the LA41 alloy (Fig 5.48, Fig 5.67). Increasing T_B from 250 °C to 300 °C caused an increase in the average d_g of the LA41, while d_g of the L4 alloy did not increase further. Water cooling is the most effective parameter reducing d_g particularly in the LA41 alloy, where R is limited by the capacity of the extrusion press. Using $T_B = 200$ °C and R 71 : 1, water cooling and air cooling result in equivalent d_g . This finding is most likely attributed to the high shear strain generating an increased nucleation rate. A high density of nucleation sites limits the growth of each nuclei (and grain) reducing d_g regardless of the applied cooling condition.

Both alloys feature conventional $\langle 10\bar{1}0 \rangle$ or $\langle 10\bar{1}0 \rangle / \langle 11\bar{2}0 \rangle$ Mg extrusion textures, which differ only in sharpness (Fig 5.50, Fig 5.69). Generally, the $\langle 11\bar{2}0 \rangle$ texture component is enhanced in MG to CG samples, while FG samples exhibit $\langle 10\bar{1}0 \rangle$ fiber. This difference indicates that GC promotes the development of the $\langle 11\bar{2}0 \rangle$ texture component as has been reported in other Mg alloys such as AZ31 [Boh05, Hup10b, Hup11] and ZM20 [Mur10b]. Furthermore, the Al addition appears to promote the $\langle 11\bar{2}0 \rangle$ texture component as it is slightly enhanced in the LA41 extrusions. This finding was confirmed using post extrusion heat treatments; an 1 h 350 °C heat treatment caused a more pronounced enhancement of the $\langle 11\bar{2}0 \rangle$ texture component (Fig 6.4).

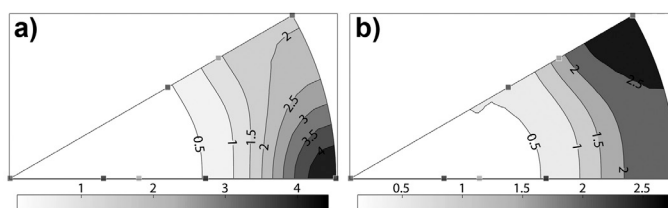


Fig 6.4: Effect of a 1 h 350 °C annealing on the texture of extrusions: a) L4, b) LA41.

Al-Samman [Als09] investigated the microstructure and texture development of L4 samples during channel-die compression at room temperature, 200 °C and 400 °C and observed that GBN as well as nucleation at triple junctions was dominant. Similar results were found in hot compression test of L4 alloy, which were performed to assess viable extrusion parameter sets (not shown). Grains, which are formed via GBN feature similar orientations like the initial deformed grains, and hence, do not introduce important texture changes [Han14], a finding which is supported through the above mentioned EBSD results (Fig 6.3). According to [Als09] the activation of more deformation modes results in a more homogeneous deformation and weaker texture. As it has been suggested that Li addition enhances $\langle a \rangle$ prismatic slip or $\langle c+a \rangle$ pyramidal slip (e.g. [Kel68, Agn01, Agn02, Als09]) a texture weakening effect might be expected in the L4 and LA41 alloys. However, the contribution of such non-basal slip systems appears to be too low to significantly alter the extrusion textures. Consequently, the predominance of $\langle a \rangle$ basal slip and GBN results in pronounced $\langle 10\bar{1}0 \rangle$ or $\langle 10\bar{1}0 \rangle / \langle 11\bar{2}0 \rangle$ fiber textures.

6.3 Effect of heat treatments on the microstructure and texture

In section 5.1.3 it was shown that heat treatments enable pronounced microstructural and texture changes in ME21 and WE54 extrusions. The microstructure and texture development will be discussed below.

6.3.1 ME21

Based on the investigations of Brömmelhoff et al. [Brö11] high temperature annealing were performed at 475 °C, 500 °C, 525 °C and 550 °C. To assess the kinetics of the texture evolution and to analyze possible temperature induced differences in texture development in-situ TOF neutron diffraction experiments were conducted at LANSCE-LC (LANL) using the HIPPO instrument. The results are displayed in section 5.1.3.1. As expected, the applied heat treatment promote the RE texture component regardless of the applied temperature. The applied temperature does not significantly alter the texture development, but its velocity. While a gradual continuous shift of the maximum intensity is observed at 475 °C, the RE texture component is predominant after 320 s at higher temperatures (Fig 5.5). As has been shown in Fig 5.6 the swiftness of texture evolution at $T \geq 500$ °C is coupled to pronounced GC.

Assuming that the observed grain growth is attributed solely to reduction of grain boundary area the driving force can be estimated using $p = 2\gamma/r$ with γ being the interfacial energy and r the radius [Got07]. Hence, the FG extrusion B provides a large driving force for GC. However, precipitates as well as solutes hinder grain boundary migration and therefore, high temperatures are required to enable rapid GC. All applied temperatures caused selective GC, where grains belonging to the RE texture component grow faster than grains of other orientations. Nevertheless, the annealing temperature is of great importance as it affects the homogeneity of the microstructure. As has been reported in [Brö11] 475 °C heat treatments result in pronounced AGG (Fig 5.6, Fig 5.7, Fig 5.8, Fig 5.11), where a limited number of grains grows substantially faster than the majority of the grains. Thereby, bimodal microstructures featuring very large grains within a matrix of significantly smaller grains are generated.

Fig 5.10 shows that the AGG is not related to the initial d_g . It was observed that some pre-existing large grains are growing faster than the surrounding grains, while others appear to shrink. This result might be expected based on previous studies and theoretical considerations. In [Hum95] it is derived that in an ideal grain assembly, large grains will always grow slower than small grains and hence, AGG is not expected. However, AGG can occur if abnormally growing grains feature some advantage (e.g. texture, precipitates, etc.) other than size over its neighbors [Hum95]. Based on the observed texture evolution a growth advantage of the RE texture component appears probable. However, a detailed examination of the orientation of abnormally grown grains using ex-situ and pseudo-in-situ EBSD revealed that grains of a variety of orientations have grown abnormally. This finding is illustrated exemplary in Fig 6.5. Furthermore, texture related AGG is commonly coupled to strong single component textures, as the (few) grains of other texture components introduce boundaries of higher energy and mobility in this case [Hum95]. This condition is not fulfilled in case of the investigated ME21 extrusions featuring relatively weak texture, which contain multiple texture components.

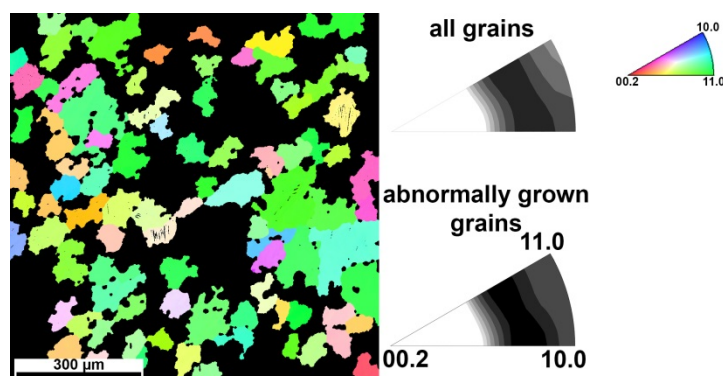


Fig 6.5: Comparison of the IPFs of all grains and AGG grains (10 h 475 °C).

In addition to texture, the presence of precipitates has been correlated to AGG. As has been discussed in the above section precipitates can generate a Zener drag decelerating or limiting GC. According to [Raa14] the Zener force is proportional to the grain boundary energy, where low energy grain boundaries are less affected by precipitates and therefore, are more likely to grow abnormally. However, no correlation between intergranular misorientations and AGG was observed and hence, AGG is not caused by a higher mobility of special grain boundaries. This finding is also supported by the homogeneous distribution of the $Mg_{12}Ce$ and the Mn precipitates within the grains. If grain boundaries are pinned by precipitates an increased precipitate density would be expected at the grain boundaries, however using optical microscopy and TEM no enrichment was observed. In addition, dissolution of precipi-

tates, which has also been correlated to AGG [Hum95], is very limited (Fig 5.12, Fig 5.13). These results indicate that AGG is not caused by precipitates. However, in [Raa14] it is suggested that AGG requires very slow normal GC, which is observed at 475 °C and might be related to the observed precipitates.

The analysis of the quasi-in-situ EBSD experiments (Fig 5.10) revealed AGG of grains, which feature a size advantage in concurrence with high intragranular misorientations and accordingly, substructured grains. Such substructured grains feature a higher defect density and therefore, the driving force for recovery and GC as well as the GC kinetics are increased during the post-extrusion heat treatments. The comparison of Fig 5.10 c) - f) shows that AGG occurs within grain 3, which is bigger than the neighboring grains and features exceptional high intragranular misorientations. In contrast grain 1 and 2, which are larger than the surrounding grains and display low intragranular misorientations shrink (grain 1) or grow continuously (grain 2) during annealing. However, the conducted EBSD analysis (Fig 5.6, Fig 5.7, Fig 5.8) revealed that AGG can be omitted increasing the annealing temperature. An increasing annealing temperature tends to enhance the grain boundary mobility accelerating normal (continuous grain growth). Consequently, CGG intensifies replacing AGG, which requires very slow CGG [Raa14].

Here, it is important to emphasize that selective GC occurs regardless of the applied annealing temperature and promotes the RE texture component as is evident from EBSD, TOF investigations and previous studies (e.g. [Hup10a, Brö11]), although it is decoupled from AGG. This finding is consistent with a reinforced RE texture component in ME21 extrusion featuring a high average d_g (Fig 5.3, Fig 5.4, Table 5.2 and section 6.2.1).

In addition, to the above discussed texture changes, high temperature heat treatments affect both precipitate fractions ($Mg_{12}Ce$ and Mn). Fig 5.12 displays the impact of 1 h 550 °C and 24 h 475 °C annealings on the $Mg_{12}Ce$ using SEM. The heat treatments cause a reduction of the precipitate density and a slight increase of the precipitate size. Similar effects were observed in case of the Mn precipitates using TEM (Fig 5.13), where the precipitate size distribution is shifted to higher equivalent diameter by the heat treatments. These findings indicate that Ostwald ripening, which denominates the dissolution of small precipitates in favor of the coarsening of large precipitates reducing the cumulative interfacial energy [Got07], takes place at the applied annealing temperatures.

6.3.2 WE54

Based on its ability to form different precipitates during heat treatments the WE54 alloy was age-hardened at 250 °C and annealed at 400 °C to investigate precipitation effects on the deformation behavior of the alloy. As has been shown in Fig 5.30 and Fig 5.33 the conducted heat treatments did not cause any major GC or texture changes indicating an almost stable grain structure ≤ 400 °C. However, the applied heat treatments caused the formation of precipitates, which were investigated using SEM (Fig 5.31) and TEM (Fig 5.32).

As might be expected from previous investigations ([Nie99, Nie00, Ant03, Gao12]) 250 °C age-hardening results in the formation of globular precipitates and $\{10\bar{1}0\}_\alpha$ plates. Using HR-TEM, FFT (cf. [Wag14]) and the orientation relations given in [Nie00] the globular precipitates were identified as β' phase, while the $\{10\bar{1}0\}_\alpha$ plates correspond either to β_1 or β . These precipitates occurred simultaneously in 16 h age-hardened materials, while the 500 h age-hardened material contained only β plates, which are significantly larger than in the 16 h age-

hardened material (Fig 5.32). This shows a transition of the metastable phases as well as Ostwald ripening after long dwell times being consistent with [Nie99, Nie00, Ant03].

In contrast to the 250 °C age-hardening the 400 °C annealing generated precipitates predominantly at grain boundaries, where a negligible amount of precipitates was found in the grain interior (Fig 5.31 d)). The precipitates contain Y and Nd, whose concentration is thereby reduced within the grains (Fig 6.6). Line scans of a (1 h 400 °C) sample confirmed decreasing Nd (from 1.8 wt% to 0.8 wt%) and Y (from 5.3 wt% to 5.0 wt%) average solute concentrations within the grain interiors due to precipitation at grain boundaries. Point measurements using EPMA revealed that the concentrations of Y and Nd within the grain boundary precipitates are almost the same, where the Y (2.8 - 3.2 at%) concentration is slight, but consistently higher than the Nd (2.2 – 2.6 at%) concentration. Here it should be noted, that the interaction volume between the beam and the sample is larger than the precipitates and therefore, the Mg matrix cannot be completely excluded.

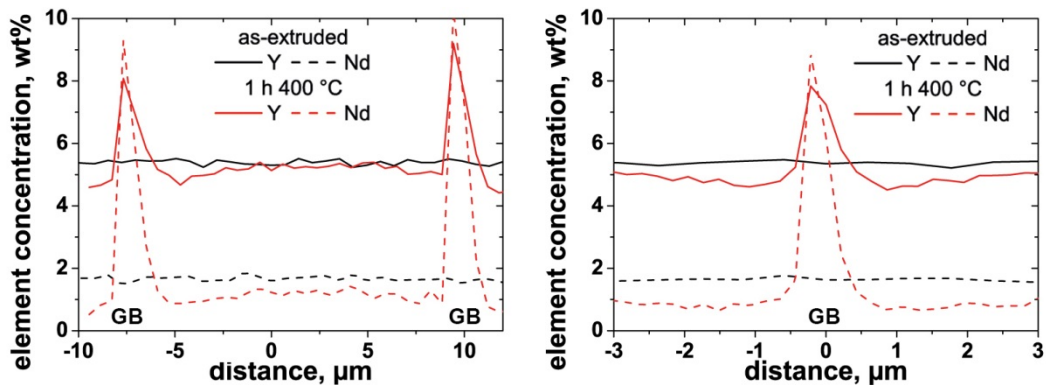


Fig 6.6: EPMA line scans illustrating the Y and Nd concentration within the vicinity of a grain boundary in as-extruded and 1 h 400 °C annealed condition. GB labels grain boundaries.

The different locations and precipitate densities suggest an important temperature effect on precipitation. At low temperatures the supersaturation of Mg matrix is very high, as the solubility decreases. In addition, diffusion processes are very limited and hence, many stable nuclei form readily causing a uniform precipitate distribution within the grains. However, at higher temperatures the supersaturation is reduced lowering the driving force for precipitation. Here, homogeneous precipitation requires large nuclei. However, grain boundaries provide sites for heterogeneous nucleation, which occurs readily in comparison to homogeneous nucleation. In addition, the higher temperature enhances diffusion enabling solute migration towards the grain boundaries. This explanation is supported by two step ageing experiments, where age-hardening was conducted subsequent to an 1 h 400 °C annealing (Fig 6.7, [Wag14]).

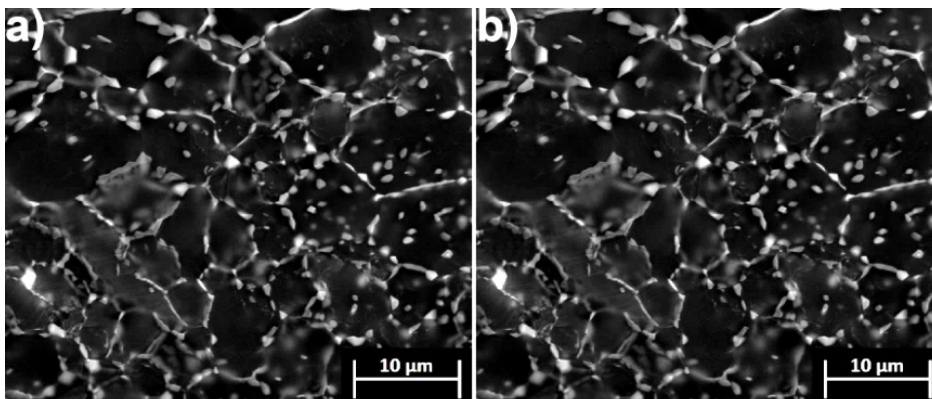


Fig 6.7: SEM images displaying the effect of two step ageing: a) 1 h 400 °C + 16 h 250 °C, b) 1 h 400 °C + 500 h 250 °C [Wag14].

From Fig 6.7 it is evident that age-hardening is not effective, if preexisting grain boundary precipitates are available. Here, (homogeneous) nucleation is omitted and the reduced solubility is compensated by growth of grain boundary precipitates.

It should be noted that the grain boundary precipitates generated through 400 °C annealings are not expected to be effective obstacles for dislocations. However, their presence reduces the solute concentration within the Mg matrix and enabling the investigation of solute effects on the deformation behavior, while the d_g and the texture are almost equivalent to the as-extruded and 250 °C age-hardened conditions.

6.4 Deformation behavior

As has been discussed in the previous section the microstructure, texture, solute and precipitate contents can be modified through variations of the extrusion parameters and post extrusion heat treatments. Within this section the effects of these changes on the deformation behavior and the mechanical properties are discussed. In addition, the different compositions of the selected alloys enable the analysis of alloying effects.

6.4.1 ME21

6.4.1.1 Grain size effects

Using the above defined extrusion parameter sets the d_g of the ME21 extrusions was varied within the range from 5 μm to 20 μm . Using these samples the d_g dependence of the CYS and TYS was evaluated according to the HP relation (Eq. 2.2). The corresponding HP plots and parameters are displayed in Fig 6.8 and Table 6.1. The fit of the experimental CYS, where the initial deformation is dominated by the activation of TTW-ing, confirms previous investigations (e.g. [Bar04, Bar08b, Tsa13]) showing the validity of the HP relation for TTW-ing. In agreement with prior studies [Bar04, Boh07b, Bar08b, Pek13, Ill14], k is higher in compression than in tension indicating that TTW-ing is more sensitive to grain refinement than crystallographic slip.

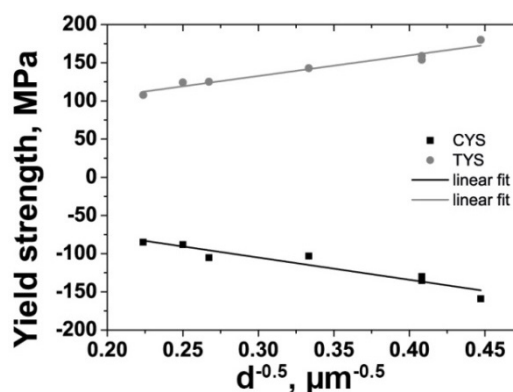


Fig 6.8: Hall-Petch plots considering CYS and TYS of the extrusions.

Table 6.1: Macroscopic Hall-Petch parameters.

ME21	k , MPa $\mu\text{m}^{0.5}$	σ_0 , MPa
CYS	-291	-18
TYS	270	52

The HP relation reflects in the applied hardening parameters (Table 5.4), which were used to model the as-extruded and heat treated materials. Here, the FG as-extruded material features substantially higher τ_0 for both TTW-ing and crystallographic slip than the CG heat

treated samples. In addition, τ_0 for TTW-ing is below τ_0 for $\langle a \rangle$ prismatic slip only in the CG 550 °C heat treated sample, which features the largest d_g being consistent with Fig 6.8. Apart from this finding it appears that grain refinement does not significantly promote or harden specific deformation modes in this alloy (Table 5.4). However, the initial hardening rate θ_0 is increased within both heat treated samples. This result indicates an increased work hardening of slip modes with increasing d_g being consistent with prior investigation by Guo et al. [Guo11] and del Valle et al. [Val06] showing a decreased work hardening rate in AZ31 alloys, if d_g is decreased.

Additionally, the d_g and the homogeneity of the microstructure appear to affect the elongation to failure of the samples. From Fig 5.16 c) it is evident that a heterogeneous microstructure reduces the elongation to failure. The 24 h 475 °C heat treated sample has undergone AGG and hence, displays very large grains, which are surrounded by substantially smaller grains. Based on the HP relation the abnormally grown grains are expected to yield at lower strains than the surrounding FG matrix. Therefore, stress concentration and strain incompatibilities are likely causing fracture at lower strains. Apart from this peculiarity d_g does not affect the tensile elongation to failure importantly; within the experimental scattering no correlation with d_g was observed. The comparison of the compression flow curves of FG and CG extrusions and heat treated samples displays no unambiguous trend (Fig 5.15, Fig 5.16, Fig 6.9). FG and CG extrusion feature comparatively low elongations to failure, while the 1 h 550 °C ($d_g = 15 \mu\text{m}$) and the 24 h 550 °C ($d_g = 17 \mu\text{m}$) annealed samples exhibit a very high ductility. These results indicate that an optimum d_g exists contributing to a high elongation to failure. However, other parameters such as precipitate size and distribution as well as texture superimpose the effect of d_g , which will be discussed in the following sections.

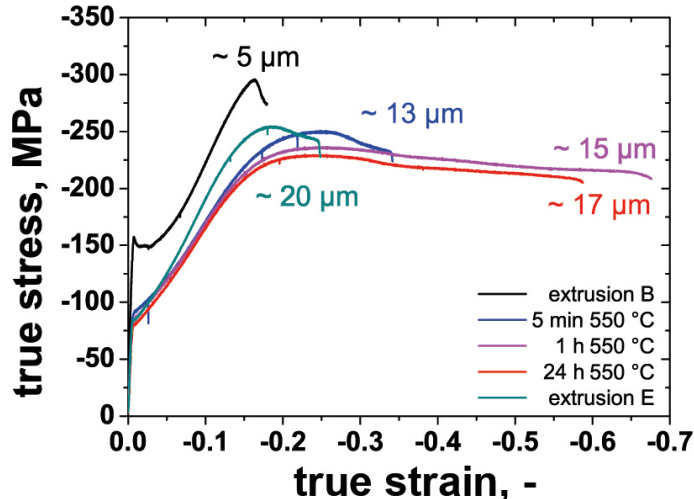


Fig 6.9: Compression flow curves of extruded and heat treated samples. The d_g of the samples is provided through labels within the figure.

6.4.1.2 Twinning

The activity of twinning was investigated via examination of the flow curves (Fig 5.15, Fig 5.16), EBSD (Fig 5.17, Fig 5.18), optical micrographs (Fig 5.19) and XRD texture analysis (Fig 5.20). Due to the initial extrusion (Fig 5.4) and annealing textures (Fig 5.5, Fig 5.9, Fig 5.14) TTW-ing is negligible in case of tension tests, while it is dominant during the initial deformation of compression samples. This finding is supported by the pronounced sigmoidal shape of the compression flow curves being characteristic for a high TTW-ing activity. In most Mg alloys TTW-ing is readily activated and overtakes parent grains readily causing low work-hardening during the initial deformation (e.g. [Kel58, Bar07a, Lou09, Kha11, Kur14, Len14a, Len15a]). This finding is supported by the conducted EBSD and texture analysis,

which showed a pronounced activation of TTW-ing at strain $< -10\%$. TTW-ing occurred in the vast majority of the grains and overtook the parent microstructure. In agreement with [Bey10], those grains, which did not display TTWs are favorably orientated for $\langle a \rangle$ basal slip and feature a low SF for TTW-ing (cf. Fig 2.12, Fig 5.17). As $\langle a \rangle$ basal slip is the softest deformation mode in Mg alloys and the low SF of TTW-ing impedes its activation, the deformation is slip controlled in such grains. This finding is further supported by the texture evolution (Fig 5.17, Fig 5.20). TTW-ing is characterized through a sudden reorientation of 86.3° about a $\langle 1\bar{2}10 \rangle$ -axis. However, the RE texture component tends to rotate gradually towards the $\langle 0002 \rangle$ pole. A gradual rotation cannot be attributed to the activation of a twin mode, but to the rotation of grains through the activation of slip modes. In uniaxial compression of single crystals the slip plane normal is rotated towards the load direction [Got07, Abb09] and therefore, the gradual rotation of RE texture component towards the $\langle 0002 \rangle$ pole can be attributed to the activation of basal slip.

However, as the parent grains are overtaken an increasing portion of the grains becomes aligned with their c-axis parallel to the load direction requiring the activation of the hard $\langle c+a \rangle$ pyramidal slip mode and causing a pronounced geometric hardening. Here, it should be noted that TTW boundaries sub-divide the parent grains, which potentially could introduce an additional HP effect. However, several investigations [Kne10, Opp12, Cap09a] suggest that TTW boundaries are ineffective barriers for dislocations in Mg. In addition, CTW-ing might be expected during c-axis compression at strains $> -10\%$. However, using EBSD no evidence of an important activation of CTW-ing or DTW-ing was observed and hence, it appears that a high CRSS of CTW-ing impedes its activation; a finding, which is also supported by the conducted tension tests. The tensile flow curves do not provide evidence of any twinning activity. Here, the majority of the grains feature a low SF for TTW-ing and therefore, deform by crystallographic slip. Although tensile deformation would favor CTW-ing, no evidence of CTWs was found. This finding is most likely related to a high CRSS of CTW-ing in the ME21 alloy, which has been reported previously for other Mg alloys (e.g. [Bar08a]), inhibiting its activation.

In summary, it was found that TTW-ing occurs readily and overtakes the parent microstructure in the ME21 alloy, if the combination of the texture and the external load enable its activation, while CTW-ing is absent regardless of the strain path. This observation highlights the importance of texture effects on the deformation behavior, which will be discussed in the following section.

6.4.1.3 Texture effects

Through the application of different extrusion parameter sets and heat treatments a variety of textures was produced (Fig 5.4, Fig 5.5, Fig 5.9, Fig 5.14), which influence the deformation behavior in terms of active deformation modes, flow stress and elongation to failure. Fig 5.15 and Fig 5.16 show the highest yield strength in samples, which feature strong $\langle 10\bar{1}0 \rangle$ and weak RE texture components. This finding can be explained through SF analysis. Grains, which correspond to the RE texture component exhibit a high SF for $\langle a \rangle$ basal slip, the softest deformation mode, and consequently exhibit lower flow stress. In contrast, grains, which correspond to $\langle 10\bar{1}0 \rangle$ or $\langle 10\bar{1}0 \rangle / \langle 11\bar{2}0 \rangle$ texture component feature a high SF for $\langle a \rangle$ prismatic slip, $\langle c+a \rangle$ pyramidal slip and (in compression) TTW-ing and SF close to zero for $\langle a \rangle$ basal slip (cf. Fig 2.12 b)). Consequently, such grains exhibit higher flow stresses. Here, it should be noted that such samples also feature large d_g reducing the yield strength as well. These superimposing effects complicate an unambiguous correlation between the flow stress

and the texture. In order to investigate the texture effect separately, EPSC simulations were conducted using the hardening parameters of the as-extruded condition (Table 5.4) and different initial textures. Fig 5.25 displays the texture effect on compression and tension flow curves as well as TTW volume fractions using the experimental textures given in Fig 5.14.

From Fig 5.22 it is evident that $\langle a \rangle$ basal and $\langle a \rangle$ prismatic slip dominate the deformation during tensile tests. Their relative activities depend on the initial texture, where an enhanced RE texture promotes the activation of $\langle a \rangle$ basal slip, as a higher percentage of grains features a high SF in this case. Consequently, the TYS depends on the initial texture, where the predicted difference of the TYS is ≈ 30 MPa. However, during the subsequent deformation the grains rotate towards the $\langle 10\bar{1}0 \rangle$ texture component (Fig 5.20, Fig 5.23) lowering the SF for $\langle a \rangle$ basal slip and increasing the SF for $\langle a \rangle$ prismatic slip. Consequently, $\langle a \rangle$ prismatic slip prevails at strains > 5 % regardless of the initial texture. The rotation towards the $\langle 10\bar{1}0 \rangle$ texture component is caused by the activation of multiple $\langle a \rangle$ slip systems. In uniaxial tension the slip plane and the slip direction of an active slip mode will rotate towards the load direction [Abb09, Got07]. Based on the conducted EPSC simulations it can be inferred that $\langle a \rangle$ prismatic and $\langle a \rangle$ basal slip are dominant during tensile deformation. Consequently, an enhancement of the $\langle 11\bar{2}0 \rangle$ texture component would be expected, if only one $\langle a \rangle$ basal slip system or one $\langle a \rangle$ prismatic slip system would be activated. However, according to the Taylor criteria five independent slip systems are required to enable the deformation of polycrystals and the cumulative activation of multiple slip systems generates the rotation towards the $\langle 10\bar{1}0 \rangle$ texture component [Len14c].

During compression tests the deformation behavior is more complex due to the activation of TTW-ing. Initially, the deformation is realized by $\langle a \rangle$ basal slip, TTW-ing and $\langle a \rangle$ prismatic slip, where an enhanced RE texture component promotes $\langle a \rangle$ basal slip, while an enhanced $\langle 10\bar{1}0 \rangle / \langle 11\bar{2}0 \rangle$ texture components promote the activation of TTW-ing and $\langle a \rangle$ prismatic slip. The initial texture does not alter the CYS significantly (Fig 5.24), however, it does control the TTW volume fraction, which varies between ≈ 40 % and ≈ 70 % in case of the as-extruded and heat treated samples (Fig 5.24). As TTW-ing proceeds and overtakes the parent microstructure its activity decreases gradually, while $\langle c+a \rangle$ pyramidal slip is rendered more active. According to the simulation the TTWs deform predominantly by $\langle a \rangle$ basal slip and $\langle c+a \rangle$ pyramidal slip. This result is caused by the low CRSS of $\langle a \rangle$ basal slip, which enables its activation, although, its SF is close to zero.

In case of the 1 h 550 °C sample, the lowest TTW volume fraction and in turn the highest $\langle a \rangle$ basal slip activity was observed, which is attributed to the enhancement of the RE texture component. As has been mentioned above, Fig 5.20 and Fig 5.23 reveal a gradual rotation of the RE texture component due to $\langle a \rangle$ basal slip, while grains corresponding to the $\langle 10\bar{1}0 \rangle / \langle 11\bar{2}0 \rangle$ texture components twin readily. Consequently, $\langle c+a \rangle$ pyramidal slip (predominantly TTWs) and of $\langle a \rangle$ basal slip (RE texture component) occur simultaneously. At strains below -20 % the activity of $\langle c+a \rangle$ pyramidal slip increases causing an increasing flow stress, however, $\langle c+a \rangle$ pyramidal slip rotates grains towards its slip plane normal (towards the $\langle 11\bar{2}2 \rangle$ texture component) increasing the SF for $\langle a \rangle$ basal slip, which in turn rotates grains towards the $\langle 0002 \rangle$ texture component. Therefore, both slip modes balance each other. As hardening is exhausted, which is evident from the ϵ_{hkl} evolution (Fig 5.21), the flow stress decreases. This balance is likely to contribute to the high elongation to failure of the sample. However, the lower elongation to failure of the 5 min 550 °C sample (Fig 5.16),

which features a very similar texture, indicates that both an optimal texture and an optimal microstructure are required to achieve high elongations to failure [Len13].

In order to elaborate the discussion of texture effects further, additional simulations (Fig 6.10) were conducted using simulated textures, which were selected to maximize the effect of $\langle a \rangle$ basal slip ($\langle 11\bar{2}2 \rangle$), $\langle c+a \rangle$ pyramidal slip ($\langle 0002 \rangle$) and a combination of TTW-ing and $\langle a \rangle$ prismatic slip ($\langle 10\bar{1}0 \rangle$). Fig 6.10 reveals a difference of ≈ 50 MPa of the CYS comparing the $\langle 0002 \rangle$ and the $\langle 11\bar{2}2 \rangle$ texture. In agreement with the above discussion, the $\langle 11\bar{2}2 \rangle$ texture, which favors $\langle a \rangle$ basal slip, features the lowest CYS and no significant work hardening. As the basal slip system rotates grains towards the $\langle 0002 \rangle$ pole some hardening was predicted at very high strains, which is correlated to the activation of $\langle c+a \rangle$ pyramidal slip. In contrast the $\langle 0002 \rangle$ texture requires a high relative activity of $\langle c+a \rangle$ pyramidal slip as the other deformation modes are largely suppressed based on their low SF and therefore, exhibits the highest CYS. Here, it should be noted that CTW-ing is not considered during the simulations. Due to high initial hardening rate θ_0 , the simulation predicts a strong increase of the flow stress. In agreement with the above description of the 1 h 550 °C sample a peak stress occurs, which is followed by texture (geometric) softening. Here, the hardening of the slip modes is exhausted and $\langle a \rangle$ basal and $\langle c+a \rangle$ pyramidal slip balance each other. The random texture displays a weakly pronounced sigmoidal shape, which is related to a higher final TTW volume fraction of ≈ 35 %. As the $\langle 10\bar{1}0 \rangle$ texture exhibits a high SF for TTW-ing its activation is enhanced (TTW volume fraction of ≈ 87 %) causing a pronounced sigmoidal shape of the flow curve based on the above described geometric hardening and subsequent texture controlled work softening.

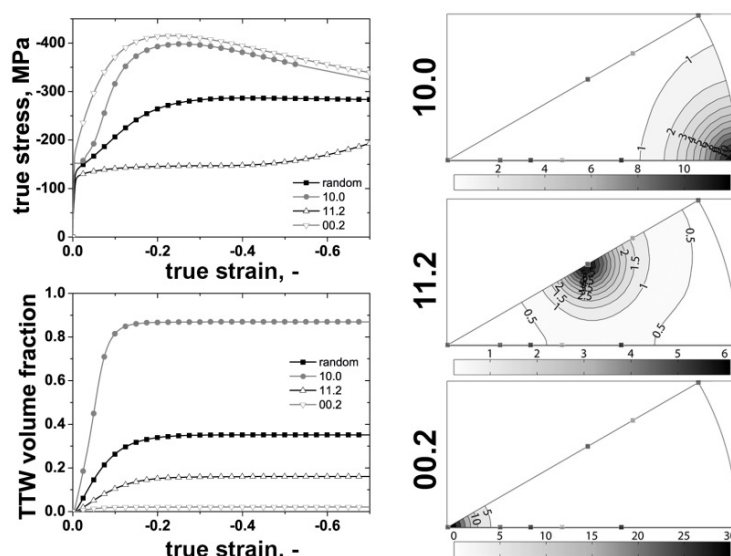


Fig 6.10: EPSC simulations of texture effects on the compression flow curve and TTW volume fraction. The hardening parameters of the as-extruded condition were applied (Table 5.4). IPFs illustrate the model fiber textures.

As has been shown above, neither d_g effects nor texture effects can separately generate the observed extraordinary elongations to failure observed in the 1 h and 24 h 550 °C sample. Therefore, the discussion will be extended to precipitates in the following section.

6.4.1.4 Precipitate effects

The size distributions and the precipitate densities were investigated using SEM (coarse fraction; mainly $Mg_{12}Ce$; Fig 5.12) and TEM (fine fraction; Mn; Fig 5.13). Fig 6.11 combines these results with additional measurements and displays the evolution of the mean equivalent diameter, which were determined from log-normal distribution fits of the experimentally

determined histograms, as a function of applied extrusion and heat treatment parameters. The error margins correspond to the standard deviation of the log-normal distribution. While different T_B do not alter the size of coarse $Mg_{12}Ce$ within the margin of error, the annealings cause an increase of 35 % to 45 % of the equivalent diameter. A high T_B of 550 °C appears to increase the equivalent diameter of the Mn precipitates, importantly. The mean equivalent diameter increases from 33 nm to 200 nm and the precipitate density drops significantly (not shown; [Len14c]), if T_B is increased from 450 °C to 550 °C. Surprisingly, this increase is much more pronounced than Mn precipitate growth during 24 h 475 °C and 1 h 550 °C heat treatments. Here, it should be noted that the increased Mn precipitate size might be related to differences between the cast billets. Although, its origin is not entirely clear the different size enables additional insights into precipitate effects on the deformation behavior.

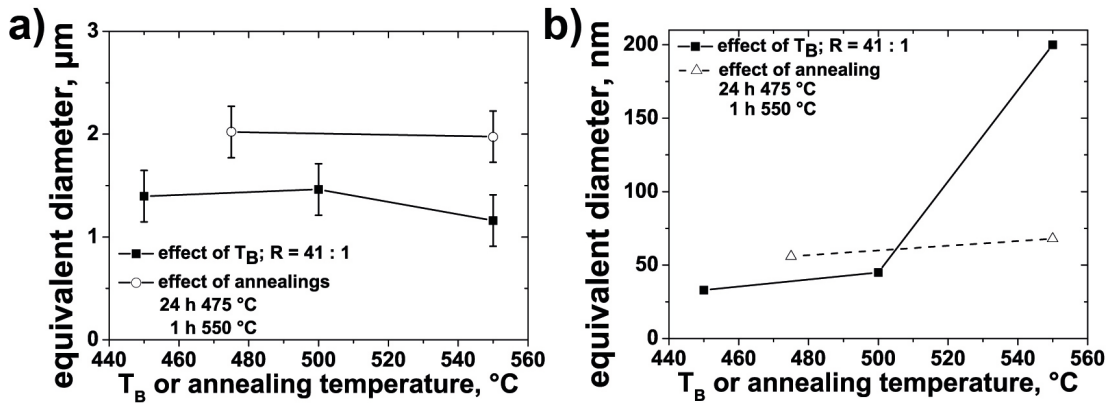


Fig 6.11: Effect of T_B and annealings on the mean equivalent diameter of precipitates: a) coarse $Mg_{12}Ce$, b) fine Mn (error margins are smaller than symbols).

According to Nie [Nie03] the Orowan strengthening for a triangular array of spherical precipitates featuring a uniform diameter d_t can be calculated via:

$$\Delta\tau = \frac{Gb}{2\pi\sqrt{1-\nu}\left(\frac{0.779}{\sqrt{f}} - 0.785\right)d_t} \ln\left(\frac{0.785d_t}{b}\right) \quad (6.1)$$

with G , b , ν and f being the shear modulus of the Mg matrix, the Burgers vector, the Poisson's ratio and the volume fraction of precipitates. Using Eq. 6.1 the strength increment $\Delta\tau$ was calculated for $\langle a \rangle$ basal slip and various precipitate volume fractions. Fig 6.12 displays $\Delta\tau$ as a function of the precipitate diameter, where black symbols correspond to the experimentally determined mean precipitate sizes. From Fig 6.12 a) it is evident that the coarse $Mg_{12}Ce$ do not contribute to the strength of the extrusion.

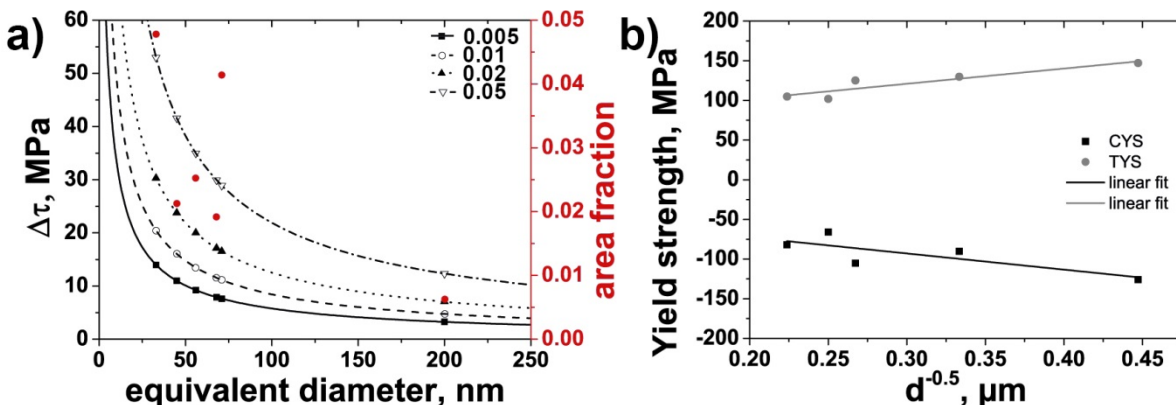


Fig 6.12: a) Orowan strengthening (symbols indicate measured precipitate sizes and area fractions), b) HP plot corrected using $\Delta\tau_{Orowan}$.

In addition, the area fraction of the precipitates (red symbols), which were determined using TEM, are plotted to estimate the precipitate volume fraction of the extruded bars. As the thickness of the TEM foil was not determined, these area fractions provide only a rough approximation of the true volume fraction and should be considered to be the upper boundary of the volume fractions. Nevertheless, Fig 6.12 a) shows that precipitation hardening is negligible in extrusion F ($d_t \approx 200$ nm), while significant hardening is expected in extrusion B ($d_t \approx 33$ nm). Thereby, it was shown that the above derived HP relation is superimposed by precipitation hardening.

In order to separate both parameters a “corrected” HP plot was generated, using the determined area fractions and the calculated $\Delta\tau$ curves and subtracting the resulting $\Delta\tau$ from the experimental yield strengths (Fig 6.12 b)). Interestingly, the corrected HP plots reveal slopes (k), which are very similar to those of the L4 and LA41 extrusion (cf. section 6.4.2.1, Fig 6.16). This shows a similar d_g dependence of the yield strength of the three alloys.

Table 6.2: Precipitate corrected Hall-Petch parameters.

ME21	k, MPa $\mu\text{m}^{0.5}$	σ_0, MPa
CYS	-203	-31
TYS	191	46

The high elongations to failure of the long term high temperature heat treated samples could not be explained solely by d_g and texture effects (cf. section 5.1.3.2 and Fig 6.9). However, the long term heat treatments generate changes of the precipitate size, density and distribution indicating that extraordinary high elongations to failure require the concurrence of an ideal texture, d_g and precipitate distributions.

6.4.1.5 Deformation mode activity and hardening parameters

The conducted experiments and simulations provide insight to the active deformation modes. In case of the ME21 alloy, the compressive deformation is initially realized by TTW-ing, $\langle a \rangle$ prismatic and $\langle a \rangle$ basal slip, while the tensile deformation is almost exclusively realized through $\langle a \rangle$ prismatic slip and $\langle a \rangle$ basal slip (cf. Fig 5.21, Fig 5.22). The obtained hardening parameters of the as-extruded conditions are very similar to those used to model AZ31 (cf. Table 2.3 and Table 5.4) suggesting no particular promotion of one slip mode, while $\langle a \rangle$ basal slip appears to be softened in the heat treated samples. Consequently, $\langle a \rangle$ basal slip appears to be dominant during the initial deformation, even though a previous study [Chi08] suggested an enhanced activity of $\langle a \rangle$ prismatic slip. The finding of $\langle a \rangle$ basal slip predominance is consistent with the texture evolution shown in Fig 5.17, where the RE texture component rotates gradually towards the $\langle 0002 \rangle$ pole. This rotation is attributed to the activation of $\langle a \rangle$ basal slip. In addition, Lynch et al. [Lyn12] provide evidence of a predominance of $\langle a \rangle$ basal slip in an Mg 0.2 wt% Ce alloy using in-situ synchrotron micro XRD. While a predominance of $\langle a \rangle$ basal slip might be little surprising, it was found that the very high elongations to failure of heat treated samples involved an important $\langle c+a \rangle$ pyramidal slip activity, although the CRSS of this deformation mode is comparatively high. The observed high $\langle c+a \rangle$ pyramidal slip activity is most likely attributed to the addition of Ce. DFT simulations by Moitra et al. [Moi14] suggest a promotion of $\langle c+a \rangle$ pyramidal slip through alloying with Ce. As the 550 °C heat treatment results in an increased solubility and water quenching was applied after removing the samples from the furnace, an increased Ce solute content might contribute to an enhanced $\langle c+a \rangle$ pyramidal slip activity and to the remarkable ductility of the alloy. This would be consistent with the lower ratio of $\text{CRSS}_{\text{pyr}} / \text{CRSS}_{\text{prism}}$ in case of the 550 °C heat treated material in comparison to the 475 °C annealed material.

However, the promoting effect of Ce appears to be too small to enable the activation of $\langle c+a \rangle$ pyramidal slip in tension test, where the predicted activity of $\langle c+a \rangle$ pyramidal slip is negligible.

The experimental investigation of TTW-ing showed a high activity of this twin mode. This finding might be surprising as first principle simulations of Muzyk et al. [Muz12] and Shang et al. [Sha14] suggest a decreasing twinnability through Mn additions. However, in the present ME21 alloy Mn is predominantly contained in fine dispersed Mn precipitates and hence the solute concentrations are low, which in turn reduces its impact on the SFEs. Therefore, the alloy exhibits a rather conventional TTW-ing behavior.

6.4.2 WE54

6.4.2.1 Grain size effects

Through the application of various extrusion parameter combinations the d_g of the WE54 extrusions was varied within the range from 7 μm to 23 μm enabling the evaluation of the HP parameters (Eq. 2.2). This data set was extended using the CYS and TYS of 550 $^\circ\text{C}$ annealed samples featuring substantially larger d_g in the range of 80 μm to 230 μm [Wag14]. The determined HP plots and parameters are displayed in Fig 6.13 and Table 6.3:

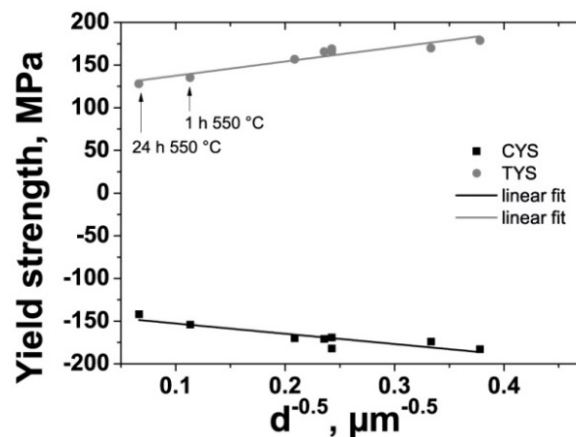


Fig 6.13: Hall-Petch plots considering CYS and TYS of the extrusions. Additional data from annealed samples was taken from [Wag14].

Table 6.3: Macroscopic Hall-Petch parameters.

WE54	k , MPa $\mu\text{m}^{0.5}$	σ_0 , MPa
CYS	-140	-120
TYS	166	120

In comparison to the ME21 extrusion, the WE54 extrusions feature a weaker d_g dependence of the yield strengths (cf. Table 6.1, Table 6.2, Table 6.3), while σ_0 is significantly higher indicating a higher intrinsic strength of the highly alloyed WE54 extrusions. Here, it should be noted that the available spread of d_g is much higher in case of the WE54 alloy. Furthermore, the as-extruded materials contained negligible amounts of coarse ($> 1 \mu\text{m}$) precipitates avoiding a superimposition of d_g and precipitation hardening. In addition, the texture of the materials is close to random and the activation of TTW-ing is significantly hindered as has been shown in section 5.2.4.2 (Fig 5.36, Fig 5.37) and will be discussed in section 6.4.2.2. Consequently, the HP parameters are almost equivalent in tension and compression. Here, the weak extrusion textures impede any correlation between the grain refinement and twinning activity. The higher intrinsic strength of the alloy, which is generated through the high

alloying element concentrations, is captured through the higher σ_0 compared to the other investigated alloys.

6.4.2.2 Twinning

In contrast to the ME21 alloy and most commercial Mg alloys, where TTW-ing occurs readily and overtakes the initial microstructure considering an appropriate strain path (e.g. [Kel58, Bar07a, Lou09, Kha11, Kur14, Len14a, Len15a]), the WE54 features an uncommonly low TTW-ing activity, where both twin nucleation and twin growth are hindered (cf. Fig 5.17, Fig 5.18 (ME21) and Fig 5.36, Fig 5.37 (WE54)). In the as-extruded condition, where the alloying elements are contained in solid solution, the majority of the TTW containing grains are not completely overtaken even at high strains (-18 %).

Interestingly, the TTW-ing activity increases in the age-hardened and the 400 °C annealed samples as has been shown through EBSD analysis (Fig 5.38, Fig 5.39) and EPSC simulations (Fig 5.41, Fig 5.45). These heat treatments result in the generation of considerable amounts of precipitates lowering the solute concentrations at the same time. Therefore, the enhanced TTW-ing activity could be introduced through the reduced solute content or precipitates being obstacles for dislocation movement and hence crystallographic slip. In case of the age-hardened samples both mechanisms superimpose as the 250 °C heat treatments result in the generation of prismatic plate-shaped precipitates within the grains. According to Agnew et al. [Agn13] these precipitates hinder $\langle a \rangle$ basal slip in particular, while the CRSS of TTW-ing appears to decrease. In contrast Robson [Rob14] proposed that prismatic plates harden $\langle a \rangle$ basal, $\langle a \rangle$ prismatic slip and TTW-ing to a similar extent (cf. Fig 2.9). However, large precipitates form at grain boundaries in case of the 400 °C annealing. Being poor obstacles for dislocation movement these precipitates are not expected to harden crystallographic slip importantly, while they reduce the solute concentration of both Y and Nd (Fig 6.6). Therefore, the reduced TTW-ing activity appears to be generated predominantly, through the reduced solute concentrations being consistent with [Agn13]. This interpretation is also supported by a very recent study by Stanford et al. [Sta15] showing that high Y solute concentrations result in a reduced $\{10\bar{1}2\}$ TTW-ing activity and the appearance of $\{11\bar{2}1\}$ twins. They proposed that the large Y atoms ($r_Y = 0.181$ nm; $r_{Mg} = 0.160$ nm [Sha05]) hinder the atomic shuffling processes accompanying the TTW-ing shear. Like Y, Nd features a similarly large atomic radius (0.182 nm [Sha05]) and hence, is likely to hinder TTW-ing analogous.

These results are also in good agreement with the very high τ_0 of TTW-ing in the as-extruded conditions and the significantly reduced τ_0 in the 500 h 250 °C and 24 h 400 °C samples (Table 5.9) providing strong experimental and modeling evidence of pronounced solute hardening of TTW-ing.

6.4.2.3 Texture effects

In contrast to the ME21 alloy, the WE54 extrusions feature very weak textures regardless of the extrusion parameters and the post extrusion heat treatments impeding the experimental analysis of texture effects on the deformation behavior. However, using in-situ EDXRD, EBSD and EPSC simulations the hardening parameters for slip (Table 5.8) and TTW-ing (Table 5.9) were determined enabling the simulation of the flow curves using the above described simulated textures (cf. section 6.4.1.3). Fig 6.14 displays the simulation results employing the hardening parameters of the as-extruded and the 500 h 250 °C condition. The analysis reveals that the weak anisotropy is indeed attributed to the close to random textures

of the investigated materials, where pronounced textures such as the simulated $\langle 0002 \rangle$, $\langle 11\bar{2}2 \rangle$ and $\langle 10\bar{1}0 \rangle$ textures cause a pronounced anisotropy.

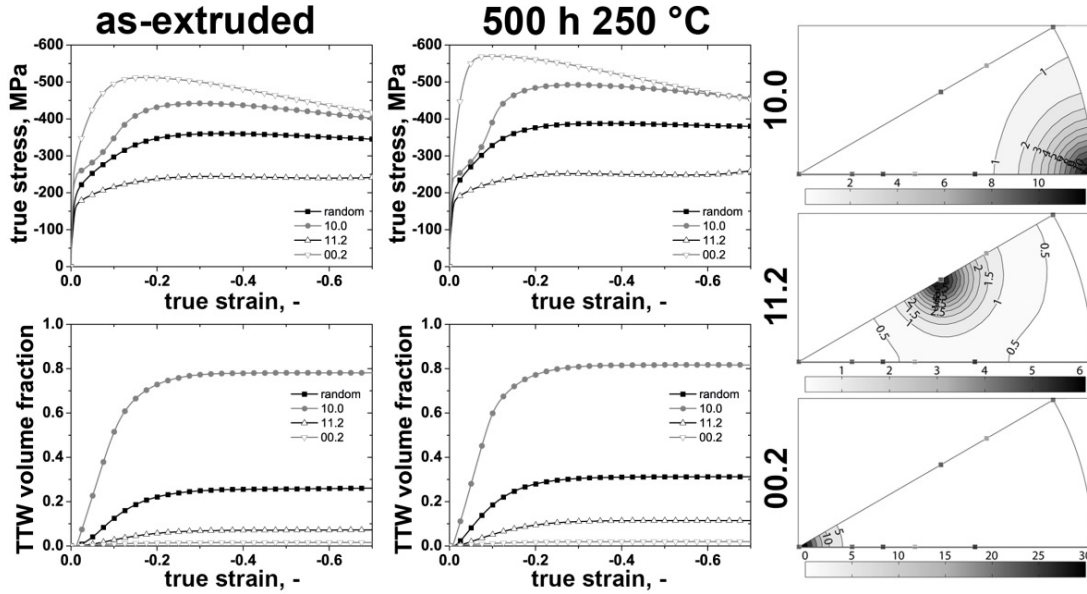


Fig 6.14: EPSC simulations of texture effects on the compression flow curve and TTW volume fraction using the hardening parameters of the as-extruded and 500 h 250 °C conditions (Table 5.8, Table 5.9). IPFs illustrate the model fiber textures.

In agreement with the above described experimental results TTW-ing is hindered and decelerated particularly in the as-extruded condition in comparison to the ME21 alloy, which reflects in a weak sigmoidal shape and lower TTW volume fractions in case of the WE54 alloy. Although, a faster progression of TTW-ing is predicted in the 500 h 250 °C material, the final TTW volume fractions are within the same range for the as-extruded conditions.

Interestingly, a pronounced $\langle 10\bar{1}0 \rangle$ texture features a high TTW volume fraction $\approx 80\%$, although the hardening parameters reveal a very high τ_0 for TTW-ing. This finding is related to a very low SF for $\langle a \rangle$ basal slip and a very high SF for TTW-ing of the $\langle 10\bar{1}0 \rangle$ texture component. Although $\langle a \rangle$ prismatic slip and $\langle c+a \rangle$ pyramidal slip feature high SFs, their relative activities are too small to prevent TTW-ing. In contrast the $\langle 11\bar{2}2 \rangle$ texture, which promotes $\langle a \rangle$ basal slip, as well as the random texture result in low TTW volume fractions. The most pronounced precipitate hardening was predicted in case of the $\langle 0002 \rangle$ texture, which is attributed to the increased τ_0 of $\langle a \rangle$ basal and the increased k_1^s of $\langle c+a \rangle$ pyramidal slip. Both parameters result in higher CRSS of $\langle a \rangle$ basal and $\langle c+a \rangle$ pyramidal slip being the dominant deformation modes in grains corresponding to the $\langle 0002 \rangle$ texture component. These predictions reveal that the absence of the sigmoidal shape of the compression curve and the very low TTW-ing activity are partially generated through the weak extrusion textures.

6.4.2.4 Precipitate and solute effects

In case of the WE54 alloy heat treatments enable the generation of plate-shaped precipitates on $\{10\bar{1}0\}_\alpha$ planes, which contribute to the strength of the extrusions via precipitation hardening. According to Nie [Nie03] the Orowan strengthening of such precipitates can be calculated via:

$$\Delta\tau = \frac{Gb}{2\pi\sqrt{1-\nu} \left(0.825 \sqrt{\frac{d_t t_t}{f}} - 0.393 d_t - 0.886 t_t \right)} \ln \left(\frac{0.886 \sqrt{d_t t_t}}{b} \right) \quad (6.2)$$

where d_t and t_t are the uniform diameter and the uniform thickness of the $\{10\bar{1}0\}_\alpha$ plates. For sake of clarity, the following discussion will focus on plate-shaped precipitates, even though additional globular precipitates were observed in the 16 h 250 °C. The observed plate shaped precipitates displayed an aspect ratio of $\approx 7 : 1$ and of $10 : 1$ in case of the 16 h and the 500 h age-hardened materials and hence the Orowan strengthening was calculated based on these aspect ratios and $\langle a \rangle$ basal slip for a variety of precipitate volume fractions (Fig 6.15). Within a rather broad size distribution the mean thickness and width of the plates were determined using TEM and are summarized in Table 6.4. The area fraction of the precipitates, which will be used as a rough estimate of the precipitate volume fractions, was determined to be $\approx 2\%$ and $\approx 7.5\%$ in case of the 16 h and the 500 °C age-hardened extrusions. Unfortunately, large errors have to be expected in phase fraction determination due to the unknown thickness of the TEM specimen. In comparison to [Agn13], where higher second phase volume fractions ranging from $\approx 6\%$ to 12% were found in cast and subsequently aged WE43 material using Rietveld refinements, these area fractions are surprisingly low.

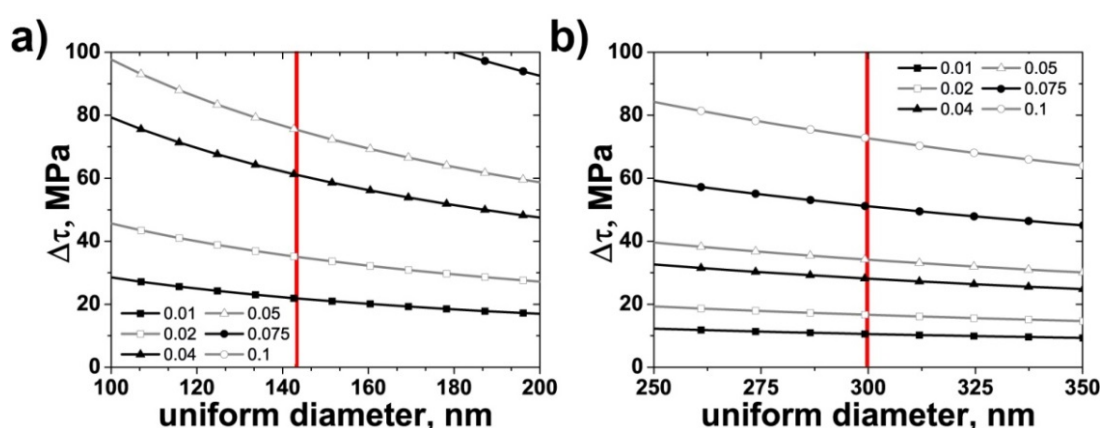


Fig 6.15: Orowan strengthening for prismatic plate-shaped precipitates: a) aspect ratio 7 : 1 (16 h 250 °C), b) aspect ratio 10 : 1 (500 h 250 °C). Red lines illustrate the experimentally determined diameter.

Based on the above determined volume fractions, strength increments of ≈ 35 MPa and ≈ 50 MPa are predicted. These predictions are somewhat higher than the experimentally observed increase of the TYS and CYS during age-hardening (cf. Table 5.7).

Table 6.4: Precipitate geometry.

Sample	Mean thickness, nm	Standard deviation, nm	Mean width, nm	Standard deviation, nm
16 h 250 °C	20	6	145	67
500 h 250 °C	30	10	300	100

The discrepancy of the experimental and the predicted strength increment can be attributed to various factors. First, the reduced solute concentration affects the CYS and the TYS. From Table 5.7, Table 5.8 and Table 5.9 it is evident that the macroscopic strength as well as the τ_0 decrease after a 24 h 400 °C annealing, where the solute concentration is reduced through grain boundary precipitates and only minor changes of d_g occur. In addition, the HP effect is relatively small in this alloy. As the 250 °C annealings result in decreasing alloying element solubilities it is expected that the solute concentration is even lower in the age-hardened samples particularly the 500 h 250 °C sample being consistent with an increased TTW-ing activity in this sample. Second, Eq. 6.2 is derived assuming an ideal arrangement of the precipitates at the center of each surface of a triangular volume in the Mg matrix [Nie03]. Within the present material this ideal arrangement is not entirely fulfilled. Third, the strengthening was calculated with respect to $\langle a \rangle$ basal slip, however, other deformation modes might be less influenced by the precipitates reducing the achieve strength increment. The

conducted EPSC simulations and the investigations of Agnew et al. [Agn13] suggest that $\{10\bar{1}0\}_\alpha$ plates are much more effective in hardening $\langle a \rangle$ basal slip than in hardening other slip modes. In addition, the calculation is based on the Orowan mechanism assuming that gliding dislocations bypass the precipitates and neglecting cutting of precipitates. In case of β plates, which feature a much larger lattice spacing than Mg ([Nie12], Fig 2.16), cutting of precipitates certainly can be excluded, however, the β_1 plates feature a lattice spacing of $a = 0.74$ nm are expected to be coherent across the $\{1\bar{1}00\}_\alpha$ habit plane [Nie00]. Here, cutting of the precipitates might be viable and the cutting stress could be lower than the Orowan stress.

6.4.2.5 Deformation mode activity and hardening parameters

In comparison to the ME21 alloy, the WE54 alloy features higher CRSS in as-extruded and age-hardened condition, a remarkably low TTW-ing activity. The higher strength in as-extruded conditions is predominantly attributed to solid solution hardening, where the WE54 alloy exhibits much higher solubilities than the ME21 alloy and the solute hardening appears to be more effective than the precipitates of the ME21 alloy. During age-hardening the solute concentration drops in the WE54 alloy, however, the precipitate density is higher and the precipitate morphology is more effective in hardening $\langle a \rangle$ basal slip [Nie03] than in the ME21 alloy resulting in a higher strength.

More importantly the WE54 alloy features a higher non-basal slip activity particularly in the as-extruded condition being consistent with prior VPSC simulations, which revealed an increased $\langle c+a \rangle$ pyramidal slip activity in Mg-Y alloys [Agn01]. These constitutive modeling results are further supported through TEM investigations and DFT simulations by Sandlöbes et al. [San11, San12, San13] analyzing pure Mg and binary Mg-Y alloys. According to their studies the I_1 SFE is reduced through Y addition resulting in a high activity of $\langle c+a \rangle$ dislocations gliding on 1st and 2nd order pyramidal planes, as stacking faults I_1 act as a heterogeneous nucleation sources for $\langle c+a \rangle$ pyramidal dislocations [San11, San12, San13, Agn15]. In [San14] an even more pronounced reduction of the I_1 SFE is predicted for Nd addition using first-principle calculations causing a further promotion of $\langle c+a \rangle$ pyramidal slip. Similarly, Zhang et al. [Zha12] predicted decreasing I_1 and I_2 SFEs via Nd alloying. A reduced I_2 SFE could lower the cross-slip probability for basal dislocations causing a less mobile basal dislocation structure and might result in a higher activity of non-basal slip modes [San12]. These experimental and simulation results provide an explanation of the tendency of WE54 alloy to resist textural changes in comparison to ME21 alloy (cf. Fig 5.17 and Fig 5.36). This tendency is caused by the reduced TTW-ing activity and the activation of non-basal slip modes, particularly $\langle c+a \rangle$ pyramidal slip, which generate further grain rotation through crystallographic slip different to the rotation through $\langle a \rangle$ basal slip.

Based on the above discussed microstructural and textural changes, the effect of the microstructure on the hardening parameters of the WE54 alloy can be discussed (Table 5.8, Table 5.9): First, Table 5.8 shows an increase of the slip activation stresses $\tau_{o,f}^S$ in the following order for all morphologies and volume fraction of precipitates: $\langle a \rangle$ basal $< \langle a \rangle$ prismatic $< \langle c+a \rangle$ pyramidal slip, as might be expected for Mg alloys. As has been observed by Agnew et al. [Agn13], the age-hardening has a significant effect on $\langle a \rangle$ basal slip, which is evident from the relative increase of 50 % in $\tau_{o,f}^S$ of $\langle a \rangle$ basal slip comparing the as-extruded and the 500 h age-hardened samples compared to the minor changes in $\tau_{o,f}^S$ for $\langle a \rangle$ prismatic and $\langle c+a \rangle$ pyramidal slip.

Second, the limited TTW-ing activity in the as-extruded and 16 h age-hardened conditions manifests in a remarkably high τ_o^t in these samples, where τ_o^t is in the range of $\tau_{o,f}^s$ for $\langle c+a \rangle$ pyramidal slip being considerably higher than that previously reported in WE43 [Agn13], in AZ31 [Cla08], where τ_o^t is similar to the $\tau_{o,f}^s$ of $\langle a \rangle$ prismatic slip. Here, it should be noted that τ_o^t is much lower in the 500 h age-hardened and the 400 °C annealed samples, where the solute concentration has dropped confirming an important hardening of TTW-ing by solutes as has been suggested in [Sta15] (cf. section 6.4.2.2). Third, $\tau_{o,f}^s$ decreases for all slip modes in the 400 °C annealed sample, where the solute concentrations have dropped through grain boundary precipitation. The modeling provides further evidence that the reduction of the solute concentration significantly reduces the impact of solution hardening, while the low density of precipitates in the grain interior and their size makes them ineffective obstacles for gliding dislocations. At the same time, k_1^s for $\langle c+a \rangle$ pyramidal slip is higher in the 400 °C annealed material than in the other material conditions. k_1^s is related to the rate of dislocation storage during deformation and its increase is likely coupled to the decreasing Y and Nd solute concentrations. As stated earlier, Sandlöbes et al. [San11, San12, San13] proposed a heterogeneous source mechanism, where intrinsic I_1 stacking faults act as a heterogeneous source for $\langle c+a \rangle$ dislocations. Through the reduction of the Y and Nd solute concentrations the I_1 SFE is expected to increase hindering this source mechanism.

6.4.3 L4 and LA41

6.4.2.1 Grain size effects

As has been shown in section 5.3.2.1 and section 5.4.2.1 neither texture modification nor precipitation hardening can be effectively employed in the Li based alloys. Specifically, they do not contain a high density of fine scale precipitates and exhibit textures, which only differ in sharpness. Since the other strengthening mechanisms are not available grain refinement is of particular importance in the L4 and LA41 alloys.

Using the above defined extrusion parameter sets the d_g of the L4 and LA41 extrusions was varied within the range from 5 μm to 30 μm and from 5 μm to 21 μm , respectively. Through the evaluation of the CYS and TYS as a function of $d_g^{-0.5}$ (Fig 6.16), the HP parameters were evaluated (Table 6.5). Being consistent with the EPSC simulations, where the same HP coefficients were used for L4 and LA41 samples (cf. Table 5.19, Table 5.14), the d_g dependence of both alloys was fitted using the same k for both alloys. It appears that the CYS is slightly more sensitive to grain refinement than the TYS, reflecting a previously reported more pronounced HP effect on TTW-ing than on crystallographic slip [Bar04, Boh07b, Bar08b, Pek13, Ill14].

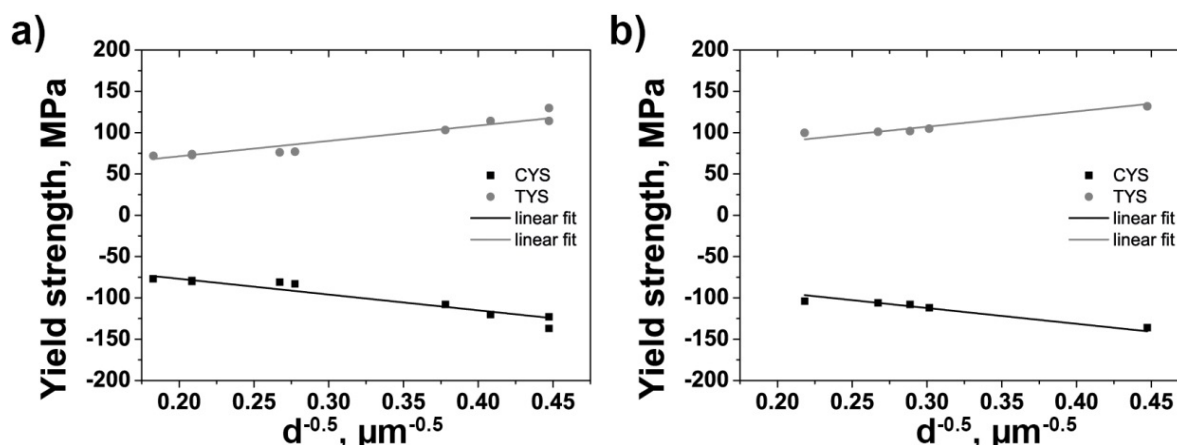


Fig 6.16: Hall-Petch plots considering CYS and TYS of the extrusions: a) L4, b) LA41.

Table 6.5: Macroscopic Hall-Petch parameters.

L4	k, MPa $\mu\text{m}^{0.5}$	σ_0, MPa
CYS	-191	-39
TYS	186	34
LA41	k, MPa $\mu\text{m}^{0.5}$	σ_0, MPa
CYS	-191	-55
TYS	186	51

In addition, to the strengthening effect of grain refinement, it was shown in Fig 5.59 and Fig 5.71 that smaller d_g result in a reduced activity of TTW-ing, CTW-ing and DTW-ing; an effect, which will be discussed in the context of the general twinning behavior in the following section.

6.4.2.2 Twinning

From the flow curves (Fig 5.51, Fig 5.70) and the SDE (Table 5.12, Table 5.17) as well as the conducted EPSC simulations (Table 5.13, Table 5.14, Table 5.18, Table 5.19) it is evident that TTW-ing is hindered in the Li based alloys. However, once twin nucleation has taken place, its propagation occurs readily in comparison to the WE54 alloy generating high TTW volume fractions and overtaking the parent microstructure. As has been shown in the sections 5.3.3.2 and 5.4.3.2 the Li based alloys feature the sequential activation of primary TTW-ing, secondary CTW-ing and tertiary DTW-ing in uniaxial compression according to Fig 2.6.

In Fig 5.52 and Fig 5.53 the sequential activation of the three generations of twins was depicted. From Fig 5.53 it is evident that first CTWs and DTWs have formed at -10 % strain marking the onset of secondary twinning. Interestingly, the relative frequency of CTW boundaries changes only very slightly within the strain range from -10 % to -18 %, while the frequency of type 1 DTWs increases importantly causing a predominance of DTW boundaries (Fig 5.53 b) - c), [Len14a]). Here, it should be noted that the DTWs correspond almost exclusively to type 1 DTWs, although a limited amount of type 2 DTWs was observed.

As the generation of DTWs requires the prior generation of CTWs, the observation of a constant frequency of CTW boundaries in concurrence with a remarkable increase of the frequency of type 1 DTW boundaries indicates that CTWs nucleate profusely in this strain interval and are quickly overtaken by DTWs. This swiftness of the CTW-DTW transition is an important aspect of the nature of DTW-ing. However, it complicates the comprehension of the transition. Therefore, in-situ EBSD experiments were conducted (Fig 5.54) visualizing the CTW-DTW transition dynamically. These experiments indicate a higher mobility of the tertiary TTW boundary compared to the preexisting CTW boundary confirming the suggestions of a high lateral growth rate of the internal twin by Cizek et al. [Ciz08] and Barnett et al. [Bar08a]. This finding is in good agreement with MD simulations by Serra et al. [Ser91] revealing a high mobility of $\{10\bar{1}2\}$ twinning dislocations, responsible for forming the DTW, and a low mobility of $\{10\bar{1}1\}$ twinning dislocations, responsible for the propagation of the CTW. It is also consistent with the suggested high CRSS of CTW-ing in comparison to the low CRSS of TTW-ing [Bar08a]. Based on the ex-situ and in-situ EBSD experiments the following sequence of events was developed: Within the strain range from -10 % to -18 % CTWs form and grow to a thickness of several microns. Once a DTW has nucleated within a secondary CTW, the internal TTW boundary propagates much faster than the CTW boundary causing a swift CTW-

DTW transition, where the DTW prevents further growth of the CTW limiting the DTW thickness.

In order to investigate the origin of the type 1 DTW predominance higher resolution techniques are required and consequently, (HR-)TEM was employed. Using conventional TEM line patterns consisting in parallel lines perpendicular to the basal plane normal of the primary TTW, the secondary CTW and the tertiary DTW were observed (Fig 5.55). The alignment of the line patterns suggests a correlation to a high basal slip activity. A similar line pattern was observed by Li et al. [Li10] within a TTW in commercially pure Mg and attributed to basal stacking faults. In [Par67] it is shown that such stacking faults are generated by the dissociation of $\langle a \rangle$ basal dislocations:

$$\frac{1}{3}[1\bar{2}10] = \frac{1}{3}[0\bar{1}10] + \frac{1}{3}[1\bar{1}00] \quad (6.3)$$

These results indicate that the line pattern is related to a high activity of basal slip and a high propensity of basal dislocation dissociation within the three generations of twins. The finding of a high basal slip activity within the primary TTW might be surprising due to the low SF of $\langle a \rangle$ basal slip. However, the CRSS of $\langle a \rangle$ basal slip is much lower than the CRSS of $\langle c+a \rangle$ pyramidal slip (cf. Table 5.13, Table 5.18). Therefore, a notable activity of $\langle a \rangle$ basal slip can occur within the primary TTW, as has been shown via EPSC simulations (e.g. [Cla08], Fig 5.21, Fig 5.64, Fig 5.76). Irrespective of this finding the secondary CTW and the tertiary DTW feature higher SF for $\langle a \rangle$ basal slip and hence an even higher propensity of this deformation mode.

Any glissile dislocation, which originates within the three twins, will glide through the respective twin. Once a dislocation encounters a grain or a twin boundary it will either pile up or dissociate. The dissociation of basal dislocations generates basal stacking faults, which are particularly important in DTW variant selection. Barnett et al. [Bar08a] proposed a correlation between the predominance of type 1 DTWs and the ease of basal slip in these twins, where the interaction of basal dislocations with twin boundaries results in the formation of twin dislocations. Beyerlein et al. [Bey12] suggested a model correlating DTW variant selection to a sequence of dissociation reactions of dislocations into $\{10\bar{1}2\}$ twin dislocations, where type 1 and type 2 DTWs require the dissociation of basal dislocations, while type 3 and type 4 DTWs are generated through the dissociation of $\langle c+a \rangle$ pyramidal dislocations. The observed predominance of type 1 DTWs and high activity of basal slip support the idea of a dislocation mechanism for $\{10\bar{1}1\}$ - $\{10\bar{1}2\}$ DTW variant selection. Additional experimental evidence for this mechanism was obtained using HR-TEM (Fig 5.56, Fig 5.57, Fig 5.58) allowing the examination of the atomic order and disorder within the vicinity of twin boundaries and the TTW-CTW-DTW triple point. Although the vicinity of this triple point was highly distorted, Fourier filtering enabled the observation of various dislocations.

Several $\langle 0001 \rangle$ dislocations were observed at the TTW-CTW interface and in the distorted area. These dislocations are visible in all twins and were located predominantly within or in the vicinity of the twin boundaries. In addition, various basal dislocations were found within the TTW, the CTW and the DTW with respect to the $(0\bar{1}10)$ planes. The available data does not allow an unambiguous identification of the basal dislocation, however, they are either projections of $\langle a \rangle$ or $\langle 0\bar{1}10 \rangle$ partial dislocations. The latter form through the dissociation of $\langle a \rangle$ dislocations (cf. Eq. 6.3, [Par67]). Based on the above discussed pronounced line pat-

tern, which was attributed to basal stacking faults, it can be assumed that a high number of these dislocations are $\langle 0\bar{1}10 \rangle$ partial dislocations. Most basal dislocations were observed within CTW, while fewer dislocations were found with respect to the DTW and the TTW lattice. Interestingly, a basal dislocation was observed within the above discussed line pattern (cf. Fig 5.58 a), d)) supporting the assumption that the patterns, are coupled to a high basal slip activity and the generation basal stacking faults, as these stacking faults are bounded by $\langle 10\bar{1}0 \rangle$ partial dislocations. The presented experimental results suggest that $\langle a \rangle$ basal dislocations dissociated into two partials at the secondary CTW boundary. This observation is consistent with the nucleation model developed by Beyerlein et al. [Bey12] and provides important experimental evidence of a connection of the predominance of type 1 DTWs and the nature of the dislocations involved in the dissociation reaction.

As DTWs have been associated to flow localizations introducing failure through a high $\langle a \rangle$ basal slip activity within the narrow DTW being surrounded by parent grain featuring a very low SF for $\langle a \rangle$ basal slip [Won67, Bar07b, Ciz08]. Therefore, it is important to identify means of suppressing DTW-ing. In Fig 5.59 and Fig 5.71 it was shown that grain refinement is an effective method suppressing CTWs and consequently DTWs. Similar d_g effects were observed by Tsai et al. [Tsa13] investigating AZ31 material.

Using uniaxial compression parallel to ED three generations of twins were generated within the same set of materials, enabling the examination of their relative dependencies on d_g . Although grain refinement decelerated primary TTW-ing, significant primary TTW volume fractions (between $\approx 65\%$ and $\approx 81\%$; cf. sections 5.3.3.2 and 5.4.3.2) were generated in all samples, while a d_g of $5 \mu\text{m}$ hindered CTW-ing and DTW-ing considerably especially in the L4 alloy. This indicates that CTW-ing features a more pronounced HP effect than TTW-ing. However, the observed contraction twins (CTWs and DTWs) correspond almost entirely to DTWs regardless of the alloy and d_g indicating a weak d_g dependence of the CTW-DTW transition, although, the number of contraction twins and hence the statistical dataset is limited. The present results, the above described low mobility of $\{10\bar{1}1\}$ twinning dislocations [Ser91] and the higher CRSS of CTWs [Bar08a] indicate that the reduction in DTW-ing activity with decreasing d_g is a consequence of a reduced CTW-ing activity in smaller grains. In order to elaborate the d_g effect on DTW-ing further compression tests were conducted perpendicular to ED using the MG extrusion L ($d_g = 23 \mu\text{m}$) and the FG extrusion J. Fig 6.17 illustrates the obtained compression flow curves and the initial textures of both materials. The difference of d_g reflects in a significantly higher CYS in case of the FG material, although, both materials feature comparable textures.

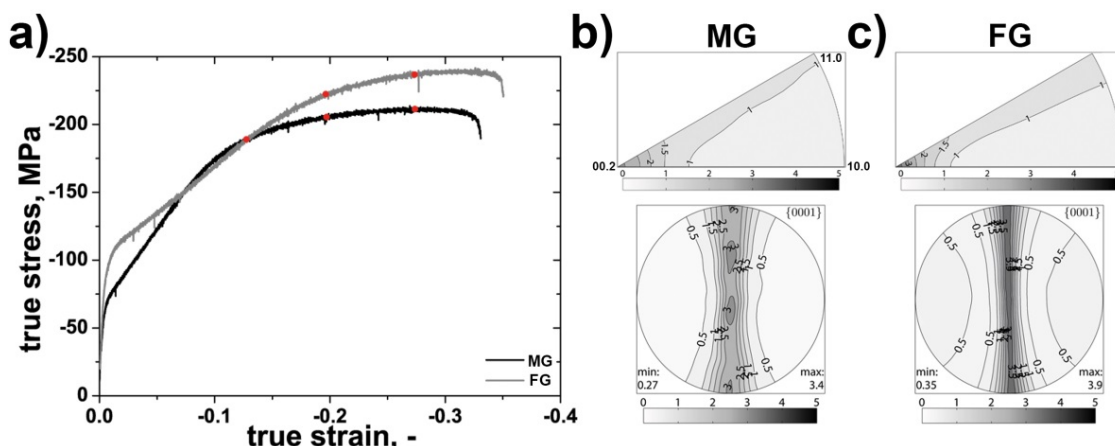


Fig 6.17: a) Compression flow curves \perp ED, b) initial texture of the L4 extrusion L, c) initial texture of the L4 extrusion J.

Due to the initial texture, which features a rotational symmetry with respect to the ED, a portion of the grains are aligned for TTW-ing while others are aligned for c-axis compression. Therefore, both materials feature a very weak sigmoidal shape. However, at strains $> -10\%$ the majority of the grains are aligned for c-axis compression as is evident from EBSD analysis displayed in Fig 6.18 and Fig 6.19. At -12% (engineering) strain several grains contain at least one DTW in case of the MG sample; during further loading the amount of DTWs increases, continuously. In contrast the amount of contraction twins is very limited in the FG material even at very high strains - close to failure. Consistent with the above discussion, the observed contraction twins correspond almost exclusively to type 1 DTWs confirming that the CTW-DTW transition is relatively insensitive to grain refinement. Surprisingly, Fig 6.17 a) shows that both alloys exhibit very similar elongations to failure, even though the MG sample exhibits a significant amount of DTWs at -12% strain being less than 50% of the elongation to failure.

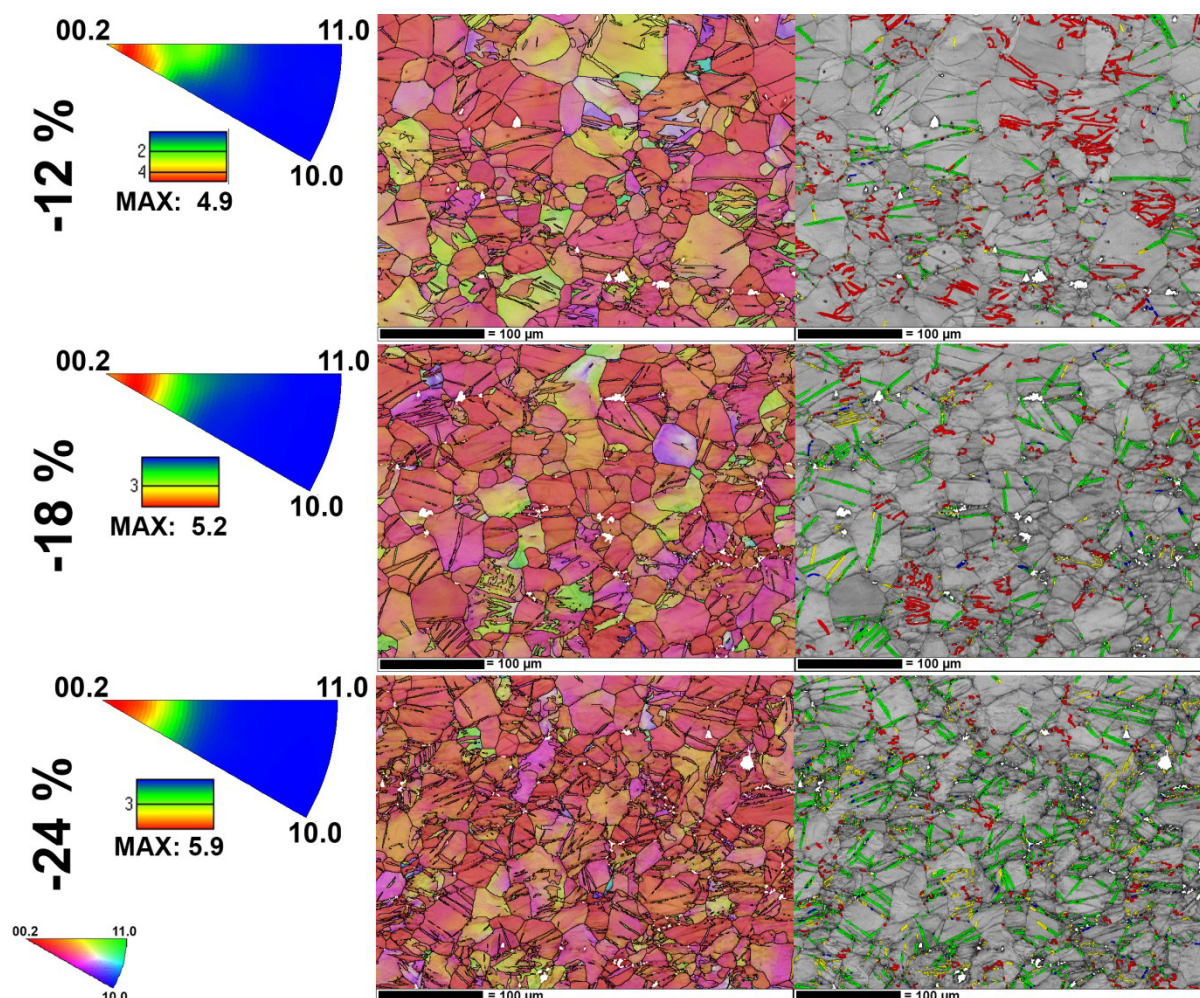


Fig 6.18: EBSD analysis of compression samples (\perp ED) of the extrusion L using IPF maps and BC maps highlighting twin boundaries ($86^\circ \langle 11\bar{2}0 \rangle = \text{red}$, $56^\circ \langle 11\bar{2}0 \rangle = \text{yellow}$, $38^\circ \langle 11\bar{2}0 \rangle = \text{green}$, $30^\circ \langle 11\bar{2}0 \rangle = \text{blue}$) and IPFs.

This finding is contradictory to previous reports correlating DTW-ing to fracture. The concurrence of a high elongation to failure and a high DTW-ing activity might be related to alloying effects promoting slip modes, which enable a sufficient strain accommodation in the vicinity of the DTWs. In addition, the 3D arrangement of the DTWs might influence the strain accommodation. Fig 6.20 displays a high magnification optical micrograph of a grain containing many DTW lamella. These appear to form a 3D network, which could allow deformation in various directions and thereby, contribute to the cumulative strain accommodation. An unam-

biguous explanation of the peculiar coincidence of relatively high elongations to failure and a high DTW density requires additional experiments including sophisticated methods such as 3D EBSD analysis, which are beyond the scope of the present study.

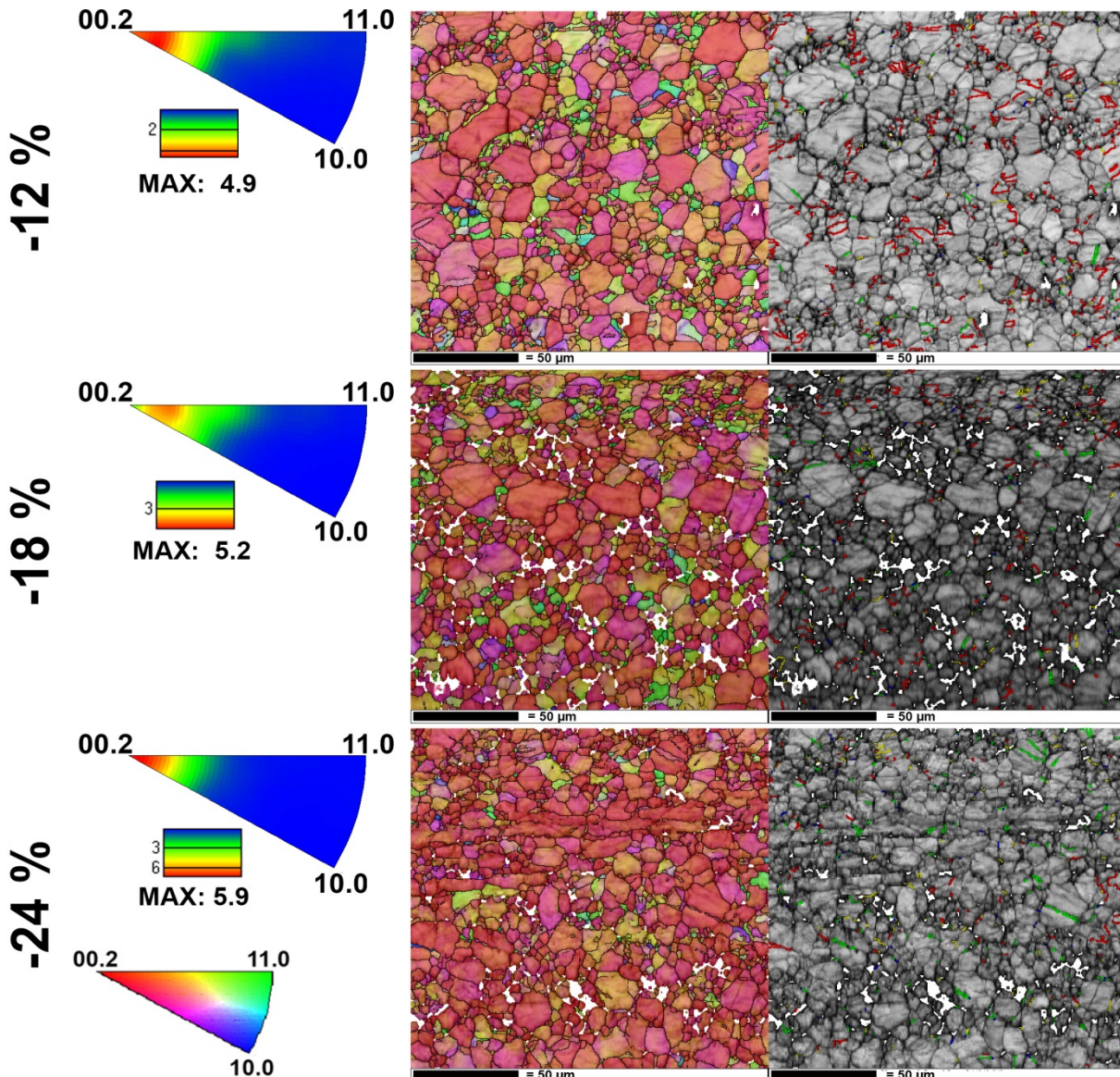


Fig 6.19: EBSD analysis of compression samples (L ED) of the extrusion J using IPF maps and BC maps highlighting twin boundaries($86^\circ \langle 11\bar{2}0 \rangle = \text{red}$, $56^\circ \langle 11\bar{2}0 \rangle = \text{yellow}$, $38^\circ \langle 11\bar{2}0 \rangle = \text{green}$, $30^\circ \langle 11\bar{2}0 \rangle = \text{blue}$) and IPFs.

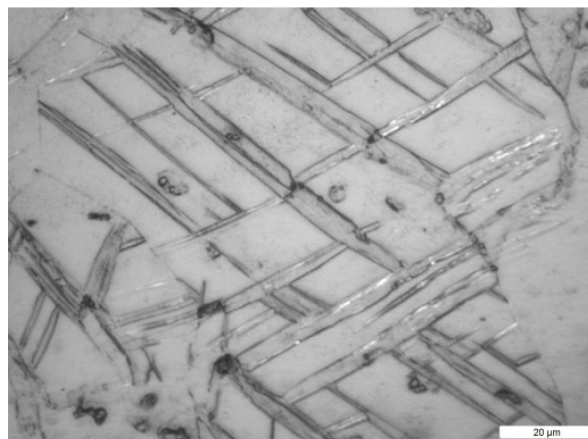


Fig 6.20: Optical micrograph of a compression sample of the MG material (extrusion L). The grains contain a high number of DTWs, which appear to intersect and form networks.

6.4.2.3 Texture effects

In contrast to the ME21 and WE54 extrusions, the L4 and LA41 extrusions feature relatively sharp $\langle 10\bar{1}0 \rangle$ or $\langle 10\bar{1}0 \rangle / \langle 11\bar{2}0 \rangle$ fiber textures (cf. Fig 5.50, Fig 5.69) promoting the activation of TTW-ing during uniaxial compression. In order to evaluate the effect of other textures EPSC simulations were conducted using the hardening parameters of the L4 alloy (Table 5.13, Table 5.14) and $d_g = 30 \mu\text{m}$ (CG) or $5 \mu\text{m}$ (FG). The simulation results are displayed in Fig 6.21.

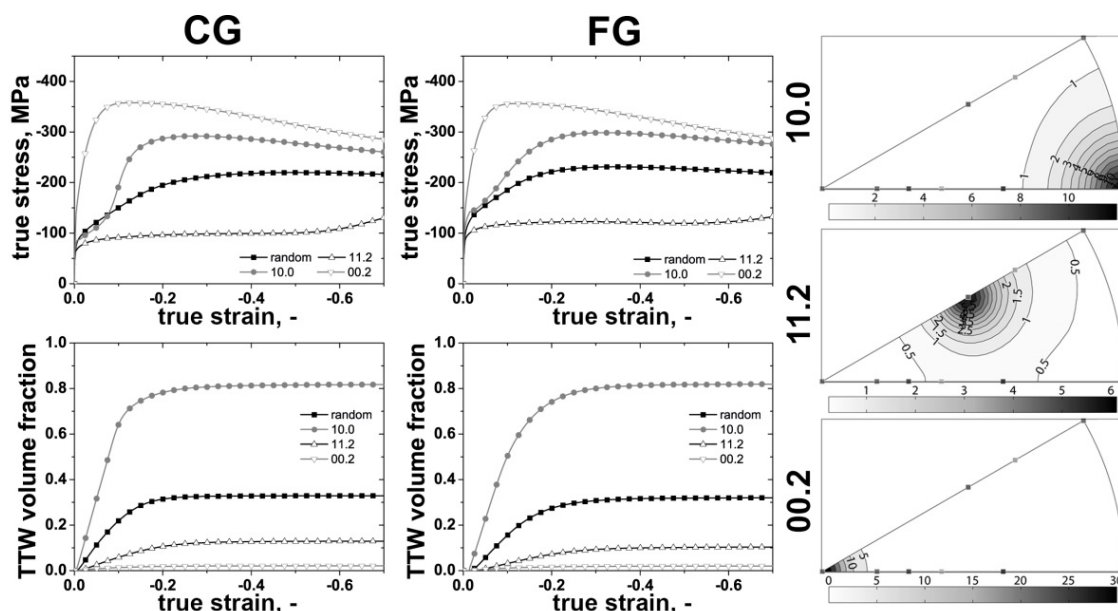


Fig 6.21: EPSC simulations of texture effects on the compression flow curve and TTW volume fraction. The hardening parameters of the CG and FG L4 samples were applied (Table 5.18, Table 5.19; CG = $30 \mu\text{m}$, FG = $5 \mu\text{m}$). IPFs illustrate the model fiber textures.

While the predicted flow curves are qualitatively similar to those of the other alloys some important additional information can be extracted. As might be expected the flow stresses are generally lower than in the ME21 and WE54 alloys. Based on the applied HP parameters the impact of the grain refinement on the yield strength is anisotropic. While the CYS is only increased by about 10 % in case of the $\langle 0002 \rangle$, the increase is in the range of 60 % in case of the $\langle 10\bar{1}0 \rangle$ texture. Comparing the predicted flow curves and the twin volume fractions of the $\langle 10\bar{1}0 \rangle$ textures of the CG material and the corresponding ME21 simulations reveals a deceleration of TTW-ing in case of the L4 alloy. Apparently, the strengthening of TTW-ing is not limited to the formation of TTWs, but also decelerates TTW propagation. This finding is even more pronounced in the FG simulations as the HP coefficient of TTW-ing is higher than those of $\langle a \rangle$ prismatic and $\langle c+a \rangle$ pyramidal slip (Table 5.13, Table 5.14).

6.4.2.4 Precipitates

As has been shown in the sections 5.3.2.1 and 5.4.2.1 the L4 and LA41 extrusions contained several second phases such as (Al)Si rich phases and Mg oxides. The size of these phases varies on the scale of several microns and therefore, no significant precipitation hardening is expected (cf. Eq. 6.1 and Fig 6.12 a)). However, these coarse precipitates or particles limit the elongation to failure of the materials particularly during uniaxial tension. In [Agn01] and [Als09] Li based alloys displayed much higher elongations to failure than the material investigated in the present study. While the microstructure of the alloys is not depicted in detail in [Agn01], Al-Samman [Als09] reported the absence of second phase precipitates in an L4 alloy being consistent with the Mg-Li phase diagram (cf. Fig 2.17 a)). These investigations

and the present results suggest that the limited observed elongations to failure are attributed to the second phase particles.

6.4.2.5 Deformation mode activity and hardening parameters

In comparison to the ME21 and the WE54 alloys the Li based alloys feature a lower strength resulting in low $\tau_{o,f}^s$. However, the L4 and LA41 alloys feature an exceptional TTW-ing behavior, where TTW formation is significantly hindered, but TTW propagation occurs readily in comparison to the WE54 alloy, resulting in uncommonly low yield strength anisotropy, where the CYS is higher than the TYS. In addition, both alloys (L4 and LA41) exhibit a non-negligible $\langle c+a \rangle$ pyramidal slip activity during tension tests. While an enhancement of $\langle c+a \rangle$ pyramidal slip was previously reported [Agn01, Agn02, Als09], the uncommon tension compression anisotropy has not been reported to the author's knowledge.

Through the evaluation of samples featuring different d_g , the slip and twin activation stresses and energies could be evaluated separately from HP effects providing four important findings:

1. The slip activation stresses $\tau_{o,f}^s$ increase in the expected order: $\langle a \rangle$ basal $< \langle a \rangle$ prismatic $< \langle c+a \rangle$ pyramidal slip (cf. Table 5.13, Table 5.18), where the addition of Al increases the $\tau_{o,f}^s$ of all slip modes, while the ranked order is preserved.
2. For both alloys, the twin activation stresses τ_0^t for TTW-ing is higher than $\tau_{o,f}^s$ for $\langle a \rangle$ prismatic (cf. Table 5.13, Table 5.14, Table 5.18, Table 5.19) deviating from the commonly observed ranking for other Mg alloys (e.g. [Cla08, Agn06a, Kne10, Opp12]). However, the high τ_0^t of TTW-ing is in good agreement with the results by Kelley and Hosford [Kel68]. They reported an increasing CRSS for TTW-ing with Li addition investigating Mg single crystals. The conducted EPSC simulations and the findings of Kelley and Hosford suggest that the uncommonly high CYS and the resulting positive SDE are linked to an exceptionally harder TTW-ing compared to prismatic slip.
3. The Al additions diminish the activation stress for TTW-ing τ_0^t . A finding which can be supported by recent first-principles calculations. Muzyk et al. [Muz12] found that Al addition lowers the formation energy of deformation twins, while Shang et al. [Sha14] reported that the propensity twinnability of dilute Mg alloys is lowered through Li additions while Al additions tend to promote the twinnability.
4. The EPSC simulations suggest that Al additions increase the activation energy g^s of $\langle c+a \rangle$ pyramidal slip being consistent with recent DFT calculations. Shang et al. [Sha14] reported that Al additions decrease the SFE I_2 , while Li additions increase this SFE. A higher I_2 SFE of the stacking promotes cross-slip and climb of dislocations [Zha12] being in good agreement with a suggestion made by Agnew et al. [Agn01, Agn02] that the enhancement of $\langle c+a \rangle$ pyramidal slip in Mg-Li alloys could be related to an increase in the basal SFE.

In order to evaluate the correlation between the macroscopic HP effect (Table 6.5, Fig 6.16) and the d_g dependence of the individual deformation modes the HP coefficients given in Table 5.13, Table 5.14, Table 5.18 and Table 5.19 were employed (cf. Eq. 4.14, Eq. 4.16). As has been mentioned above, TTW boundaries were not considered as barriers in simulation. Based on previous studies [Kne10, Opp12, Cap09a] it is assumed that the quick propagation of TTWs makes TTW boundaries ineffective barriers for dislocations.

The performed simulations suggest that $\langle a \rangle$ prismatic slip and TTW-ing feature a higher sensitivity to grain refinement than $\langle a \rangle$ basal and $\langle c+a \rangle$ pyramidal slip (Table 5.13, Table

5.18, Fig 5.63, Fig 5.75) being consistent with previous reports of higher macroscopic HP coefficients for twinning than for slip in other Mg alloys [Bar04, Bar08b, Pek13]. The enhanced d_g dependence of TTW-ing found for the present alloys suggests an important impact of grain refinement on the TTW-ing activity. A finding, which is experimentally confirmed using EBSD in Fig 5.59.

6.5 Mg-Li superlattice

In Fig 5.55 b) and c) the Laue pattern of three domains were evaluated to determine the orientation of a primary TTW, a secondary CTW and a tertiary DTW. Using the $[2\bar{1}\bar{1}0]$ ZA the misorientations of the twins could be directly determined. However, the recorded Laue pattern contained additional (forbidden) $0002n+1$ reflections ($n = 0, \pm 1, \dots$), which were not expected as they do not correspond to hcp diffraction pattern. In order to analyze the origin of these diffraction spots, dark field images were recorded using the “forbidden” reflections to identify potential secondary phases or inclusions that might cause the additional reflection. With this method, however, no additional phases were detected. Rather, each forbidden reflection could be associated with a separate twin region: the primary (red), secondary (yellow) or tertiary (green) twin. These forbidden reflections correspond to a hexagonal primitive lattice and therefore, are presumably caused by a lithium superlattice. If Li atoms are located predominantly in $[1/3, 2/3, 1/2]$ positions the difference in atomic scattering factors of Mg and Li would cause an incomplete extinction of the forbidden reflections being consistent with the investigation of Hauser et al. [Hau56] revealing a decreasing c/a ratio with increasing Li concentration. Based on the smaller atomic radius of Li (0.152 nm, [Sha05]) a predominant localization at the B plane would result in a decreasing length of the c -axis.

The generation of a superlattice is expected to provide an important impact on the activity of crystallographic slip and deformation twinning and is therefore, of great importance. The presented EPSC results indicate that TTW-ing is indeed significantly hindered and $\langle c+a \rangle$ pyramidal slip is enhanced in the L4 alloy (Table 5.13, Table 5.14). However, the unambiguous determination of a superlattice requires additional sophisticated experiments, which are beyond the scope of this research project.

7. Summary and conclusions

Within this study the deformation behavior of the extruded Mg alloys ME21, WE54, L4 and LA41 was investigated using a variety of microscopy and diffraction based techniques as well as crystal plasticity simulations. Covering the process chain from the cast material to semi-finished extruded and heat treated products, the investigations provide processing parameters, which allow to tailor the microstructure and hence the mechanical properties for further forming processes or applications. Through the application of different extrusion parameters and heat treatments a variety of microstructures were generated enabling the investigation of grain size, texture, precipitate and solute effects on the mechanical properties and the deformation behavior of the alloys. The extracted conclusions are summarized briefly:

ME21

- Application of different extrusion parameters and post extrusion heat treatments give rise to a variety of textures enabling the promotion of individual deformation modes through increasing their Schmid factor. The effect of the initial texture on the yield strength is limited considering the experimentally observed texture. However, the subsequent plastic deformation and the final tension twin volume fraction are altered by textural changes.
- Annealing temperatures ≤ 500 °C result in abnormal grain growth generating a bimodal microstructure, where large grains are embedded in a matrix of substantially smaller grains. Grains featuring abnormal grain growth occur at sites, where substructured grains, high internal misorientations and an initial grain size advantage occur simultaneously. High annealing temperatures increase the grain boundary mobility and hence, the growth rate of all grains is increased replacing abnormal grain growth by continuous grain growth and generating a homogeneous microstructure.
- Heat treatments enable the generation of exceptionally high elongations to failure in compression tests. The heat treatments result in important grain growth, reduced precipitate densities and higher equivalent diameters of these as well as an enhanced RE texture component. Thereby, the initial critical resolved shear stress decreases while work hardening is enhanced. Exceptional high compression strains are supported by high $\langle a \rangle$ basal and $\langle c+a \rangle$ pyramidal slip activities. These slip systems balance each other keeping their activities almost constant and causing texture softening. 475 °C heat treated samples display early failure, which is caused by an inhomogeneous microstructure causing high intergranular stresses.
- Although short high temperature heat treatments are sufficient to produce textures favoring the activation $\langle a \rangle$ basal slip, the extraordinary high elongations to failure could not be generated.

WE54

- The WE54 alloy appears to be less sensitive to grain refinement than the other investigated alloys.
- In contrast to most Mg alloys, the WE54 alloy displays a very low $\{10\bar{1}2\}\langle 10\bar{1}\bar{1} \rangle$ tension twinning activity particularly in the as-extruded and 16 h at 250 °C age-hardened conditions.

- The $\{10\bar{1}2\}\langle 10\bar{1}\bar{1}\rangle$ twinning activity increases subsequent to age-hardening for 500 h at 250 °C or 24 h at 400 °C annealing. These heat treatments lower the solute concentrations of Y and Nd and form precipitates within the grain interior or the grain boundaries. The EPSC simulations indicate that precipitate formation at the grain boundaries does not provide suitable obstacles to hinder crystallographic slip. Therefore, the enhanced tension twinning activity of the 400 °C annealed samples cannot be caused by selective hardening of slip, but is generated through lower solute concentrations.
- The plate-shaped precipitates on $\{10\bar{1}0\}_\alpha$ planes, which form during 250 °C age-hardening, are most effective hindering $\langle a \rangle$ basal slip, while other slip modes are only slightly hardened.
- The solid solution hardening of Y, Nd and further heavy rare earth elements is more effective than the precipitation hardening in the ME21 alloy. The experimental data and the simulation results suggest that Y and Nd solutes enhance the activity of the $\langle c+a \rangle$ pyramidal slip system. The tendency of the WE54 alloy to resist textural changes is correlated to the enhanced activation of the $\langle c+a \rangle$ pyramidal slip systems and a reduced activity of $\{10\bar{1}2\}\langle 10\bar{1}\bar{1}\rangle$ tension twinning.

L4 and LA41

- The Li based alloys feature an uncommonly low tension-compression yield, where the compression yield strength is higher than the tension yield strength.
- Alloying 1 wt% Al increases the compression and the tension yield strength by approximately 30 % and the hardening rates.
- The dislocation based EPSC model successfully predicts flow curves, texture evolution and elastic lattice strains allowing the following conclusions: (1) Al addition increases the activation stresses of the basal $\langle a \rangle$, prismatic $\langle a \rangle$ and pyramidal $\langle c+a \rangle$ slip modes, while their relative order is maintained and reduces the activation stress for $\{10\bar{1}2\}\langle 10\bar{1}\bar{1}\rangle$ tension twinning, (2) the Li alloys exhibit an enhanced $\langle c+a \rangle$ pyramidal slip activity, (3) the Hall-Petch coefficients are significantly lower for $\langle a \rangle$ basal slip and $\langle c+a \rangle$ pyramidal slip than for $\langle a \rangle$ prismatic slip and tension twinning, and (4) the positive SDE is generated by a higher activation stress for tension twinning compared to that for $\langle a \rangle$ prismatic slip.
- Coarse grained L4 and LA41 extrusions feature a sequential activation primary $\{10\bar{1}2\}\langle 10\bar{1}\bar{1}\rangle$ tension twinning, secondary $\{10\bar{1}1\}\langle 10\bar{1}\bar{2}\rangle$ compression twinning and tertiary $\{10\bar{1}1\}\{10\bar{1}2\}$ double twinning, where the double twinning activity is remarkably high and the double twins correspond almost exclusively to type 1. The growth rate of internal tension twin (forming the double twin) is much higher than that of the compression twin resulting in a predominance of double twins.
- Basal slip is highly active in the three generations of twins. A high number of basal dislocations was observed in the vicinity of TTW-CTW-DTW triple point. Additionally $\langle 0001 \rangle$ dislocations were observed especially within the TTW-CTW interface.
- Residual secondary compression twins contribute to the strain accommodation within the primary tension twin and the tertiary double twin interface. The primary tension

twin and the tertiary double twin do not possess a common crystallographic twin system, while the secondary compression twin shares a $\{10\bar{1}1\}\langle 10\bar{1}\bar{2}\rangle$ twin boundary with the primary tension twin and a $\{10\bar{1}2\}\langle 10\bar{1}\bar{1}\rangle$ twin boundary with the tertiary double twin.

- Grain refinement suppresses compression twinning and thereby subsequent double twinning. Compression twinning appears to be more grain size sensitive than tension twinning.
- The transition from the compression twin into a double twin is found to be insensitive to grain refinement. It appears that the grain size does not affect double twinning.
- In contrast to previous reports investigating different alloys, the elongation to failure of the Li based alloys is insensitive to the presence of double twins.

8. Directions for future research

Within the conducted research project the large impact of solutes on the deformation behavior of Mg alloys including both crystallographic slip and twinning was observed. While several studies employed first principle simulations to assess the effect of solutes on the stacking fault energies and the deformation behavior have been published (e.g. [Muz12, San14, Sha14]) recently, the experimental analysis of solute effects is not as advanced. The present results as well as other recent publications (e.g. [Agn13, Nie13, Sta15]) provide evidence through experiments and simulations that solutes might be exceptionally effective in hardening twinning, which would at the same time reduce the plastic anisotropy significantly. These finding could motivate further research investigating both the efficiency of solutes in terms of affecting individual deformation modes and the mechanisms involved in hardening particular twin modes. In this regard the potential Mg-Li superlattice, which is suggested by Laue diffraction pattern could be of particular interest. The generation of an ordered structure is expected to have significant impact on the deformation behavior including twinning and might be related to the uncommon tension-compression anisotropy, which was observed in the present study.

The investigation of double twinning could be another topic for additional investigations. As has been shown in section 6.4.2.2 the elongations to failure of the L4 and the LA41 alloys appear to be insensitive to the presence of double twins; a finding, which is contrary to the common assumption of a correlation of double twins and fracture through flow localization. Here, further investigations are required to clarify the origin of the negligible effect of double twins on the elongation to failure in Li based alloys. Subject to the three dimensional arrangement of the double twins, they could enable grain refinement procedures. If the double twin lamellas create a three dimensional network sub-dividing the initial grains many times, suitable annealing of highly deformed samples could be a viable method to generate fine grained materials. Eventually, a supposed double twin network could be used following the concepts of grain boundary engineering. In addition, double twins might be exploited in terms of texture randomization during recrystallization. In this context Hantzsche et al. [Han10] observed the appearance of deformation bands containing twins in RE containing alloys featuring weak textures. If the double twins do not cause preliminary fracture, they introduce additional orientations, which could influence the orientation of the viable recrystallization nuclei.

9. References

- [Abb09] R. Abbaschian, L. Abbaschian, R.E. Reed-Hill: Physical metallurgy principles, Cengage Learning, 4th edition, 2009.
- [Abr04] M.D. Abramoff, P.J. Magalhaes, S.J. Ram: *Biophot. Inter.*, 2004, 11, 36-42.
- [Agn01] S.R. Agnew, M.H. Yoo, C.N. Tomé: *Acta Mater.*, 2001, 49, 4277-4289.
- [Agn02] S.R. Agnew, J.A. Horton, M.H. Yoo: *Metall. Mater. Trans. A*, 2002, 33, 851-858.
- [Agn03] S.R. Agnew, C.N. Tomé, D.W. Brown, T.M. Holden, S.C. Vogel: *Scripta Mater.*, 2003, 48, 1003-1008.
- [Agn05] S.R. Agnew, P. Mehrotra, T.M. Lillo, G.M. Stoica, P.K. Liaw: *Acta Mater.*, 2005, 53, 3135-3146.
- [Agn06a] S.R. Agnew, D.W. Brown, C.N. Tomé: *Acta Mater.*, 2006, 54, 4841-4852.
- [Agn06b] S.R. Agnew, J.W. Senn, J.A. Horton: *JOM*, 2006, 58, 62-69.
- [Agn13] S.R. Agnew, R.P. Mulay, F.J. Polesak III, C.A. Calhoun, J.J. Bhattacharyya, B. Clausen: *Acta Mater.*, 2013, 61, 3769-3780.
- [Agn15] S.R. Agnew, L. Capolungo, C.A. Calhoun: *Acta Mater.*, 2015, 82, 255-265.
- [Ahm65] A. Ahmadi, J. Mitchell, J.E. Dorn: *Trans Metall Soc AIME*, 1965, 233, 1130-1137.
- [Als08a] T. Al-Samman: Magnesium- The role of crystallographic texture, deformation conditions and alloying elements on formability, Cuvillier Verlag, Dissertation, RWTH Aachen, 2008.
- [Als08b] T. Al-Samman, G. Gottstein: *Mater. Sci. Eng. A*, 2008, 490, 411-420.
- [Als09] T. Al-Samman: *Acta Mater.*, 2009, 57, 2229-2242.
- [Als10] T. Al-Samman, X. Li, G. Chowdhury: *Mater. Sci. Eng. A*, 2010, 527, 3450-3463.
- [Als11] T. Al-Samman, X. Li: *Mater. Sci. Eng. A*, 2011, 528, 3809-3822.
- [Als13] T. Al-Samman: *Mater. Sci. Eng. A*, 2013, 560, 561-566.
- [Ant03] C. Antion, P. Donnadieu, F. Perrard, A. Deschamps, C. Tassin, A. Pisch: *Acta Mater.*, 2003, 51, 5335-5348.
- [Bac03] F.-W. Bach, M. Scharper, C. Jaschik: *Mater. Sci. Forum*, 2003, 419-422, 1037-1042.
- [Bac10] F. Bachmann, R. Hielscher, H. Schaeben: *Solid State Phenom*, 2010, 160, 63-68.
- [Bal94] E.A. Ball, P.B. Pragnell: *Scripta Metall. Mater.*, 1994, 31, 111-116.
- [Bar04] M.R. Barnett, Z. Keshavarz, A.G. Beer, D. Atwell: *Acta Mater.*, 2004, 52, 5093-5103.
- [Bar07a] M.R. Barnett: *Mater. Sci. Eng. A*, 2007, 464, 1-7.
- [Bar07b] M.R. Barnett: *Mater. Sci. Eng. A*, 2007, 464, 8-16.
- [Bar08a] M.R. Barnett, Z. Keshavarz, A.G. Beer, X. Ma: *Acta Mater.*, 2008, 56, 5-15.
- [Bar08b] M.R. Barnett: *Scripta Mater.*, 2008, 59, 696-698.
- [Bas13] I. Basu, T. Al-Samman, G. Gottstein: *Mater. Sci. Eng. A*, 2013, 579, 50-56.
- [Bas14] I. Basu, T. Al-Samman: *Acta Mater.*, 2014, 67, 116-133.
- [Bau01] M. Bauser, G. Sauer, K. Siegert: *Strangpressen*, Aluminium-Verlag, 2001.
- [Bey08] I.J. Beyerlein, C.N. Tomé: *Int. J. Plasticity*, 2008, 24, 867-895.
- [Bey10] I.J. Beyerlein, L. Capolungo, P.E. Marshall, R.J. McCabe, C.N. Tomé: *Philos. Mag.*, 2010, 90, 2161-2190.
- [Bey11a] I.J. Beyerlein, R.J. McCabe, C.N. Tomé: *Multiscale Computational Engineering*, 2011, 9, 459-480.

- [Bey11b] I.J. Beyerlein, R.J. McCabe, C.N. Tomé: *J. Mech. Phys. Solids*, 2011, 59, 988-1003.
- [Bey12] I.J. Beyerlein, J. Wang, M.R. Barnett C.N. Tomé: *Proc. R. Soc. A*, 2012, 468, 1496-1520.
- [Boh05] J. Bohlen, S.B. Yi, J. Swiostek, D. Letzig, H.G. Brokmeier, K.U. Kainer: *Scripta Mater.*, 2005, 53, 259–264.
- [Boh07a] J. Bohlen, M.R. Nürnberg, J.W. Senn, D. Letzig, S.R. Agnew: *Acta Mater.*, 2007, 55, 2101-2112.
- [Boh07b] J. Bohlen, D. Letzig, K.U. Kainer: *Mater. Sci. Forum*, 2007, 546-549, 1-10.
- [Boh08] J. Bohlen, S.B. Yi, J. Swiostek, D. Letzig, H.G. Brokmeier: *Scripta Mater.*, 2005, 53, 259-264.
- [Boh10] J. Bohlen, S. Yi, D. Letzig, K.U. Kainer: *Mater. Sci. Eng. A*, 2010, 527, 7092-7098.
- [Brö11] K. Brömmelhoff, M. Huppmann, W. Reimers: *Int. J. Mat. Res.*, 2011, 102, 1133-1141.
- [Bur52] E.C. Burke, W.R. Hibbard: *Trans. Metall. Soc. AIME*, 1952, 194, 295-303.
- [Bun93] H.J. Bunge: *Program System ODF-Analysis*, Cuvillier Verlag, 1993.
- [Cap09a] L. Capolungo, I.J. Beyerlein, C.N. Tomé: *Scripta Mater*, 2009, 60, 32-35.
- [Cap09b] L. Capolungo, P. Marshall, R.J. McCabe, I.J. Beyerlein, C.N. Tomé: *Acta Mater.*, 2009, 57, 6047-6056.
- [Cer07] E. Cerreta, C.A. Yabalinsky, G.T. Gray, S.C. Vogel, D.W. Brown: *Mater. Sci. Eng. A*, 2007, 456, 243-251.
- [Che97] N. Chetty, M. Weinert: *Physical Review B*, 1997, 56, 844-851.
- [Chi08] Y. Chino, M. Kado, M. Mabuchi: *Mater. Sci. Eng. A*, 2008, 494, 343-349.
- [Chr70] J.W. Christian, V. Vitek: *Rep. Prog. Phys.*, 1970, 33, 307-411.
- [Chr95] J.W. Christian, S. Mahajan: *Prog. Mater. Sci.*, 1995, 39, 1-157.
- [Ciz08] P. Cizek, M.R. Barnett: *Scr. Mater.*, 2008, 59, 959-962.
- [Cla08] B. Clausen, C.N. Tomé, D.W. Brown, S.R. Agnew: *Acta Mater.*, 2008, 56, 2456-2468.
- [Cou09] W.A. Counts, M. Friák, D. Raabe, J. Neugebauer: *Acta Mater.*, 2009, 57, 69-76.
- [Czi06] H. Czichos, T. Saito, L. Smith: *Handbook of materials measurement methods*, Springer, 2006.
- [Doh97] R.D. Doherty, D.A. Hughes, F.J. Humphreys, J.J. Jonas, D. Juul Jensen, M.E. Kassner, W.E. King, T.R. McNelley, H.J. McQueen, A.D. Rollett: *Mater. Sci. Eng. A*, 1997, 238, 219-274.
- [Dro04] Z. Drozd, Z. Trojanová, S. Kúdela: *J. Alloy Compd.*, 2004, 378, 192-195.
- [Dud13] N.V. Dudamell, P. Hidalgo-Manrique, A. Chakkedath, Z. Chen, C.J. Boehlert, F. Gálvez, S. Yi, J. Bohlen, D. Letzig, M.T. Pérez-Prado: *Mater. Sci. Eng. A*, 2013, 583, 220-231.
- [Eco83] N. Ecob, B. Ralph: *J. Mater. Sci.*, 1983, 18, 2419-2429.
- [Ege05] R.F. Egerton: *Physical principles of electron microscopy*, Springer Verlag, 1st edition, 2005.
- [Fec13] D. Fechner, C. Blawert, N. Hort, H. Dieringa, K.U. Kainer: *Mater. Sci. Eng. A*, 2013, 576, 222-230.
- [Fri06] H. Friedrich, B.L. Mordike: *Magnesium technology*, Springer Verlag, 1st edition, 2006.
- [Gal01] A. Galiyev, R. Kaibyshev, G. Gottstein: *Acta Mater.*, 2001, 49, 1199-1207.

- [Gal12] S. Gall: Grundlegende Untersuchungen zum Strangpressen von Magnesiumblechen und deren Weiterverarbeitung: Mikrostruktur und mechanische Eigenschaften, Dissertation, TU Berlin, 2012.
- [Gal13] S. Gall, R.S. Coelho, S. Müller, W. Reimers: *Mater. Sci. Eng. A*, 2013, 579, 180-187.
- [Gao12] Y. Gao, H. Liu, R. Shi, N. Zhou, Z. Xu, Y.M. Zhu, J.F. Nie, Y. Wang: *Acta Mater*, 2012, 60, 4819-4832.
- [Geh05] R. Gehrman, M.M. Frommert, G. Gottstein: *Mater. Sci. Eng. A*, 2005, 395, 338-349.
- [Gen07] C. Genzel, I.A. Denks, J. Gibmeier, M. Klaus, G. Wagener: *Nucl. Instrum. Meth. A*, 2007, 578, 23-33.
- [Got07] G. Gottstein: *Physikalische Grundlagen der Materialkunde*, Springer Verlag, 3rd edition, 2007.
- [Guo11] L. Guo, Z. Chen, L. Gao: *Mater. Sci. Eng. A*, 2011, 528, 8537-8545.
- [Had12] J.P. Hadorn, K. Hantzsche, S. Yi, J. Bohlen, D. Letzig, J.A. Wollmershauser, S.R. Agnew: *Metall. Mater. Trans. A*, 2012, 43, 1347-1362.
- [Had13] J.P. Hadorn, R.P. Mulay, K. Hantzsche, S.B. Yi, J. Bohlen, D. Letzig, S.R. Agnew: *Metall. Mater. Trans. A*, 2013, 44, 1566-1576.
- [Haf00] H. Haferkamp, M. Niemeyer, R. Boehm, U. Holzkamp, C. Jaschik, V. Kaese: *Mater. Sci. Forum*, 2000, 350-351, 31-42.
- [Hal51] E.O. Hall: *Pro. Phys. Soc. London*, 1951, B64, 747-753.
- [Han10] K. Hantzsche, J. Bohlen, J. Wendt, K.U. Kainer, S.B. Yi, D. Letzig: *Scripta Mater.*, 2010, 63, 725-730.
- [Han11] J. Han, X.M. Su, Z.-H. Jin, Y.T. Zhu: *Scripta Mater.*, 2001, 64, 693-696.
- [Han14] K. Hantzsche: *Zur Texturentwicklung von gewalzten Seltene-Erden-haltigen Magnesium-Knetlegierungen*, Dissertation, TU Berlin, 2014.
- [Hau56] F.E. Hauser, P.R. Landon, J.E. Dorn: *Trans ASM*, 1956, 48, 986-1002.
- [Hid14] P. Hidalgo-Manrique, S.B. Yi, J. Bohlen, D. Letzig, M.T. Pérez-Prado: *Metall. Mater. Trans. A*, 2014, 45, 3282-3291.
- [Hir82] J.P. Hirth, J. Lothe: *Theory of dislocations*, Krieger Publishing Company, 2nd edition, 1982.
- [Hir13] J. Hirsch, T. Al-Samman: *Acta Mater.*, 2013, 61, 818-843.
- [Hul61] D. Hull: *Acta Metall.*, 1961, 9, 191-204.
- [Hum95] F.J. Humphreys, M. Hatherly: *Recrystallization and related annealing phenomena*, Pergamon, 1st edition, 1995.
- [Hup10a] M. Huppmann, S. Gall, S. Müller, W. Reimers: *Mater. Sci. Eng. A*, 2010, 528, 342-354.
- [Hup10b] M. Huppmann, W. Reimers: *Int. J. Mat. Res.*, 2010, 101, 1264-1271.
- [Hup11] M. Huppmann: *Charakterisierung der Verformungsmechanismen der stranggepressten Magnesiumlegierungen AZ31 und ME21 unter monotoner und zyklischer Belastung*, Dissertation, TU Berlin, 2011.
- [Ill14] K. Illkova, P. Dobroň, F. Chmelík, K.U. Kainer, J. Balík, S. Yi, D. Letzig, J. Bohlen: *J. Alloys Compd.*, 2014, 617, 253-264.
- [Ion82] S.E. Ion, F.J. Humphreys, S.H. White: *Acta Metall.*, 1982, 30, 1909-1919.
- [Jai08] A. Jain, O. Duygulu, D.W. Brown, C.N. Tomé, S.R. Agnew: *Mater. Sci. Eng. A*, 2008, 486, 545-555.
- [JCP00] JCPDS-International Centre for Diffraction Data, PCPDFWIN v. 2.1, 2000.
- [Kai03] K.U. Kainer: *Magnesium – alloys and technologies*, Wiley-VCH, 2003.
- [Kam00] C. Kammer: *Magnesium Taschenbuch*, Aluminium Verlag, 1st edition, 2000.

- [Kel68] E.W. Kelley, W.F. Hosford: *Trans. Metall. Soc. AIME*, 1968, 242, 5-13.
- [Kha11] A.S. Khan, A. Pandey, T. Gnäupel-Herold, R.K. Mishra: *Int. J. Plast.*, 2011, 27, 688-706.
- [Kne10] M. Knezevic, A. Levinson, R. Harris, R.K. Mishra, R.D. Doherty, S.R. Kalidindi: *Acta Mater.*, 2010, 58, 6230-6242.
- [Kne13] M. Knezevic, I.J. Beyerlein, D.W. Brown, T.A. Sisneros, C.N. Tomé: *Int. J. Plasticity*, 2013, 49, 185-198.
- [Koc00] U.F. Kocks, C.N. Tomé, H.-R. Wenk: *Texture and anisotropy*, Cambridge University Press, 1st edition, 2000.
- [Kur14] S. Kurukuri, M.J. Worswick, D.G. Tari, R.K. Mishra, J.T. Carter: *Phil. Trans. R. Soc. A* 372 (2014) doi:10.1098/rsta.2013.0216.
- [Las05] J.F. Lass: *Untersuchungen zur Entwicklung einer magnesiumgerechten Strangpresstechnologie*, Dissertation, Leibniz Universität Hannover, 2005.
- [Len13] M. Lentz, M. Klaus, W. Reimers, B. Clausen: *Mater. Sci. Eng. A*, 2014, 586, 178-189.
- [Len14a] M. Lentz, R.S. Coelho, B. Camin, C. Fahrenson, N. Schaefer, S. Selve, T. Link, I.J. Beyerlein, W. Reimers: *Mater. Sci. Eng. A*, 2014, 610, 54-64.
- [Len14b] M. Lentz, A. Behringer, C. Fahrenson, I.J. Beyerlein, W. Reimers: *Metall. Mater. Trans. A*, 2014, 45, 4737-4741.
- [Len14c] M. Lentz, M. Klaus, R.S. Coelho, N. Schaefer, F. Schmack, W. Reimers, B. Clausen: *Metall. Mater. Trans. A* 2014, 45, 5721-5735.
- [Len14d] M. Lentz, S. Gall, F. Schmack, H.M. Mayer, W. Reimers: *J. Mater. Sci.* 2014, 49, 1121-1129.
- [Len15a] M. Lentz, M. Klaus, I.J. Beyerlein, M. Zecevic, W. Reimers, M. Knezevic: *Acta Mater.*, 2015, 86, 254-268.
- [Len15b] M. Lentz, M. Klaus, M. Wagner, C. Fahrenson, I.J. Beyerlein, M. Zecevic, W. Reimers, M. Knezevic: *Mater. Sci. Eng. A*, 2015, 628, 396-409.
- [Lin63] T.G. Lindley, R.E. Smallman: *Acta Metall*, 1963, 11, 361-371.
- [Li10] B. Li, P.F. Yan, M.L. Sui, E. Ma: *Acta Mater.*, 2010, 58, 173-179.
- [Li11] X. Li, T. Al-Samman, S. Mu, G. Gottstein: *Mater. Sci. Eng. A*, 2011, 528, 7915-7925.
- [Liu14] B.-Y. Liu, J. Wang, B. Li, L. Lu, X.-Y. Zhang, Z.-W. Shan, J. Li, C.-L. Jia, J. Sun, E. Ma: *Nat. Commun.*, 2014, 5, 3297-3303.
- [Lou07] X.Y. Lou, M. Li, R.K. Boger, S.R. Agnew, R.H. Wagoner: *Int. J. Plast.*, 2007, 23, 44-86.
- [Lun13] S. Lun Sin, A. Elsayed, C. Ravindran: *International Materials Reviews*, 2013, 58, 419-436.
- [Lyn12] P.A. Lynch, A.W. Stevenson, D. Liang, C.J. Bettles: *Mater. Sci. Eng. A*, 2012, 550, 1-9.
- [Mad02] R. Madec, B. Devincre, L.P. Kubin: *Phys. Rev. Lett.*, 2002, 89, 255508.
- [Mar10] É Martin, L. Capolungo, L. Jiang, J.J. Jonas: *Acta Mater.*, 2010, 58, 3970-3983.
- [Mec81] H. Mecking, U.F. Kocks: *Acta Metall. Mater.*, 1981, 29, 1865-1875.
- [Mey01] M.A. Meyers, O. Vöhringer, V.A. Lubarda: *Acta Mater.*, 2001, 49, 4025-4039.
- [Mis28] R. von Mises: *Z. Angew. Math. Mech.*, 1928, 8, 161-185.
- [Mis08] R.K. Mishra, A.K. Gupta, P.R. Rao, A.K. Sachdev, A.M. Kumar, A.A. Luo: *Scripta Mater.*, 2008, 59, 562-565.
- [Moi14] A. Moitra, S.-G. Kim, M.F. Horstemeyer: *Acta Mater.*, 2014, 75, 106-112.
- [Mu12] S. Mu, J.J. Jonas, G. Gottstein: *Acta Mater.*, 2012, 60, 2043-2053.

- [Mur03] T. Murai, S. Matsuoka, S. Miyamoto, Y. Oki: *J. Mater. Process. Tech.*, 2003, 141, 207-212.
- [Mur08] O. Muránsky, D.G. Carr, M.R. Barnett, E.C. Oliver, P. Sittner: *Mater. Sci. Eng. A*, 2008, 14-24.
- [Mur10a] O. Muránsky, M.R. Barnett, S. Vogel: *Mater. Sci. Eng. A*, 2010, 527, 1383-1394.
- [Mur10b] O. Muránsky, M.R. Barnett, D.G. Carr, S.C. Vogel, E.C. Oliver: *Acta Mater.* 2010, 58, 1503-1517.
- [Mül03] K. Müller: *Grundlagen des Strangpressens*, Expert Verlag, 2003.
- [Mül07] S. Müller: *Weiterentwicklung des Strangpressens von AZ Magnesiumlegierungen im Hinblick auf eine Optimierung der Mikrostruktur, des Gefüges und der mechanischen Eigenschaften*, Dissertation, TU Berlin, 2007.
- [Muz12] M. Muzyk, Z. Pakiela, K.J. Kurzydowski: *Scripta Mater.*, 2012, 66, 219-222.
- [Nas14] L. Nascimento Silva Ferri: *High cycle fatigue behavior of extruded Mg alloys containing Nd*, Dissertation, TU Berlin, 2014.
- [Nav04] M.D. Nave, M.R. Barnett: *Scr. Mater.*, 2004, 51, 881-885.
- [Nei10] C.J. Neil, J.A. Wollmershauser, B. Clausen, C.N. Tomé, S.R. Agnew: *Int. J. Plast.*, 2010, 26, 1772-1791.
- [Nie99] J.F. Nie, B.C. Muddle: *Scripta Mater.*, 1999, 40, 1089-1094.
- [Nie00] J.F. Nie, B.C. Muddle: *Acta Mater.*, 2000, 48, 1691-1703.
- [Nie03] J.F. Nie: *Scripta Mater.*, 2003, 48, 1009-1015.
- [Nie12] J.F. Nie: *Metall. Mater. Trans. A*, 2012, 43, 3891-3939.
- [Nie13] J.F. Nie, Y.M. Zhu, J.Z. Liu, X.Y. Fang: *Science*, 2013, 340, 957-960.
- [Oba73] T. Obara, H. Yoshinaga, S. Morozumi: *Acta Metall.* 1973, 21, 845-853.
- [Opp12] A.L. Oppedal, H. El Kadiri, C.N. Tomé, G.C. Kaschner, S.C. Vogel, J. C. Baird, M.F. Horstemeyer: *Int. J. Plasticity*, 2012, 30-31, 41-61.
- [Par67] P.G. Partridge: *Metallurgical Reviews*, 1967, 12, 169-194.
- [Pek13] M.O. Pekguleryuz, K.U. Kainer, A.A. Kaya: *Fundamentals of magnesium alloy metallurgy*, Woodhead Publishing, 2013.
- [Per02] M.T. Pérez-Prado, O.A. Ruano: *Scripta Mater.* 2002, 46, 149-155.
- [Pet53] N.J. Petch: *J. Iron and Steel Inst*, 1953, 174, 25-28.
- [Pro07] G. Proust, C.N. Tomé, G.C. Kaschner: *Acta Mater.*, 2007, 55, 2137-2148.
- [Pro09] G. Proust, C.N. Tomé, A. Jain, S.R. Agnew: *Int. J. Plast.*, 2009, 25, 861-880.
- [Qin14] H. Qin, J.J. Jonas: *Acta Mater.*, 2014, 75, 198-211.
- [Qui62] R.M. Quimby, J.D. Mote, J.E. Dorn: *Trans ASM*, 1962, 55, 149-157.
- [Raa14] D. Raabe: *Physical Metallurgy*, Elsevier, 5th edition, 2014.
- [Ran00] V. Randle, O. Engler: *Introduction to texture analysis – microtexture, microtexture and orientation mapping*, CRC, 2000.
- [Rei08] W. Reimers, A.R. Pyzalla, A. Schreyer, H. Clemens: *Neutrons and synchrotron radiation in engineering materials science*, Wiley-VCH, 2008.
- [Rie69] H.M. Rietveld: *J. Appl. Crystallogr.*, 1969, 2, 65-71.
- [Rob09] J.D. Robson, D.T. Henry, B. Davis: *Acta Mater.*, 2009, 57, 2739-2747.
- [Rob10] J.D. Robson, N. Stanford, M.R. Barnett: *Scripta Mater.*, 2010, 63, 823-826.
- [Rob11a] J.D. Robson, N. Stanford, M.R. Barnett: *Acta Mater.*, 2011, 59, 1945-1956.
- [Rob11b] J.D. Robson, D.T. Henry, B. Davis: *Mater. Sci. Eng. A*, 2011, 528, 4239-4247.
- [Rob13] J.D. Robson, N. Stanford, M.R. Barnett: *Metall. Mater. Trans. A*, 2013, 44, 2984-2994.
- [Rob14] J.D. Robson: *Metall. Mater. Trans. A*, 2014, 45, 5226-5235.

- [Roh03] L.L. Rohklin: Magnesium alloys containing rare earth metals, Taylor & Francis, 2003.
- [San96] A. Sanschagrín, R. Tremblay, R. Angers, D. Dubé: *Mater. Sci. Eng. A*, 1996, 220, 69-77.
- [San11] S. Sandlöbes, S. Zaefferer, I. Schestakow, S. Yi, R. Gonzalez-Martinez: *Acta Mater.*, 2011, 59, 429-439.
- [San12] S. Sandlöbes, M. Friák, S. Zaefferer, A. Dick, S. Yi, D. Letzig, Z. Pei, L.-F. Zhu, J. Neugebauer, D. Raabe: *Acta Mater.*, 2012, 60, 3011-3021.
- [San13] S. Sandlöbes, M. Friák, J. Neugebauer, D. Raabe: *Mater. Sci. Eng. A*, 2013, 576, 61-68.
- [San14] S. Sandlöbes, Z. Pei, M. Friák, L.-F. Zhu, F. Wang, S. Zaefferer, D. Raabe, J. Neugebauer: *Acta Mater.*, 2014, 70, 92-104.
- [Sch10] A.J. Schwartz, M. Kumar, B.L. Adams, D.P. Field: *Electron backscatter diffraction in materials science*, Springer, 2nd edition, 2010.
- [Sen08] J.W. Senn, S.R. Agnew: *Magnesium Technology*, 2008, 153-158.
- [Ser91] A. Serra, D.J. Bacon: *Philos. Mag. A*, 1991, 63, 1001-1012.
- [Sha05] J.F. Shackelford: *Werkstofftechnologie für Ingenieure*, Pearson Studium, 6th edition, 2005.
- [Sha14] S.L. Shang, W.Y. Wang, B.C. Zhou, Y. Wang, K.A. Darling, L.J. Kecskes, S.N. Mathaudhu, Z.K. Liu: *Acta Mater.*, 2014, 67, 168-180.
- [Smi07] A.E. Smith: *Surface Science*, 2007, 601, 5762-5765.
- [Son04] G.S. Song, M. Staiger, M. Kral: *Mater. Sci. Eng. A*, 2004, 371, 371-376.
- [Spi09] L. Spieß, G. Teichert, R. Schwarzer, H. Behnken, C. Genzel: *Moderne Röntgenbeugung*, Vieweg-Teubner, 2nd edition, 2009,
- [Sta08a] N. Stanford, M.R. Barnett: *Mater. Sci. Eng. A*, 2008, 496, 399-408.
- [Sta08b] N. Stanford, D. Atwell, A. Beer, C. Davies, M.R. Barnett: *Scripta Mater.*, 2008, 59, 772-775.
- [Sta08c] N. Stanford, M. Barnett: *Scripta Mater.*, 2008, 58, 179-182.
- [Sta09] N. Stanford, M.R. Barnett: *Mater. Sci. Eng. A*, 2009, 516, 226-234.
- [Sta10a] N. Stanford, D. Atwell, M.R. Barnett: *Acta Mater.*, 2010, 58, 6773-6783.
- [Sta10b] N. Stanford: *Mater. Sci. Eng. A*, 2010, 527, 2669-2677.
- [Sta11] N. Stanford, G. Sha, J.H. Xia, S.P. Ringer, M.R. Barnett: *Scripta Mater.*, 2011, 65, 919-921.
- [Sta12] N. Stanford, J. Geng, Y.B. Chun, C.H.J. Davies, J.F. Nie, M.R. Barnett: *Acta Mater.*, 2012, 60, 218-228.
- [Sta15] N. Stanford, R.K.W. Marceau, M.R. Barnett: *Acta Mater.*, 2015, 82, 447-456.
- [Stj05] D.H. StJohn, M. Qian, M.A. Easton, P. Cao, Z. Hildebrand: *Metall. Mater. Trans. A*, 2005, 36, 1669-1679.
- [Sto04] T.B. Stoughton, J.-W. Yoon: *Int. J. Plast.*, 2004, 20, 705-731.
- [Swi06] J. Swiostek, J. Göken, D. Letzig, K.U. Kainer: *Mater. Sci. Eng. A*, 2006, 424, 223-229.
- [Tay38] G.I. Taylor: *J. Inst. Met.* 1938, 62, 307-324.
- [Tom84] C.N. Tomé, G.R. Canova, U.F. Kocks, N. Christodoulou, J.J. Jonas: *Acta Metall.*, 1984, 32, 1637-1653.
- [Tom10] C.N. Tomé, E.C. Oliver, J.A. Wollmershauser: *Code elasto-plastic self-consistent (EPSC)*, Manual version 4, 2010.
- [Tsa13] M.S. Tsai, C.P. Chang: *Materials Science and Technology*, 2013, 29, 759-763.
- [Tur94] P.A. Turner, C.N. Tomé: *Acta Metall. Mater.*, 1994, 42, 4143-4153.

- [Yi04] S.B. Yi, H.-G. Brokmeier, J. Bohlen, D. Letzig, K.U. Kainer: *Physica B*, 2004, 350, e507-e509.
- [Yoo81] M.H. Yoo: *Metall. Trans. A*, 1981, 12, 409-418.
- [Uem06] Y. Uematsu, K. Tokaji, M. Kamakura, K. Uchida, H. Shibata, N. Bekku: *Mater. Sci. Eng. A*, 2006, 434, 131-140.
- [Val06] J.A. del Valle, F. Carreño, O.A. Ruano: *Acta Mater.*, 2006, 54, 4247-4259.
- [Wag14] M. Wagner: *Charakterisierung des Ausscheidungszustandes und der mechanischen Eigenschaften von wärmebehandelten WE54 Strangpressprodukten*, Masterarbeit, TU Berlin, 2014.
- [Wan10] H. Wang, P.D. Wu, M.A. Gharghour: *Mater. Sci. Eng. A*, 2010, 527, 3588-3594.
- [Wat01] H. Watanabe, H. Tsutsui, T. Mukai, K. Ishikawa, Y. Okanda, M. Kohzu, K. Higashi: *Mater. Trans.*, 2001, 7, 1200-1205.
- [Wen03] H.-R. Wenk, L. Lutterotti, S. Vogel: *Nucl. Instrum. Meth. A*, 2003, 515, 575-588.
- [Wen09] L. Wen, P. Chen, Z.-F. Tong, B.-Y. Tang, L.-M. Peng, W.-J. Ding: *Eur. Phys. J. B*, 2009, 72, 397-403.
- [Wen10] H.-R. Wenk, L. Lutterotti, S. Vogel: *Powder Diffraction*, 2010, 25, 283-296.
- [Won67] B.C. Wonsiewicz, W.A. Backofen: *Trans. Metall. Soc. AIME*, 1967, 239, 1422-1431.
- [Zae00] S. Zaefferer: *J. Appl. Cryst.*, 2000, 33, 10-25.
- [Zha12] Q. Zhang, T.W. Fan, L. Fu, B.Y. Tang, L.M. Peng, W.J. Ding: *Intermetallics*, 2012, 29, 21-26.

Project related own publications

M. Lentz, M. Klaus, W. Reimers, B. Clausen: Mater. Sci. Eng. A, 2013, 586, 178-189. *Effect of high temperature heat treatments on the deformation behavior of Mg-2%Mn-0.7%Ce extrusions investigated by in-situ energy-dispersive synchrotron X-ray diffraction and elasto-plastic self-consistent modeling.*

M. Lentz, S. Gall, F. Schmack, H.-M. Mayer, W. Reimers: J. Mater. Sci., 2014, 49, 1121-1129. *Hot working behavior of a WE54 magnesium alloy.*

M. Lentz, R. S. Coelho, B. Camin, C. Fahrenson, N. Schaefer, S. Selve, T. Link, I.J. Beyerlein, W. Reimers: Mater. Sci. Eng. A, 2014, 610, 54-64. *In-situ, ex-situ EBSD and (HR-)TEM analyses of primary, secondary and tertiary twin development in an Mg-4 wt%Li alloy.*

M. Lentz, A. Behringer, C. Fahrenson, I.J. Beyerlein, W. Reimers: Metall. Mat. Trans. A, 2014, 45, 4737-4741. *Grain size effects on primary, secondary and tertiary twin development in Mg-4 wt pct Li (-1 wt pct Al) alloys.*

M. Lentz, M. Klaus, R.S. Coelho, N. Schaefer, F. Schmack, W. Reimers, B. Clausen: Metall. Mat. Trans. A, 2014, 45, 5721-5735. *Analysis of the deformation behavior of magnesium-rare earth alloys Mg-2 pct Mn-1 pct rare earth and Mg-5 pct Y-4 pct rare earth by in situ energy-dispersive X-ray synchrotron diffraction and elasto-plastic self-consistent modeling.*

M. Lentz, M. Klaus, I.J. Beyerlein, M. Zecevic, W. Reimers, M. Knezevic: Acta Mater., 2015, 86, 254-268. *In-situ X-ray diffraction and crystal plasticity modeling of the deformation behavior of extruded Mg-Li-(Al) alloys: an uncommon tension-compression asymmetry.*

M. Lentz, M. Klaus, M. Wagner, C. Fahrenson, I.J. Beyerlein, M. Zecevic, W. Reimers, M. Knezevic: Mater. Sci. Eng. A, 2015, 628, 396-409. *Effect of age hardening on the deformation behavior of an Mg-Y-Nd alloy: In-situ X-ray diffraction and crystal plasticity modeling.*